MONTAN
UNIVERSITÄT
LEOBEN

Chair of Designing Plastics and Composite Materials

Doctoral Thesis

Virtual Optimization of 3D Printed Structures with Tailored Mechanical and Functional Properties

Andreas Thalhamer, M.Sc.

April 2024

MONTANUNIVERSITÄT LEOBEN
www.unileoben.ac.at

AFFIDAVIT

I declare on oath that I wrote this thesis independently, did not use any sources and aids other than those specified, have fully and truthfully reported the use of generative methods and models of artificial intelligence, and did not otherwise use any other unauthorized aids.

I declare that I have read, understood and complied with the "Good Scientific Practice" of the Montanuniversität Leoben.

Furthermore, I declare that the electronic and printed versions of the submitted thesis are identical in form and content.

Date 25.04.2024

Signature Author
Andreas Thalhamer

Acknowledgements

The research work for this thesis was performed within the COMET-Module project "Chemitecture" (project-no.: 21647048) at the Polymer Competence Center Leoben GmbH (PCCL, Austria) within the framework of the COMET-program of the Federal Ministry for Climate Action, Environment, Energy, Mobility, Innovation and Technology and the Federal Ministry for Digital and Economic Affairs with contributions by Montanuniversität Leoben, Technische Universität Dortmund, BTO-Epoxy GmbH, In-Vision Technologies AG and TDK Electronics AG. The PCCL is funded by the Austrian Government and the State Governments of Styria, Lower Austria and Upper Austria.

First of all, I want to thank Univ. Prof. Dr. techn. Clara Schuecker for taking over the academic supervision of this work and for sharing her knowledge and experience with me during our many helpful discussions. Special thanks go to DI Dr. Peter Fuchs, MBA for giving me the opportunity to work at PCCL. I am grateful for all his guidance and support during the last 4 years as my supervisor at PCCL and for encouraging a motivated and friendly working environment in his division. I also want to thank DI Dr. Michael Berer for all the vital feedback and discussions provided, and for including me in all the social events of his work group. My thanks also go to Priv.-Doz. Dr. Sandra Schlögl for taking over the mentorship of this work. I would also like to thank all my coullegues at PCCL for all their help and for creating a pleasant and friendly working atmosphere. In particular I want to thank Mathias Fleisch, whose vast amount of ideas contributed a lot to the progress of this work.

Last but certainly not least, I want to thank my family and friends for their ongoing support and encouragement, without them this work would not have been possible. My deepest gratitude goes to Tina for her love, patience and encouragement which kept me going even in difficult times.

Abstract

Metamaterials are a class of artificially structured materials with special and often unique material properties due to their distinctive unit cell-based periodic architecture. The multiscale nature of metamaterials in combination with the strong link between material properties and unit cell geometry creates a high customization and optimization potential. The actual unit cell geometry, however, can be significantly influenced by the manufacturing process, due to their frequently very intricate, design. The possibility to predict the effect of the manufacturing process on the geometry is therefore vital for the design process and a comprehensive optimization of metamaterials. Their special characteristics lead to the necessity of new strategies tailored specifically towards the design process of metamaterials in order to exploit their full potential.

This thesis presents two simulation-based frameworks to improve the efficiency of the entire design process, and to create the first steps towards a comprehensive optimization strategy for metamaterial parts. Due to the high potential for optimization and the need for an accurate prediction of geometric parameters after manufacturing, an optimization framework and a process simulation tool are developed. The optimization framework covers the optimization of the unit cell distribution in metamaterial components to achieve a predefined deformation behavior. The process simulation complements the optimization framework by the prediction of the manufacturing effects of the Digital Light Processing 3D printing method. The developed optimization framework combines numerical homogenization, stiffness tensor interpolation and Finite Element simulation-based black-box optimization. A separation into a material pre-processing part and the actual optimization part results in an improved optimization efficiency. Furthermore, the addition of an automated material section discretization routine reduces the dependency of the framework on the user-defined material section discretization, and improves the convergence behavior. Regarding the process simulation, a cure kinetics model, a degree of cure-dependent material model and an element activation routine are implemented into the Abaqus Finite Element software. Thereby, the framework facilitates the evaluation of effects such as residual stresses, warpage and print accuracy during the manufacturing process. The developed process simulation uses a modular setup to enable the ability to choose the level of detail, and the associated computational expense based on the user's needs. Additional modules take the effects of the uncured resin surrounding a part and the temperature evolution due to the exothermic reaction into account.

The simulation-based frameworks developed as part of this thesis represent a successful implementation of custom tools to help with designing metamaterial components thus providing a starting point for further development of a comprehensive optimization strategy for supporting their design process.

Kurzfassung

Metamaterialien sind eine Klasse von Materialien mit künstlich erzeugter Struktur, die aufgrund ihres charakteristischen Aufbaus, basierend auf periodisch angeordneten Einheitszellen, spezielle und ungewöhnliche Eigenschaften aufweisen können. Aufgrund der inhärenten „multiscale“ Eigenschaften und des starken Einflusses der Einheitszellengeometrie auf Materialeigenschaften ergibt sich ein hohes Optimierungspotential. Durch den oftmals sehr komplexen und feingliedrigen Aufbau der Einheitszellen kann deren Geometrie jedoch stark vom Herstellungsprozess beeinflusst werden. Dies führt dazu, dass die Vorhersage des Einflusses des Herstellungsprozesses auf die Geometrie auch Bestandteil einer umfassenden Optimierungsstrategie für Metamaterialen sein sollte. Die speziellen Eigenschaften von Metamaterialien erfordern neue, auf deren Eigenheiten angepasste Optimierungsstrategien und Designprozesse, um das volle Potential dieser Materialklasse ausschöpfen zu können.

In dieser Arbeit werden zwei simulationsbasierte Konzepte vorgestellt, welche einerseits einen effizienteren Designprozess ermöglichen sollen und andererseits die Grundlage für eine umfassende Optimierungsstrategie für Bauteile aus Metamaterialien bilden. Aufgrund des hohen Optimierungspotentials und der Notwendigkeit für eine genau Vorhersage der Einflüsse des Herstellverfahren auf die Einheitszellengeometrie wurden ein Optimierungsframework für Metamaterialien und ein Simulationstool für einen 3D Druck Herstellprozess entwickelt. Das Optimierungsframework beinhaltet eine Methode zur Optimierung der Einheitszellenverteilung in Metamaterialien, um ein vordefiniertes Deformationsverhalten zu erreichen. Die Prozesssimulation ergänzt das Optimierungsframework mit der Möglichkeit zur Vorhersage der Fertigungseffekte im „Digital Light Processing“ 3D Druck Verfahren. Das entwickelte Optimierungsframework kombiniert eine numerischen Homogenisierungsmethode, eine Methode zur Interpolation des Steifigkeitstensors und eine Black-Box Optimierungsmethode, basierend auf Finite Elemente Simulationen. Die Unterteilung in einen „Pre-Processing“ Teil und den eigentlichen Optimierungsteil führt dabei zu einem effizienten Optimierungsablauf. Für ein verbessertes Konvergenzverhalten der Methode sorgt eine zusätzliche Routine zur automatischen Anpassung der Diskretisierung der Bereiche mit verschiedenen Materialeigenschaften. Die in der Finite Elemente Software Abaqus implementierte Prozesssimulation des 3D Druck Verfahrens beinhaltet ein Model zur Berechnung der Aushärtekinetik und ein Model zur Bestimmung der aushärtegradabhängigen Materialeigenschaften sowie eine Routine zur Elementaktivierung. Dadurch ermöglicht das Simulationstool die Darstellung von prozessbedingten Eigenspannungen, Verformungen und Abweichungen in der Druckgenauigkeit. Das entwickelte Simulationstool verwendet einen modularen Aufbau und ermöglicht so die Auswahl des Detailgrades der Modellierung und den damit verbundenen rechnerischen Aufwand, basierend auf den Bedürfnissen des Anwenders. Der Einfluss des nicht ausgehärteten Harzes, welches das Bauteil umgibt, auf den Druckprozess sowie die zeitlich abhängige Temperatur-

verteilung aufgrund der exothermen Aushärtereaktion im Prozess können durch zusätzliche Module berücksichtigt werden.

Die beiden, in dieser Arbeit entwickelten, simulationsbasierten Tools stellen eine Implementierung von maßgeschneiderten Methoden für einen effizienten Designprozess von Komponenten aus Metamaterialien dar und bilden damit auch den Startpunkt für die weitere Entwicklung einer umfassenden Optimierungsstrategie für Metamaterialien.

Contents

Part I - Preamble

Part II - Publications

List of Abbreviations and Symbols

Abbreviations

AM	Additive Manufacturing
BESO	Bi-directional Evolutionary Structural Optimization
CAD	Computer Aided Design
CHILE	Cure Hardening Instantaneous Linear Elastic
DLP	Digital Light Processing
DMA	Dynamic Mechanical Analysis
DMD	Micro Mirror Device
ES	Evolutionary Strategies
FE	Finite Element
GA	Genetic Algorithm
LCD	Liquid Crystal Display
MSD	Material Section Discretization
pDSC	Photo Differential Scanning Calorimetry
SIMP	Solid Isotropic Material with Penalization
UC	Unit Cell

Symbols

S_{ij}	Stress tensor entry
ν	Poisson’s ratio

List of Figures

List of Tables

Part I - Preamble

1 Introduction

Artificially structured materials with a wide range of special and often uncommon material properties, also known as metamaterials, have been known for many years. However, due to the steady advancement in additive manufacturing (AM) methods, more and more of these complex structures have crossed the line from hypothetical designs to producible materials. As a consequence, the topic of metamaterials has attracted attention in the scientific community in recent years. This resulted in a wide range of different categories including electromagnetic, acoustic, seismic, thermal, mass transport and mechanical metamaterials which exhibit material properties such as a negative refraction index, bandgaps, near perfect absorption, negative thermal conductivity, negative Poisson's ratio and many more [1]. The underlying concept, which causes the extraordinary properties of most of the metamaterials, is their unit cell (UC) based periodic architecture. Therefore, metamaterials are not only characterized by their constituent material but also, and even more importantly, by their UC design. For material scientists and engineers this opens up immense possibilities regarding the development of new customized materials for special purposes.

In the mechanical context, metamaterials allow for exceptional properties like negative Poisson's ratios [2], [3], high strength to density ratios [4], [5], deformation-rotation coupling [6], high energy absorption [7], [8] and the general possibility to shape the stress-strain behavior and deformation behavior as needed [9]. Responsible for these effects is the deformation behavior of the individual UCs in combination with the spatial periodic stacking [1]. In the case of lattice structures, the size of the UC can also influence the material properties. Due to the so called 'size effect', very small unit cell dimensions can lead to an increase in the strength to density ratio [5]. Mechanical metamaterials can exhibit isotropic, orthotropic or anisotropic material behavior and there are 2D extruded as well as 3D variants [10]. There is already a large number of various UCs to choose from when designing a metamaterial-based part, and the number of newly developed UCs is still rising. The spatial distribution of the UCs with different geometric parameters is another degree of freedom when it comes to the design of metamaterial parts. This creates the means to add property gradients into a part, such as spatially changing stiffness [11] or changing Poisson's ratio [12]. Due to the wide range of achievable overall material properties and the high potential for customizability, the number of possible applications has increased over the past years and includes fields such as medical, aerospace, sport, and textile industry.

The design freedom and customizability go hand in hand with the need for appropriate design and optimization tools to harvest the full potential of metamaterial parts. New strategies are needed to address the complex hierarchical structures with their inherent multi-scaled design problems. Creating an optimized metamaterial part with all its advantages needs some additional steps along the design process compared to a part composed of a conventional material. When designing a part using conventional materials, the fundamental properties are given by the material choice, and the part properties can then be tuned by optimization of the material distribution. In comparison, when designing a metamaterial, the fundamental material properties are defined by the combination of material choice and the UC geometry, and therefore can be tuned and optimized by changing the geometric design of the UC. This tunability of each individual UC in turn allows for the optimization of the spatial material property distribution to improve the part performance.

A step that is shared with the design process for conventional materials, but plays a more important role for metamaterials due to their complex structure, is the assessment of the influences of the manufacturing process on the part geometry. The overall material and part properties of a metamaterial are strongly affected by deviations in the geometry of the individual UCs. Due to their small size and often intricate design, manufacturing of a metamaterial part with a precisely defined UC geometry can be difficult. Thus, knowledge of the effect of the manufacturing process on the geometry as early as possible in the design process is vital. Therefore, process simulations are key to a comprehensive virtual design process of metamaterials. A general overview of the design process and the differences between the two design approaches of conventional and metamaterial parts are highlighted in Fig. 1.1.

The overall objective of this thesis is to unlock the full potential of metamaterials during the design process by developing the basis for an optimization strategy specifically tailored towards metamaterials. Due to the high potential for optimization of the material property distribution and the importance of accurate prediction of geometric parameters after manufacturing, the intention is to combine these two aspects into one comprehensive optimization framework. The present thesis focuses on the development of the two indiviudal simulation frameworks needed to perform the optimization and the manufacturing process effect assessment, which provide the basis for the combined optimization strategy. The combination of the two parts into one single framework is not part of this thesis and is a topic for future work.

For a metamaterial part, optimization can be performed on two different length scales, namely on the UC level and the part level. The main approach to bridge the gap between the UC level and part level is numerical homogenization in order to correlate the UC design to the effective material properties at the part level. A common optimization approach on the UC level is to use topology optimization in combination with computational homogenization to create metamaterials with defined effective material properties [13]–[15]. The focus of this work, however, lies on the optimization of entire metamaterial parts and therefore considers only an optimization strategy on the part level with the usage of parameterized UCs. On the part level, topology optimization can also be used to generate distributions of UCs with varying geometric parameters to improve the lightweight performance of a part [11]. However, when looking at the optimization of the deformation behavior or if trying to achieve

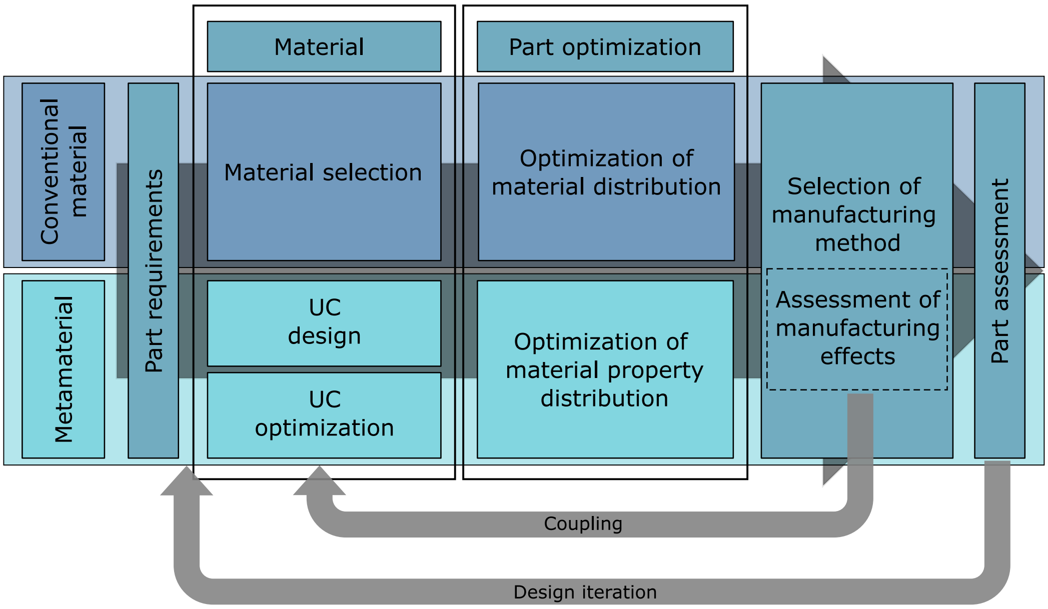

Figure 1.1: Comparison of the design process for a part made from UC-based metamaterials with the design process for conventional isotropic materials.

specific deformation patterns of a entire part, the commonly used density-based topology optimization methods are limited in their objective function, and more general parameter optimization approaches have to be utilized. Methods to solve such parameter optimization problems include the combination of evolutionary algorithms with pre-calculated or analytical correlations between UC geometry and material properties [12].

The objective of the present thesis with respect to the optimization methodology on the part level is to create a framework for the optimization of the unit cell distribution in metamaterial parts. Most of the existing methods are limited to specific types of metamaterials by their choice of design variables or the coupling between effective material properties and design variables. Therefore, the intention is to develop a universal framework, which can be used for various objectives and constraints, as well as with multiple types of metamaterials. At first, simulation tools like standard structure mechanical FE simulation and numerical homogenization are tested and employed during the development of new UC designs in preliminary studies. During these studies information and knowledge about the limitations of the various methods concerning applicability in optimization problems is gathered. This knowledge of is then used for the development of the optimization framework. The framework uses a pre-calculated correlation between unit cell parameter and a full homogenized stiffness tensor in combination with FE simulation-based black-box optimization. The framework is limited to parameterized UCs in order to decrease the amount of design variables for the optimization, and thereby increasing efficiency. The initial implementation of the framework uses a commercial optimization toolbox, and is used to illustrate the concept on simple two-dimensional test cases. A subsequent implementation extends the framework to include a more versatile genetic algorithm (GA), implemented in python, and a method for adapting the spatial material section discretization (MSD). Due to the chosen black-box-based optimization strategy, the developed framework offers high adaptability concerning the selection of optimization objectives and constraints. Furthermore, the general homogenization approach, using the geometric UC parameters and the full stiffness tensor, provides flexibility regarding the types of unit cell-based materials that can be used.

Regarding the topic of the manufacturing effects assessment, the present thesis focuses on AM technologies. AM is the most common way to fabricate metamaterials since it offers optimal freedom to create the intricate structures and details needed. In AM, a part is built by adding layers of material based on the computer aided design (CAD) data of the part [16]. Based on the type of the forming process, AM methods can be classified into material jetting, binder jetting, vat photopolymerization, powder bed fusion, material extrusion, energy deposition and sheet lamination [17]. In vat photopolymerization techniques, each layer of the part is fabricated by curing photo-sensitive resins via illumination from a light source. These techniques offer a high-resolution with respect to print details and therefore are well suited to produce complex structures like metamaterials. In the present thesis the focus is set on the digital light processing (DLP) method, which is a sub-category of the vat photopolymerization-based techniques. It is based on the projection of a light pattern from a projector or screen on photo-curable resins and offers the advantage of high resolution in combination with illumination of the entire layer in one step, and therefore enables fast printing times. For the DLP method, a reliable modeling approach should include the cure kinetics of the material including the thermal behavior, a description of the material properties depending on the degree of cure and temperature of the material, as well as the layer-by-layer build up during printing. Solving of the combined chemical reaction kinetics and the thermo-mechanical problem is achieved by using a dedicated multiphysics solver [18] or by including the reaction kinetics models into standard Finite Element (FE) software [19], [20].

The objective of this thesis with respect to the manufacturing effects assessment is the development of a modular process simulation framework for the assessment of the printed geometry in the DLP additive manufacturing process. The framework is based on an FE simulation including a curing model, an appropriate state of cure-depending material model, and an element activation routine for modeling the layer-by-layer illumination of the resin. An FE implementation is chosen, because it is the most common approach in the literature, and it allows for a good compatibility with the developed optimization framework. In order to differentiate the developed framework from existing methods, a modular approach with multiple levels of modeling detail is chosen, which facilitates the possibility to select the proper degree of model complexity depending on the defined goals and available resources. The main module of the framework contains the necessary parts in order to model the residual stresses and warpage after printing, and additional modules enable the consideration of the effect of uncured resin in cavities and the heat generation during curing.

The thesis is based on the content of the papers A,B,C,D,E and F. In order to facilitate readability Part I of the thesis is divided into Section 2 and Section 3, which each stands for a separate framework, as is shown in Fig. 1.2. Both sections contain a corresponding discussion of the state of the art, as well as a description of the methods used and the respective publication overview. Section 2 and Section 3 are summarized in a combined conclusion. A list of all underlying papers and their full-text versions are given in Part II

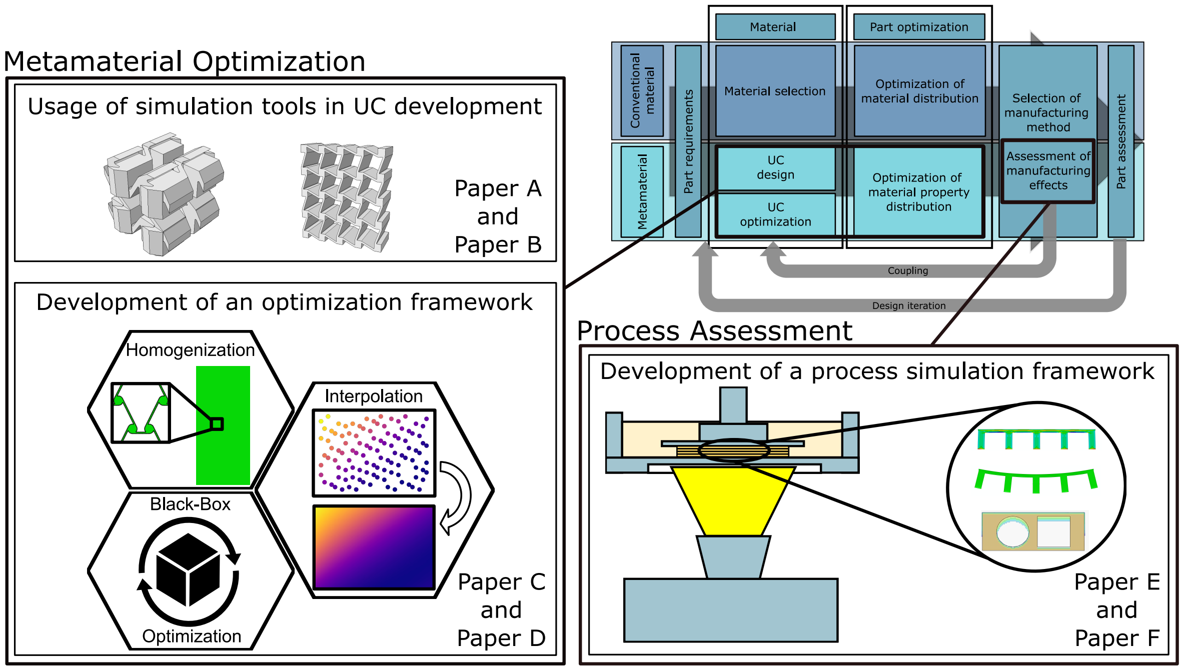

Figure 1.2: Partitioning of the thesis into separate sections with respect to the different steps along the design process of a metamaterial part.

2 Metamaterial Optimization

In this section, the development of a framework for the optimization of the UC distribution on a metamaterial part in order to achieve a defined objective is described. A predefined deformation of a part under a specific load case is chosen as an example of an objective. The aspiration is to create an efficient and flexible framework by combining FE simulation-based black-box optimization strategies, numerical UC homogenization and stiffness tensor interpolation. The basis of the proposed method is the capability of mechanical metamaterials to change their material properties by modifying geometric parameters of the UC.

2.1 State of the Art - Metamaterial Optimization

The inherent multi-scale nature of metamaterials enables the possibility for optimization on different length scales. On the one hand, there is the option to optimize the UC in order to achieve a specific goal regarding the overall mechanical properties, and on the other hand, there is the possibility to optimize the distribution of UCs on the part level. One key factor in both options is the correlation between the design of the UC at the micro scale, and the resulting macro scale material behavior at the part level. Homogenization is a common tool to bridge the gap between the two scales, and it can be used to predict the effective macroscopic properties based on the response of the underlying microstructure [21]. Thereby, it also allows the substitution of FE models consisting of the complex UCs with a simplified model consisting of an equivalent homogeneous material. Simple analytical homogenization methods based on the rule of mixture have been proposed by Voigt [22] and Reuss [23] with the assumption of uniform strain and uniform stress within a heterogenous material, respectively. More sophisticated analytical methods are based on the work of Eshelby [24] and include the Mori-Tanaka model [25], which also approximates the interaction between different phases in a UC. These models however are limited to linear elastic behavior of UCs with ellipsoidal inclusions. For more complex UCs, as they often appear in metamaterials, numerical homogenization methods are commonly used for predicting the material response at the macro scale [26]. They entail the numerical solving of a boundary value problem at the UC level with specific periodic boundary conditions, and the subsequent calculation of the averaged field variables in order to create the homogenized macroscopic properties [27]. This procedure assumes an infinitesimal small UC on the macro scale, and therefore has limitations regarding the size difference between the macro scale and UC size [28]. Furthermore, local effects such as stress concentrations or local deformation behavior cannot be predicted when using a homogenized representation of a given metamaterial.

For the optimization of metamaterial parts, the general concepts of structural optimization can be applied. In structural optimization there are three categories: size optimization, shape optimization, and topology optimization [29]. In size and shape optimization, the basic topology of a structure is prescribed, and only individual geometric parameters are used as design variables for the optimization process. Topology optimization, on the other hand, uses the entire material distribution inside a given design space for the optimization. Concerning structural optimization for metamaterials, both the parameterized shape optimization [9], [12], [30]–[33] as well as topology optimization [11], [13]–[15], [34]–[36] have been used. Although the focus of this thesis lies on the optimization of the UC distribution on the part level, for the sake of completeness the next paragraphs also include a short summery of existing methods for the optimization on the UC level.

On the UC level, topology optimization in combination with numerical homogenization is a common approach to design and optimize metamaterial UC geometries. Schwerdtfeger et al. [13] used the well-known Solid Isotropic Material with Penalization (SIMP) method to improve the auxetic behavior of an initial UC design. To create periodic UC-based materials with a prescribed tangent stiffness tensor, Behrou et al. [14] developed a method using a numerical homogenization approach for the geometrically nonlinear regime combined with a SIMP topology optimization approach. Chen and Huang [15] proposed a combination of a numerical homogenization based on the couple-stress theory and the floating projection topology optimization method to design 3D metamaterials with auxetic properties. Zhang et al. [34] combined an asymptotic homogenization with a SIMP-based topology optimization, and an independent point-wise density interpolation model to enhance the design of bi-material metamaterial UCs. These are only a few examples, a more detailed review of topology optimization in metamaterials can be found in [26].

Machine learning technology has also been used on the UC level in order to further increase the efficiency of various optimization methods in recent years. Challapalli et al. [37] optimized lattice structures with an inverse machine learning approach using generative adversarial networks for an improved compression modulus to density ratio. The network was trained on a data set of lattice structures generated by randomly creating truss connections between a number of fixed vertices. Kollmann et al. [38] predicted optimal 2D metamaterial UC designs regarding bulk modulus, shear modulus, or Poisson's ratio by setting up a convolutional neural network-based deep learning approach. The network was trained on results from topology optimization with various optimization settings. Liao et al. [39] used an inverse design framework with a surrogate model in order to optimize a non-uniform rational basis spline-based tetra-chiral structure, based on a deep neural network. In another approach Garland et al. [40] trained a convolutional network on stiffness and elastic wave speed data from simulations of randomly generated lattice structures, and used the trained network with a genetic algorithm to optimize new UC designs.

The UC concept in metamaterials not only allows for the optimization of the UC itself but also for material property gradients by spatially varying the geometric parameter of the individual

UCs on an object. This principle can be used to optimize the material property distribution on the part level to create a defined mechanical behavior. For that purpose, topology optimization is a widely used tool. Panesar et al. [11] employed the SIMP-based topology optimization and used the resulting volume fraction distribution to define the underlying UC based on libraries of lattice and triply periodic minimal surfaces UCs, thus creating functionally graded parts. This allowed for fast optimization and minimization of the strain energy due to the very efficient implementation, however, the density based SIMP approach limits the application with respect to other optimization objectives. To concurrently optimize the stiffness of a structure and the design of the underlying UCs, Xia and Breitkopf [35] used the Bi-directional Evolutionary Structural Optimization (BESO) algorithm on both size scales. The definition of the material properties at each macroscopic material point was done by numerical homogenization of the optimized cellular material at that point. Zhang et al. [36] proposed a method combining the parametric level set method on the microstructure level, and the SIMP topology optimization on the level of the overall structure, with a numerical homogenization method building the link between the two levels. These concurrent optimization methods exhibit an excellent capability to improve the performance of parts, as each UC is individually optimized for the local loads. This advantage, however, comes with the drawback of very high computational expense and thus limits its applicability.

When working with more general optimization objectives like predefined deformation patterns, the stiffness- or density-based topology optimization strategies are not sufficient, and other approaches have to be employed. A popular methodology is to use general parameterized optimization in the form of simulation-based black-box methods (black-box optimization). Black-box methods consists of unknown functions that, given a list of inputs, generate corresponding outputs without knowledge of the detailed internal structure [41]. In the case of simulation-based black-box optimization, the simulations are treated as the unknown function with only inputs and outputs. A common class of algorithms for the solving of simulation-based black-box optimization problems are heuristic methods. This includes Genetic Algorithms, Evolutionary Strategies (ES), Simulated Annealing, Tabu Search and Simplex Search methods [42]. GA and ES are frequently used for structural optimization problems due to their ability to avoid local optima, handle high dimensionality, and due to their robustness across a wide rang of problem classes [43]. Both algorithms are based on the concepts of natural evolution including selection, crossover, and mutation steps. Selection guarantees the exploitation of solutions with high fitness, whereas crossover and mutation ensure the exploration of the parameter space and the diversity of solutions.

For the optimization of metamaterials on the part level, and in particular for the optimization of the material property distribution in order to create a specific deformation behavior, parameter optimization with the above mentioned methods GA and ES are used in various studies. To create structures with a predefined deformation under a given load, Han and Lu [31] used an evolutionary algorithm with discrete cosine transform encoding to optimize the Poisson's ratio distribution of reentrant honeycomb structures. The fitness evaluation during optimization was based on the difference between the deformation of linear static FE simulations and a given deformation target. The calculation of the correlation between the internal angle in the reentrant cells and the Poisson's ratio of the individual cells was done separately, and during optimization an isotropic material model with a fixed Young's modulus was used, and only the Poisson's ratio of the UCs was varied. The proposed method allowed for efficient optimization, and produced good reproduction of the given deformation patterns. However, using only a simple correlation between internal angle and effective Poisson's ratio in combination with a fixed Young's modulus limits the applicability of the method concerning other types of metamaterials. Yao et al. [12] used a similar approach to optimize the UC-based Poisson's ratio distribution of perforated metamaterials to create a defined lateral deformation of tensile test specimens. They used a differential evolution algorithm to optimize the distribution of five different UCs with varying Poisson's ratios inside a test specimen. The method showed good results for various deformation patterns, but the lack of a general UC homogenization method limits the applicability concerning other types of metamaterials. Recently, Liang et al. [33] developed a new method by using a mathematical relationship between the geometric parameters of individual chiral cells and their deformation vector under load. Combining it with a GA allowed them to design structures with predefined complex deformations. This method offers very fast optimization times due to the direct correlation between UC geometry and deformation. However, it limits the proposed method to the used chiral UCs. Aside from deformation optimization, Abdeljaber et al. [30] used a GA to create an optimal distribution of chiral nodes with different geometric parameters inside a finite flexible beam to reduce the global vibration level. This work shows the versatility of optimized mechanical metamaterials, but the lack of a homogenization approach and the highly problem-specific set up of the optimization decreases the transferability of this method to other problems.

Looking at the state of the art concerning optimization of entire metamaterial parts, three major approaches can be distinguished: density-based topology optimization on the part level, concurrent topology optimization on part and UC level, and parameter optimization with heuristic optimization algorithms. The density-based topology optimization is known for its efficiency but lacks in flexibility with respect to possible objective functions, and in case of concurrent topology optimization, the computational expenses increase significantly. In order to avoid these drawbacks, a parameterized UC in combination with black-box optimization and a GA are chosen for the framework developed in this work. The choice of a parameterized UC reduces the optimization variables, and using a GA ensures flexibility regarding the optimization objectives. To improve the developed framework in comparison to the already existing methods using parameterized optimization, a more general and flexible approach regarding the possible choices of metamaterial UCs is needed. The existing methods are mostly limited to a particular kind of UC due to their specific correlation between UC geometry and effective material properties. In order to overcome this restriction, the developed framework includes a general numerical homogenization method for the correlation between UC geometry and effective material properties. Overall, the objective of this thesis concerning the part optimization is to keep the developed framework as general as possible for applicability with various metamaterials and different optimization objectives, while at the same time keeping it as efficient and robust as possible.

2.2 Methods and Papers - Metamaterial Optimization

To achieve the desired flexibility and generality of the optimization method, black-box optimization, computational homogenization, and stiffness tensor interpolation are combined into a single framework. In Fig. 2.1 the proposed concept for a deformation based optimization of a tri-anti-chiral structure is depicted. To keep it efficient, a sequential approach is chosen to separate the time-consuming task of creating the correlation between UC parameters and homogenized material from the actual optimization task. The correlation is created in a preliminary step by using numerical homogenization and stiffness tensor interpolation. Subsequently, the pre-calculated correlation is used in the optimization step. For high flexibility regarding the objective function, a black-box optimization strategy based on FE simulations with homogenized models is used. The underlying UC discretization of the actual part is represented by partitioning of the homogenized FE models into different material sections. Preliminary studies with a focus on the development of new metamaterials evaluate the capabilities of homogenization and conventional simulation tools and gather information about the advantages and limitations of these methods. A detailed description of these studies is provided in Paper A and Paper B. The initial implementation of the developed framework using a commercial optimization toolbox and testing of the framework by an exemplary optimization of the deformation behavior of tri-anti-chiral metamaterials is described in Paper C. An Extension of the framework including a variable material section discretization (MSD) and utilizing a GA is described in Paper D.

2.2.1 Preliminary Studies

In two studies with the primary focus on designing and developing new metamaterials, FE simulation-based homogenization is used to support the design process. As a fast and efficient way for assessing the linear elastic material behavior of new UC designs during the development process the homogenization method is applied. In addition, it is used for evaluating the influence of the geometric UC parameters on the material behavior. Furthermore, homogenization leads to a reduction in necessary mechanical tests and thus to cost and time savings during the design phase. In both studies the same numerical homogenization method, implemented as a plugin in the commercial FE software Abaqus (Dassault Systemes, Vèlizy-Villacoublay Cedex, France) [44], is used. The method itself is based on six displacement-

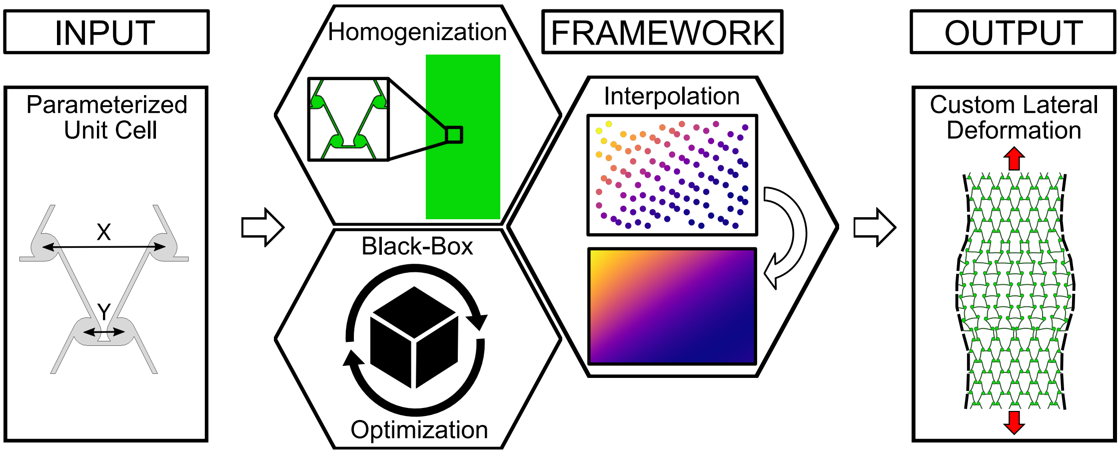

Figure 2.1: Overview of the developed metamaterial optimization concept demonstrated by an example of a tri-anti-chiral material.

controlled FE simulations of the UCs with unit load cases and periodic boundary conditions. During the simulations nonlinear material and geometric behavior can be considered, but due to the generation of a homogenized linear elastic material this effects cannot be transferred to the resulting material. The result of the homogenization is the entire homogenized linear elastic stiffness tensor, which is subsequently used to calculate the needed engineering constants.

The development of a new mechanical metamaterial with independently tunable effective Young's modulus in three spatial directions is described in Paper A. The UC of the developed metamaterial consists of four cubes connected with angled struts in an alternating arrangement, as is shown in Fig. 2.2(a). This arrangement allows for independent variation of stiffness in the three spatial directions. The design of the UC also allows for a variation of geometric UC parameters between two UCs, and thereby enables property gradients along multiple UCs. The development of a chiral-based material which allows for a tunable normal-strain/shear coupling effect is described in Paper B. Chiral structures are a well known type of mechanical metamaterials, and due to their wide range of possible material properties, including auxetic behavior, they are frequently used in relation to optimization tasks [6], [15], [33], [34], [39]. A structure is called chiral if it cannot be superposed to its mirrored image by rotation and translation alone [45]. It typically consists of circular nodes connected with tangentially attached struts. Under mechanical loading the deformation of the struts leads to a rotation of the nodes, which can result in an auxetic behavior of the UC [46]. Chiral structures can be classified by the number of connection struts (tri-, tetra-, hexachiral) or by the type of symmetry inside the UC (chiral, anti-chiral, meta-chiral) [47]. To enhance the tunability of the compression/shear coupling effect of tetra-chiral materials, the circular node inside the UC is changed to a rectangular one and the shape of the bounding box is changed from square to rectangular in the present study. These changes introduce new geometric degrees of freedom for tuning of the normal-strain/shear coupling effect, compression modulus and porosity. A structure comprising of multiple modified UCs is illustrated in Fig. 2.2(b).

In the case of both developed metamaterials, homogenization of the individual UCs is used to assess the influence of the geometric parameters on the considered material properties and demonstrate the improved tunability of the new UC designs. 3D printed samples are used in compression tests to characterize the compression modulus as well as the shear coupling effect in case of the tetra-chiral structure. The capability of the homogenization method to predict the linear elastic material behavior of the newly developed metamaterials is validated with a standard mechanical FE simulation of the whole test samples as well as with the results of the compression tests. The comparison of the compression modulus for various sample geometries for the variable stiffness structure and the shear coupling structure, respectively, is depicted in Fig. 2.2(a) and Fig. 2.2(b). The results of the comparison show a good agreement between predicted values of the compression modulus via homogenization, the prediction via FE simulations of the samples and the actual compression test results. However, due to the limitation of the used homogenization approach concerning the prediction of only linear elastic material behavior, other approaches have to be used if nonlinearities are to be considered.

The gained general knowledge from the preliminary studies regarding the use of homogenization and general FE simulation tools for metamaterials is used to help with the development of the optimization framework. Especially the selection of a suitable homogenization and optimization strategy is based on the results of the preliminary studies.

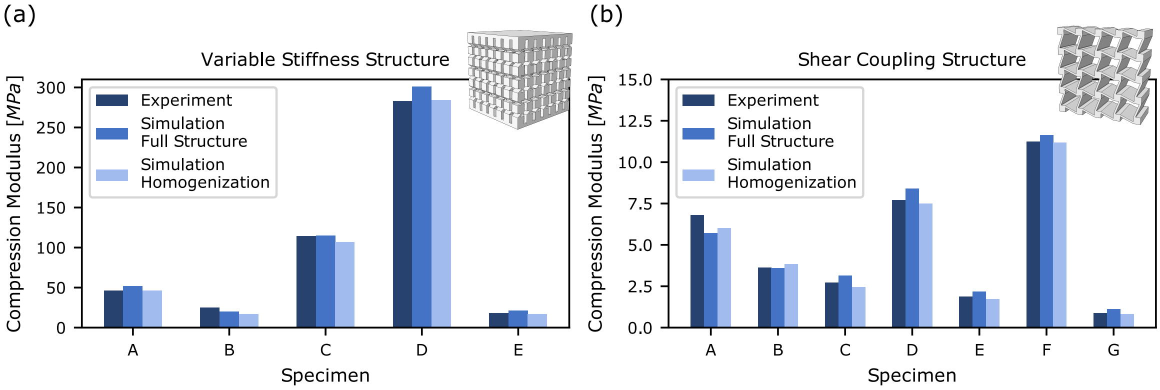

Figure 2.2: Comparison of the compression modulus between experimental results, simulation of full structures and homogenization of a single UC using different test samples for (a) the variable stiffness structure and (b) the shear coupling structure.

2.2.2 Initial Optimization Concept

The framework is separated in a material pre-processing part and a black-box optimization part (Fig. 2.1). In the material pre-processing part, the correlation between the UC parameters and the respective homogenized material behavior is defined. Before starting with the material pre-processing, the changeable geometric parameters of the UC and the range of the parameters have to be defined for the investigated metamaterial. During pre-processing, numerical homogenization is performed for multiple UCs with varying values of its geometric parameters within the defined parameter space. The homogenization method is the same as used in the preliminary studies. Subsequently, the continuous correlation between UC parameters and homogenized stiffness tensor is created by linear interpolation between the individual tensor entries of all the different UCs. The material pre-processing step has to be done only once for a given metamaterial, and not for each optimization run. The resulting interpolation object is exported to the black-box optimization part of the framework in order to facilitate a fast correlation between UC parameters and homogenized material properties during runtime. In the present thesis, the black-box consists of a FE simulation of the homogenized version of the given metamaterial part. To account for areas with different UC parameters, the models are partitioned into multiple material sections. This allows for the clustering of UCs with the same parameters and results in a reduction of the overall number of variables during the optimization. Inputs for the black-box are the geometric parameters of the UCs in each material section, and output is the difference of the deformation of a given point, edge or surface of the FE model to a specific target deformation under a given load. During optimization, the input of the black-box serves as design variables for the optimization and the output as result of the objective function. For the initial concept, the commercially available tool LSOPT (LS-OPT 6.0.0/Livermore Software Technology Corporation, Livermore, CA, USA) with a sequential metamodel-based optimization with domain reduction is used for the black-box optimization problem. A detailed description of the initial framework and first test examples, as well as a discussion of its advantages and limitations can be found in Paper C.

The basis for testing the developed framework is a tri-anti-chiral metamaterial with additional geometric parameters and a newly developed transition unit cell. The design of the UC used is based on the work in [3], and the work from Paper B. The additional geometric degrees of freedom allow for a wide range of obtainable Poisson's ratios from negative to positive values. In addition, the design facilitates the variation of the Poisson's ratio within the structure. The objective of the optimization tests is the creation of predefined lateral deformations of simple 2D shapes under tensile load by optimizing the distribution of the tri-anti-chiral UCs. The FE models for the simulations consist of a homogenized representation of the examined structures with multiple material sections, representing the areas consisting of UCs with different geometric parameters. A linear elastic material model defined by a full anisotropic stiffness tensor is used to describe the material behavior of the homogenized material. The stiffness tensor in turn is calculated by the interpolation object from the pre-processing step. For testing of the framework, an interpolation object is created based on the homogenization of 961 tri-anti-chiral UCs with varying geometric parameters. The accuracy of the interpolation object is evaluated for 900 points in the parameter space in between the initial data points used for the interpolation object. The resulting interpolation error is found to be very small for the stiffness tensor entries, as well as the calculated engineering constants. Furthermore, the applicability of the homogenization approach used is tested at several values of global strains by performing simulations of a fully modelled tri-anti-chiral structure under several load conditions, and comparing the resulting lateral deformations with simulations of the homogenized counterpart. The comparison identifies the tensile load case to be the most critical concerning the deviation between fully modeled and homogenized structures, with a limit for an accurate representation of 1% global deformation of the structure under tension.

The optimization framework is then tested on various predefined lateral deformation patterns with different numbers of material sections, in which geometric parameters are changed. Examples of lateral deformation targets under load in Y-direction with the defined material section discretization of the homogenized part, and the respective results of the optimization in terms of the optimized distribution of the Poisson's ratio are shown in Fig. 2.3(a) and Fig. 2.3(b). Overall, the results demonstrate the ability to optimize the UC distribution to create the given deformation patterns for the chosen examples. However, the accuracy of the framework is significantly reduced for large deformations due to the limits of the implemented homogenization approach. Furthermore, the fixed number and distribution of material sections have a significant impact on the convergence behavior of the optimization, and therefore the choice of the material section distribution is a potential area to improve the optimization framework.

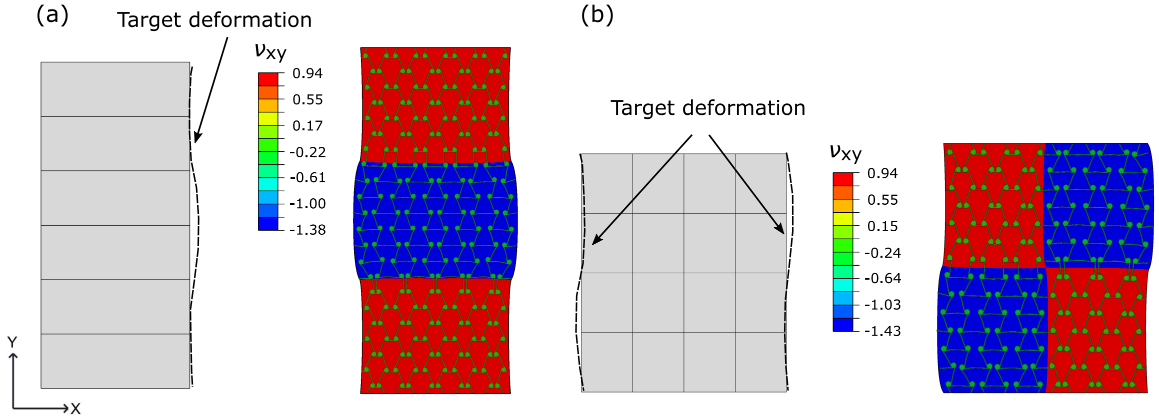

Figure 2.3: Material section discretization, target deformation and the resulting Poisson's ratio distribution after optimization for (a) a part with 1x6 material sections and for (b) a part with 4x4 material sections.

2.2.3 MSD Algorithm

In order to improve the generality and the overall convergence behavior of the developed framework, it is extended with an adaptive material section discretization scheme. The idea is to link the local resolution of the MSD to a variable field of the optimization with adaptive updating during run time. Thus, the user-defined initial resolution of the MSD can be kept coarser, and the necessary knowledge of the required MSD resolution for a good result is reduced. A more effective MSD is also expected to help with the encountered convergence problems caused by high resolution MSDs.

An MSD evaluation algorithm is integrated into the initial framework to enable the adaptive MSD updating scheme. In order to facilitate this integration, a genetic algorithm [48], implemented in python, is used instead of the commercial LSOPT optimizer. The GA solves an optimization problem by performing fitness-based selection, crossover, and mutation operations on a population of variables over multiple generations. The material pre-processing part with the homogenization and the tensor interpolation is kept unchanged from the initial optimization concept. The overall goal of the optimization stays the same, namely the creation of a predefined lateral deformation under load by optimization of the UC distribution. Likewise, the processes of setup and solving of the homogenized simulations inside the optimization loop remains unchanged. The general steps during the optimization are now the following:

1. The MSD algorithm is initialized based on the user input about the minimal and maximal MSD size and spatial discretization of the given part.
2. For the first run of the GA, the variable sets of the initial population are randomly generated inside the parameter space of the given UC.
3. The GA optimization is started and the parent selection, crossover, mutation and fitness evaluation steps are performed for each generation to optimize the UC distribution on the part.
4. After a user-defined number of generations, the specified field variables are exported to the MSD algorithm.
5. Based on the field variables and given decision criteria, the MSD is locally updated and refined.
6. The new MSD is exported to the GA, and a new initial population is built from the last one with additional variables according to the new MSD.
7. The process starts again at step 3.
8. The entire optimization process is stopped when either the stopping criterion of the MSD algorithm, or one of the stopping criteria of the GA is satisfied.

The MSD algorithm does not directly influence or control the optimization procedure of the GA, it only acts as a soft constraint by specifying the local refinement of the MSD depending on a chosen UC-based variable. Therefore, the effect of the MSD algorithm on the efficiency and accuracy of the optimization depends on the selection of the field variable. The tri-anti-chiral structures which are already known from the initial concept are used for testing, and the gradient of the geometric UC variables is used as the field variable for the MSD updating algorithm. The variable gradient is chosen since it is directly affected by the resolution of the MSD, and thereby is able to control the MSD refinement properly. A reduction in the variable gradients should also lead to a reduction in material property gradients, and thus reduce the possibility of high stress and strain discontinuities. The variable gradient can also be seen as an example of a possible manufacturing constraint since high variable gradients may pose a problem to manufacturability. In the present study the influence of the variable gradient on material property gradient, stress discontinuities, and manufacturability of tri-anti-chiral materials is not explored in detail. The variable gradient is only used to demonstrate the implementation of the combined MSD and GA algorithm. A detailed description of the extended framework can be found in Paper D.

The capabilities of the extended optimization framework are again tested with a tri-anti-chiral metamaterial. Simple 2D rectangular structures with various predefined lateral deformation patterns are used. Initially the extended framework with a fixed MSD is compared to the initial concept in order to evaluate the performance of the GA on its own. Furthermore, comparisons regarding variable gradient, convergence, and accuracy are made for various deformation patterns between optimization with and without MSD updating algorithm. The GA on its own, without the MSD algorithm, leads to a decrease in performance. However, the open source python implementation of the GA allows for an easy adaption and implementation of additional parts as shown with the MSD updating algorithm. Activation of the MSD algorithm results in a decreased time to reach the same accuracy (maximum fitness) compared to the initial concept. For the comparison example, the local refinement of the MSD algorithm leads to a reduction in the number of material sections used, and thereby increases the efficiency of the optimization. For the tested target deformations, as shown in Fig. 2.4(a), the activation of the MSD algorithm results in an improvement of performance compared to the examples with the GA only, as is shown in Fig. 2.4(b). Furthermore, the local refinement of the MSD scheme leads to a decrease in the mean variable gradient. However, the refinement can lead to an increase of the variable gradient in individual material sections due to the lack of a strict constraint on the material gradient. Overall, the extension of the initial concept with an adaptive material section discretization scheme is another step towards a more generalized and efficient optimization method.

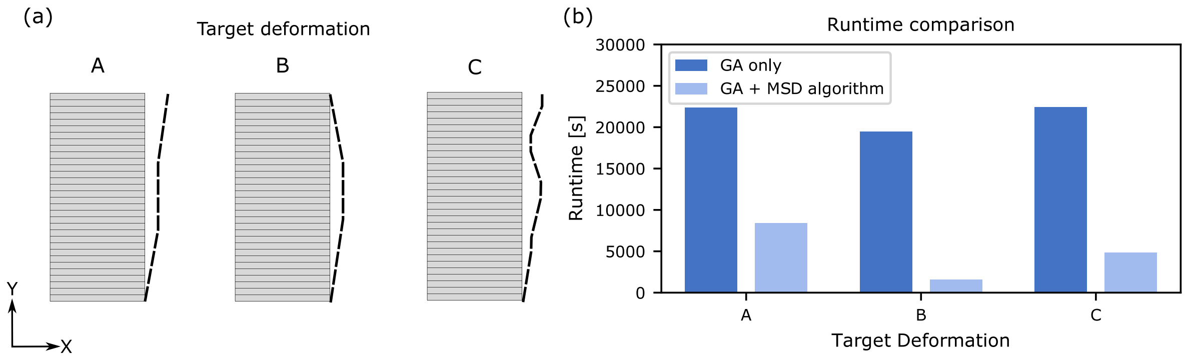

Figure 2.4: Depiction of (a) the tested target deformation patterns and (b) the respective optimization runtimes to achieve the maximum fitness with and without activated MSD algorithm .

3 Process Assessment DLP

This section describes the development of a simulation framework to predict the influences of the manufacturing process on geometry and material properties in the photopolymerization-based DLP 3D printing process. The goal is to create a modular framework with flexibility regarding the modeling detail and characterization effort. To this end, a base module with the capabilities to model the layer-by-layer build, evolution of the degree of cure, and the cure-depending material properties is developed. Additional modules include modeling of the uncured resin surrounding the part during printing and modeling of the curing-induced temperature generation and distribution.

3.1 State of the Art - Process Assessment DLP

During DLP 3D printing, an object is built layer-by-layer via polymerization of a photo sensitive resin. Each layer is cured by illumination with the light pattern of the cross section of a correlating slice in the part. Regarding the overall function and process steps, the DLP method can be subdivided in ’bottom-up’ and ’top-down’ techniques. The two methods differ in the location of the light source and the movement of the build platform in relation to the resin vat. The present simulation framework models the steps of the ’bottom up’ variant because it is the most common variant. The first step in 3D printing an object is to create the CAD design of the part to be printed, and slice it with the specified layer thickness in order to create the information about the individual layers. Next, the illumination time for each layer, as well as the movement speed of the build platform have to be set. After starting the DLP print job, the build platform is lowered into the resin vat until the distance between platform and bottom of the vat is equal to the specified layer thickness. The light source is switched on and the resin is illuminated with the pattern of the current layer of the part. After the specified illumination time, the platform is moved up and the now cured layer is thereby removed from the bottom of the vat. For the next layer, the platform is again lowered into the resin vat until the distance between the last layer and the bottom of the vat equals again the specified layer thickness, and the curing process is repeated with the next layer pattern.

The light pattern in a DLP process is produced via a digital micromirror device (DMD) inside a DLP projector, or with a simple liquid crystal display (LCD) screen [49]. Due to the pixel-based light sources each layer is only an approximation of the original part geometry. Therefore, the smallest possible detail depends on the size of the individual pixels, which in turn is subject to the overall size of the projection area and the resolution of the light source. A higher resolution of the source thus leads to a better approximation of the original geometry. In modern printers a resolution of up to 4k is already possible with DMD-based systems [49] or up to 8k for LCD-based systems [50]. Due to the layer-by-layer nature of the printed parts there is also a ’stair case' effect in the printing direction perpendicular to the image plane of each layer. The severity of the effect depends on the chosen thickness of the individual layers. Common used layer thicknesses range from 12 to 150 µm [51]. In order to avoid this effect, the continuous liquid interface production (CLIP) method has been developed [52]. The basis of this method is the inclusion of an oxygen permeable window below the projection plane which results in a thin zone where polymerization is inhibited. This allows for the continuous building of the part without adhesion to the bottom of the vat and individual layer illumination. Further improvements to the method have been made regarding multi-material printing [53]–[55] and processable materials [56]–[58].

In DLP as well as other stereolithographic processes, the curing of the individual layers is based on photopolymerization reactions. In this process the cross linking is triggered by the illumination with light at a specific wavelength. A photo initiator is required to convert the energy from the photons to create the reactive species which advances the chain growth through the reaction mechanism. The two polymerization mechanisms in 3D printing applications are radical- and cationic polymerization [59]. In radical polymerization, four types of reactions are involved: generation of radicals (initiation), addition of the radicals to the monomers (propagation), atom transfer and atom abstraction reactions (chain transfer and termination by disproportionation) and radical-radical recombination (termination by recombination) [60]. Cationic polymerization, on the other hand, depends on the formation and propagation of positive ionic species [61]. Examples for frequently used materials in photopolymerization and DLP printing are (Meth)acrylate monomers/oligomers [59] and diglycidyl ether (DGEBA) [62] for radical and cationic systems, respectively.

An essential part for modeling the DLP printing method is an adequate model for describing the cure kinetics during the process. Common model types to describe the cure kinetics are mechanistic and phenomenological models [63]. In mechanistic models the concentrations of all species are considered during the photopolymerization reaction, and therefore they allow for modeling the detailed effects during the reaction, but with the cost of higher model fitting and implementation costs. Phenomenological models treat the conversion of monomers as the only variable and are therefore restricted regarding the modeling detail, however, the effort for model fitting and implementation is reduced. Both model types are suitable for the description of the curing behavior of radical as well as cationic polymerization reactions in additive manufacturing applications. Esposito Corcione et al. [64] used a mechanistic model, modified from Nelson et al. [65], to describe the curing kinetics up to complete cure, and the subsequent dark reaction of the cationic polymerization of a commercial epoxy-based resin for stereolithography. Emami and Rosen [66] developed an improved mechanistic model for the radical polymerization, taking into account the effect of oxygen inhibition, species diffusion and the variations in photo initiator absorbance along the thickness of the illuminated resin. Regarding phenomenological models, a common analytical description of the curing kinetics is provided by the autocatalytic models proposed by Kamal and Sourour

[67] and Šesták and Berggren [68]. The capability of the autocatalytic model to predict the cationic curing of cycloaliphatic (di)epoxides was shown by Voytekunas et al. [69] and by Golaz et al. [70]. In addition, Rhebein et al. [71] used it for modeling the radical curing of a commercial acrylate-based photopolymer.

Another key aspect in modeling the DLP printing method is the evolution of the mechanical properties depending on the changing degree of cure in each layer. Due to the increase in crosslinking during curing the material properties change until the fully cured state is reached. Various models for describing the material behavior during curing have been proposed, distinguishable by the modeling detail, complexity and numerical efficiency. A common and simple model is the Cure Hardening Instantaneous Linear Elastic (CHILE) model. It is a linear elastic model where the Young's modulus is time independent and changing only as a function of degree of cure and temperature [72]. Despite its simple assumptions, the model has been successfully used to describe the formation of residual strains during curing in various applications [73]–[76]. More sophisticated modeling approaches include the viscoelastic behavior of the material during the curing process. Early studies were performed by White and Hahn [77], who proposed a viscoelastic model based on the classical laminate theory to study the residual stress in thin laminates during curing. Zhu and Geubelle [78] created a more generally applicable model by considering the full 3D thermo-chemo-viscoelastic problem throughout the cure cycle of thermoset composites. To find a good compromise between prediction accuracy and modeling complexity, Zobeiry et al. [79] developed a pseudo-visco-elastic CHILE model by appropriately calibrating a CHILE model with the viscoelastic relaxation modulus at a specific time. Regarding photopolymerization, Wu et al. [80] developed a multibranch nonlinear viscoelastic model using a phase evolution model to describe the coupling between mechanical loading and crosslink network evolution during the curing process. Recently, Brighenti et al. [81] proposed a modeling approach to describe the mechanical properties in polymers obtained via photo-induced polymerization. For that purpose they used a multiphysics formulation including coupling of the chain formation in the liquid resin to a statistical micromechanical approach in order to describe the evolution of the properties as a function of the degree of cure.

Although the individual parts describing the photopolymerization process are well studied, only few frameworks for modeling the DLP process in its entirety have been proposed so far. Gao et al. [18] developed a multiphysics modeling approach combining a comprehensive mechanistic cure kinetics model for radical polymerization with a thermo-mechanical material model considering curing-dependent isotropic linear elasticity and plasticity. The models were implemented in the multiphysics simulation software COMSOL Multiphysics with routines to switch from an empty material to the monomer material at the start of each layer, and illuminate the layer with a given pattern. Zhang et al. [20] proposed a modeling approach using a mechanistic cure kinetics model in combination with a phenomenological phase evolution model with curing-dependent equilibrium modulus. The developed approach was implemented in the commercial FE package Abaqus using a material subroutine. To simulate the layer-by-layer process, an inactive element method with additional elements at the adjacent areas of the part to model, the refilling during shrinkage was used. Westbeek et al. [19] incorporated a phenomenological conversion law with a simple mathematical formulation for oxygen inhibition and an elastic material model with a linear dependency on the degree of cure into a dedicated custom FE code. The model included a detailed light intensity distribution for each individual pixel, as well as an 'immersed' mesh setting to allow for updating the contour during the curing of each layer.

Looking at the available literature, there is only a small number of already existing simulation frameworks for the DLP method, and most of them with very detailed modeling of specific aspects of the process. These detailed models often go hand in hand with a high material characterization and model fitting effort as well as a high computational expense. The intention of the framework, developed in this thesis, is to enable the user to choose the modeling fidelity, and thereby the needed characterization and computational effort based on the required model accuracy and available resources.

3.2 Methods and Papers - Process Assessment DLP

For the prediction of residual stresses, warpage and print accuracy effects in DLP 3D printing, a FE-based modeling framework is implemented in the commercial FE software Abaqus with the help of custom user subroutines. The framework is separated into multiple modules in order to provide the possibility to choose the level of detail and the associated computational expense based on the user's needs. The main modules include routines to model the layer-by-layer nature of the process, and models for the prediction of the evolution of the material properties. Element activation and a moving light source is used to represent the layer-by-layer nature, and the prediction of the evolution of the material properties include models for cure kinetics, cure-dependent mechanical properties, and chemical shrinkage. Two additional modules are developed to cover the effect of the uncured resin surrounding a part on print accuracy, as well as the temperature evolution and corresponding thermo-mechanical behavior caused by the reaction heat. An overview of the developed framework with its individual modules is detailed in Fig. 3.1. The individual parts of the modules and the necessary material characterization for the cure kinetic part are described in Paper E, and a more detailed look at the thermal simulation of the DLP framework is provided in Paper F. It has to be mentioned, that Paper E and Paper F have been written with a background in printing of complex electrically conductive structures. This, however, has no influence on the generality of the developed method nor on the applicability to the topic of the present thesis.

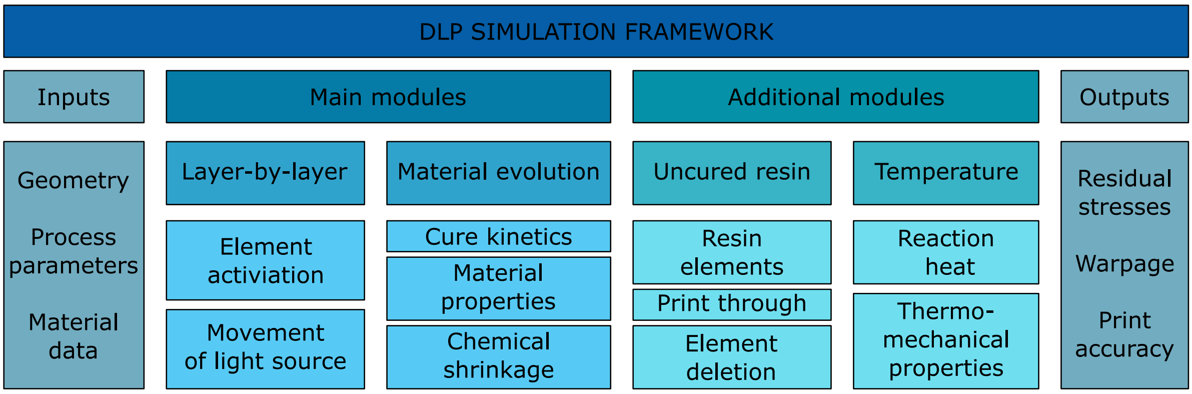

Figure 3.1: Overview of the modules and their content inside the DLP process simulation.

3.2.1 Main Modules

The main modules include all necessary parts to perform a basic DLP process simulation without consideration of heat generation or the effect of the uncured resin around a part. The general sequence during the simulation is performed in the following way. In a pre-processing step, the model is prepared and all the necessary process and material data is specified. At the start of the simulation all elements of the model are deactivated. The curing of each layer is represented in its own simulation step. At the beginning of each step, the elements of the appropriate layer are activated, and the virtual light source is moved to the top of the layer. The illumination is then started and the evolution of the degree of cure is calculated for all illuminated and active elements based on their distance to the light source. Simultaneously, the calculations of chemical shrinkage, material property evolution, and general stresses and strains are performed. This procedure is repeated for all layers until all elements are activated and the entire printing process is reproduced. In a last step, the boundary conditions are altered to account for the release of the printed part from the build platform. A detailed explanation of the main parts of the simulation framework as well as some example simulations are given in Paper E.

The pre-processing step involves importing of the part geometry, slicing of the geometry into individual layers, meshing, creation of the correct boundary conditions, and preparation of the input file with the necessary parameters for the subroutines. The entire pre-processing step is automated by a python script. In order to decrease the number of elements and thus decreasing the computational costs in the standard module, the geometry alone is imported and sliced according to the specified layer thickness without accounting for the surrounding resin. Recreating the additive nature of the process is done by using an element activation subroutine. The element activation is controlled by an Abaqus Eventseries specifying the location of an activation box in space and time during the simulation. In addition, the time between the element activation steps defines the illumination time of each layer, and the top coordinate of the current activated layer defines the position of the light source. Using the Abaqus Eventseries format therefore allows for the definition of the illumination time, layer thickness, and light source location of each individual layer. All the Abaqus Eventseries information is conveniently stored in a single list and can be easily passed to the material subroutine for use in the cure kinetics model.

Since the surrounding resin is not modeled in the main module, no actual light pattern needs to be projected onto the elements, and the degree of cure is simply calculated for all active elements beneath the light source. The cure kinetics modeling is done by using an autocatalytic model adapted from [70] to calculate the curing rate. A Beer-Lambert law correlation is used to account for the decrease of the light intensity with the distance to the light source. This type of curing model has been chosen since it is easy to implement and because it has previously been successfully implemented to predict the curing behavior of cationic [70], as well as radical [71] photopolymerization reactions. Furthermore, it offers a good compromise between modeling accuracy and characterization effort. A potential drawback of the model used is the inability to account for changes of the composition of the modeled resin, and therefore it needs to be fitted again each time the resin system is changed. In order to describe the material behavior during the process, a linear elastic model is used and the material evolution is described using a multi-step CHILE model adapted from [76]. It accounts for the change of the Young's modulus depending on the temperature and degree of cure, and it can be fitted by simple dynamic mechanical analysis (DMA) measurements. This implementation considers no viscoelastic effects during curing, thus keeping the material characterization effort low while maintaining the option to be extended to a pseudo-viscoelastic formulation [79]. To account for the effect of gelation in the model, the Young's modulus only starts to rise after the degree of cure has reached a specific threshold correlating with the gelation of the material. The Poisson's ratio is assumed to be constant during the curing process. To model the chemical shrinkage that occurs during the curing reaction, an additional shrinkage strain is added to the material model. A linear correlation between the shrinkage and the degree of cure is used, and only takes effect immediately after the gel point is reached.

Material characterization for the implemented simulation framework is carried out using a customized epoxy resin with a light induced cationic polymerization reaction. Photo differential scanning calorimetry (pDSC) experiments at various temperatures and light intensities are used to fit the parameters for the autocatalytic cure kinetics. A pDSC machine has the same reaction heat measuring functionality as a standard differential scanning calorimetry machine, with the additional possibility to illuminate the samples with light at a given wavelength and intensity. It therefore allows for measuring the light-induced curing reaction and directly calculating the curing rate over time, depending on temperature and light intensity. The LSOPT optimization tool is used to find the best parameters for the curing model. The fitted model is able to accurately reproduce the measured curing rates as exemplarily shown in Fig. 3.2(a) for three different temperatures. Gel point and maximum shrinkage strain are evaluated by photo-rheology measurements. A photo-rheology device offers the possibility to illuminate the samples with light at a given wavelength and intensity thus allowing the measurement of the rheological behavior of a material during a light-induced curing reaction. The gel point is evaluated as the point of cross-over between dynamic shear loss modulus and dynamic shear storage modulus. Creating the correlation between light intensity and distance to the light source is done by fitting the Beer-Lambert law parameters with so-called bottom exposure tests. This involves illuminating a single layer of the material without build platform on a DLP 3D printer with multiple exposure times and afterwards measuring the thickness of the printed layer. To characterize the parameters of the CHILE material model, Young's modulus values depending on temperature at different curing degrees are needed. Tensile DMA measurements with samples at various curing states are a proposed method for the characterization of the material [80]. However, due to problems in sample manufacturing and the brittle nature of the developed epoxy resin, no mechanical characterization of the material for a CHILE model could be performed and only data from the literature [76] is used for the set up of the material model.

In order to test the capability of the framework regarding the prediction of stress evolution and the resulting warpage, simulations with various parts and process parameter are set up. Only overall qualitative comparison against similar structures from the literature are performed, due to the above-mentioned material characterization problems. A simple beam and bridge-like structure are adapted from [18] and [20], respectively. Fig. 3.2(b) shows the calculated stress distribution and warpage for the bridge-like structure. The qualitative stress distribution and warpage after printing show the expected trends and align with the data from the literature. However, neglecting effects like heat generation during curing and the additional resin around the part will likely have a negative effect on the accuracy of the proposed method. The base module is therefore only suitable for qualitative studies of the overall deformation behavior during printing.

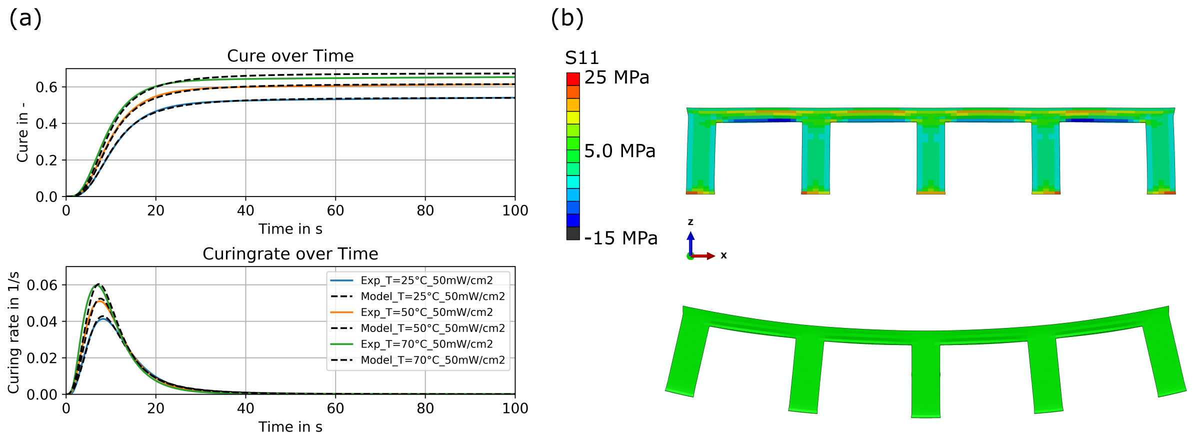

Figure 3.2: (a) Comparison between pDSC results and the fitted autocatalytic model and (b) resulting residual stress distribution and warpage calculated with the main module for an exemplary bridge-like structure.

3.2.2 Uncured Resin Module

Resin elements are added around the printed part, thereby enabling the modeling of effects like the refilling of space after shrinkage, influence of the resolution of the light source, and unwanted curing in resin-filled cavities. In order to facilitate the modeling of these effects, some additions and changes are made to the various parts of the main modules. During preprocessing, once the imported part is sliced, the information of the slices is stored in a separate file. Afterwards, the part is replaced by a single cube with the maximum dimensions of the part to represent the entire uncured resin in the vat. By meshing the cube with an element size correlating to the pixel size of the actual process, the influence of the resolution of the light source can also be considered. However, this mostly leads to a very high number of elements and therefore is only practical for small models or submodels. During the simulation, the layer activation works the same as in the main modules. For the cure calculation however, only selected elements are illuminated when using this module. Therefore, the data from the sliced part is used in a point-in-polygon routine to check if an element is inside the given pattern of a slice. Only elements inside the pattern are illuminated and thus cured. The cure calculation itself is carried out in an identical manner to the main module. The verification whether or not an element is inside the pattern is repeated in each time increment thus allowing for an element to move into the pattern during curing because of deformation caused by the chemical shrinkage. At the end of the simulation, the final printed geometry is produced by deleting all elements with a degree of cure below the degree of cure of the gel point. Since the cure kinetics model and the material model have not changed compared to the main module, no additional material characterization is necessary. A detailed explanation of the implemented module is provided in Paper E.

The capabilities of the framework are shown by simulating a geometry with two channels perpendicular to the printing direction. In Fig. 3.3(a) the geometry with an overlay of the resulting geometry and the degree of cure from the process simulation with the uncured resin module is shown. Material models are the same as for the test of the base module and therefore only comparison to literature data is possible again. The results of the simulation show a clear decrease of the cross-section of the channels due to curing inside the resin-filled cavities, and an area of low degree of cure at the edge of the part due to elements transferring into the illuminated light pattern during the simulation. Both of these effects are in line with previous findings [20]. Therefore, it shows the potential of the module to predict process specific effects on printing accuracy. The advantage of increased model accuracy comes at the cost of computational efficiency and simulation time. The increase in simulation time is mainly caused by the increased number of elements, and the addition of the point-in-polygon routine. This leads to a limitation regarding the size of the geometry used in the simulation, depending on the layer thickness and chosen element size.

3.2.3 Temperature Module

In the temperature module, a sequential thermo-mechanical approach is used to calculate the temperature evolution during curing, and its effect on cure kinetics and mechanical properties. The approach includes heat generation caused by the exothermal reaction as a main source of the temperature change in the material during curing. In the sequential approach, a transient heat transfer simulation is weakly coupled with a mechanical simulation. There is only a one-way coupling as the temperature field affects the mechanical fields but not vice versa. In order to facilitate a good transfer of the data between the two simulations, the thermal part also includes the element activation routine to ensure the same mesh in all time steps for both simulations. The temperature module can be used with only the base module, or with the additional uncured resin module. However, due to the significant effect of the thermal conductivity of the surrounding resin on the temperature distribution, it is recommended to use the additional module. During pre-processing, the only difference compared to the modules as described above is the definition of the additional thermal properties and boundary conditions. The transient heat transfer simulation of the entire process is conducted after pre-processing. The heat generation from the exothermic reaction is calculated by correlating the computed curing rate to the theoretical reaction energy of the complete curing reaction until full cure. The heat flow caused by the light source is neglected as it is insignificant in comparison to the reaction heat flow. Considering the heat source and the appropriate boundary conditions, the temperature distribution and evolution is calculated during the curing of each layer. The resulting spatial and time-dependent temperature distribution is afterwards transferred to the mechanical simulation for the calculation of residual stresses, warpage, and print accuracy. The set up and general workings of the subsequent mechanical simulation is identical to the base or uncured resin module, depending on which one is chosen. The only additional step is the definition of the calculated temperature distribution as a predefined field. Regarding necessary material characterization, the transient heat transfer simulation calls for additional material data. To test and validate the implementation of the thermal simulation, the specific heat capacity and thermal conductivity, as well as curing kinetics are characterized for a specifically developed acrylate resin. The thermal properties are only characterized in a fully cured state due to lacking characterization equipment for liquid samples. Therefore, no cure dependency is considered for the thermal properties. A detailed description of the set up and implementation, as well as a validation experiment for the heat transfer simulation inside the temperature module can be found in Paper F.

So far only the transient heat transfer simulation of this module has been tested and validated. For the validation of the temperature calculation during curing, a simple test scenario is set up. For that purpose, the resin is illuminated with a simple rectangular shape for 10s. The illumination is performed without the use of a build platform in order to allow for the insertion of a temperature measuring probe into the resin in the middle of the illuminated square. A process simulation with the temperature module is set up for the same scenario with the appropriate boundary conditions and material data. For the validation, the calculated temperature at the location of the temperature probe is compared to the actual temperature readings of the probe. The comparison shows good agreement between measured and simulated values (see Fig. 3.3(b)), and only the beginning of the temperature increase is slightly delayed in the simulation. The results indicate the ability of the proposed approach to predict the temperature inside the resin during the printing process. Overall, the sequential approach allows for an easy set up without much additional effort. However, the amount of additional uncured resin elements needed to create the appropriate boundary conditions can lead to a high number of elements, thereby decreasing the computational efficiency of the method. Furthermore, improvement of the accuracy can be achieved by adding degree of cure-dependent thermal properties to the material model.

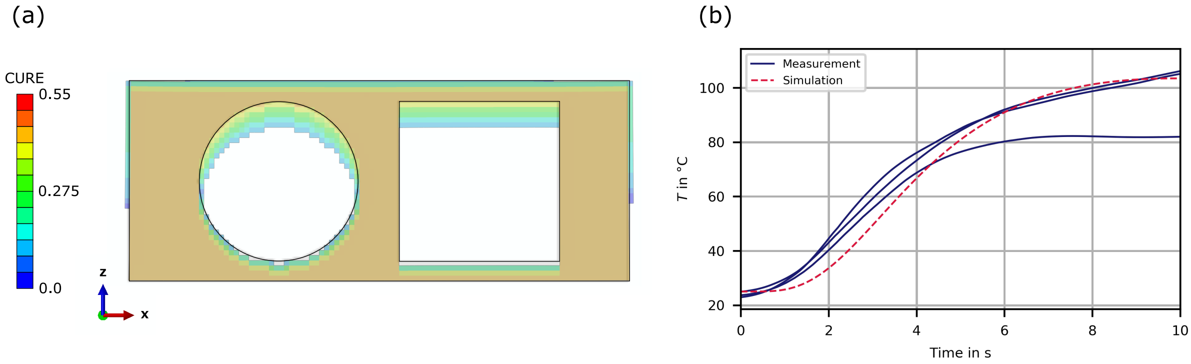

Figure 3.3: Results of the additional modules, (a) calculated degree of cure for a part simulated with the uncured resin module showing the print-through effect, (b) comparison of the temperature evolution during printing between the simulation with the temperature module and the experimental validation data.

4 Summary & Conclusion

The unit cell-based periodic architecture of metamaterials facilitates the creation of materials with exceptional properties which cannot be achieved with conventional materials. The inherent multiscale structure of metamaterials allows for a high degree of customizability. However, utilizing the full potential of metamaterials and their UC-based structure calls for new approaches during the development cycle of a component. Optimization strategies have to account for the multiple size scales and the accompanied possibilities as well as complexities. In addition, knowledge of the effect of the manufacturing process on the geometry of the individual UCs is vital, as the overall material and part properties are strongly affected by the UC geometry. Therefore, combining an optimization framework specifically tailored towards metamaterials, with a methodology for the prediction and consideration of manufacturing effects is necessary to create a comprehensive optimization strategy for metamaterial parts. The objective of the present thesis is to provide the basis for such a combined optimization strategy by developing the two individual simulation frameworks needed to perform the optimization, and the manufacturing process effect assessment.

In preliminary studies, concerning the design and development of new metamaterials, knowledge about the applicability of numerical homogenization and general FE simulation tools during the development of metamaterials is gathered first. In these studies a new mechanical metamaterial with independently tunable effective Young's modulus, and a chiral-based mechanical metamaterial with enhanced tunability of the normal-strain/shear coupling effect are developed. In both studies, homogenization is used to assess the influence of the geometric parameters on the considered material properties. Each time, the capability of the homogenization method to predict the effective material properties is validated with results of compression tests, as well as standard mechanical FE simulations of the whole test samples. The comparison shows good agreement of the predicted values of the compression modulus from homogenization, standard FE simulations and the actual compression test results. The preliminary studies provide information about the applicability and limits of the numerical homogenization method, as well as general knowledge about the design process of metamaterials, and therefore are vital for the development of the optimization strategy.

The presented optimization framework combines homogenization, interpolation, and black-box optimization into a flexible framework for optimizing the unit cell distribution on a metamaterial part in order to achieve a given objective. In the present thesis, a specified target deformation under a given load is chosen as an example objective. To allow for an efficient correlation of the unit cell geometry and the associated material properties during optimization, an interpolation object is created in a separate material pre-processing part of the framework. The interpolation object is generated using linear interpolation between the individual entries of the homogenized stiffness tensor of multiple unit cells with various geometric parameters. A numerical homogenization method is used to calculate the individual homogenized stiffness tensors. During the optimization, FE simulations of a homogenized representation serve as the black-box objective functions. For the initial implementation of the framework, the commercial optimization tool LSOPT is used to solve the black-box optimization problem. The framework is tested via the optimization of UC distribution of simple 2D tri-anti-chiral parts to follow a specific lateral target deformation under tensile load.

Results from tests of the initial implementation show good convergence and accuracy for the given test cases. Furthermore, the structure of the framework with the numerical homogenization approach, considering the full elastic stiffness tensor, and the general black-box optimization method allows for a high flexibility with respect to the used underlying metamaterial and possible optimization targets. However, the accuracy of the optimization is limited by the capabilities of the implemented homogenization method. For the test structures used, the overall global strain has to be kept small in order to ensure a good representation of the homogenized structures. Furthermore, the convergence behavior is significantly affected by the spatial discretization of the material sections on the homogenized part during optimization. This highlights the importance of the definition of the spatial discretization of the material sections for finding a good compromise between convergence and accuracy.

To address the issue regarding the definition of the spatial discretization of the material sections, the framework is extended to include an automated MSD routine. The goal is to reduce the user input and the necessary trial and error iterations needed to obtain a good discretization. In the extended framework, a genetic algorithm combined with a MSD scheme for local discretization refinement is implemented. The implementation allows for the definition of soft constraints to steer the local discretization refinement. The framework was tested again with the same tri-anti-chiral structures, and the discretization is refined based on the gradient of the geometric UC variables.

For the investigated test cases, the automated local refinement leads to a reduction in the variable gradient, and to an improved convergence and accuracy compared to cases without automated refinement. However, as there is no direct link between fitness function and refinement variable, the effect of the discretization refinement on the convergence and accuracy is highly dependent on the chosen refinement variable. Moreover, the genetic algorithm is less efficient and needs more simulation evaluations than the LSOPT optimization tool in cases with no refinement steps. The high number of required simulations is a general downside of the proposed framework. Thus, reducing the time needed for the evaluation of each simulation is a key requirement for future improvements of the framework. For example, substitution of the FE simulations with data-based surrogate models would be a possible route for improving the efficiency. Furthermore, the limitations caused by the homogenization method chosen are also relevant for the extended framework. Implementation of a nonlinear homogenization method to expand the range of validity would be an approach for further improvement of the framework.

The presented process assessment tool for the DLP additive manufacturing process provides a modular framework for evaluating effects such as residual stresses, warpage, and print accuracy. The framework is divided into the main modules and two additional modules. The main modules include all necessary parts to perform a basic DLP process simulation without consideration of heat generation or the effect of the uncured resin around a part. They are based on an FE simulation including a curing model, an appropriate degree of cure-dependent material model, and an element activation routine for modeling the layer-by-layer illumination of the resin. An autocatalytic model is used to describe the cure kinetics of the resins based on the temperature and light intensity. A multi-step CHILE model is used to calculate the temperature and degree of cure-dependent material properties during the process. The additional modules include the incorporation of the uncured surrounding resin during the process and the temperature evolution caused by the exothermic curing reaction. The framework is implemented for the Abaqus FE software utilizing subroutines. The necessary material characterization is performed for an epoxy, as well as for an acrylate resin. The fitting of the mechanical model cannot be performed due to problems with sample manufacturing, and therefore literature data is used for the CHILE material model. The function of the framework is tested by simulating the printing process of various simple parts and the temperature evolution is validated with experiments.

The results of the tests shows the capability of the developed tool to predict the residual stresses, warpage, and print-through errors caused by the manufacturing process. However, due to the lack of actual material data, only qualitative conclusions can be drawn. Compared to other existing frameworks, the implemented framework offers the advantage of a modular approach with the flexibility to choose the level of detail and computational effort. For a complete assessment of the developed modules further testing with actual material model data is needed, as well as validation against test prints in order to evaluate the qualitative accuracy of the proposed framework. The extension of the linear elastic material model to include viscoelasticity would be the next step for an improved description of the material behavior during the curing process.

The two individual frameworks of this thesis present an essential initial part in the process of creating a comprehensive optimization strategy for metamaterial parts. Both frameworks represent a step towards improving the design process of components made from metamaterials, and as a result also towards unlocking the full potential of this special class of materials. The goal of future investigations will be combining both frameworks by considering the manufacturing effects during the optimization to further improve the efficiency of the design process of metamaterial parts.

5 References

[1] Holliman, J. E., Schaef, H. T., McGrail, B. P. and Miller, Q. R. S., 'Review of foundational concepts and emerging directions in metamaterial research: Design, phenomena, and applications', *Materials Advances*, vol. 3, no. 23, pp. 8390–8406, 2022.

[2] Kolken, H. M. A. and Zadpoor, A. A., 'Auxetic mechanical metamaterials', *RSC Advances*, vol. 7, no. 9, pp. 5111–5129, 2017.

[3] Fleisch, M., Thalhamer, A., Meier, G., Fuchs, P. F., Pinter, G., Schlögl, S. and Berer, M., 'Asymmetric chiral and antichiral mechanical metamaterials with tunable poisson's ratio', *APL Materials*, vol. 10, no. 6, 061105, 2022.

[4] Zheng, X., Lee, H., Weisgraber, T. H. *et al.*, 'Ultralight, ultrastiff mechanical metamaterials', *Science*, vol. 344, no. 6190, pp. 1373–1377, 2014.

[5] Bauer, J., Meza, L. R., Schaedler, T. A., Schwaiger, R., Zheng, X. and Valdevit, L., 'Nanolattices: An emerging class of mechanical metamaterials', *Advanced materials*, vol. 29, no. 40, 1701850, 2017.

[6] Frenzel, T., Kadic, M. and Wegener, M., 'Three-dimensional mechanical metamaterials with a twist', *Science*, vol. 358, no. 6366, pp. 1072–1074, 2017.

[7] Lu, Q., Qi, D., Li, Y., Xiao, D. and Wu, W., 'Impact energy absorption performances of ordinary and hierarchical chiral structures', *Thin-Walled Structures*, vol. 140, no. 4a, pp. 495–505, 2019.

[8] Zhang, J., Lu, G. and You, Z., 'Large deformation and energy absorption of additively manufactured auxetic materials and structures: A review', *Composites Part B: Engineering*, vol. 201, no. G4, 108340, 2020.

[9] Wang, Y., Luo, Z., Zhang, N. and Kang, Z., 'Topological shape optimization of microstructural metamaterials using a level set method', *Computational Materials Science*, vol. 87, pp. 178–186, 2014.

[10] Barchiesi, E., Spagnuolo, M. and Placidi, L., 'Mechanical metamaterials: A state of the art', *Mathematics and Mechanics of Solids*, vol. 24, no. 1, pp. 212–234, 2019.

[11] Panesar, A., Abdi, M., Hickman, D. and Ashcroft, I., 'Strategies for functionally graded lattice structures derived using topology optimisation for additive manufacturing', *Additive Manufacturing*, vol. 19, pp. 81–94, 2018.

[12] Yao, J., Su, Y., Scarpa, F. and Li, Y., 'An optimization approach to design deformation patterns in perforated mechanical metamaterials using distributions of poisson's ratio-based unit cells', *Composite Structures*, vol. 281, no. 9, 115015, 2022.

[13] Schwerdtfeger, J., Wein, F., Leugering, G., Singer, R. F., Körner, C., Stingl, M. and Schury, F., ‘Design of auxetic structures via mathematical optimization’, *Advanced materials*, vol. 23, no. 23, pp. 2650–2654, 2011.

[14] Behrou, R., Ghanem, M. A., Macnider, B. C., Verma, V., Alvey, R., Hong, J., Emery, A. F., Kim, H. A. and Boechler, N., ‘Topology optimization of nonlinear periodically microstructured materials for tailored homogenized constitutive properties’, *Composite Structures*, vol. 266, no. 37, 113729, 2021.

[15] Chen, W. and Huang, X., ‘Topological design of 3d chiral metamaterials based on couple-stress homogenization’, *Journal of the Mechanics and Physics of Solids*, vol. 131, pp. 372–386, 2019.

[16] Gibson, I., Rosen, D. W. and Stucker, B., *Additive Manufacturing Technologies*. Boston, MA, USA: Springer Science + Business Media, LLC, 2010.

[17] Saleh Alghamdi, S., John, S., Roy Choudhury, N. and Dutta, N. K., ‘Additive manufacturing of polymer materials: Progress, promise and challenges’, *Polymers*, vol. 13, no. 5, 763, 2021.

[18] Gao, K., Ingenhut, B., van de Ven, A., Valega Mackenzie, F. O. and ten Cate, A. T., ‘Multiphysics modelling of photo-polymerization in stereolithography printing process and validation’, in *Proceedings of the 2018 Comsol Conference in Lausanne*, Lausanne, Switzerland, 2018, pp. 22–24.

[19] Westbeek, S., Remmers, J., van Dommelen, J., Maalderink, H. H. and Geers, M., ‘Prediction of the deformed geometry of vat photo-polymerized components using a multi-physical modeling framework’, *Additive Manufacturing*, vol. 40, no. 24, 101922, 2021.

[20] Zhang, Q., Weng, S., Hamel, C. M., Montgomery, S. M., Wu, J., Kuang, X., Zhou, K. and Qi, H. J., ‘Design for the reduction of volume shrinkage-induced distortion in digital light processing 3d printing’, *Extreme Mechanics Letters*, vol. 48, no. 3, 101403, 2021.

[21] Saeb, S., Steinmann, P. and Javili, A., ‘Aspects of computational homogenization at finite deformations: A unifying review from reuss’ to voigt’s bound’, *Applied Mechanics Reviews*, vol. 68, no. 5, 2391, 2016.

[22] Voigt, W., ‘Ueber die Beziehung zwischen den beiden Elasticitätsconstanten isotroper Körper’, *Annalen der Physik*, vol. 274, no. 12, pp. 573–587, 1889.

[23] Reuss, A., ‘Berechnung der Fließgrenze von Mischkristallen auf Grund der Plastizitätsbedingung für Einkristalle’, *ZAMM - Journal of Applied Mathematics and Mechanics / Zeitschrift für Angewandte Mathematik und Mechanik*, vol. 9, no. 1, pp. 49–58, 1929.

[24] Eshelby, J., D., ‘The determination of the elastic field of an ellipsoidal inclusion, and related problems’, *Proceedings of the Royal Society of London. Series A. Mathematical and Physical Sciences*, vol. 241, no. 1226, pp. 376–396, 1957.

[25] Mori, T. and Tanaka, K., ‘Average stress in matrix and average elastic energy of materials with misfitting inclusions’, *Acta Metallurgica*, vol. 21, no. 5, pp. 571–574, 1973.

[26] Esfarjani, S. M., Dadashi, A. and Azadi, M., ‘Topology optimization of additive-manufactured metamaterial structures: A review focused on multi-material types’, *Forces in Mechanics*, vol. 7, no. 1, 100100, 2022.

[27] Zohdi, T. I., ‘Homogenization methods and multiscale modeling’, in *Encyclopedia of Computational Mechanics*. Chichester, GBR: John Wiley & Sons, Ltd, 2004.

[28] Geers, M., Kouznetsova, V. G. and Brekelmans, W., ‘Multi-scale computational homogenization: Trends and challenges’, *Journal of Computational and Applied Mathematics*, vol. 234, no. 7, pp. 2175–2182, 2010.

[29] Harzheim, L., *Strukturoptimierung: Grundlagen und Anwendungen*, 1. Aufl. Frankfurt, Germany: Wissenschaftlicher Verlag Harri Deutsch GmbH, 2007.

[30] Abdeljaber, O., Avci, O. and Inman, D. J., ‘Optimization of chiral lattice based metastructures for broadband vibration suppression using genetic algorithms’, *Journal of Sound and Vibration*, vol. 369, pp. 50–62, 2016.

[31] Han, Y. and Lu, W., ‘Evolutionary design of nonuniform cellular structures with optimized poisson’s ratio distribution’, *Materials & Design*, vol. 141, no. 5, pp. 384–394, 2018.

[32] Wang, L. and Liu, H.-T., ‘Parameter optimization of bidirectional re-entrant auxetic honeycomb metamaterial based on genetic algorithm’, *Composite Structures*, vol. 267, no. 1, 113915, 2021.

[33] Liang, X., Shan, J., Zhou, X., Li, S., Yu, W., Liu, Z., Wen, Y., Liang, B. and Li, H., ‘Active design of chiral cell structures that undergo complex deformation under uniaxial loads’, *Materials & Design*, vol. 217, no. 31, 110649, 2022.

[34] Zhang, H., Luo, Y. and Kang, Z., ‘Bi-material microstructural design of chiral auxetic metamaterials using topology optimization’, *Composite Structures*, vol. 195, pp. 232–248, 2018.

[35] Xia, L. and Breitkopf, P., ‘Concurrent topology optimization design of material and structure within fe2 nonlinear multiscale analysis framework’, *Computer Methods in Applied Mechanics and Engineering*, vol. 278, pp. 524–542, 2014.

[36] Zhang, Y., Xiao, M., Li, H., Gao, L. and Chu, S., ‘Multiscale concurrent topology optimization for cellular structures with multiple microstructures based on ordered SIMP interpolation’, *Computational Materials Science*, vol. 155, pp. 74–91, 2018.

[37] Challapalli, A., Patel, D. and Li, G., ‘Inverse machine learning framework for optimizing lightweight metamaterials’, *Materials & Design*, vol. 208, no. 13, 109937, 2021.

[38] Kollmann, H. T., Abueidda, D. W., Koric, S., Guleryuz, E. and Sobh, N. A., ‘Deep learning for topology optimization of 2d metamaterials’, *Materials & Design*, vol. 196, no. 4, 109098, 2020.

[39] Liao, Z., Wang, Y., Gao, L. and Wang, Z.-P., ‘Deep-learning-based isogeometric inverse design for tetra-chiral auxetics’, *Composite Structures*, vol. 280, no. 7, 114808, 2022.

[40] Garland, A. P., White, B. C., Jensen, S. C. and Boyce, B. L., ‘Pragmatic generative optimization of novel structural lattice metamaterials with machine learning’, *Materials & Design*, vol. 203, no. 3, 109632, 2021.

[41] Shan, S. and Wang, G. G., ‘Survey of modeling and optimization strategies to solve high-dimensional design problems with computationally-expensive black-box functions’, *Structural and Multidisciplinary Optimization*, vol. 41, no. 2, pp. 219–241, 2010.

[42] Carson, Y. and Maria, A., ‘Simulation optimization: Methods and applications’, in *Proceedings of the 1997 Winter Simulation Conference*, Atlanta, GA, USA, 1997, pp. 118–126.

[43] Kicinger, R., Arciszewski, T. and Jong, K. D., ‘Evolutionary computation and structural design: A survey of the state-of-the-art’, *Computers & Structures*, vol. 83, no. 23, pp. 1943–1978, 2005.

[44] 3DEXPERIENCE, *Micromechanics Plugin: For Abaqus/CAE, Version 1.15*. 2017.

[45] Wu, W., Hu, W., Qian, G., Liao, H., Xu, X. and Berto, F., ‘Mechanical design and multifunctional applications of chiral mechanical metamaterials: A review’, *Materials & Design*, vol. 180, 107950, 2019.

[46] Mousanezhad, D., Haghpanah, B., Ghosh, R., Hamouda, A. M., Nayeb-Hashemi, H. and Vaziri, A., ‘Elastic properties of chiral, anti-chiral, and hierarchical honeycombs: A simple energy-based approach’, *Theoretical and Applied Mechanics Letters*, vol. 6, no. 2, pp. 81–96, 2016.

[47] Kelkar, P. U., Kim, H. S., Cho, K.-H., Kwak, J. Y., Kang, C.-Y. and Song, H.-C., ‘Cellular auxetic structures for mechanical metamaterials: A review’, *Sensors*, vol. 20, no. 11, 3132, 2020.

[48] Gad, A. F., *Pygad: An intuitive genetic algorithm python library*, 2021.

[49] Amini, A., Guijt, R. M., Themelis, T., de Vos, J. and Eeltink, S., ‘Recent developments in digital light processing 3d-printing techniques for microfluidic analytical devices’, *Journal of chromatography. A*, vol. 1692, 463842, 2023.

[50] Vedhanayagam, A., Golfetto, M., Ram, J. L. and Basu, A. S., ‘Rapid micromolding of sub-100 µm microfluidic channels using an 8k stereolithographic resin 3d printer’, *Micromachines*, vol. 14, no. 8, 1519, 2023.

[51] Pagac, M., Hajnys, J., Ma, Q.-P., Jancar, L., Jansa, J., Stefek, P. and Mesicek, J., ‘A review of vat photopolymerization technology: Materials, applications, challenges, and future trends of 3d printing’, *Polymers*, vol. 13, no. 4, 598, 2021.

[52] Tumbleston, J. R., Shirvanyants, D., Ermoshkin, N. *et al.*, ‘Continuous liquid interface production of 3d objects’, *Science*, vol. 347, no. 6228, pp. 1349–1352, 2015.

[53] Han, D. and Lee, H., ‘Recent advances in multi-material additive manufacturing: Methods and applications’, *Current Opinion in Chemical Engineering*, vol. 28, pp. 158–166, 2020.

[54] Khatri, B., Frey, M., Raouf-Fahmy, A., Scharla, M.-V. and Hanemann, T., ‘Development of a multi-material stereolithography 3d printing device’, *Micromachines*, vol. 11, no. 5, 532, 2020.

[55] Choi, J.-W., Kim, H.-C. and Wicker, R., ‘Multi-material stereolithography’, *Journal of Materials Processing Technology*, vol. 211, no. 3, pp. 318–328, 2011.

[56] Fantino, E., Chiappone, A., Roppolo, I., Manfredi, D., Bongiovanni, R., Pirri, C. F. and Calignano, F., ‘3d printing of conductive complex structures with in situ generation of silver nanoparticles’, *Advanced materials (Deerfield Beach, Fla.)*, vol. 28, no. 19, pp. 3712–3717, 2016.

[57] Gonzalez, G., Chiappone, A., Roppolo, I., Fantino, E., Bertana, V., Perrucci, F., Scaltrito, L., Pirri, F. and Sangermano, M., ‘Development of 3d printable formulations containing CNT with enhanced electrical properties’, *Polymer*, vol. 109, pp. 246–253, 2017.

[58] Tiller, B., Reid, A., Zhu, B., Guerreiro, J., Domingo-Roca, R., Curt Jackson, J. and Windmill, J., ‘Piezoelectric microphone via a digital light processing 3d printing process’, *Materials & Design*, vol. 165, 107593, 2019.

[59] Bagheri, A. and Jin, J., ‘Photopolymerization in 3d printing’, *ACS Applied Polymer Materials*, vol. 1, no. 4, pp. 593–611, 2019.

[60] Matyjaszewski, K. and Davis, T. P., *Handbook of Radical Polymerization*. Hoboken, N.J., USA: John Wiley & Sons, Inc., 2002.

[61] Odian, G., *Principles of polymerization*, Fourth edition. Hoboken, N.J, USA: John Wiley & Sons, Inc., 2010.

[62] Chaudhary, R., Fabbri, P., Leoni, E., Mazzanti, F., Akbari, R. and Antonini, C., ‘Additive manufacturing by digital light processing: A review’, *Progress in Additive Manufacturing*, vol. 8, no. 2, pp. 331–351, 2023.

[63] Lang, M., Hirner, S., Wiesbrock, F. and Fuchs, P., ‘A review on modeling cure kinetics and mechanisms of photopolymerization’, *Polymers*, vol. 14, no. 10, 2074, 2022.

[64] Esposito Corcione, C., Greco, A. and Maffezzoli, A., ‘Photopolymerization kinetics of an epoxy-based resin for stereolithography’, *Journal of Applied Polymer Science*, vol. 92, no. 6, pp. 3484–3491, 2004.

[65] Nelson, E. W., Jacobs, J. L., Scranton, A. B., Anseth, K. S. and Bowman, C. N., ‘Photo-differential scanning calorimetry studies of cationic polymerizations of divinyl ethers’, *Polymer*, vol. 36, no. 24, pp. 4651–4656, 1995.

[66] Emami, M. M. and Rosen D., W., ‘An improved vat photopolymerization cure model demonstrates photobleaching effects’, in *Proceedings of the 29th Annual International Solid Freeform Fabrication Symposium*, Austin, TX, USA, 2018.

[67] Kamal, M. R. and Sourour, S., ‘Kinetics and thermal characterization of thermoset cure’, *Polymer Engineering and Science*, vol. 13, no. 1, pp. 59–64, 1973.

[68] Šesták, J. and Berggren, G., ‘Study of the kinetics of the mechanism of solid-state reactions at increasing temperatures’, *Thermochimica Acta*, vol. 3, no. 1, pp. 1–12, 1971.

[69] Voytekunas, V. Y., Ng, F. L. and Abadie, M. J., ‘Kinetics study of the uv-initiated cationic polymerization of cycloaliphatic diepoxide resins’, *European Polymer Journal*, vol. 44, no. 11, pp. 3640–3649, 2008.

[70] Golaz, B., Michaud, V., Leterrier, Y. and Månson, J.-A., ‘UV intensity, temperature and dark-curing effects in cationic photo-polymerization of a cycloaliphatic epoxy resin’, *Polymer*, vol. 53, no. 10, pp. 2038–2048, 2012.

[71] Rehbein, T., Lion, A., Johlitz, M. and Constantinescu, A., ‘Experimental investigation and modelling of the curing behaviour of photopolymers’, *Polymer Testing*, vol. 83, 106356, 2020.

[72] Johnston, A. A., ‘An integrated model of the development of process-induced deformation in autoclave processing of composite structures’, PhD Thesis, The University of British Columbia, Canada, 1997.

[73] Li, D., Li, X., Dai, J. and Xi, S., ‘A comparison of curing process-induced residual stresses and cure shrinkage in micro-scale composite structures with different constitutive laws’, *Applied Composite Materials*, vol. 25, no. 1, pp. 67–84, 2018.

[74] Dai, J., Xi, S. and Li, D., ‘Numerical analysis of curing residual stress and deformation in thermosetting composite laminates with comparison between different constitutive models’, *Materials*, vol. 12, no. 4, 572, 2019.

[75] D’Mello, R. J. and Waas, A. M., ‘Virtual curing of textile polymer matrix composites’, *Composite Structures*, vol. 178, no. 1072, pp. 455–466, 2017.

[76] Yuksel, O., Sandberg, M., Baran, I., Ersoy, N., Hattel, J. H. and Akkerman, R., ‘Material characterization of a pultrusion specific and highly reactive polyurethane resin system: Elastic modulus, rheology, and reaction kinetics’, *Composites Part B: Engineering*, vol. 207, no. 26, 108543, 2021.

[77] White, S. R. and Hahn, H. T., ‘Process modeling of composite materials: Residual stress development during cure. Part I. Model formulation’, *Journal of Composite Materials*, vol. 26, no. 16, pp. 2402–2422, 1992.

[78] Zhu, Q., Geubelle, P. H., Li, M. and Tucker, C. L., ‘Dimensional accuracy of thermoset composites: Simulation of process-induced residual stresses’, *Journal of Composite Materials*, vol. 35, no. 24, pp. 2171–2205, 2001.

[79] Zobeiry, N., Vaziri, R. and Poursartip, A., ‘Computationally efficient pseudo-viscoelastic models for evaluation of residual stresses in thermoset polymer composites during cure’, *Composites Part A: Applied Science and Manufacturing*, vol. 41, no. 2, pp. 247–256, 2010.

[80] Wu, J., Zhao, Z., Hamel, C. M., Mu, X., Kuang, X., Guo, Z. and Qi, H. J., ‘Evolution of material properties during free radical photopolymerization’, *Journal of the Mechanics and Physics of Solids*, vol. 112, pp. 25–49, 2018.

[81] Brighenti, R., Cosma, M. P., Marsavina, L., Spagnoli, A. and Terzano, M., ‘Multiphysics modelling of the mechanical properties in polymers obtained via photo-induced polymerization’, *The International Journal of Advanced Manufacturing Technology*, vol. 117, no. 1, pp. 481–499, 2021.

Part II - Publications

Collection of Papers

This section contains the publications of this thesis. A reference to the papers and their processing status is given in Tab. 5.1 and the contribution of the Ph.D. candidate to the individual papers is stated in Tab. 5.2.

Table 5.1: List of publications.

Paper	Bibliography	Status
A	Fleisch, M., Thalhamer, A., Meier, G., Raguž, I., Fuchs, P. F., Pinter, G., Schlögl, S. and Berer, M., 'Functional mechanical metamaterial with independently tunable stiffness in the three spatial directions', *Materials Today Advances*, vol. 11, 100155, 2021	published
B	Fleisch, M., Thalhamer, A., Meier, G., Huber, P. A. F., Fuchs, P. F., Pinter, G., Schlögl, S. and Berer, M., 'Chiral-based mechanical metamaterial with tunable normal-strain shear coupling effect', *Engineering Structures*, vol. 284, 115952, 2023	published
C	Thalhamer, A., Fleisch, M., Schuecker, C., Fuchs, P. F., Schlögl, S. and Berer, M., 'A black-box optimization strategy for customizable global elastic deformation behavior of unit cell-based tri-anti-chiral metamaterials', *Advances in Engineering Software*, vol. 186, 103553, 2023	published
D	Thalhamer, A., Fleisch, M., Schuecker, C., Fuchs, P. F., Schlögl, S. and Berer, M., 'An optimization strategy for customizable global elastic deformation of unit cell-based metamaterials with variable material section discretization', *Submitted*, 26.04.2024	submitted
E	Thalhamer, A., Fuchs, P., Strohmeier, L., Hasil, S. and Wolfberger, A., 'A simulation-based assessment of print accuracy for microelectronic parts manufactured with DLP 3d printing process', in *2022 23rd International Conference on Thermal, Mechanical and Multi-Physics Simulation and Experiments in Microelectronics and Microsystems (EuroSimE)*, St Julian, Malta: IEEE, 2022, pp. 585–595	published
F	Thalhamer, A., Rossegger, E., Hasil, S., Hrbinič, K., Feigl, V., Pfost, M. and Fuchs, P., 'Thermomechanical and electrical material characterization for a DLP printing process simulation of electrically conductive parts', in *2023 24th International Conference on Thermal, Mechanical and Multi-Physics Simulation and Experiments in Microelectronics and Microsystems (EuroSimE)*, Graz, Austria: IEEE, 2023, pp. 1–10	published

Table 5.2: The contribution of the Ph.D. candidate to the publications.

Activity	Paper A	Paper B	Paper C	Paper D	Paper E	Paper F
Conceptualization	20 %	20 %	80 %	100 %	100 %	100 %
Method development	20 %	20 %	80 %	100 %	100 %	100 %
Numerical study	70 %	90 %	100 %	100 %	100 %	100 %
Experimental work	0 %	0 %	– %	– %	0 %	10 %
Writing - Original Draft	10 %	10 %	90 %	100 %	100 %	100 %
Writing - Review and Editing	40 %	40 %	0 %	0 %	0 %	0 %

Paper A

Functional mechanical metamaterial with independently tunable stiffness in the three spatial directions

Authors: Fleisch, M.
Thalhamer, A.
Meier, G.
Raguz, I.
Fuchs, P.F.
Pinter, G.
Schlögl, S.
Berer, M.

Materials Today Advances
DOI: 10.1016/j.mtadv.2021.100155

Materials Today Advances 11 (2021) 100155

Contents lists available at ScienceDirect

Materials Today Advances

journal homepage: www.journals.elsevier.com/materials-today-advances/

Functional mechanical metamaterial with independently tunable stiffness in the three spatial directions

M. Fleisch [a], A. Thalhamer [a], G. Meier [a], I. Raguž [a], P.F. Fuchs [a], G. Pinter [b], S. Schlögl [a], M. Berer [a, *]

[a] *Polymer Competence Center Leoben GmbH, Roseggerstrasse 12, Leoben, 8700, Austria*
[b] *Department of Polymer Engineering and Science, Montanuniversitaet Leoben, Otto-Gloeckel Strasse 2, Leoben, 8700, Austria*

ARTICLE INFO

Article history:
Received 15 April 2021
Received in revised form
17 June 2021
Accepted 21 June 2021
Available online 21 July 2021

Keywords:
Neural network
Design
Mechanical testing
Additive manufacturing
Numerical

ABSTRACT

Mechanical metamaterials with variable stiffness recently gained a lot of research interest, as they allow for structures with complex boundary and load conditions. Herein, we highlight the design, additive manufacturing, and mechanical testing of a new kind of bending-dominated metamaterial. By advancing from well-established mechanical metamaterials, the proposed geometry allows for varying the stiffness in the three spatial directions independently. Therefore, structures with different orientational properties can be designed, ranging from isotropic to anisotropic structures, including orthotropic structures. The compression modulus can be varied in the range of several orders of magnitude. Gradual transitions from one unit cell to the next can be realized, enabling smooth transitions from soft to hard regions. Specimens have been additively manufactured with acrylic resins and polylactic acid using Digital Light Processing and Fused Filament Fabrication, respectively. Two different numerical models have been employed using ABAQUS to describe the mechanical properties of the structure and verified by the experiments. Compression tests were performed to investigate the linear elastic properties of isotropic structures. Numerical models, based on three-point-bending test data, have been employed to study orthotropic structures. Compression test results for orthotropic and anisotropic structures are shown to highlight the independent variability. The manufacturing of the structures is not limited to the presented techniques and materials but can be expanded to all available additive manufacturing techniques and their respective materials. For a video of the compression tests of a specimen with three different compression moduli along the spatial axes, see the Supplementary Data available online.

1. Introduction

The stiffness of a material or structure plays a crucial role in the design process of products. The demand for versatile materials or structures with variable mechanical properties is increasing. The possibility to change or tune mechanical properties opens the prospect for a new design philosophy. Developments in materials research made it possible to change mechanical properties by the use of external fields, e.g. by temperature with shape memory polymers (SMPs) [1,2], magnetic fields [3], or electric fields [4]. Usually, the bandwidth of variation is limited and can sometimes only be varied in distinct steps (rigidity switching [5–7]). Variable mechanical properties can also be achieved with metamaterials and have gained a lot of interest for structural applications [8,9]. Mechanical metamaterial refers to a structure with unique mechanical properties based on its geometry. Lightweight structures (LSs) and (anti-/meta-)-chiral structures (AMCs) are two examples of metamaterials, which have attracted increased attention [10–14]. LSs aim at structures with a high stiffness at a minimal material expense. They are typically assembled from struts or plates connected at an angle [15]. AMCs are usually built from rigid nodes connected by struts [16]. When compressed, the bending of the struts leads to a rotation and higher packing density of the nodes, resulting in a negative Poisson's ratio [17]. Different designs have been proposed, which allow for 3D structures based on AMCs [18–21]. Both, LSs and AMCs, can be used to vary the

---

* Corresponding author.
E-mail address: michael.berer@pccl.at (M. Berer).

https://doi.org/10.1016/j.mtadv.2021.100155

stiffness of a structure, e.g. by changing the strut thickness or diameter. The major drawback of using these geometries for variable stiffness structures is that the stiffness cannot easily be varied independently along the three spatial axes [22]. By varying the strut diameter in LSs, at least two axes are affected simultaneously. This can be overcome by having a gradient structure [23]. But this increases the complexity of the structure and the design process. Due to the rotation of nodes in AMCs, out-of-plane deformation occurs, which again influences the mechanical properties in at least one additional axis. In this study, we present the design, manufacturing and experimental results of a mechanical metamaterial, which allows for varying the stiffness in a broad range and independently along the three spatial axes. Additionally, structures with local directional properties can be generated, paving the way toward the fabrication of 'multimaterial-features' with one material, as well as gradual transitions from soft to hard regions. Five different structures were fabricated, using two different additive manufacturing (AM) techniques to demonstrate the versatility of the concept. Acrylic resin-based specimens were manufactured with Digital Light Processing (DLP) and polylactic acid (PLA) specimens with Fused Filament Fabrication (FFF). The proposed metamaterial is not limited to these two AM techniques but can be manufactured with all available AM methods, including non-polymer-based ones. The properties of the structures were determined by mechanical tests in the form of compression tests. These experiments are compared to the results of numerical simulations based on the geometry of the tested specimens and a homogenization technique. Based on the results of the homogenization, a neural network is used to predict intermediate values to cover a broader parameter space. The material model for the simulations is based on three-point-bending tests. An overview of the presented topics in this paper is depicted in Fig. 1.

2. Materials and methods

Metamaterials are usually built from unit cells (UCs) and are stacked in the three spatial directions to create different geometries. First, the design of the UC and its respective geometric parameters is presented. The initial design allows for a versatile structure at the cost of a more complex design process. For reducing the complexity, different simplifications are given for special cases (e.g. isotropic and orthotropic structures). Next, the design and additive manufacturing process of the tested specimens is described. Finally, the experimental setup to obtain the mechanical properties of the parent material and the specimens is presented.

2.1. Unit cell

2.1.1. Unit cell geometry

Fig. 2 shows a 3D sketch of the UC with indicated cross-sections. The respective cross-sections are depicted in Fig. 3 ((a): XY-cross-section, (b): XZ-cross-section). The parameters of the UC are listed in Table 1. When a compression force is applied, the alternating arrangement of struts leads to in-plane movement of the cubes but no out-off-plane deformation. This property makes it possible to vary the stiffness in the three spatial directions independently.

This set of parameters enables structures with global directional properties:

1. Isotropic: if $D: = DX_1 = DX_2 = DY_1 = DY_2 = DZ_1 = DZ_2$ *and* $T = T_{ix} = T_{iy} = T_{iz} = TX_1 = TX_2 = TY_1 = TY_2 = TZ_1 = TZ_2$
2. Orthotropic: e.g. if $D_1 := DX_1 = DX_2 = DY_1 = DY_2$, $D_2 := DZ_1 = DZ_2$, $T_1 = T_{ix} = T_{iy} = TX_1 = TX_2 = TY_1 = TY_2$ *and* $T_2 = TZ_1 = TZ_2$
3. Anisotropic (along each axis): if $D_x := DX_1 = DX_2$, $D_y := DY_1 = DY_2$, $D_z = : DZ_1 = DZ_2$, $T_x := T_{ix} = TX_1 = TX_2$, $T_y := T_{iy} = TY_1 = TY_2$ *and* $T_z := T_{iz} = TZ_1 = TZ_2$

The fillets were introduced to reduce mechanical stress peaks, which would otherwise form in the transition from the struts to the cubes. By stacking UCs with different parameters, structures with local directional properties can be obtained. The parameters DX_1, DX_2, DY_1, ...*and* TX_1, TX_2, TY_1, ...allow for a gradient transition between UCs. For example, a structure with varying stiffness along one axis can be generated, which would resemble a non-linear spring with varying spring constants. Another possible design for the UC of the structure is to have only half of the struts on both sides of the two cubes, leading to a symmetric UC. But this approach limits the flexibility of the design because the geometric parameters of the connecting UCs are needed to avoid kinks in the struts between two adjacent UCs. For the homogenization simulations, the symmetric UC was used since the numerical tools require symmetric boundary conditions.

The main focus of this study is the experimental and numerical investigation of isotropic structures. The reduced set of geometric parameters for an isotropic structure is listed in Table 2. More complex structures are analyzed numerically. Examples of compression tests of orthotropic and anisotropic structures are also presented.

2.1.2. Relative density

When designing structures for an application, relative density is an important parameter. Equation (1) shows the volume V_s of a UC

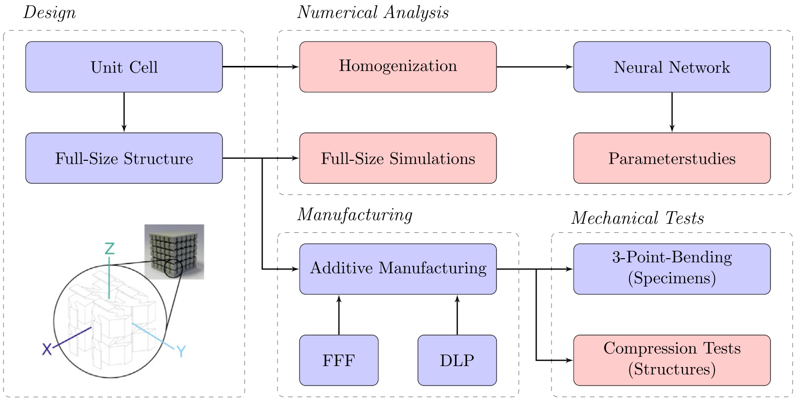

Fig. 1. Overview of the presented topics in this paper. Blue nodes indicate design and preparation steps, whereas red nodes highlight intermediate and final results. The arrows connecting the nodes illustrate the interdependency between the individual steps.

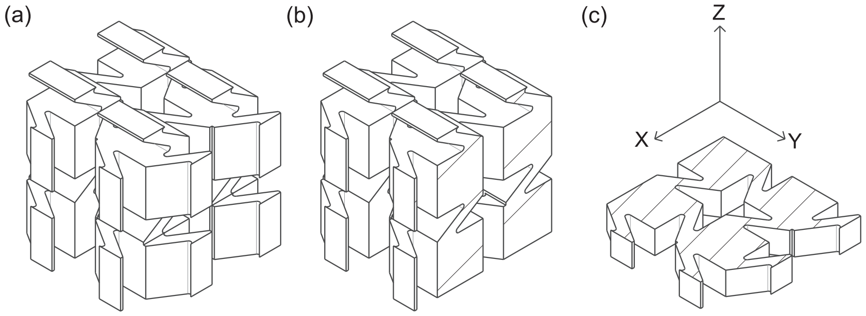

Fig. 2. 3D sketch of the unit cell with indicated cross section. (a): Complete unit cell, (b): X-Z cross section, (c): X–Y cross section.

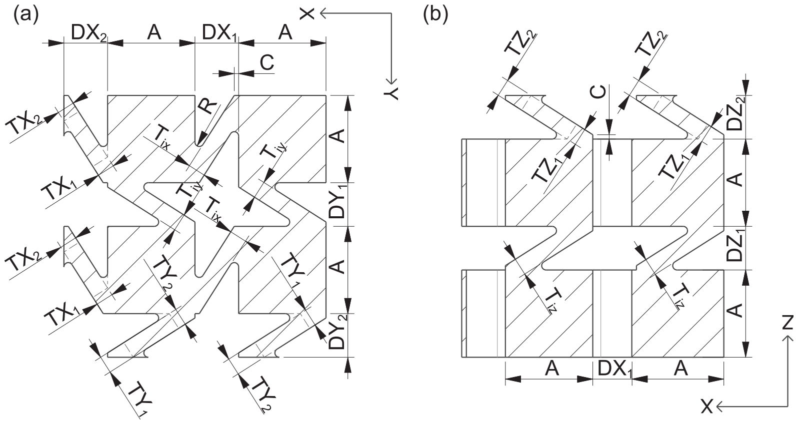

Fig. 3. Cross sections with geometric parameters of the unit cell. (a): X–Y cross section, (b): X-Z cross section.

without gradient transition ($TX_1 = TX_2 = TX$, $TY_1 = TY_2 = TY$, $TZ_1 = TZ_2 = TZ$), $R = 0$ and $C = 0$. Here, R and C are neglected because they only account for a small portion of the volume, and it reduces the complexity of the derived formula. By dividing the volume of the UC with the volume of the bounding box V_{BB} (equation (2)), the relative density ρ_{rel} can be obtained.

$$V_S = 8A^3 + 4A \sum_{\substack{D = DX_j, DY_j, DZ_j \\ T = TX, TY, TZ, T_{ix}, T_{iy}, T_{iz} \\ j = 1,2;\ i = 1,2,3}} \left(D \left(A - \frac{D}{\tan\left(\arctan\left(\frac{D}{A}\right) + \arcsin\left(\frac{T}{\sqrt{A^2+D^2}}\right)\right)} \right) \right) \tag{1}$$

$$V_{BB} = (2A + DX_1 + DX_2)(2A + DY_1 + DY_2)(2A + DZ_1 + DZ_2) \tag{2}$$

The resulting relative density $\rho_{rel,IS}$ for an isotropic structure is given in Equation (3). Fig. 4 shows the relative density for isotropic UCs with different ratios of cube length (A) to distance between cubes (D). With increasing distance between the cubes (D), less space is filled with material, and the relative density decreases. Consequentially, the relative density increases with the ratio A/D and the strut thickness (T).

$$\rho_{rel,IS} = \frac{8A^3 + 24AD\left(A - \frac{D}{\tan\left(\arctan\left(\frac{D}{A}\right) + \arcsin\left(\frac{T}{\sqrt{A^2+D^2}}\right)\right)} \right)}{8(A+D)^3} \tag{3}$$

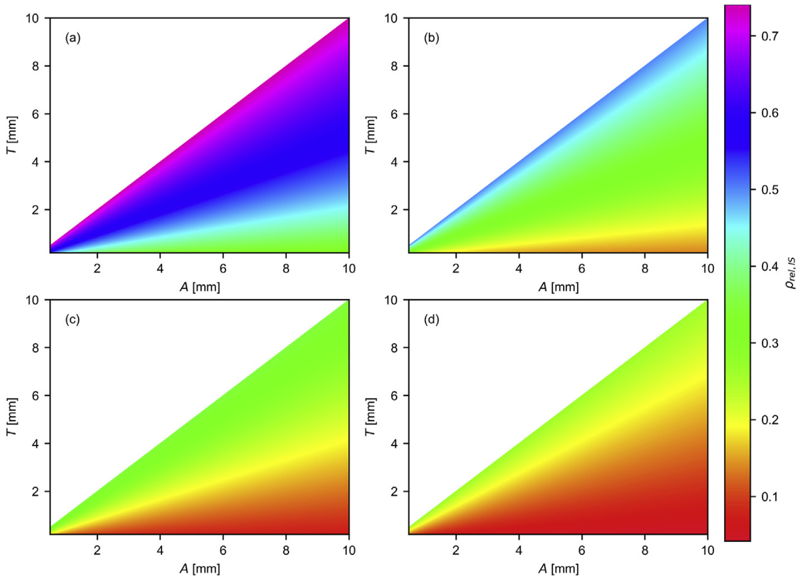

Fig. 4. Relative density for isotropic unit cells for different ratios of cube length (*A*) to distance between cubes (*D*). (a): *A*:*D* = 2:1, (b): *A*:*D* = 1:1, (c): *A*:*D* = 1:1.5, (d): *A*:*D* = 1:2. The white areas are geometrically not possible, since *T* < *A*.

2.2. Geometry of sample structures

The compression test geometries were created by stacking UCs alongside the three spatial directions. For the geometric parameters in this study, 3–4 UCs per spatial direction were enough to minimize the size effect. The UC parameters for the individual specimens were chosen, such that a volume of 50 × 50 × 50 mm^3 could be filled with an integer number of UCs. On the top and bottom, a 2 mm thick, solid compression surface was added to ensure an optimal force transmission into the UCs. This results in a total dimension of the tested specimens of 50 × 50 × 54 mm^3. Fig. 5 (a) shows a CAD model of a specimen used for compression tests. Table 3 lists the geometric parameters and the weight of the tested specimens. The values are obtained from a representative specimen. 5 specimens of each geometry were manufactured and tested.

2.3. Additively manufactured specimens

The specimens were manufactured using two different additive manufacturing techniques, Digital Light Processing (DLP) and Fused Filament Fabrication (FFF). Examples of the additively manufactured specimens are depicted in Fig. 5 (b).

An ‘Elegoo Mars’ (Elegoo Inc., Shenzhen, China) UV LCD printer was employed to print the DLP specimens with the acrylic-based resin ‘Formfutura Platinum LCD Series’ (Solid Light Grey, Formfutura, Nijmegen, Netherlands). This material will be referred to as ‘resin’ in this study. For this printing technique, no support structures were needed, and a layer height of 0.05 mm was used. The exposure time of the first five layers was set to 60 s, and the remaining were illuminated for 13 s. After the printing process, the specimens were cleaned with ethanol in a magnetic stirrer for 5 min. Post-curing was performed in a heated UV chamber (‘Formlabs Form Cure’, Formlabs Inc., Somerville, USA) for 1 h at 80 °C.

The FFF preparation of samples was done with an ‘Ender 3 Pro’ (Creality 3D, Shenzhen, China) and a thermoplastic filament made of PLA (‘Formfutura Premium PLA Black’, Formfutura, Nijmegen, Netherlands). By rotating the specimen geometry, only external support structures are needed and were printed with the same material. The nozzle and bed temperatures were set to 210 °C and 60 °C, respectively. All specimens were printed with 100% infill and a layer height of 0.2 mm.

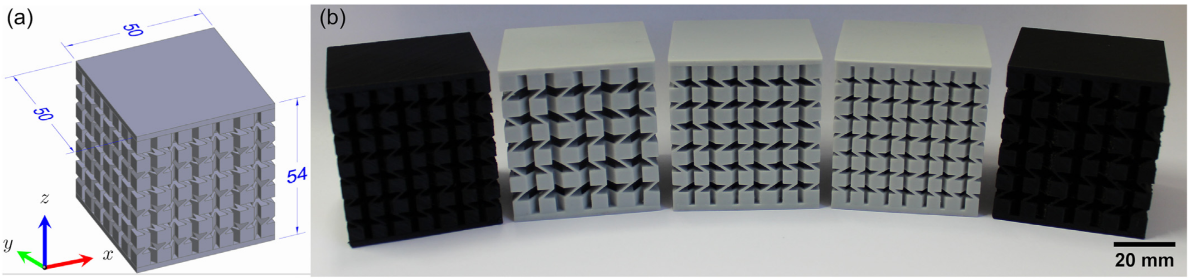

Fig. 5. Specimens for compression tests. (a): CAD model of the specimen (units: mm), (b): Additively manufactured specimens (from left to right: A, B, C, D, E).

Table 1
Geometric parameters of the unit cell.

Name	Description
A	Side length of cubes
DX_1, DY_1, DZ_1	Distance between cubes (inside)
DX_2, DY_2, DZ_2	Distance between cubes (to next UC)
T_{ix}, T_{iy}, T_{iz}	Thickness of struts (inside)
TX_1, TY_1, TZ_1	Thickness of struts (to next UC, start)
TX_2, TY_2, TZ_2	Thickness of struts (to next UC, end)
R	Radius of fillets
C	Overhang of cubes

2.4. *Experimental testing*

2.4.1. *Properties of the parent materials*

In order to investigate the properties of the parent materials, 10 three-point-bending samples of each material were printed and tested according to DIN EN ISO 178 [24] (size: 80 × 10 × 4 mm^3), using a 'Zwick/Roell Z010' (Zwick GmbH & Co. KG., Ulm, Germany). The testing speed was set to 2 mm/min, with a preload of 0.1 MPa and was performed at room temperature. The DLP specimens were printed upright to avoid the influence of the first layers being exposed longer. The FFF samples were printed flat with an infill direction of 45°/135°. An infill of 100% was used for both materials. Three-Point-bending tests were chosen because the main deformation in the structure is the bending of struts when a compression force is applied.

2.4.2. *Quasi-static compression tests of specimens*

The mechanical behavior of the specimens was investigated by means of compression tests. The tests were carried out using a 'Zwick/Roell Z250' (Zwick GmbH & Co. KG., Ulm, Germany) at room temperature. The displacement was measured globally and locally using a digital image correlation system, 'ARAMIS 4 M' (GOM GmbH, Braunschweig, Germany). The specimens were prepared for the optical measurement by applying a spray pattern. For the determination of the global displacement, the digital image correlation system was used as a video extensometer. In order to reduce boundary effects, the virtual extensometers were placed in the middle of the structure. The top and bottom compression surfaces, as well as the outermost column, were excluded (see Fig. 6). The lengths of the extensometers were 49 mm in the z-direction and between 30 mm and 40 mm in the x-direction. The tests were conducted with a deformation rate of 10 mm/min until fracture or until the specimens were compressed to 14% of their initial length (whichever came first). For reducing friction, the contact surfaces between the specimen and the pistons were lubricated with a PTFE spray ('CRC Dry Lube-F 32602-AA', CRC Industries, Inc., Horsham Township, USA).

Table 2
Geometric parameter of isotropic unit cells.

Name	Description
A	Side length of cubes
D	Distance between cubes
T	Thickness of struts
R	Radius of fillets
C	Overhang of cubes

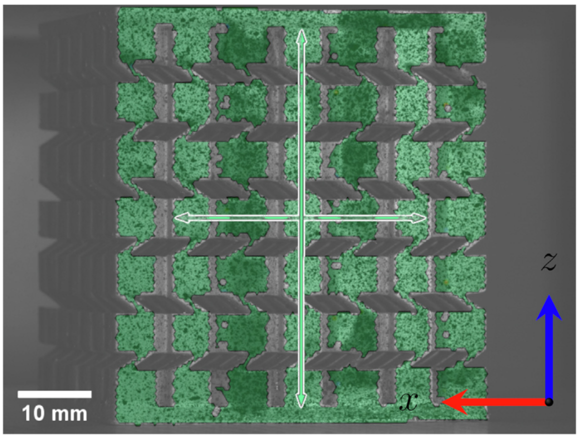

Fig. 6. Extensometer placement for compression tests (specimen C-2).

3. Finite element analysis (FEA)

In order to simulate the behavior of the specimens under quasi-static compression, finite element (FE) models were employed using Abaqus CAE 2019 software [25]. Two different simulation techniques were used. First, simulations on the full-size structures were performed to verify the applicability of simulations to represent the compression tests. Second, a homogenization method was implemented to reduce the computational cost of the simulations. The homogenization results were complemented by a neural network, which was trained to predict mechanical values based on the simulation results.

3.1. *Simulation models*

3.1.1. *Full-size structures*

For predicting global and local properties of the geometry, simulations of the full-size structures (50 × 50 × 54 mm^3) were conducted. The models were created based on the geometry of the samples used in the compression tests. The boundary conditions were defined with the aim of representing the real conditions during the compression test as accurately as possible. Therefore, the bottom faces of the geometries were fixed in the *z*-direction, and on the top faces of the geometries, a defined force *F* was applied in the negative *z*-direction. Friction interaction between the test specimen and the pistons of the test device was not modeled due to the lubricated contact surfaces (see section 2.4.2). The model was

Table 3
Geometric parameters of the tested samples (parameters measured with a microscope after manufacturing, relative density obtained from CAD program, values obtained from a representative sample).

Name	A [mm]	D [mm]	T [mm]	R [mm]	C [mm]	ρ_{rel}	Material	Weight [g]
A	5.0	2.5	0.80	0.2	0.1	0.43	PLA	77
B	5.5	3.4	0.76	0.4	0.1	0.35	Resin	80
C	5.0	2.5	0.92	0.4	0.1	0.46	Resin	96
D	4.5	2.0	0.95	0.4	0.1	0.53	Resin	107
E	5.5	3.4	0.80	0.2	0.1	0.34	PLA	67

meshed using tetrahedral quadratic elements, as shown in Fig. 7, and solved with the Abaqus standard solver. An elastic-plastic material model was used to describe the material behavior during compression. The material model parameters for both materials analyzed within this study were calibrated based on the experimental three-point-bending test data independently. The elastic behavior of the model is defined by Young's modulus and Poisson's ratio. The nonlinear behavior is defined by the yield curve (yield stress/plastic strain). Young's modulus was directly calculated from the experimental results of the bending tests. The yield curve was determined by applying a parameter identification routine in LS-OPT [26]. The general principle of this method is the comparison of experimental results to results of simulated bending tests [27]. An optimization algorithm (sequential domain reduction in LS-OPT) was used to find the material model parameters for the best fit. In doing so, the bending test was modeled in agreement with the experimental setup (see section 2.4.1). The parameters of the material model were then optimized to achieve agreement between simulation and experimental results of the bending tests.

3.1.2. Homogenization based on unit cell

Homogenization methods are a useful tool when describing metamaterial properties, as they enable the calculation of macroscale properties in a multiscale problem [28]. For this study, a numerical homogenization method was used to assess the influence of the geometric parameters in the unit cell onto the metamaterial properties. For the simulations, six separate uniform load cases with periodic boundary conditions were used. These boundary conditions can be described with equation (4), which defines the relative displacement of the opposing boundary surfaces.

$$u_i(x_2) = u_i(x_1) + \left(\frac{\partial u_i}{\partial x}\right)(x_2 - x_1) \tag{4}$$

Here, $u_i(x_1)$ and $u_i(x_2)$ describe the displacement in the direction i of two points on the opposite side of the UC and $(\partial u_i/\partial x)$ being the gradient of the displacement inside the UC in the direction i. The directions of the applied strains for the different load cases are depicted in Fig. 8. The volume-averaged global stress of the unit cell, $\overline{\sigma}$, was calculated based on equation (5) for each load case.

$$\overline{\sigma} = \frac{1}{V_{UC}} \int_{V_{UC}} \sigma(x) dV \tag{5}$$

Here, V_{UC} is the volume of the UC and $\sigma(x)$ is the local stress distribution. With linear elastic assumptions, the global stiffness tensor $\overline{C}$ is related to the global stress and global strain $\overline{\varepsilon}$ by equation (6).

$$\overline{\sigma} = \overline{C} : \overline{\varepsilon} \tag{6}$$

The compression moduli of the three spatial directions, E_x, E_y and E_z were then calculated with the entries of the inverse global stiffness tensor, $\overline{S}_{ii}$ (equation (7)).

$$E_x = \frac{1}{\overline{S}_{11}}, \quad E_y = \frac{1}{\overline{S}_{22}}, \quad E_z = \frac{1}{\overline{S}_{33}} \tag{7}$$

For the setup of the homogenization calculations, an Abaqus micromechanics plugin [29], as well as a self-made homogenization script, were used. The plugin requires opposite surfaces to be of the same form. For this reason, a design with only half of the struts on both sides was used instead of the proposed geometry of the UC (see Fig. 8), as mentioned in section 2.1.1. The linear-elastic material properties obtained from the three-point-bending tests were used to define the material model.

3.2. Performance prediction with machine learning

The number of geometric parameters of the structure results in a large parameter space, which would need a lot of simulations to be fully covered. For reducing the computation time, a neural-network (NN) was used. The NN was implemented with Keras [30], an open-source NN library written in Python [31]. A Sequential network with regular densely connected layers was used. The layer structure is listed in Table 4 (the parameters not listed were set to default). The input layers dimension corresponds to the number of parameters relevant for the analyzed geometry. For example, an isotropic structure has five parameters, and thus, n = 5. First, a set of homogenization simulations, covering the parameter space broadly, was performed. The NN was then trained with the simulation results and used to predict the intermediate values. The activation functions (f_1 and f_2) of the hidden layers were chosen to minimize the loss by testing all combinations of available activation functions (relu, sigmoid, softmax, softplus, softsign, tanh, selu, elu, or exponential). The output returns the value of interest. For the results presented in this study, either the compression modulus or the Poisson's Ratio were set as the output value. The input data was scaled to the interval (0, 1) with a MinMaxScaler. For each individual analysis, a new NN was trained with 10,000 epochs. The incorporation of NN to predict mechanical properties of structures also allows for optimization techniques. Geometric parameters for a given mechanical property can be obtained by inverting the

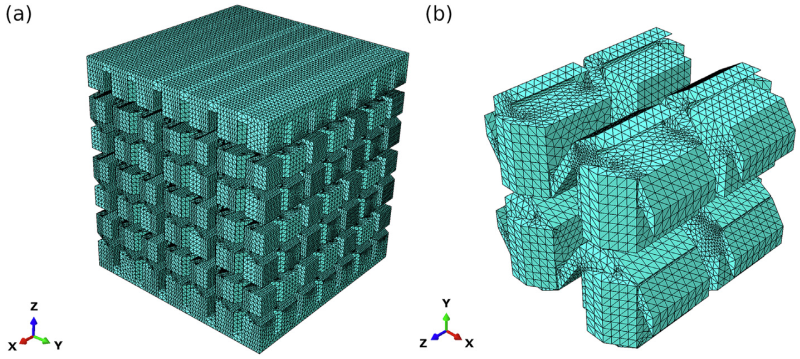

Fig. 7. Comparison of meshes used for the simulations. (a): Full-size simulations, (b): Homogenization.

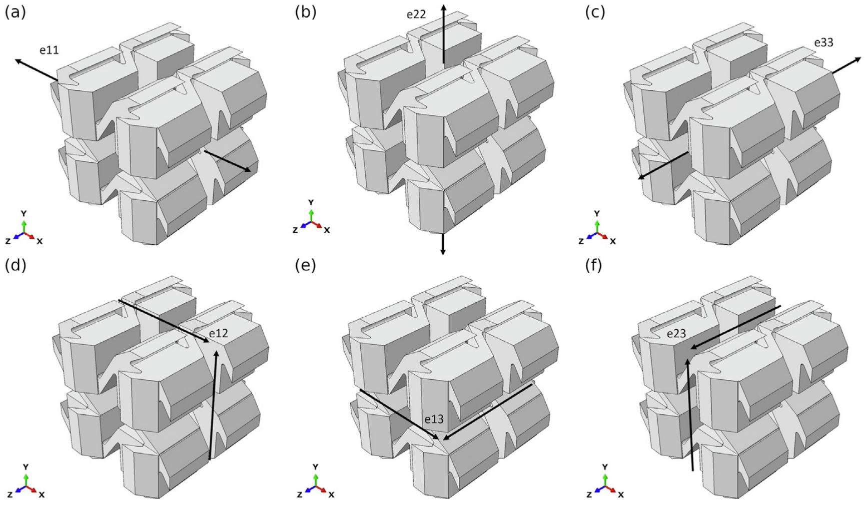

Fig. 8. Individual load cases for the homogenization method. (a): e_{11}, (b): e_{22}, (c): e_{33}, (d): e_{12}, (e): e_{13}, (f): e_{23}.

Table 4
Layer structure for the neural network (n*: the input dimension was chosen according to the number of parameters relevant for the geometry, e.g. n = 5 for an isotropic structure, **: functions chosen such that the loss is minimized).

Type	Input Dimension	Output Dimension	Activation Function	Kernel Initializer
Input	n*	20	Tanh	Uniform
Hidden	20	20	f_1**	Uniform
Hidden	20	15	f_2**	Uniform
Output	15	1	Linear	Uniform

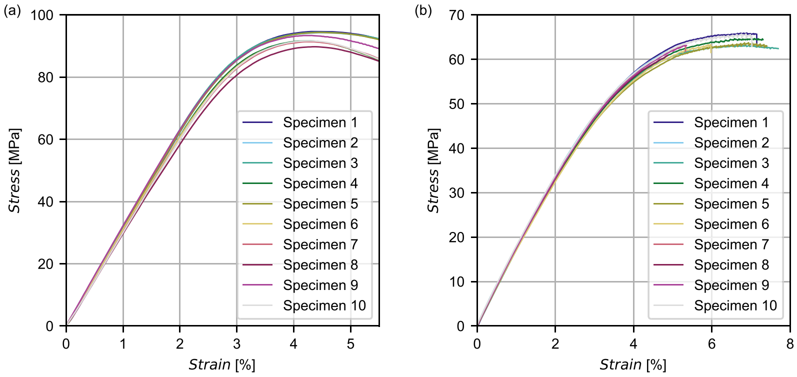

Fig. 9. Quasi-static stress-strain curves of the parent materials of 10 three-point-bending specimens each. (a): PLA, (b): Resin.

structure of a trained NN and applying global, constrained, and non-linear optimization techniques (e.g. simplicial homology global optimization (shgo) [32]).

Table 5
Mechanical parameters obtained from the three-point-bending tests (* no fracture within 12% strain).

Material Parameter	PLA	Resin
Flexural Modulus [MPa]	3134 ± 81	1798 ± 59
Max. Stress [MPa]	92,7 ± 1,8	63,6 ± 1,6
Strain at Break [%]	>12*	6,3 ± 1,2
Modulus of Toughness [MPa]	>8.2*	2,68 ± 0,71

4. Results

4.1. Bending test results

Fig. 9 shows the stress-strain curves for the three-point-bending tests. While the resin specimens fractured at a strain of 6.3%, the PLA specimens did not fracture within 12% of strain, and the measurements were stopped. The obtained values with their respective standard deviation are listed in Table 5. Since the PLA specimens did not break before the measurements were stopped, the listed values for the modulus of toughness and strain at break are only a lower bound, and the real values are higher. The smallest value of the measurements, calculated up to 12% strain, is listed in the table. For the FE models, the data was restricted to a maximum strain of 5%, as recommended in DIN EN ISO 178 [24].

4.2. Compression test results

In the following discussion, the results of the quasi-static compression tests are labeled ‘nominal’, because the stress and strain values are calculated with the nominal dimensions of the structure. These values do not represent ‘real’ or local stresses and strains within the structure. They were calculated as:

$$\sigma = \frac{F}{A_{total}} \tag{8}$$

where σ is the nominal stress, F is the force and A_{total} is the measured area of the cube (approx. 50 mm × 50 mm = 2500 mm^2) and

$$\varepsilon = \frac{\Delta l}{l_0} \tag{9}$$

with ε being the nominal strain, Δl is the global displacement of the structure, determined with the extensometer and l_0 is the initial length of the extensometer (z-direction: 49 mm, x-direction: 30 mm–40 mm). The Poisson’s Ratio is defined as

$$\nu_{12} = -\frac{\varepsilon_2}{\varepsilon_1} \tag{10}$$

where ε_2 is the strain perpendicular to ε_1, caused by stress σ_1 ($1, 2 = x, y, z$).

4.2.1. Compression modulus

Fig. 10 shows the stress-strain curves for each of the five additively manufactured sample geometries ((a) – (e)) and a comparison of the curves ((f)). For each sample geometry, five specimens were tested. Specimen B-5 was excluded from the analysis, as uncured resin accumulated in the transition from the struts to the cubes during printing and was not properly cleaned off. This led to an increase in the effective radius of the fillets and consequently to an increase in the compression modulus.

The PLA-based specimens (A and E) showed no fracture but a collapsing of struts. This is in contrast to the resin-based specimens (B, C, and D), where a partial fracture of struts was observed (C and D), or a complete fracture of one strut-row (B) was present. This is mainly caused by the lower strain atbreak value of the resin when compared to PLA. The higher toughness of the PLA prevents fracture in this loading regime. The different fracture behavior of specimen B can be explained by its reduced strut thickness and higher distance between the cubes when compared to the other DLP structures. This leads to a higher susceptibility to tensile forces caused by the in-plane movement of the layers. The other specimens show comparable mechanical behavior (see Fig. 11 (a)). First, an elastic regime, defined by the geometric parameters of the structure, is observed. The compression modulus was calculated in this regime in the strain range of 0.05%–0.25%, similar to DIN EN ISO 604 [33]. This does not pertain to specimens B, where a range of 0.5%–1.5% was used. The elastic regime is followed by a plateau regime, where partial fracture of individual struts takes place. Not all struts fractured simultaneously, but the individual layers stayed connected until the end of the measurement. Finally, after the global deformation has led to the individual cubes touching each other, the densification regime starts, and the mechanical properties are defined by the parent material. The modulus of toughness and maximum stress were calculated either up to 14% strain or until fracture (specimen B). The mean values and their respective standard deviation of the observed mechanical parameters are listed in Table 6. Fig. 11 and Table 7 show a comparison of the experimental and simulation results of the compression modulus for the tested structures. Both simulation techniques are in good agreement with the experimental values. Only the simulations based on full-size structures show a higher stiffness than the homogenization results. This is mainly attributed to the coarser mesh used for the full-size simulations for computational efficiency reasons. Coarser meshes with tetrahedron-shaped elements tend to have a higher stiffness when compared to a finer mesh, especially in bending-dominated structures [34]. The good agreement between

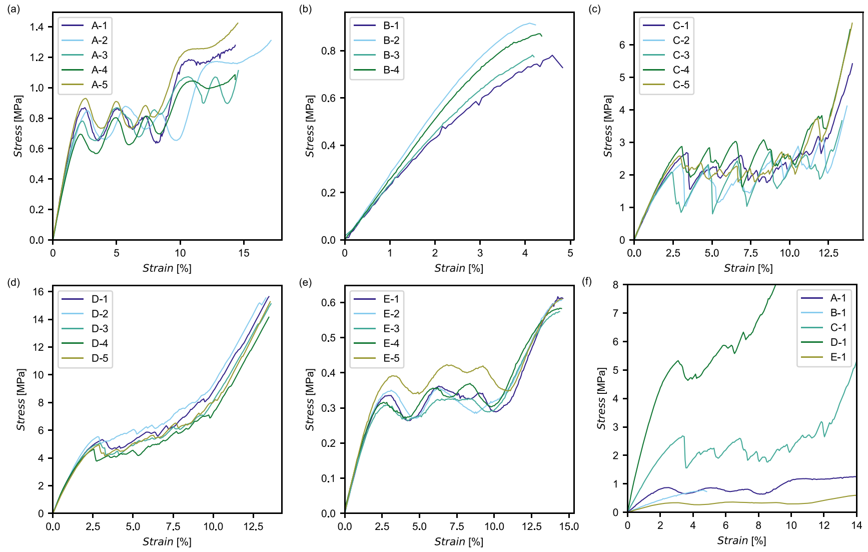

Fig. 10. Quasi-static stress-strain curves for the compression tests. (a): Specimens A, (b): Specimens B, (c): Specimens C, (d): Specimens D, (e): Specimens E, (f): Comparison of specimens A – E.

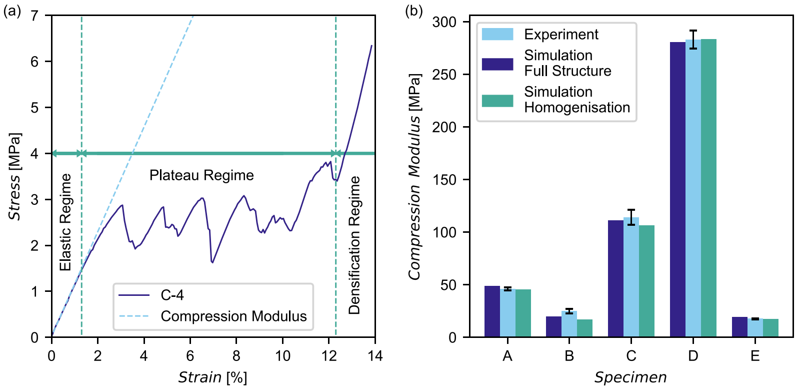

Fig. 11. Compression test results. (a): Quasi-static stress-strain curve for specimen C-4 showing three different regimes when compressed (elastic regime, plateau regime, and densification regime). (b): Comparison of compression modulus obtained from compression tests and simulations based on the full structures and homogenization.

Table 6
Mechanical properties obtained from the compression tests of the additively manufactured structures (* calculated up to 14% strain, the lowest value is listed, ** no global fracture but local collapsing of struts, *** only partial fracture of struts).

Sample Parameter	A	B	C	D	E
Compression Modulus [MPa]	46.1 ± 1.5	25.0 ± 2.2	114.1 ± 7.1	282.9 ± 8.5	17.61 ± 0.38
Max. Stress [MPa]	>1.1*	0.837 ± 0.068	>3.7*	>14.2*	>0.58*
Strain at Break [%]	- **	4.40 ± 0.29	- ***	- ***	- **
Modulus of Toughness [MPa]	>0.11*	0.0216 ± 0.0019	>0.27*	>0.83*	>0.047*

experimental results and homogenization allows reducing the computational complexity of the design process since the homogenization is much faster than the full-size simulations.

Fig. 12 shows numerical results for compression moduli, based on calculations with isotropic UCs. For each cube side length (A) in the range of 0.5 mm—10 mm, the strut thickness (T) and distance between the cubes (D) were varied in the range of 0.2 mm—10 mm and 0.5 mm—20 mm, respectively. UCs with $T > A$ are geometrically not possible, and hence, not included. For each individual plot, a constant ratio of A/D was chosen. The other geometric parameters were set to $R = 0.2$ mm and $C = 0.1$ mm. First, 2897 FE simulations, based on the homogenization method, were performed to scan the parameter space broadly. The intermediate values were calculated with a neural-network (f_1 = sigmoid, f_2 = selu) as described in section 3.2.The material model for PLA was used for the calculations. Fig. 12 shows the broad range of possible compression modulus, ranging from 2 MPa to 1700 MPa, which can be obtained with our structural design. A fixed ratio of $A/D = 2/1$ is already suitable to cover a broad range of possible compression moduli, thus further reducing the parameter space by one parameter and the complexity of the modeling process. Lower values of A/D allow for soft structures with subtle changes in stiffness. With increasing relative density (Fig. 4), an increase of the compression modulus can be observed. The most distinct changes in stiffness are observed with varying strut thickness. This can be explained by the bending resistance of a rectangular beam. The bending resistance is proportional to the second moment of inertia. Equation (11) shows the second moment of inertia for the struts in the different spatial directions, excluding structures with gradient transitions ($i = x, y, z$). It scales cubically with the strut thickness, while the strut depth, which is equivalent to the cube side length (A), only affects the second moment of inertia linearly.

Table 7
Comparison of compression moduli, obtained from compression tests, simulations based on the full structure and based on the UC homogenization (rounded to the nearest integer).

Sample Compression Modulus	A	B	C	D	E
Experiment [MPa]	46	25	114	283	18
Full Structure Simulation [MPa]	52	20	115	301	21
Unit Cell Simulations [MPa]	46	17	107	284	17

$$I_j = \frac{T_i^3 A}{12} \tag{11}$$

In the limit of $D \rightarrow 0$, a full block of the parent material is obtained, and the compression modulus is given by the parent material. Hence, the obtainable compression modulus ranges from a few MPa to one of the parent materials.

Fig. 13 shows simulation results for orthotropic geometries, based on the homogenization method and additional full-size simulations. The strut thickness in the x-direction was held constant at $T_x = 0.8$ mm, while the thickness in y- and z-direction was varied from 0.2 mm to 3.0 mm simultaneously. The other geometric parameters were set to $A = 5$ mm, $D = 2.5$ mm, $R = 0.2$ mm and $C = 0.1$ mm for all simulations. The compression modulus in the x-direction only changes from 45 MPa to 46 MPa (2.2% change), while the compression modulus in the y- and z-direction changes from 2 MPa to 1046 MPa (52,200% change). This highlights that the compression modulus can be varied in each direction independently. For verifying the homogenization results, additional simulations with full structures at values of $T_y = T_z = 0.2$ mm, 0.8 mm, 1.5 mm, and 3.0 mm were performed. The same behavior is observed, and only the absolute values are higher when compared to the homogenization results (approx. 55 MPa). This is consistent with the simulation results for the full-size structures, where

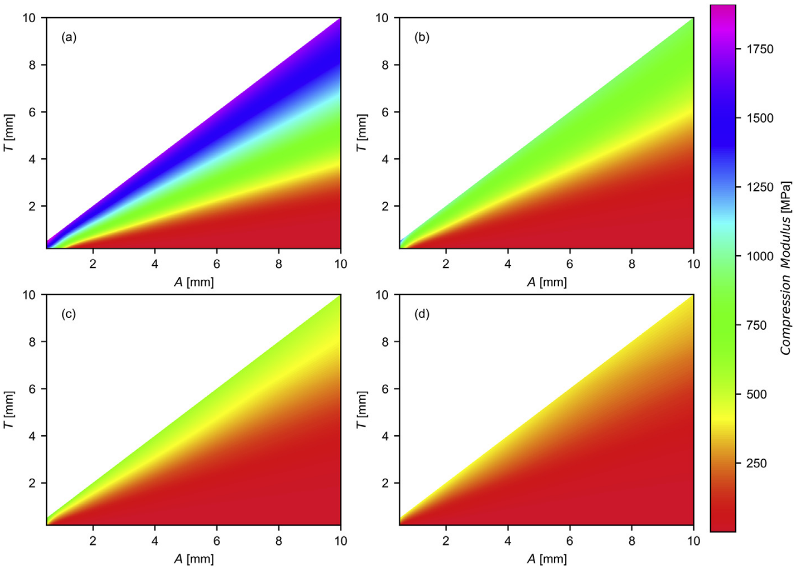

Fig. 12. Calculated compression modulus based on FEA and machine learning for four different ratios of cube length (A) to distance between the cubes (D). (a): A:D = 2:1, (b): A:D = 1:1, (c): A:D = 1:1.5, (d) A:D = 1:2. The white areas are geometrically not possible, since $T < A$.

higher values are attributed to the coarser mesh of the full-size structure simulations.

4.2.2. *Poisson's ratio*

The strut thickness of the tested geometries is small compared to the side length of the cubes. Thus, the deformation under compression is mainly bending-dominated. The bending of struts leads to an alternating in-plane movement of the connected cubes in a direction perpendicular to the applied compression. Although the movement is not restricted, only small deformations occur, indicating a small Poisson's Ratio. Fig. 14 (a) shows the strain perpendicular to the compression direction, ε_x, as a function of the strain in the direction of compression, ε_z, for the geometry with the highest absolute value of transversal strain (samples D). A comparison of the tested geometries for a representative specimen is shown in Fig. 14 (b). Even for the geometry with the biggest observed transversal strain at $\varepsilon_x = 0.15\,\%$ in the linear elastic regime, this would only correspond to a total deformation of 0.06 mm (extensometer length l_0 = 40 mm). Such small deformations could not be captured with the measurement setup used. Hence, the Poisson's Ratio is discussed with simulation results only.

Simulation results for the Poisson's Ratio, based on homogenization simulations and a neural-network analysis (f_1 = relu, f_2 = linear), are shown in Fig. 15. For each cube side length (A) in the range of 0.5 mm–10 mm, the strut thickness (T) and distance between the cubes (D) were varied in the range of 0.2 mm–10 mm and 0.5 mm–20 mm, respectively. Only isotropic structures are considered. For each individual plot, a constant ratio of A/D was chosen. The values of the Poisson's Ratio vary in the range of 0–0.25. When compared to the stiffness (Fig. 12), it can be observed that the Poisson's Ratio increases with the stiffness, as well as the

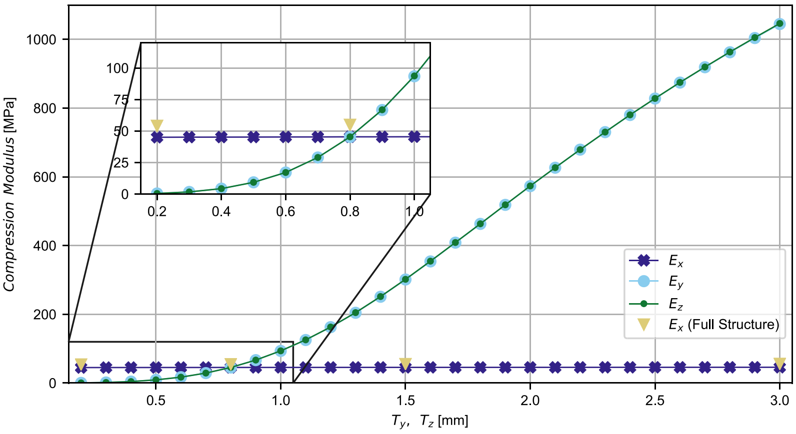

Fig. 13. Compression moduli as a function of strut thickness in y- and z-direction for an orthotropic structure based on homogenization simulations and full structures.

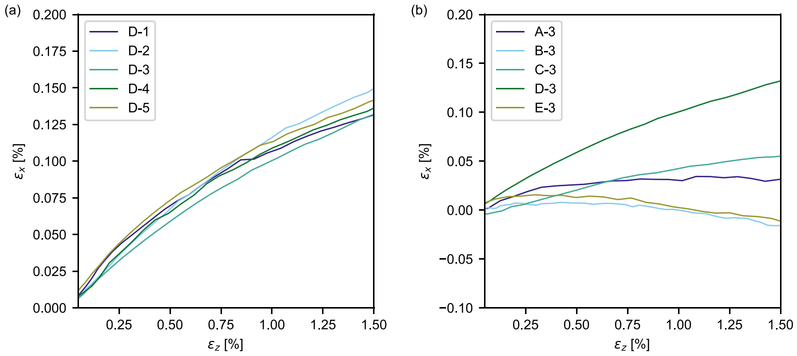

Fig. 14. Strain in the perpendicular direction (x) as a function of the strain in compression direction (z). (a): Comparison of strain curves for sample D, (b): Comparison of tested sample geometries.

relative density (Fig. 4). With increasing strut thickness, the main deformation of the struts changes from bending to compression. The Poisson's Ratio is then no longer defined by the in-plane movement of the cubes, but the compression of the struts. Consequently, Poisson's Ratio of the structure approaches the Poisson's Ratio of the parent material. Additionally, with increasing cube length (A), more volume is filled with material, and since the deformation of the cubes is mainly compression-dominated, an increasing Poisson's Ratio can be observed. Since the compression resistance of the cubes is much higher than the bending resistance of the struts, the strut thickness has a greater influence on the Poisson's Ratio.

For a small thickness of connecting struts in the y-direction, no deformation is expected when a compression force is applied in the x-direction because each row of cubes moves as a whole. Thus, the Poisson's Ratio ν_{xy} is expected to be close to zero. Again, with increasing strut thickness, the Poisson's Ratio of the structure will approach the Poisson's Ratio of the parent material.

4.2.3. *Examples of complex structures*

For demonstrating the variability of the proposed design, examples of structures with more complex directional properties were additively manufactured. The specimens were produced with an FFF printer, 'CreatBot F430' (Henan Suwei Electronic Technology Co., LTD., Zhengzhou City, China). A thermoplastic polyurethane (TPU) ('NinjaTek NinjaFlex', Fenner Inc., Manheim, USA) was used as the parent material. The specimens were printed with a nozzle and bed temperature of 230 °C and 40 °C, respectively. The geometric parameters and the compression test results are listed in Table 8. The other geometric parameters were set to $R = 0.2$ mm and $C = 0.1$ mm. In contrast to the samples discussed in section 2.3, no compression surfaces were added. One sample of each specimen was manufactured and rotated accordingly to measure the properties in the three spatial directions. The compression moduli were directly obtained from the compression tests. The tests were performed with an 'Instron 5500' (Instron, Norwood, USA) and a testing speed of 5 mm/min.

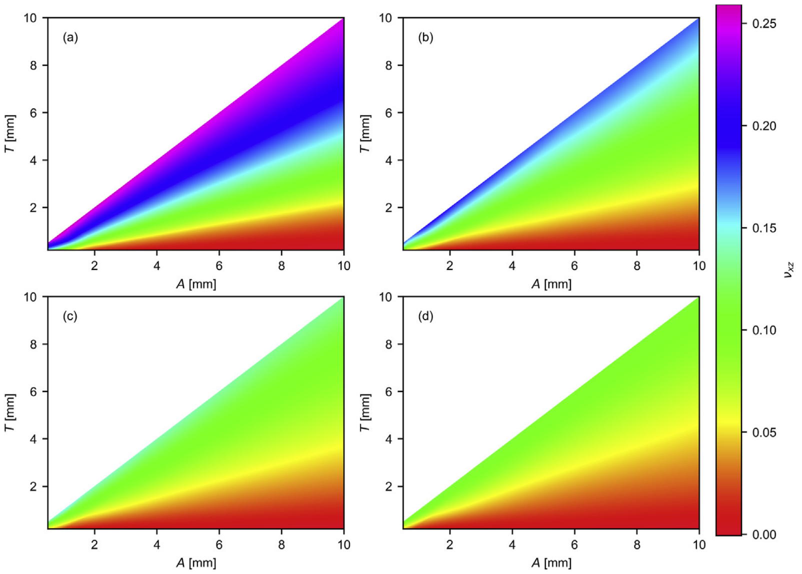

Fig. 15. Calculated Poisson's Ratio based on FEA and machine learning for four different ratios of cube length (A) to distance between the cubes (D). (a): A:D = 2:1, (b): A:D = 1:1, (c): A:D = 1:1.5, (d) A:D = 1:2. The white areas are geometrically not possible, since $T < A$.

Table 8
Geometric parameters and compression test results for anisotropic and orthotropic structures.

Sample	A [mm]	$D_x = D_y = D_z$ [mm]	T_x	T_y	T_z	E_x [MPa]	E_y [MPa]	E_z [MPa]
A	5	2.5	0.8	1.2	1.6	0.80	2.02	3.43
B	5	2.5	0.8	0.8	1.6	0.77	0.74	3.13
C	5	2.5	0.8	1.6	1.6	0.84	3.27	3.13

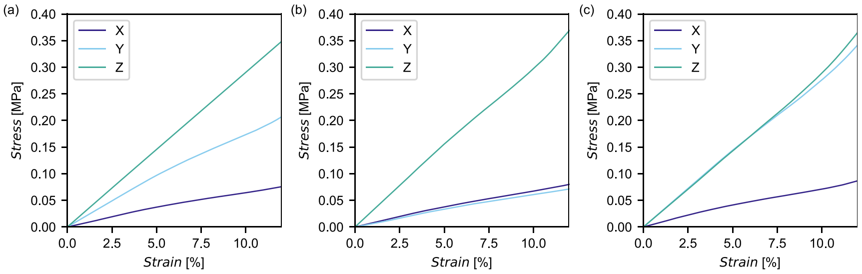

Fig. 16. Quasi-static stress-strain curves for three different additively manufactured specimens with stiffness variation in the three spatial directions. (a): Anisotropic (sample A), (b): Orthotropic (sample B), (c): Orthotropic (sample C).

The stress-strain curves of the tested specimens are shown in Fig. 16 ((a): anisotropic, (b) and (c): orthotropic). The anisotropic sample highlights the tunability of the proposed structure. A video of the compression tests of the anisotropic sample is available in the Supplementary Data online. Both orthotropic structures show good agreement in the directions where the parameters were the same. Only at higher strain values (>7%) and past the linear elastic regime, a deviation is observed. This deviation can be caused by the different layer directions of the struts during the additive manufacturing process with FFF.

5. Concluding remarks

In this study, a design for a new metamaterial with variable compression properties was introduced. The bending-dominated structure permits varying the compression modulus in a broad range, independently in the three spatial directions. For a small strut thickness, the Poisson's Ratio of the structure is close to zero. The design allows the manufacture of structures for complex load and boundary conditions with only a few geometric parameters. The main parameters are the strut thickness (*T*) and the ratio of cube length to the distance between the cubes (*A*/*D*). This reduced set of parameters can be used to reduce the complexity of optimization strategies. For example, topology optimization in 3D can be utilized to further reduce the material consumption of existing structures. The incorporation of neural networks also opens the possibility to obtain a set of geometric parameters for a specific mechanical property. This can be achieved with constrained, multidimensional global optimization techniques. Since this is usually a computationally complex problem, the reduction of the parameter space is beneficial to decrease the computational cost. Numerical simulations, both on full-size structures and using homogenization strategies, show good agreement with the experimental compression test results. Examples with variable directional properties (orthotropic and anisotropic) highlight the variability and independent tunability of the proposed geometry. So far, only linear elastic properties were investigated for the proposed geometry. Further studies on plastic deformation and fracture behavior are of importance for future applications. Additionally, studies with locally varying unit cells or gradient transitions are to be expected for future investigations. A patent application has been filed for the design of the structure and is pending.

Authors' contributions

Mathias Fleisch: Conceptualization, Methodology, Software, Validation, Formal analysis, Investigation, Data Curation, Writing - Original Draft, Writing - Review & Editing, Visualization. **Andreas Thalhamer**: Methodology, Software, Validation, Formal analysis, Investigation, Data Curation, Writing - Original Draft, Writing – review & editing, Visualization. **Gerald Meier**: Investigation. **Ivan Raguž**: Investigation. **Peter Filipp Fuchs**: Resources, Supervision, Writing – review & editing. **Gerald Pinter**: Resources, Supervision, Writing – review & editing. **Sandra Schlögl**: Supervision, Writing – review & editing, Project administration, Funding acquisition. **Michael Berer**: Conceptualization, Software, Validation, Data Curation, Resources, Supervision, Writing – review & editing, Project administration, Funding acquisition

Data Availability

The raw data required to reproduce these findings cannot be shared at this time due to technical limitations. The processed data required to reproduce these findings cannot be shared at this time due to technical limitations but can be provided upon request.

Declaration of competing interest

The authors declare that they have no known competing financial interests or personal relationships that could have appeared to influence the work reported in this paper.

Acknowledgments

The research work of this study was performed in the COMET-Module project 'CHEMITECTURE" (project-no.: 21647048) at the Polymer Competence Center Leoben GmbH (PCCL, Austria) within the framework of the COMET-program of the Federal Ministry for Climate Action, Environment, Energy, Mobility, Innovation and Technology and the Federal Ministry for Digital and Economic Affairs with contributions by Materials Science and Testing of

Polymers/Montanuniversitaet Leoben. The PCCL is funded by the Austrian Government and the State Governments of Styria, Lower Austria, and Upper Austria.

Appendix A. Supplementary data

Supplementary data to this article can be found online at https://doi.org/10.1016/j.mtadv.2021.100155.

References

[1] Y. Chen, J. Sun, Y. Liu, J. Leng, Variable stiffness property study on shape memory polymer composite tube, Smart Mater. Struct, 21 94021 (2012), https://doi.org/10.1088/0964-1726/21/9/094021.

[2] E. Rossegger, R. Höller, D. Reisinger, J. Strasser, M. Fleisch, T. Griesser, S. Schlögl, Digital light processing 3D printing with thiol–acrylate vitrimers, Polym. Chem. 12 (2021) 639–644, https://doi.org/10.1039/d0py01520b.

[3] Z. Varga, G. Filipcsei, M. Zrínyi, Magnetic field sensitive functional elastomers with tuneable elastic modulus, Polymer 47 (2006) 227–233, https://doi.org/10.1016/j.polymer.2005.10.139.

[4] B.D. Chin, M.-S. Chun, H. Henning Winter, Modulus-switching viscoelasticity of electrorheological networks, Rheol. Acta 48 (2009) 177–189, https://doi.org/10.1007/s00397-008-0326-8.

[5] Z. Ren, W. Hu, C. Liu, S. Li, X. Niu, Q. Pei, Phase-changing bistable electroactive polymer exhibiting sharp rigid-to-rubbery transition, Macromolecules 49 (2016) 134–140, https://doi.org/10.1021/acs.macromol.5b02382.

[6] J.R. Amend, E. Brown, N. Rodenberg, H.M. Jaeger, H. Lipson, A positive pressure universal gripper based on the jamming of granular material,, IEEE Trans. Robot. 28 (2012) 341–350, https://doi.org/10.1109/TRO.2011.2171093.

[7] M. Taghavi, T. Helps, B. Huang, J. Rossiter, 3D-Printed ready-to-use variable-stiffness structures, IEEE robot, Autom. Lett. 3 (2018) 2402–2407, https://doi.org/10.1109/lra.2018.2812917.

[8] J.U. Surjadi, L. Gao, H. Du, X. Li, X. Xiong, N.X. Fang, Y. Lu, Mechanical metamaterials and their engineering applications, Adv. Eng. Mater. 21 (2019), 1800864, https://doi.org/10.1002/adem.201800864.

[9] X. Yu, J. Zhou, H. Liang, Z. Jiang, L. Wu, Mechanical metamaterials associated with stiffness, rigidity and compressibility: a brief review,, Prog. Mater. Sci. 94 (2018) 114–173, https://doi.org/10.1016/j.pmatsci.2017.12.003.

[10] X. Zheng, H. Lee, T.H. Weisgraber, M. Shusteff, J. DeOtte, E.B. Duoss, J.D. Kuntz, M.M. Biener, Q. Ge, J.A. Jackson, S.O. Kucheyev, N.X. Fang, C.M. Spadaccini, Ultralight, ultrastiff mechanical metamaterials, Science (New York, N.Y.) 344 (2014) 1373–1377, https://doi.org/10.1126/science.1252291.

[11] T.A. Schaedler, A.J. Jacobsen, A. Torrents, A.E. Sorensen, J. Lian, J.R. Greer, L. Valdevit, W.B. Carter, Ultralight metallic microlattices, Science (New York, N.Y.) 334 (2011) 962–965, https://doi.org/10.1126/science.1211649.

[12] D. Mousanezhad, B. Haghpanah, R. Ghosh, A.M. Hamouda, H. Nayeb-Hashemi, A. Vaziri, Elastic properties of chiral, anti-chiral, and hierarchical honeycombs: a simple energy-based approach,, Theoretical and Applied Mechanics Letters 6 (2016) 81–96, https://doi.org/10.1016/j.taml.2016.02.004.

[13] A. Alomarah, S.H. Masood, I. Sbarski, B. Faisal, Z. Gao, D. Ruan, Compressive properties of 3D printed auxetic structures: experimental and numerical studies, Virtual Phys. Prototyp. 15 (2020) 1–21, https://doi.org/10.1080/17452759.2019.1644184.

[14] E. Truszkiewicz, A. Thalhamer, M. Rossegger, M. Vetter, G. Meier, E. Rossegger, P. Fuchs, S. Schlögl, M. Berer, Mechanical Behavior of 3D-Printed Polymeric Metamaterials for Lightweight Applications, Additive Manufacturing, 2021.

[15] L.J. Gibson, M.F. Ashby, Cellular solids: structure and properties, Cambridge University Press (2014), https://doi.org/10.1017/CBO9781139878326.

[16] J.N. Grima, R. Gatt, P.-S. Farrugia, On the properties of auxetic meta-tetrachiral structures, Phys. Status Solidi 245 (2008) 511–520, https://doi.org/10.1002/pssb.200777704.

[17] H.M.A. Kolken, A.A. Zadpoor, Auxetic mechanical metamaterials, RSC Adv. 7 (2017) 5111–5129, https://doi.org/10.1039/C6RA27333E.

[18] H. Ebrahimi, D. Mousanezhad, H. Nayeb-Hashemi, J. Norato, A. Vaziri, 3D cellular metamaterials with planar anti-chiral topology, Mater. Des. 145 (2018) 226–231, https://doi.org/10.1016/j.matdes.2018.02.052.

[19] T. Frenzel, M. Kadic, M. Wegener, Three-dimensional mechanical metamaterials with a twist, Science (New York, N.Y.) 358 (2017) 1072–1074, https://doi.org/10.1126/science.aao4640.

[20] I. Fernandez-Corbaton, C. Rockstuhl, P. Ziemke, P. Gumbsch, A. Albiez, R. Schwaiger, T. Frenzel, M. Kadic, M. Wegener, New twists of 3D chiral metamaterials, adv, Mater 31 (2019), e1807742, https://doi.org/10.1002/adma.201807742.

[21] W. Wu, D. Qi, H. Liao, G. Qian, L. Geng, Y. Niu, J. Liang, Deformation mechanism of innovative 3D chiral metamaterials, Scientific reports, 8 12575 (2018), https://doi.org/10.1038/s41598-018-30737-7.

[22] A. Bacigalupo, L. Gambarotta, Homogenization of periodic hexa- and tetrachiral cellular solids, Compos. Struct. 116 (2014) 461–476, https://doi.org/10.1016/j.compstruct.2014.05.033.

[23] W. Chen, X. Zheng, S. Liu, Finite-element-mesh based method for modeling and optimization of lattice structures for additive manufacturing, Materials 11 (2018), https://doi.org/10.3390/ma11112073.

[24] DIN EN ISO, 178–4: Kunststoffe - Bestimmung der Biegeeigenschaften.

[25] Michael Smith, ABAQUS/Standard User's Manual, Dassault Systèmes Simulia Corp, United States, 2009, Version 6.9.

[26] N. Stander, A. Basudhar, W. Roux, K. Witowski, T. Eggleston, T. Goel, K. Craig, LS-OPT®User's Manual: A DESIGN OPTIMIZATION and PROBABILISTIC ANALYSIS TOOL for the ENGINEERING ANALYST.

[27] J. Effelsberg, A. Förderer, K. Witowski, M. Feucht, M. Söllner, Identifikation von Materialparametern mit LS-OPT®: GISSMO und andere Anwendungen (2014). https://www.dynamore.de/de/download/presentation/2014-und-aelter/download-infotag-optimierung/02-2-identifikation-von-materialparametern-mit-ls.pdf/view. (Accessed 17 March 2021).

[28] M.G.D. Geers, V.G. Kouznetsova, W.A.M. Brekelmans, Multi-scale computational homogenization: trends and challenges, J. Comput. Appl. Math. 234 (2010) 2175–2182, https://doi.org/10.1016/j.cam.2009.08.077.

[29] 3DEXPERIENCE, Micromechanics Plugin: for Abaqus/CAE, 2017, Version 1.15.

[30] F. Chollet, Keras, 2015. https://github.com/fchollet/keras. (Accessed 17 March 2021).

[31] G. van Rossum, F.L. Drake, Python 3 Reference Manual, CreateSpace, Scotts Valley, CA, 2009.

[32] S.C. Endres, C. Sandrock, W.W. Focke, A simplicial homology algorithm for Lipschitz optimisation,, J. Global Optim. 72 (2018) 181–217, https://doi.org/10.1007/s10898-018-0645-y.

[33] DIN EN ISO, 604: Kunststoffe - Bestimmung von Druckeigenschaften.

[34] M. Bäker, How to Get Meaningful and Correct Results from Your Finite Element Model, 2018.

Paper B

Chiral-based mechanical metamaterial with tunable normal-strain shear coupling effect

Authors: Fleisch, M.
Thalhamer, A.
Meier, G.
Huber, P.A.F.
Fuchs, P.F.
Pinter, G.
Schlögl, S.
Berer, M.

Engineering Structures
DOI: 10.1016/j.engstruct.2023.115952

Engineering Structures 284 (2023) 115952

Contents lists available at ScienceDirect

Engineering Structures

journal homepage: www.elsevier.com/locate/engstruct

Chiral-based mechanical metamaterial with tunable normal-strain shear coupling effect

Mathias Fleisch[a], Andreas Thalhamer[a], Gerald Meier[a], Philipp Arno Franz Huber[a], Peter Filipp Fuchs[a], Gerald Pinter[b], Sandra Schlögl[a], Michael Berer[a,*]

[a] *Polymer Competence Center Leoben GmbH, Roseggerstrasse 12, 8700 Leoben, Austria*
[b] *Department of Polymer Engineering and Science, Montanuniversitaet Leoben, Otto-Gloeckel Strasse 2, 8700 Leoben, Austria*

ARTICLE INFO

Keywords:
Mechanical metamaterial
Shear coupling
Additive manufacturing
Mechanical characterization
Finite element analysis

ABSTRACT

Different designs for mechanical metamaterials with tunable normal-strain shear coupling effect have been demonstrated over the last years. Their adjustable shear deformation makes them suitable as building blocks for soft robotics applications or structures with a desired deformation behavior, such as shape morphing structures. Herein, we present a modified 2.5D and 3D chiral-based mechanical metamaterials with tunable normal-strain shear coupling effect and Poisson's Ratios close to zero. Advancing from conventional chiral-based metamaterials by introducing additional geometric freedoms into the design of the unit cell, a broad range of shear deformations, compression moduli and porosities can be achieved. 2.5D specimens with selected geometric parameters were additively manufactured with polypropylene using Fused Filament Fabrication. Compression tests were performed to investigate the mechanical properties and shear deformation. Two different numerical models were employed using ABAQUS to study the influence of the geometric parameters onto the mechanical properties and were verified by the experiments. The numerical material models were based on three-point-bending test data. The three-dimensional design was investigated with numerical simulations based on a homogenization approach to cover a broad range of geometric parameters.

1. Introduction

Metamaterials are architected materials that exhibit properties and capabilities usually not found in conventional materials [1]. Metamaterials with unusual optical [2], acoustical [3] and thermal [4] properties have been demonstrated. Mechanical metamaterials [5–8] exploit the deformation behavior of carefully constructed structures to obtain uncommon mechanical properties. These properties include, but are not limited to, lightweight structures [9–12], variable stiffness structures [13–15] and structures with zero or negative Poisson's Ratio [16–21]. Some mechanical metamaterials exhibit more than one unusual mechanical property. Tetra-chiral based structures [16,22–24] usually have a Poisson's Ratio of zero, or close to zero [25], similar to cork [26]. They are typically composed of circular or point-like nodes with tangentially attached struts. Under compression, the bending of the struts leads to a rotation of the nodes and subsequent shearing of the structure. Thus, showing an additional normal-strain shear coupling effect. Different (2.5 D) designs exploiting this effect have been demonstrated, e.g. chiral-based structures with semicircular [27], V-shaped [28] or cosinoidal beams [29]. The shear coupling effect was also demonstrated in three-dimensional mechanical metamaterials to create twisting structures [30]. Advancing from an observation in a previous study on asymmetric tetra-chiral structures [16], where the introduced asymmetry lead to a decreasing shear coupling effect, we present a modified design for a chiral-based mechanical metamaterial with improved tunability of the normal-strain shear coupling effect. By changing the circular or point-like node to a rectangular node and the square bounding box of the unit cell to a rectangular bounding box, new degrees of geometric freedom are introduced. Those degrees of freedom allow to tune the normal-strain shear coupling effect, compression modulus and porosity of the proposed structure simultaneously in a broad range. In metamaterials the properties of interest are usually not independent, but are correlated to each other. By introducing the new degrees of geometric freedom, this dependency can be reduced or circumvented. For example, the presented design allows to create structures with the same shear-coupling effect at different stiffnesses. This

---

* Corresponding author.
E-mail address: michael.berer@pccl.at (M. Berer).

https://doi.org/10.1016/j.engstruct.2023.115952

permits to expand the capabilities of metamaterial mechanisms [31,32] and soft adaptive structures for soft robotic applications [33]. Herein, we present the design, additive manufacturing (AM), experimental test results and numerical investigation of different tetra-chiral based structures. Seven structures with different shear coupling effect, porosity and compression modulus were additively manufactured with Fused Filament Fabrication (FFF) using a filament made of polypropylene (PP). The mechanical properties of the structures were obtained by means of mechanical tests in the form of compression tests. The investigations were complemented by numerical simulations based on finite element analysis (FEA). Two different simulation techniques were used. First, full-scale simulations based on the geometries of the tested sample structures were performed to investigate the deformation behavior during the compression tests. Secondly, a homogenization technique was used to cover a broad range of geometric parameters and their influence onto the mechanical parameters. The material model for the numerical simulations was based on three-point bending tests. In addition to the 2.5 D design, we also present a three-dimensional version of the proposed structure with tunable shear coupling effect in one additional dimension. Different three-dimensional designs based on chiral unit cells have been demonstrated in literature. They can either be constructed by connecting 2.5 D cells at their protruding struts at various angles [22,30,34] or a chiral arrangement of struts to a regular grid of nodes [35–37]. Derived from the presented 2.5 D structure, the three-dimensional version consists of a regular grid of variable cuboids with chiral connections. This permits to create structures with specified shear deformation in two spatial directions by applying a (compression) load in one direction. Similar to the 2.5 D variant, additional geometric parameters allow to tune the mechanical response of the structure with more control. The mechanical properties are obtained from numerical simulations based on the homogenization approach.

2. Materials and methods

Metamaterials are usually composed of an arrangement of unit cells (UCs). The UC already possesses the special properties of interest. By stacking them in the spatial directions, metamaterial structures for an application are created. In this section, first the design and the characteristic parameters of the UC are presented. Next, the design and additive manufacturing process of the investigated sample structures are described. Finally, the experimental setup and evaluation methods to obtain the mechanical properties of the parent material and the sample structures is presented.

Table 1
Geometric parameters of the unit cell shown in Fig. 1 and their description.

Parameter	Description
L_x, L_y, L_z	Length of the bounding box in X, Y and Z direction
A_x, A_y	Length of the rectangular node in X and Y direction
T	Thickness of the struts
R	Radius of the fillet

2.1. Design of the unit cell

The design of the tunable normal-strain shear coupling UC is based on a tetra-chiral structure, a well-established metamaterial [16,22–25]. Usually the UC of tetra-chirals is constructed with a square bounding box and a circular node in the center. Four connecting struts are then tangentially attached to the circular node. In order to allow for more geometrical degrees of freedom, we instead use a rectangular bounding box and rectangular node with side lengths L_xL_y and A_xA_y, respectively. Struts with thickness T are connected at the four edges of the node. A fillet with radius R at the connection of the strut to the node is introduced to reduce stress concentrations. Another benefit of fillets is the reduced complexity for manufacturing since sharp edges are usually more time consuming and sometimes impossible to produce. In order to create a three-dimensional body, the structure is extruded in the third dimension by L_z. Fig. 1 (a) shows the cross-section with indicated dimensions of the proposed UC. A three-dimensional view of the UC is depicted in Fig. 1 (b). The geometric parameters and their description are listed in Table 1. To obtain a valid geometry, the following constraints have to be satisfied.

$$\begin{cases} T \leq A_x < L_x \\ T \leq A_y < L_y \end{cases} \tag{1}$$

A chiral unit cell is not superimposable onto its mirror image [38]. The strut attachment can either be right-handed or left-handed. In this study we present the left-handed variant, but the same principle can be applied to obtain a right-handed version.

The strut angles, α and β, can be derived from this set of geometric parameters, resulting in.

$$\begin{cases} \alpha = \sin^{-1}\left(\dfrac{T}{\sqrt{A_x^2 + \left(L_y - A_y\right)^2}}\right) + \tan^{-1}\left(\dfrac{L_y - A_y}{A_x}\right) \\ \beta = \sin^{-1}\left(\dfrac{T}{\sqrt{A_y^2 + \left(L_x - A_x\right)^2}}\right) + \tan^{-1}\left(\dfrac{L_x - A_x}{A_y}\right) \end{cases} \tag{2}$$

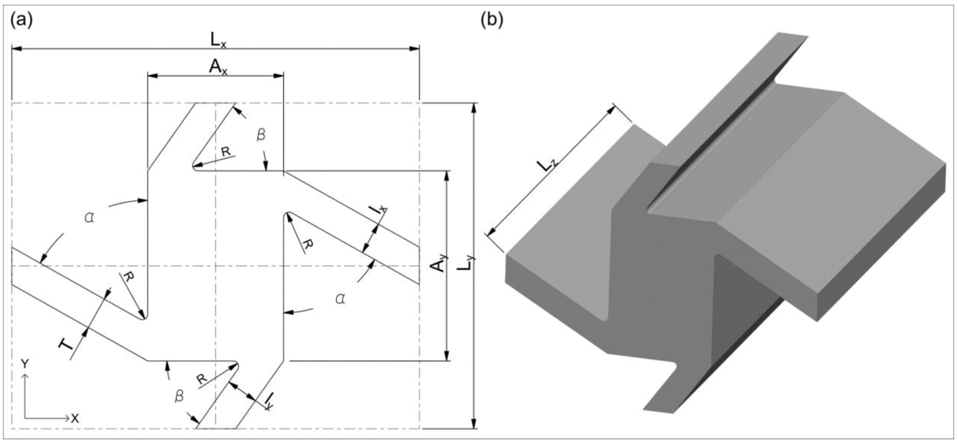

Fig. 1. Unit cell of the proposed structure with tunable normal-strain shear coupling effect. (a) Cross-section with indicated geometric parameters and (b) 3D view of the unit cell.

The strut lengths, l_x and l_y, can be obtained by geometric considerations and are given as.

$$\begin{cases} l_x = \dfrac{L_x - A_x}{2sin\alpha} \\ l_y = \dfrac{L_y - A_y}{2sin\beta} \end{cases} \tag{3}$$

A characteristic value for cellular materials and metamaterials is the relative density, ρ_r, defined as.

$$\rho_r = \frac{\rho}{\rho_0} \tag{4}$$

where ρ and ρ_0 are the densities of the structure and the parent material, respectively. For a metamaterial or cellular structure made of a single material, this relation can be simplified to the ratio of UC volume and bounding box volume. For an extruded geometry, this is equivalent to the ratio of their respective cross-sectional areas, that is $\rho_r = A_{UC}/A_{BB}$. The area of the unit cell, A_{UC}, is given by.

$$\begin{aligned} A_{UC} = {} & \underbrace{A_xA_y}_{Node} + \underbrace{2Tl_x}_{Struts\ in\ x} + \underbrace{2Tl_y}_{Struts\ in\ y} + \underbrace{\left(\frac{2R\cos\beta}{\cos\beta + \sin\beta - 1} - R\right) - \frac{R^2(\pi - \beta)}{2}}_{Fillets\ in\ x} \\ & + \underbrace{\left(\frac{2R\cos\alpha}{\cos\alpha + \sin\alpha - 1} - R\right) - \frac{R^2(\pi - \alpha)}{2}}_{Fillets\ in\ y} \end{aligned} \tag{5}$$

The area of the bounding box, A_{BB}, can be calculated as follows.

$$A_{BB} = L_xL_y \tag{6}$$

Fig. 2 shows the relative density as a function of selected geometric parameters of the unit cell. It is shown that a broad range of relative densities can be obtained for the specified set of geometric parameters, ranging from 0.1 to 0.9. With increasing node dimensions, A_x and A_y, the relative density increases as well, whereas the relative density decreases with increasing bounding box dimensions, L_x and L_y. Similar to the node dimensions, the relative density increases with increasing strut thickness T. The fillet radius R only has a small influence on the relative density. The relative density is also a direct measure of the porosity P of a cellular material, that is $P = 1 - \rho_r$.

Note that as $L_x = L_y \rightarrow L$, $A_x = A_y \rightarrow 0$ and $R \rightarrow 0$ the structure transforms into a square honeycomb structure. By integrating these values into the closed-form solution for ρ_r, we obtain $\rho_r = 2T/L$, which is the relative density of a square honeycomb structure [39].

2.2. Design of the sample structures

The sample structures for the compression tests were created by stacking UCs along two spatial directions. Five identical copies in each direction were used to reduce the size effect. The protruding struts were excluded to ensure a well-defined contact surface and an optimal force transmission into the structure during the compression tests. The exterior dimensions of the sample structures were given by $S_x \times S_y \times L_z$ (refer to Fig. 3 (b) for a sketch of the sample geometries). For the structures analyzed in this study, constant values of $L_x = L_y = 15$ mm, $L_z = 24.5$ mm, $T = 1.2$ mm and $R = 0.2$ mm were chosen. The strut thickness of 1.2 mm was chosen to be a multiple of the nozzle diameter used to manufacture the sample structures, as described in section 2.3. The node side lengths, A_x and A_y, were varied in the range of 5 – 10 mm, resulting in structures with side lengths of 64 – 69 mm. In total, seven different geometries were investigated. A sketch of these UCs is depicted in Fig. 3 (a). Table 2 lists the geometric parameters, relative densities and weights of the UCs and sample structures finally used for the compression tests. The values were obtained after the additive manufacturing process and were also used as input parameters for the numerical simulations.

2.3. Additive manufacturing

The three-point bending test specimens for the parent material characterization and the sample structures were manufactured by means of an additive manufacturing technique, Fused Filament Fabrication (FFF). The preparation was done with a “QIDI TECH X-Plus” (QIDI Technology, Rui’an, China) and a filament made of polypropylene (PP, “Verbatim PP”, Verbatim GmbH, Eschborn, Germany). PP was our material of choice because of its unique combination of relatively high stiffness (Young’s modulus about 430 MPa) and good flexibility characteristics. Due to the semi-crystallinity of PP, structures tended to shrink during the additive manufacturing process and were prone to detach from the build plate. Two measures were taken to prevent this. First, at each of the four edges, thin discs (1 layer of 0.28 mm) were added to increase the surface area (see Fig. 4 (a)). In contrast to brims or rafts, these discs were easy to remove after the manufacturing process. Secondly, a thin layer of adhesive, designed for the use with PP (“Magigoo Pro PP”, Thought3D Ltd., Paola, Malta), was applied to the build plate before the printing of each structure. For the three-point bending test specimens no discs were needed and only the adhesive was applied. The printing parameters are listed in Table 3. Three examples of additively manufactured sample structures are shown in Fig. 4 (b)–(d). For the sake of completeness and to emphasize that these 2.5D structures can also be applied in areas, where additive manufacturing is not an option, it has to be mentioned that they can also be manufactured with conventional techniques, such as laser cutting, water jet cutting or milling. However, the 3D structures presented in section 5 can only be manufactured via additive manufacturing. Different methods can be used for this. These methods include, but are not limited to, powder-based manufacturing techniques like selective laser sintering where the unsintered powder provides support during the printing process, or multi-material capable processes like Fused Filament Fabrication and Multi Jet Modeling where additional support material can be used and

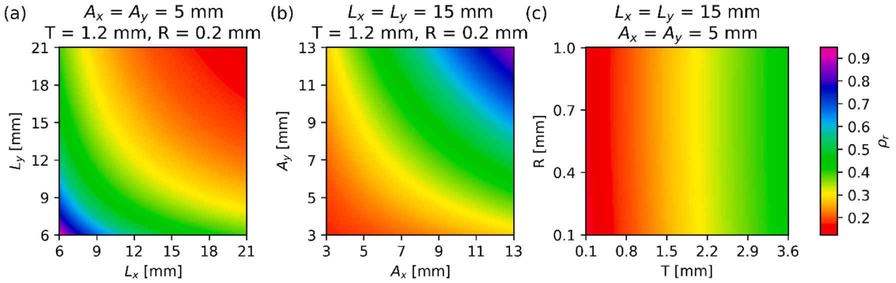

Fig. 2. Relative density as a function of the geometric parameters of the unit cell. (a) L_x and L_y with constant values of T = 1.2 mm and R = 0.2 mm, (b) A_x and A_y with constant values of T = 1.2 mm and R = 0.2 mm and (c) T and R with constant values of $L_x = L_y = 15$ mm and $A_x = A_y = 5$ mm.

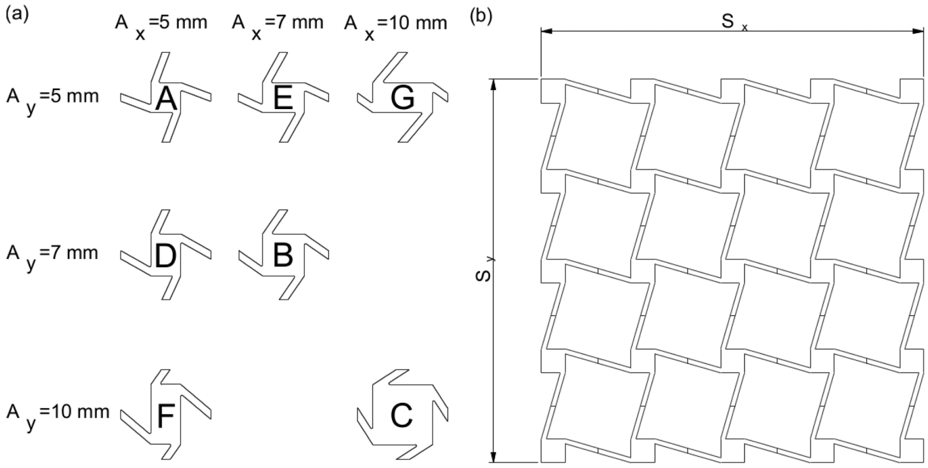

Fig. 3. Design of the sample structures for the compression tests. (a): Unit cell geometries used for the compression tests, the letters correspond to the structure labels listed in Table 2 (L_x = L_y = 15 mm, T = 1.2 mm and R = 0.2 mm), (b): Compression test sample with indicated outer dimensions.

Table 2
Geometric parameters of the unit cells and sample structures used for the compression tests. The geometric parameters were obtained after the additive manufacturing process from a representative sample. The relative density was calculated with Eqs. (5) and (6) and $L_x = L_y = 15$ mm.

Label	A_x[mm]	A_y[mm]	T [mm]	R [mm]	ρ_r	S_x[mm]	S_y[mm]	L_z[mm]	Weight [g]
A	5.13	5.13	1.18	0.2	0.23	64.00	64.05	24.50	21.66
B	7.08	7.08	1.20	0.2	0.33	66.15	66.10	24.45	32.13
C	10.07	10.07	1.20	0.2	0.56	69.00	68.95	24.55	55.35
D	5.07	6.98	1.17	0.2	0.27	64.25	65.90	24.45	25.87
E	7.02	5.04	1.23	0.2	0.27	65.90	63.90	24.50	25.84
F	5.00	10.00	1.21	0.2	0.33	64.00	68.85	24.50	32.28
G	10.12	5.06	1.19	0.2	0.34	68.80	64.05	24.55	32.19

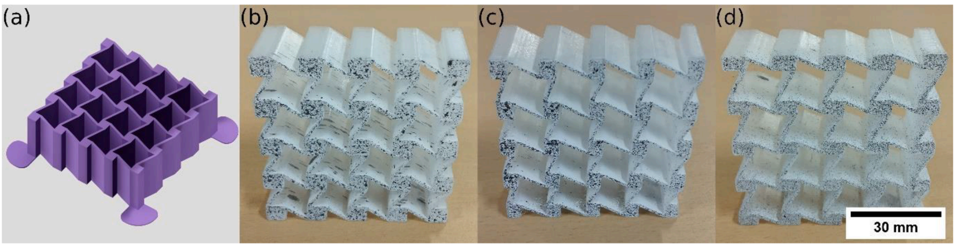

Fig. 4. (a) CAD model of a sample structure (structure A) with bottom discs added to increase the surface area during the additive manufacturing process, (b) sample structure B-1, (c) sample structure D-1 and (d) sample structure E-1 (the sample structures are shown with the applied spray pattern needed for the optically aided compression measurements).

Table 3
Printing parameters of the additively manufactured specimens and sample structures.

Parameter	Value
Temperature nozzle / bed [°C]	240 / 80
Layer thickness [mm]	0.28
Line width / nozzle diameter [mm]	0.4 / 0.4
Printing speed [mm/s]	25
Infill [%]	100
Infill orientation [°]	45/135
Wall line count	2
Cooling [%]	20, starting at third layer

removed afterwards.

2.4. Experimental testing and evaluation

2.4.1. Properties of the parent material

The properties of the parent material were obtained by means of three-point bending tests. For this, 10 specimens were additively manufactured as described in section 2.3. The size was chosen according to ISO 178 (80 × 10 × 4 mm^3) [40]. Two exemplary specimens with the corresponding dimensions are depicted in Fig. 5 (a). The tests were carried out using a “Zwick/Roell Z010” (Zwick GmbH & Co. KG., Ulm, Germany) universal testing machine equipped with a Zwick Makro extensometer for the precise measurement of the bending deflection (see Fig. 5 (b)). A constant testing speed of 2 mm/min and a preload of 0.1 MPa were used throughout the measurements. All specimens were

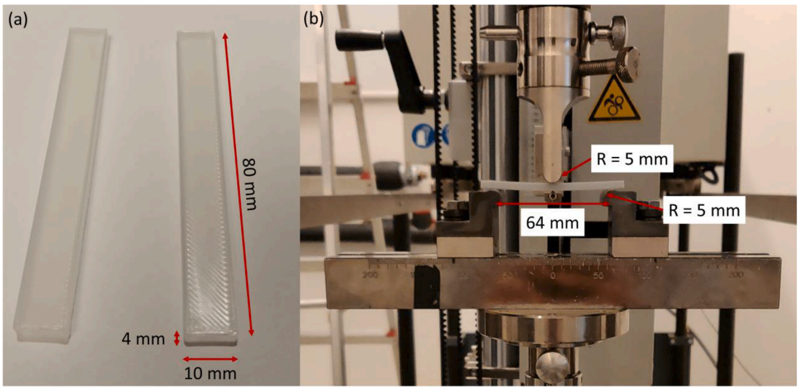

Fig. 5. Three-point bending test specimens and setup. (a) Additively manufactured test specimens with indicated dimensions and (b) test setup with indicated parameters.

tested up to a strain of 15 %. No fracture of the specimens occurred within this range. The tests were conducted at room temperature. The mechanical parameters were calculated from the machine data according to ISO 178 [40]. Three-point bending tests were chosen because the main deformation of the structure under compression (and tension) is based on the local bending deformation of the struts.

2.4.2. *Quasi-static compression tests of the sample structures*

The mechanical behavior of the sample structures was investigated by means of compression tests. The tests were carried out using an “Instron 5500” (Instron GmbH, Darmstadt, Germany) universal testing machine and at room temperature. To match the three-point bending tests and to avoid excessive strain-rate influence, a constant deformation rate of 2 mm/min was used. The preload was reduced to 0.015 MPa, since the compliant structures have smaller load bearing capabilities than the dense parent material. To reduce friction, the contact surfaces between the specimens and the compression plates were lubricated with a PTFE spray (“CRC Dry Lube-F 32602-AA”, CRC Industries, Inc., Horsham Township, USA). The global displacement in the sample structures was measured using the digital image correlation system “ARAMIS 4M” (GOM GmbH, Braunschweig, Germany). The sample structures were prepared for the optical measurements by applying a spray pattern. The further analysis of the digital image correlation data was conducted with the software tool “GOM Correlate” (GOM GmbH, Braunschweig, Germany). For the determination of the global displacement, the digital image correlation system was used as a video extensometer. For each sample, five virtual extensometers were placed both, in the longitudinal and transversal direction (see Fig. 6 (a)). To reduce the influence of local deformations, the samples longitudinal and transversal strain values, ε_l and ε_t, respectively, were the average of these five virtual extensometers. They were calculated as.

$$\begin{cases} \varepsilon_l = \dfrac{1}{5l_0}\sum_{i=1}^{5}\Delta l_{l,i} \\ \varepsilon_t = \dfrac{1}{5l_0}\sum_{i=1}^{5}\Delta l_{t,i} \end{cases} \tag{7}$$

where $l_0 = 60$ mm is the initial length of the virtual extensometer and $\Delta l_{l,i}$ and $\Delta l_{t,i}$ are the changes in longitudinal and transversal lengths, respectively. To characterize the normal-strain shear coupling effect, the shear angle of the structure was examined as well. For this, two angles, defined by three points each, were used as depicted in Fig. 6 (b). The

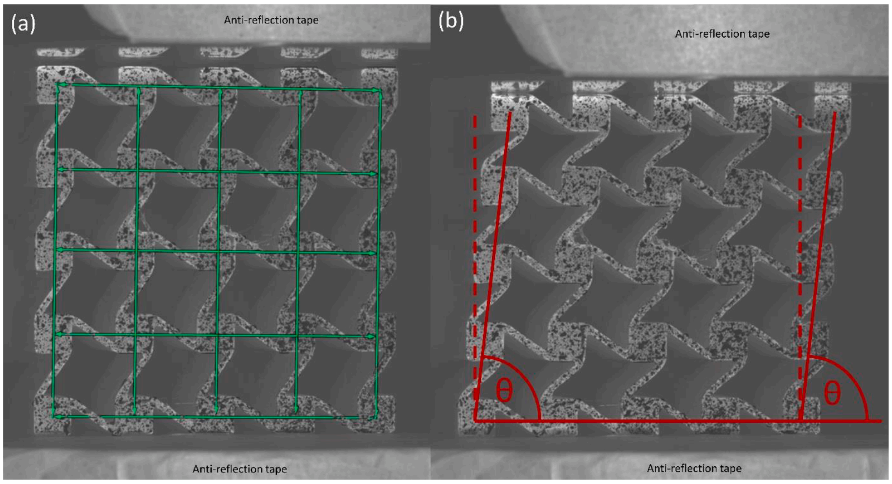

Fig. 6. Evaluation procedure for the compression tests (exemplarily shown for sample B-1). (a) Virtual extensometer analysis paths to obtain the displacement in longitudinal and transversal direction (undeformed structure) and (b) angle measurement to quantify the shear deformation of the structure (deformed structure). The diffuse surfaces on the top and bottom compression plates were anti-reflection tapes added to improve the image quality.

sample's shear angle denotes the average of those two angle measurements. With the angles defined as in Fig. 6 (b), an angle of 90° denotes no shearing and angles smaller than 90° indicate shearing of the top surface to the right. The same evaluation methods to obtain the strains and shear angles were used for the simulations based on the full-size structures, which are described later in section 3.1. For each type of sample structure examined (A – G according to Table 2), three structures were manufactured and tested. The reported values are the average of these three structures.

3. Finite element analysis

Two simulation approaches were pursued to study the influence of different geometric parameters on the overall mechanical properties of the structure as well as on the normal-strain shear coupling effect. Finite element simulations of the fully modeled structures were used to predict the mechanical properties and the detailed deformation behavior for larger applied global strains. To obtain the global linear elastic material behavior of the structure for a large variety of geometric values, a numerical unit cell-based homogenization approach was used. Both simulation models were validated with experimental compression test results. An illustration of the full-scale 2D model and the extruded unit cell (UC) model for homogenization is shown in Fig. 7.

3.1. Full-size structures

Prediction of the nonlinear deformation behavior and the normal-strain shear coupling effect was done with FE models of the full compression test specimens in the finite element software ABAQUS (Abaqus 2019/Dassault Systemes, Vélizy-Villacoublay Cedex, France). The size and geometry of the models was based on the compression test samples described in Table 2. Due to the extruded nature of the geometries, 2D plane strain models were derived from the 3D geometries to improve the computational efficiency. Reduced quadratic quadrilateral plain strain elements with a side length of 0.3 mm were used to mesh the models. The boundary conditions were chosen to represent the conditions during the compression test. Therefore, two additional rigid beam parts were added to act as compression plates and the contact to the sample was modeled using the general contact algorithm. During the simulation the bottom plate was fixed in all dimensions and the top plate was moved in negative Y direction to compress the model. To capture the nonlinear behavior, the top plate was lowered until a global compression strain of 20% was reached. The simulations were solved using the Abaqus standard solver with an elastic–plastic material model to describe the material behavior during compression. A reverse engineering approach was applied to calibrate the elastic plastic model from the bending test results shown in Section 4.1. In this approach, the bending test set up was modeled in ABAQUS and the simulated force displacement results were compared to the actual test results as further described in [11,16]. Using the LSOPT optimization software (LS-OPT 6.0.0/Livermore Software Technology Corporation, Livermore, CA, USA), the material parameters of the elastic plastic model were then optimized to create the best fit between simulation and experiment. A similar strategy was used to estimate the friction coefficient for the contact interaction between sample and compression plate. For this, the stress–strain curves of a simulation and the corresponding experiment were compared. In an iterative process, the friction coefficient, which led to the best representation of the actual test conditions, was then determined. This was done for one arbitrarily selected sample. Since the testing conditions were kept constant, the friction coefficient was assumed to be roughly the same for all experiments. Therefore, the friction coefficient $\mu = 0.04$, determined on one model, was used in all subsequent simulations.

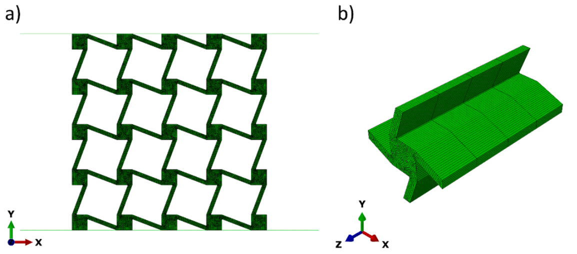

Fig. 7. Simulation models for the numerical analysis. (a) Full-scale 2D simulation model and (b) extruded unit cell model for the homogenization approach.

3.2. Homogenization

Homogenization methods enable the calculation of macro scale properties in a multi scale problem [41] and therefore allow an efficient way to determine the elastic material properties of metamaterials based on their UC design [13,16]. For this study, a numerical homogenization method was used to assess the influence of the geometric parameters in the UC onto the properties with focus on the normal-strain shear coupling effect. The homogenization approach is based on the simulations of six separate uniform load cases with periodic boundary conditions on the bounding box surfaces of the UC [42]. These boundary conditions can be described with Eq. (8),which defines the relative displacement of the opposing boundary surfaces.

$$u_i(x_2) = u_i(x_1) + \left(\frac{\partial u_i}{\partial x}\right)(x_2 - x_1) \tag{8}$$

Here, $u_i(x_1)$ and $u_i(x_2)$ describe the displacement in direction i of two points on the opposite sides of the UC and $(\partial u_i/\partial x)$ being the gradient of the displacement u_i inside the UC between the two points. The applied global strain $\overline{\varepsilon} = (\varepsilon_{11}, \varepsilon_{22}, \varepsilon_{33}, \gamma_{12}, \gamma_{13}, \gamma_{23})^T$ for each load case is given in Table 4. The volume-averaged global stress of the UC,$\overline{\sigma} = (\sigma_{11}, \sigma_{22}, \sigma_{33}, \tau_{12}, \tau_{13}, \tau_{23})^T$, was calculated based on Eq. (9) [43] for each load case.

$$\overline{\sigma} = \frac{1}{V_{UC}} \int_{V_{UC}} \sigma(x) dV \tag{9}$$

Here, V_{UC} is the volume of the UC and $\sigma(x)$ is the local stress distribution. With linear elastic assumptions, the global stiffness tensor $\overline{C}$ is related to the global stress $\overline{\sigma}$ and global strain $\overline{\varepsilon}$ by Eq. (10).

$$\overline{\sigma} = \overline{C} : \in \tag{10}$$

For the setup of the homogenization calculations, the Abaqus micromechanics plugin [44] in combination with an in-house developed script was employed. The linear part of the material model created from the bending test data presented in Section 4.1 was used as material model for the UC simulations. Reduced quadratic hexahedral continuum elements, with a side length of 0.3 mm in the x-y-plane and four elements with a side length of 6 mm along the z-direction ($L_z = 24$ mm), were applied to mesh the different UCs. The increased side length in z-direction was chosen to minimize the computational cost and due to the

Table 4
Global strain tensors of the six load cases used for the homogenization simulations.

Load Case (LC)	Applied Global Strain Tensor $\overline{\varepsilon}$
LC1	$\overline{\varepsilon} = (1,0,0,0,0,0)^T$
LC2	$\overline{\varepsilon} = (0,1,0,0,0,0)^T$
LC3	$\overline{\varepsilon} = (0,0,1,0,0,0)^T$
LC4	$\overline{\varepsilon} = (0,0,0,1,0,0)^T$
LC5	$\overline{\varepsilon} = (0,0,0,0,1,0)^T$
LC6	$\overline{\varepsilon} = (0,0,0,0,0,1)^T$

fact that the stiffness in the extruded direction had no significant influence on the analyzed behavior in the x-y-plane. The models were solved using the Abaqus Standard solver. The full global stiffness tensor $\overline{C}$ was obtained from the homogenization method.

3.3. *Property evaluation*

Based on the stiffness tensor, $\overline{C}$, obtained from the homogenization simulations, the compliance matrix, $\overline{S} = \overline{C}^{-1}$, can be calculated such that.

$$\overline{\varepsilon} = \overline{S} : \overline{\sigma} \tag{11}$$

The mechanical properties can be obtained from the entries of the compliance matrix, given in matrix form as.

$$\begin{pmatrix} \varepsilon_{11} \\ \varepsilon_{22} \\ \varepsilon_{33} \\ \gamma_{12} \\ \gamma_{13} \\ \gamma_{23} \end{pmatrix} = \begin{pmatrix} 1/E_1 & -\nu_{21}/E_2 & -\nu_{31}/E_3 & 0 & 0 & 0 \\ -\nu_{12}/E_1 & 1/E_2 & -\nu_{32}/E_3 & 0 & 0 & 0 \\ -\nu_{13}/E_1 & -\nu_{23}/E_2 & 1/E_3 & 0 & 0 & 0 \\ 0 & 0 & 0 & 1/G_{12} & 0 & 0 \\ 0 & 0 & 0 & 0 & 1/G_{13} & 0 \\ 0 & 0 & 0 & 0 & 0 & 1/G_{23} \end{pmatrix} \begin{pmatrix} \sigma_{11} \\ \sigma_{22} \\ \sigma_{33} \\ \sigma_{12} \\ \sigma_{13} \\ \sigma_{23} \end{pmatrix} \tag{12}$$

For example, the Young's modulus in the compression direction (y) can then be calculated as.

$$E_2 = \frac{1}{\overline{S}_{2,2}}$$

where $\overline{S}_{2,2}$ is the second column and second row entry of the compliance matrix. With the stress state $\overline{\sigma} = (0, \sigma_{22}, 0, 0, 0, 0)^T$ representing a stress in the y-direction, as present in the compression tests, the resulting shear strain in the x- and y-direction, γ_{12}, can be obtained as.

$$\gamma_{12} = \overline{S}_{2,4}\sigma_{22} \tag{13}$$

where $\overline{S}_{2,4}$ is the second column and fourth row entry of the compliance matrix. Analogous to the definition of the shear modulus, the shear angle, θ, can then be calculated as.

$$\theta = \frac{\pi}{2} - tan^{-1}\left(\overline{S}_{2,4}\sigma_{22}\right) \tag{14}$$

The factor $\pi/2$ is needed to match the definition of the shear angle as introduced in Section 2.4.2 (see Fig. 6 (b)). It has to be noted that Eq. (14) is only valid for small strain (and stress) values. In the full-scale 2D models, the compression modulus and the shear angle were analyzed using the same methodology as described in Section 2.4.2 and calculated as presented in Section 4.2.

4. Results and discussion

4.1. *Properties of the parent material*

Fig. 8 shows the stress strain curves of the three-point bending tests. The average mechanical values and their respective standard deviation obtained from these measurements are listed in Table 5. Since the specimens did not break before the measurements were stopped, the reported values for the strain at break and modulus of toughness are only a lower bound and the real values are higher. For the finite element analysis, the data was restricted to a maximum strain of 5 %, as recommended in ISO 178 [40].

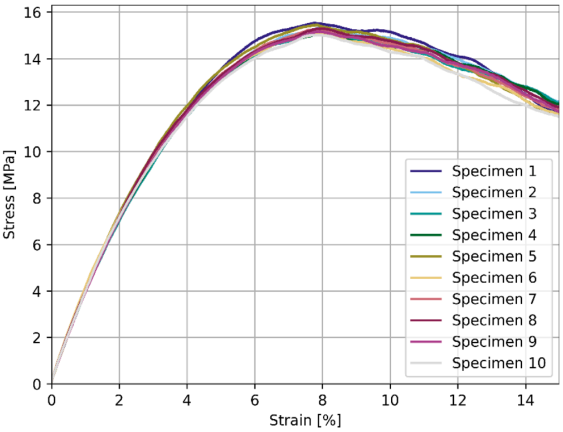

Fig. 8. Quasi-static stress strain curves of the parent material obtained from three-point-bending tests.

Table 5
Mechanical parameters of the parent material obtained from three-point bending tests (* no fracture within 15 % strain, the lowest observed value is reported).

Parameter	Value
Flexural Modulus [MPa]	427 ± 12
Max. Stress [MPa]	15.29 ± 0.26
Strain at Break [%]	>15*
Modulus of Toughness [MPa]	>1.9*

4.2. *Compression test results of the sample structures*

In the following discussion, the results of the quasi-static compression tests are labeled "nominal" because the stress and strain values were calculated with the nominal dimensions of the sample structures. These values do not represent "real" or local stresses and strains within the structure. The nominal stress, σ, was calculated as.

$$\sigma = \frac{F}{A_{total}} \tag{15}$$

where F is the compression force obtained from the testing machine and A_{total} is the measured area of the compression surface according to Table 2. The nominal strain was calculated as described in section 2.4.2. Under compression, two different regimes can be distinguished (see Fig. 9). First, an elastic regime is observed. In this regime, the compression modulus of each sample structure was obtained from a linear fit in the range of 0.05 % to 0.25 % nominal (longitudinal) strain, following ISO 604 [45]. The same method was applied to obtain the compression modulus of the full-scale simulations. The elastic regime is followed by a plateau regime, where the compression force needed to deform the structure does not change significantly. Usually, the plateau regime is followed by a densification regime [13,16]. The densification regime is observed when the nodes start to touch each other, resulting in an increasing compression force and stress. Depending on the size of the nodes, this occurs at different levels of applied strain. However, the compression experiments were stopped before this regime was reached to prevent the structures from slipping off the compression plates. Therefore, the maximum strain differs between the observed structures. Moreover, each individual compression test was stopped manually before the densification regime was reached, resulting in small deviations in the maximum applied strain between individual samples of one type. The detailed stress–strain curves of the tested structures are shown in Fig. 9 (a)–(g). During the compression test of the sample structure G-3 an inhomogeneous deformation behavior was observed and the measurement was stopped prematurely. A comparison of the stress–strain curves of the seven tested sample structures is depicted in Fig. 9 (h). The obtained values for the compression moduli range from

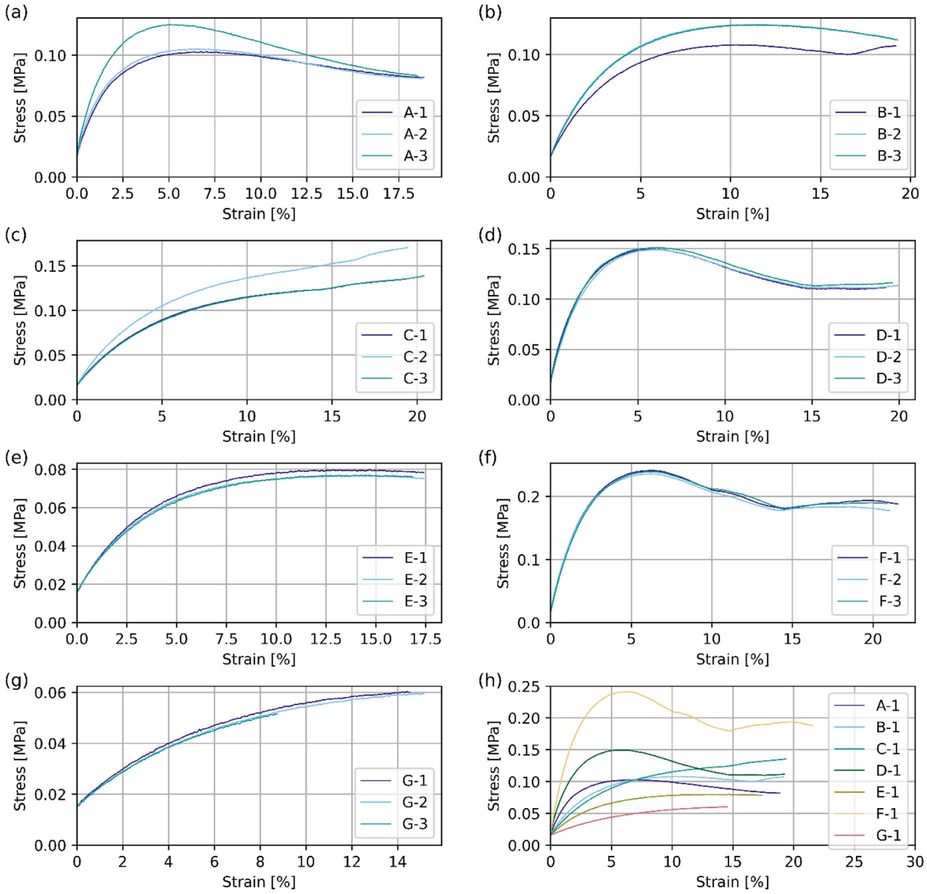

Fig. 9. Quasi-static stress–strain curves from the compression tests of the different additively manufactured sample structures. (a) Samples A, (b) Samples B, (c) Samples C, (d) Samples D, (e) Samples E, (f) Samples F, (g) Samples G and (h) Comparison of Samples A – G.

(0.89 ± 0.13) MPa to (11.25 ± 0.16) MPa. Fig. 10 (a) shows a comparison of the compression moduli, obtained from the experimental and both numerical methods. Both simulation techniques are in good agreement with the experimental results. The shear angles at a longitudinal strain of $\varepsilon_l = 2$ % are depicted in Fig. 10 (b). The results of the full-scale simulation were directly obtained at the corresponding displacement of the top surface. To obtain the shear angle from the homogenization results, the corresponding stress value at $\varepsilon_l = 2$ % from

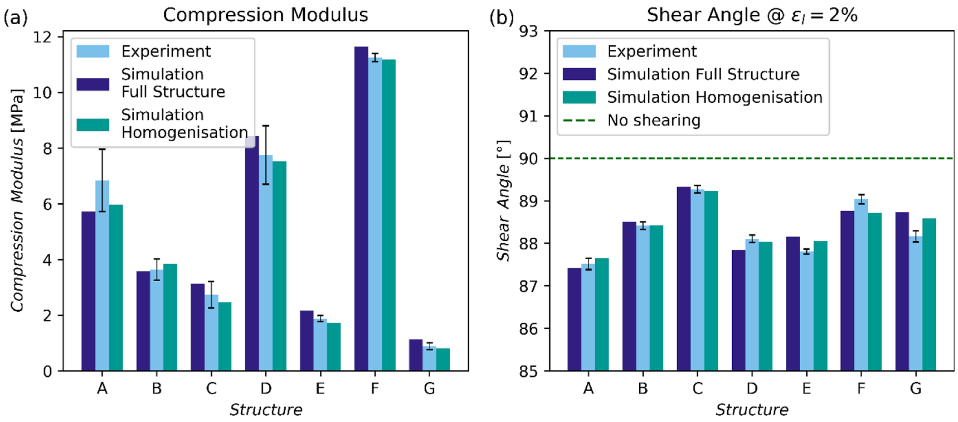

Fig. 10. Comparison of experimental results (average of three measurements, error bars represent standard deviation) and two numerical models (full-scale simulations and homogenization). (a) Compression modulus and (b) shear angle at a longitudinal strain ε_l of 2 %.

the full-scale simulations was used as the input for Equation (14). The deviation in stiffness across the individual sample structures of one geometry is quite noticeable. The main reason for the observed deviation in stiffness is attributed to the challenges in printing polypropylene (PP) by Fused Filament Fabrication. PP has a high tendency to shrink and warp during the additive manufacturing process [46], which can negatively affect part quality and mechanical properties [47]. However, the deviation in the shear angle is much less pronounced. This indicates that the shear deformation is a relatively stable parameter and not strongly dependent on the manufacturing conditions. This makes it suitable for applications where a prescribed shear deformation is of importance, e.g. for shape morphing applications. It can also be observed that structures with distinctive stiffness differences can lead to similar shear angles (for example structures F and G). Thus, both, the stiffness and shear deformation, can be tailored to the application of interest simultaneously. The results of the experimental and numerical analysis are summarized in Table 6. An optical impression of the deformation behavior during the compression tests of two different sample structures, E-1 and C-3, is given in Fig. 11 (a) and (b), respectively. A video of the compression tests is available online as a multimedia file.

Fig. 12 shows the geometry dependence of different mechanical properties obtained from the homogenization simulations. Constant values of $L_x = L_y = 15$ mm, $T = 1.2$ mm and $R = 0.2$ mm were used (similar to the experimental sample structures). The node dimensions, A_x and A_y, were varied in the range of 3–10 mm in steps of 0.2 mm. In total, 1296 unique geometries were simulated and evaluated. The range of the mechanical parameters obtained is summarized in Table 7. It can be observed that for the geometric parameters examined, the stiffness in a given direction is mainly influenced by the node dimension in the perpendicular direction (see Fig. 12 (a) and (b)). By increasing the node dimension in one direction, the strut angle in the perpendicular direction decreases, leading to an increased bending load of this perpendicular strut and a reduced stiffness in this perpendicular direction. Although also the strut angle along the extended node dimension decreases, the stiffness in this direction increases. This can be explained by an increased axial loading (reduced bending) of the strut. Since the structures possess a 90° rotational similarity, this is present in both directions. For the analyzed set of geometric parameters, the values for E_1 and E_2 range from 0.80 to 25.92 MPa. The values for E_3 can directly be obtained from the relative density, that is $E_3 = E\rho_r$, where E is the Young's Modulus of the parent material. Here it ranges from 73.0 to 234.2 MPa. The same values were obtained from the homogenization simulations. Due to the 90° rotational symmetry of the unit cell, the shear modulus G_{12} (Fig. 12 (c)) is identically influenced by the node dimension in both directions. Hence, a radial pattern is observed. With increasing node dimension, the shear modulus increases as well with values ranging from 0.20 to 2.37 MPa. The Poisson's Ratio υ_{12} is shown in Fig. 12 (d) with values ranging from −0.00025 to 0.04719. Values of zero, or close to zero, are common for chiral based structures [16,25]. When compressed in the x- or y-direction, the main deformation is shearing and almost no lateral contraction or expansion is present. However, out-off-plane compression (or tension) is not affected by the structure in the x-y-plane, resulting in constant values for the Poisson's Ratios $\upsilon_{31} = \upsilon_{32} = 0.43$ (almost incompressible), independent of the geometric parameters. The results of the homogenization simulations are summarized in Table 7.

Fig. 13 shows the shear angle for the same set of geometric parameters and for a constant stress of $\sigma_{22} = 0.05$ MPa. The shear angle was obtained from the compliance matrices of the homogenization simulations and calculated with Equation (14). It can be observed that for a constant bounding box size of $L_xL_y = 15 \times 15$ mm^2 and only changing the node dimensions, shear angles in the range of 85.0° to 89.8° can be obtained. This highlights the wide range of achievable shear deformations with the proposed design by only using two of the seven geometric parameters of the unit cell. Similar to the shear modulus, a radial pattern is observed. With increasing strut length in the y-direction (l_y), the shear angle decreases. This permits to simultaneously adapt the shear angle, stiffness and porosity of the structure for a given application.

Table 6
Mechanical properties obtained from compression tests (average ± standard deviation of three measurements) and two numerical models (full-scale simulations and homogenization).

Sample Structure	Parameter		
	Relative Density	Compression Modulus [MPa] Experiment Full-Scale Simulation Homogenization	Shear Angle @ $\varepsilon_l = 2$ % [°] Experiment Full-Scale Simulation Homogenization
A	0.23	6.8 ± 1.2	87.52 ± 0.14
		5.7	87.42
		6.0	87.65
B	0.33	3.63 ± 0.38	88.417 ± 0.087
		3.58	88.508
		3.84	88.418
C	0.56	2.73 ± 0.48	89.272 ± 0.086
		3.13	89.327
		2.46	89.233
D	0.27	7.7 ± 1.1	88.104 ± 0.089
		8.4	87.844
		7.5	88.031
E	0.27	1.88 ± 0.11	87.802 ± 0.062
		2.17	88.157
		1.73	88.052
F	0.33	11.25 ± 0.16	89.03 ± 0.11
		11.64	88.76
		11.19	88.72
G	0.34	0.89 ± 0.13	88.16 ± 0.14
		1.13	88.72
		0.81	88.58

4.3. *Non-linear Normal-Strain shear coupling and friction influence*

For the sample structures, the linear elastic regime only accounts for a small part of the deformation behavior under load (see Fig. 9). Hence, the homogenization method with its linear elastic material law is not able to describe the mechanical response of a structure at high strains. Consequently, only the full-scale simulations are considered for this purpose. Fig. 14 (a) shows the experimental and numerical results for the shear angle as a function of the applied (compressive) strain for three different sample structures (A, B and C). The numerical results are in good agreement with the experimental data. The maximum deviation is less than 1° and the main deviation arises from local deformations at higher strains.

To assess the influence of friction onto the shear deformation of the structures, simulations with varying friction coefficients were performed for one of the sample structures (A). The friction coefficients were varied from 0.012 to 0.1, resulting in shear angle values from 68.5° to 76.6° at a strain of 18 %. The experimental and full-scale simulation values with a friction coefficient of $\mu = 0.04$ are 72.8° and 72.5°, respectively, at this strain level. With increasing friction coefficient, the lateral movement of the top surface is hindered, thus reducing the shear angle. However, for strains below 10 % only a small influence is observed. This again indicates that the shear angle is a relatively robust parameter and not strongly dependent on the manufacturing deviations or testing conditions. It has to be noted that the investigated set of friction coefficients assumed that the surface in contact with the compression plate was lubricated. Without lubrication, that is μ 0.3, the top surface is blocked and no shear deformation occurs. However, the lubrication can also be replaced by friction reducing coating.

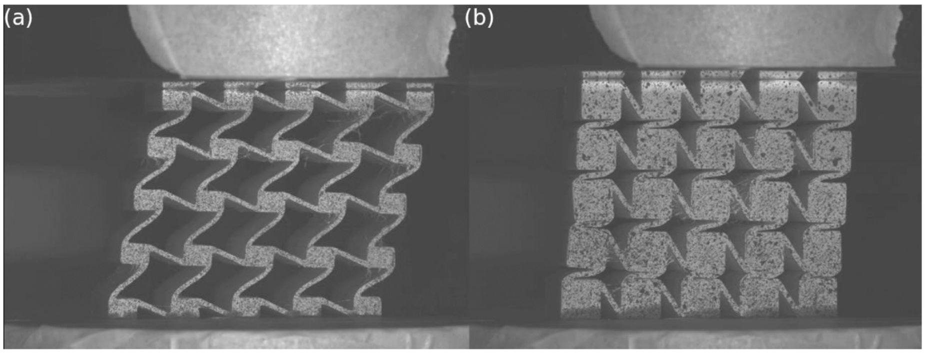

Fig. 11. Comparison of the deformation behavior during the compression test of two different sample structures. (a) Sample E-1 and (b) sample C-3.

Table 7
Range of mechanical properties of the normal-strain shear coupling structure obtained from the homogenization simulations for $L_x = L_y = 15$ mm, $T = 1.2$ mm, $R = 0.2$ mm, $A_x = 3$–10 mm and $A_y = 3$–10 mm and corresponding relative density.

Parameter	Value Range	Relevant Figure
Relative Density [–]	0.15–0.54	Fig. 2
E_1, E_2 [MPa]	0.80–25.92	Fig. 11 (a) and (b)
E_3 [MPa]	73.0–234.2	
G_{12} [MPa]	0.20–2.37	Fig. 11 (c)
G_{13}, G_{23} [MPa]	9.9–19.7	
$\upsilon_{12}, \upsilon_{21}$ [–]	−0.00025–0.04719	Fig. 11 (d)
$\upsilon_{13}, \upsilon_{23}$ [–]	0.003–0.108	
$\upsilon_{31}, \upsilon_{32}$ [–]	0.4297–0.4304	
Shear angle @ $\sigma_{22} = 0.05$ MPa [°]	85.0–89.8	Fig. 12

5. Extension to the third dimension

Based on the proposed design for the 2.5D normal-strain shear coupling structure, a 3D variant is deduced in the following section. The structure was obtained by starting from a solid rectangular prism with volume $L_xL_yL_z$. At each of the three spatial planes (X-Y, X-Z and Y-Z) a 2D sketch similar to Fig. 1 was drawn. By extruding the inverted sketch, thus removing the outside region of these three sketches, the proposed 3D normal-strain shear coupling structure is obtained as depicted in Fig. 15. The bounding box and central node have a volume of $L_xL_yL_z$ and $A_xA_yA_z$, respectively. The thickness of the struts and radius of the fillets are labled T and R, respectively. The geometric parameters of the UC and their respective descriptions are listed in Table 8.

Similar to Equation (14) the shear angles of the three-dimensional structure can be calculated from homogenization simulations. For a compression in the z-direction, that is a stress state $\overline{\sigma} = (0, 0, \sigma_{33}, 0, 0, 0)^T$, the resulting shear angles can be calculated as

$$\begin{cases} \theta_{13} = \dfrac{\pi}{2} - \tan^{-1}\left(\overline{S}_{3,5}\sigma_{33}\right) \\ \theta_{23} = \dfrac{\pi}{2} - \tan^{-1}\left(\overline{S}_{3,6}\sigma_{33}\right) \end{cases} \tag{16}$$

where θ_{13} and θ_{23} are the angles in x- and y-direction, respectively. Here two angles are needed since the structure exhibits simultaneous shearing in two directions. Again, the term $\pi/2$ was introduced to match the definition as described in Section 2.4.2. Fig. 16 (a) and (b) show the mechanical properties of the proposed 3D structure obtained from homogenization simulations. For these simulations, the unit cell model from Fig. 7 (b) was adapted to the three-dimensional situation and constant values of $L_x = L_y = L_z = 15$ mm, $T = 1.2$ mm and $R = 0.2$ mm were used. The node dimensions, A_x and A_y, were varied in the range of 3–10 mm in steps of 0.5 mm. In total, 3375 different geometries were simulated and evaluated. For better clarity, only the slices where $A_z = 3$ mm, $A_z = 6.5$ mm and $A_z = 10$ mm are shown in Fig. 16. For the investigated set of parameters, the compression moduli E_1, E_2 and E_3 varied from 0.02 MPa to 1.07 MPa. Due to the similarity of the three-dimensional structure to the 2.5D structure, the same influence of the geometric parameters onto the mechanical properties is observed. This means that the compression moduli (E_1 and E_2 in Fig. 16 (a) and (b), respectively) are mainly influenced by the two node dimensions perpendicular to the load direction: the longer they are the softer the behavior. Contrary, the longer the parallel node dimension the stiffer (but to a much smaller extent) the structure becomes. Both tendencies are related to a change in the strut angles and the resulting change in the (local) bending fraction of the load. In all three cases, the strut angles decrease with increasing node dimension. For the perpendicular node dimensions, this, as the dominating effect, increases the bending load of the two corresponding in load direction-oriented struts resulting in a softer global response. On the other hand, for the parallel node dimension, the (four) perpendicular struts (with respect to the load direction) become "more parallel" resulting in a reduced bending of them and a stiffer global response. Compared to the 2.5D structure, the three-dimensional variant exhibits a 90° rotational similarity along one additional axis. Thus, a similar spherical, instead of radial, pattern is observed for the shear moduli, G_{12}, G_{13} and G_{23}, with values ranging from 0.009 MPa to 0.097 MPa (Fig. 16 (c)). Owing to the additional structure in the third dimension, instead of a simple extrusion, the Poisson's Ratios are zero, or close to zero, in all six cases. The values range from −0.0007 to 0.0172 (Fig. 16 (d)). The shear angles, θ_{13} and θ_{23}, are depicted in Fig. 16 (e) and (f), respectively. This highlights the normal-strain shear coupling effect in one additional axis, when compared to the 2.5D structure. A compression load in one direction (e.g. along the z-axis) results in a shear deformation along two directions (e.g. in the x-y-plane). Therefore, the presented structure provides a building block in applications where three-dimensional positioning with compliant materials is needed, e.g. in soft robotic or soft actuator applications [48]. The tunable shear-deformation allows to optimize the mechanical (and positional) response under load, making them easier to control than conventional compliant materials. The range of mechanical parameters obtained from the homogenization simulations is summarized in Table 9.

The visualization of mechanical properties with only slices is limited to values along the three spatial axes. A more complete picture can be obtained from a three-dimensional representation of the mechanical properties. For this, the stiffness surface of selected unit cells was obtained with an elastic tensor analysis package, ELATE [49], implemented in Python [50] and visualized with PyVista [51]. The stiffness surface, E_s, was calculated as

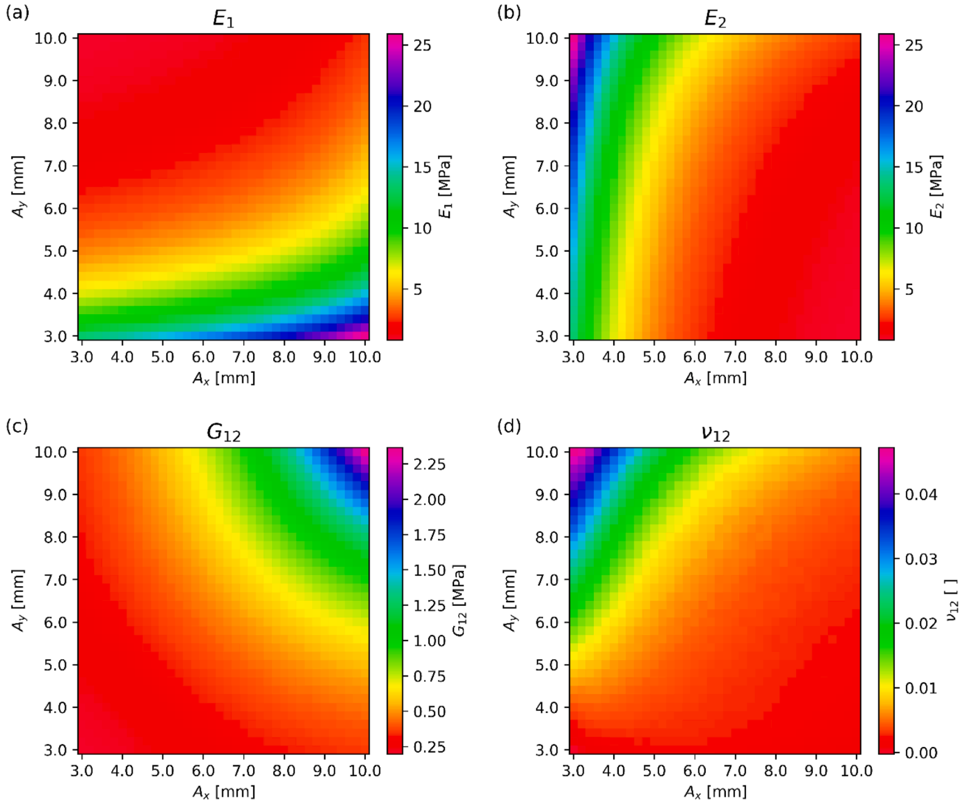

Fig. 12. Mechanical properties of the tunable normal-strain shear coupling structure obtained from homogenization simulations for $L_x = L_y = 15$ mm, $T = 1.2$ mm and $R = 0.2$ mm. (a) E_1, (b) E_2, (c) G_{12} and (d) ν_{12}.

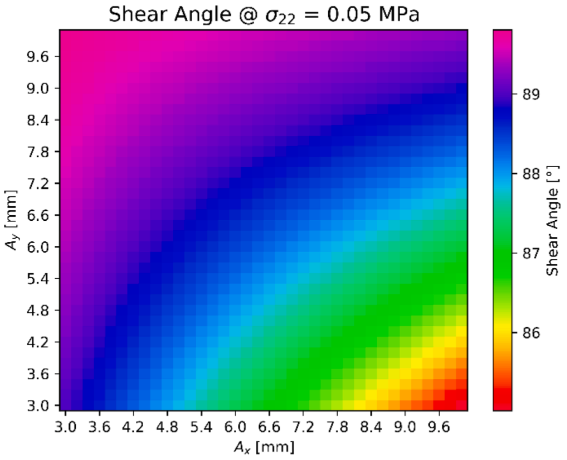

Fig. 13. Shear angle of the tunable normal-strain shear coupling structure obtained from homogenization simulations for $L_x = L_y = 15$ mm, $T = 1.2$ mm and $R = 0.2$ mm at a constant stress of$\sigma_{22} = 0.05$ MPa.

$$E_s = \sqrt{E_1^2 + E_2^2 + E_3^2} \tag{17}$$

Fig. 17 shows four selected unit cells and their respective stiffness surface. An animation of these stiffness surfaces is also available as a multimedia file online. It can be observed that the maximum stiffness occures along the direction of the struts. This is especially noticable for small node dimensions (Fig. 17 (a)). In addition, the 3D plots illustrate the wide variety of achievable stiffness properties in the different directions. In combination with the tunable shear coupling in the three spatial dimensions, this leads to an highly customizable unit cell for the use in spezialized deformable structures.

6. Concluding remarks

In this study, enhanced designs for 2.5D and 3D chiral-based mechanical metamaterials with tunable normal-strain shear deformation, stiffness and porosity were introduced. By expanding the parameter space with additional geometric freedoms, we were able to achieve variations of these properties in a broad range. Instead of circular or point-like nodes and a square bounding box, we generalized the design of chiral structures to a rectangular node and bounding box. The geometric parameters of the bounding box and node can be used to tailor the shear response, whereas the stiffness can be varied with the thickness of the struts. This allows to fine tune the shear deformation and mechanical response of chiral-based metamaterials, thus opening new applications for those structures. For example, the capabilities of twisting metamaterials [30] or similar metamaterials based on anti-chiral [16,36,52] or metachiral [22] structures can be expanded. Additionally, the 2.5D design can also be integrated in already existing three-dimensional chiral-based metamaterials [30,37,53–55]. By introducing more geometric freedom into the chiral-based unit cell, we were able to create structures with similar shear-responses, but different stiffnesses. For the analysis of the structural designs, experimental and numerical techniques were used in this study. The numerical

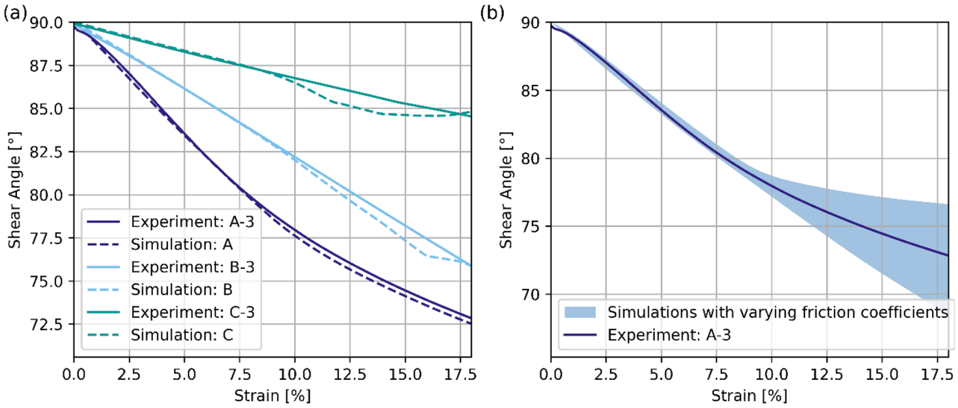

Fig. 14. Shear angle as a function of the applied (compressive) strain. (a) Comparison of experimental and numerical full-scale simulation data and (b) comparison of experiment and full-scale simulations with varying friction coefficients (the friction coefficient was varied between 0.012 and 0.1).

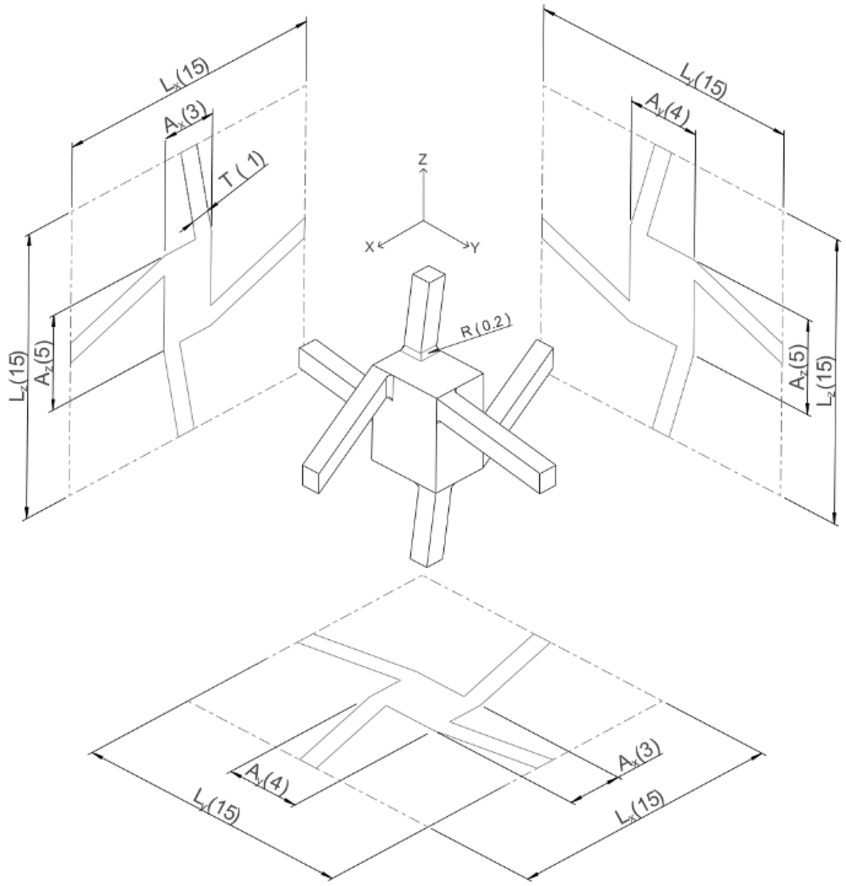

Fig. 15. Three-dimensional variant of the unit cell with tunable normal-strain shear coupling effect with indicated geometrical parameters and example dimensions in brackets (units: mm).

simulations, both on full-size structures and using a homogenization strategy, showed good agreement with the experimental test results. The presented three-dimensional variant introduces a tunable design for a chiral-based metamaterial with tunable normal-strain shear coupling effect in a broad range. The capability of three-dimensional positioning makes them suitable for soft robotic or soft actuator applications as they are easier to control than conventional compliant materials.

Data Availability.

Table 8
Geometric parameters of the proposed three-dimensional unit cell as depicted in Fig. 15.

Parameter	Description
L_x, L_y, L_z	Length of the bounding box in X, Y and Z direction
A_x, A_y, A_z	Length of the rectangular node in X, Y and Z direction
T	Thickness of the struts
R	Radius of the fillet

The raw data required to reproduce these findings cannot be shared at this time due to technical limitations. The processed data required to reproduce these findings cannot be shared at this time due to technical limitations, but can be provided upon request.

CRediT authorship contribution statement

Mathias Fleisch: Conceptualization, Methodology, Software, Validation, Formal analysis, Investigation, Data curation, Writing – original draft, Writing – review & editing, Visualization. **Andreas Thalhamer:** Methodology, Software, Validation, Formal analysis, Investigation, Data curation, Writing – original draft, Writing – review & editing, Visualization. **Gerald Meier:** Investigation. **Philipp Arno Franz Huber:** Investigation. **Peter Filipp Fuchs:** Resources, Supervision, Writing – review & editing. **Gerald Pinter:** Resources, Supervision, Writing – review & editing. **Sandra Schlögl:** Supervision, Writing – review & editing, Project administration, Funding acquisition. **Michael Berer:** Conceptualization, Software, Validation, Data curation, Resources, Supervision, Writing – review & editing, Project administration, Funding acquisition.

Declaration of Competing Interest

The authors declare that they have no known competing financial interests or personal relationships that could have appeared to influence the work reported in this paper.

Data availability

Data will be made available on request.

Table 9
Mechanical properties obtained from the homogenization simulations for $L_x = L_y = L_z$ 15 mm, $T = 1.2$ mm, $R = 0.2$ mm, $A_x = 3$–10 mm, $A_y = 3$–10 mm and $A_z = 3$–10 mm.

Parameter	Values (Range)
E_1, E_2, E_3 [MPa]	0.02 – 1.07
G_{12}, G_{13}, G_{23} [MPa]	0.009 – 0.097
$\nu_{12}, \nu_{21}, \nu_{13}, \nu_{31}, \nu_{23}, \nu_{32}$ [-]	−0.0007 – 0.0172
θ_{13}, θ_{23} [°]	35.9 – 87.3

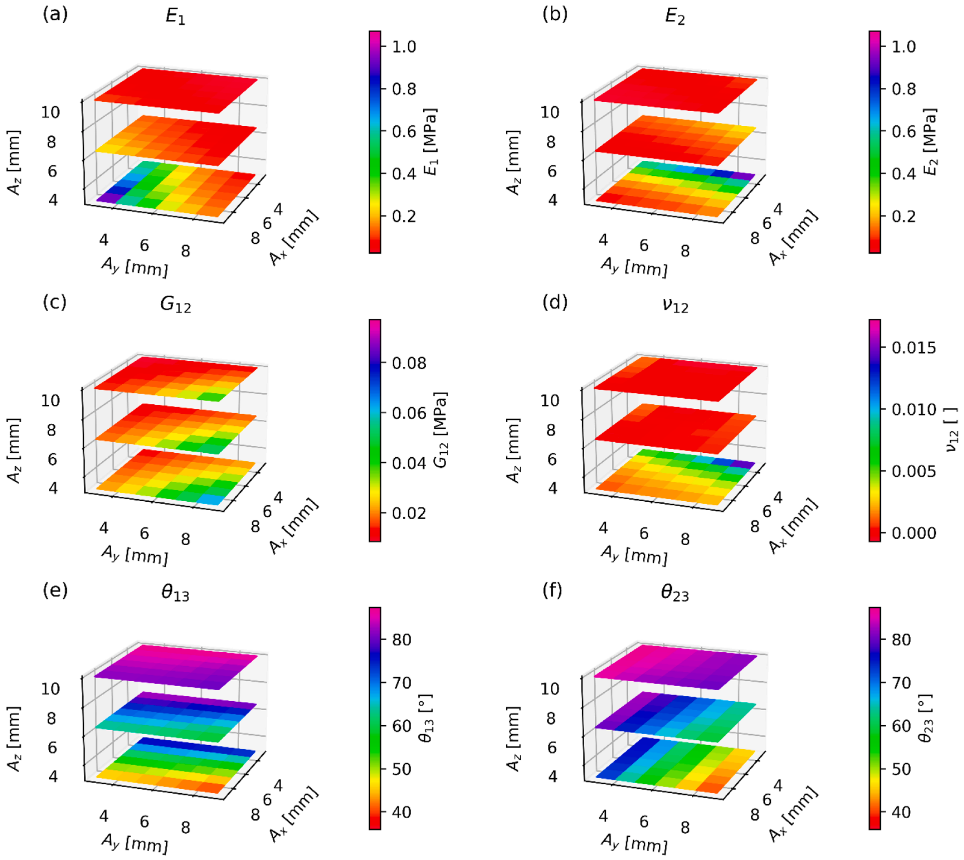

Fig. 16. Mechanical parameters of the three-dimensional tunable normal-strain shear coupling structure obtained from homogenization simulations for constant values of $L_x = L_y = L_z = 15$ mm, $T = 1.2$ mm and $R = 0.2$ mm. (a) E_1, , (b) E_2, (c) G_{12}, (d) ν_{12}, (e) θ_{13} and (f) θ_{23}.

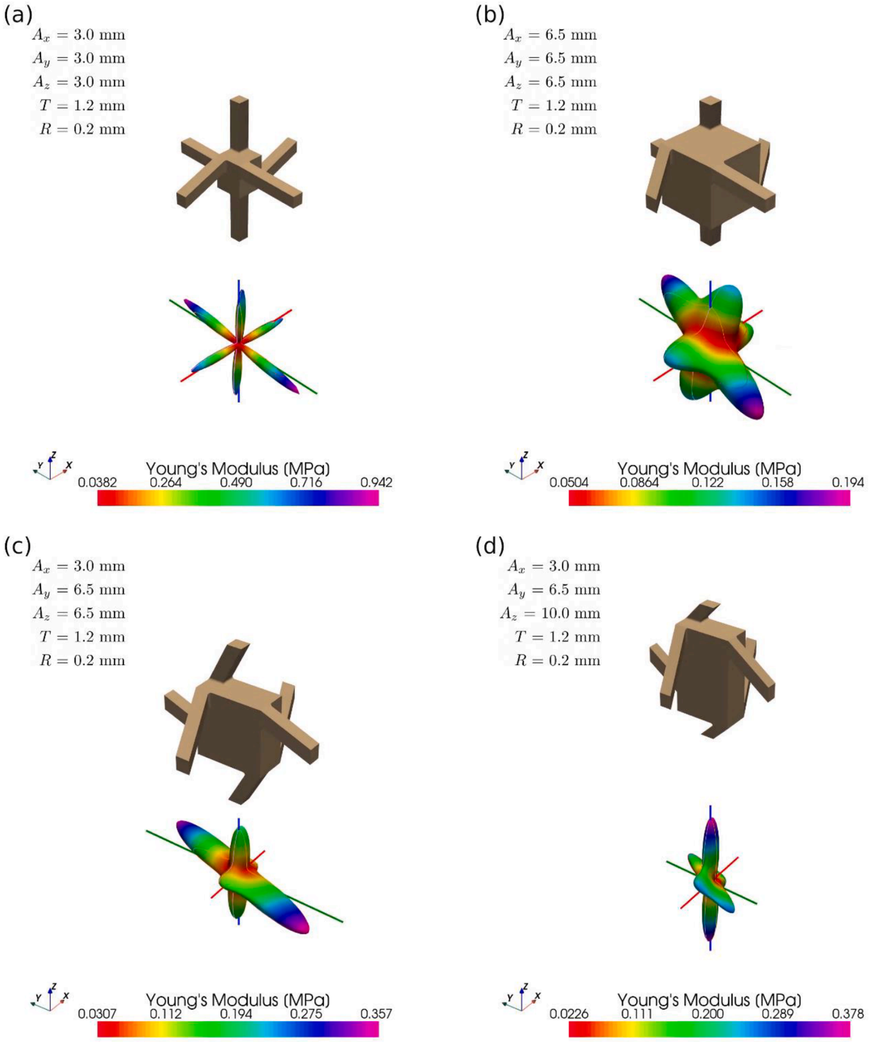

Fig. 17. Unit cells and their corresponding stiffness surface of selected geometries for constant values of $L_x = L_y = L_z = 15$ mm, $T = 1.2$ mm and $R = 0.2$ mm. (a) $A_x = A_y = A_z = 3.0$ mm, (b) $A_x = A_y = A_z = 6.5$ mm, (c) $A_x = 3.0$ mm, $A_y = A_z = 6.5$ mm and (d) $A_x = 3.0$ mm, $A_y = 6.5$ mm and $A_z = 10.0$ mm.

Acknowledgments

The research work of this study was performed in the COMET-Module project “CHEMITECTURE“ (project-no.: 21647048) at the Polymer Competence Center Leoben GmbH (PCCL, Austria) within the framework of the COMET-program of the Federal Ministry for Climate Action, Environment, Energy, Mobility, Innovation and Technology and the Federal Ministry for Digital and Economic Affairs with contributions by Materials Science and Testing of Polymers / Montanuniversitaet Leoben. The PCCL is funded by the Austrian Government and the State Governments of Styria, Lower Austria and Upper Austria.

References

[1] Kadic M, Milton GW, van Hecke M, Wegener M. 3D metamaterials. Nat Rev Phys 2019;1:198–210. https://doi.org/10.1038/s42254-018-0018-y.

[2] Soukoulis CM, Wegener M. Past achievements and future challenges in the development of three-dimensional photonic metamaterials. Nat Photon 2011;5:523–30. https://doi.org/10.1038/nphoton.2011.154.

[3] Cummer SA, Christensen J, Alù A. Controlling sound with acoustic metamaterials. Nat Rev Mater 2016;1:2059. https://doi.org/10.1038/natrevmats.2016.1.

[4] Schittny R, Kadic M, Guenneau S, Wegener M. Experiments on transformation thermodynamics: molding the flow of heat. Phys Rev Lett 2013;110:195901. https://doi.org/10.1103/PhysRevLett.110.195901.

[5] Christensen J, Kadic M, Kraft O, Wegener M. Vibrant times for mechanical metamaterials. MRC 2015;5:453–62. https://doi.org/10.1557/mrc.2015.51.

[6] Surjadi JU, Gao L, Du H, Li X, Xiong X, Fang NX, et al. Mechanical metamaterials and their engineering applications. Adv Eng Mater 2019;21:1800864. https://doi.org/10.1002/adem.201800864.

[7] Bertoldi K, Vitelli V, Christensen J, van Hecke M. Flexible mechanical metamaterials. Nat Rev Mater 2017;2:17066. https://doi.org/10.1038/natrevmats.2017.66.

[8] Barchiesi E, Spagnuolo M, Placidi L. Mechanical metamaterials: a state of the art. Math Mech Solids 2019;24:212–34. https://doi.org/10.1177/1081286517735695.

[9] Schaedler TA, Jacobsen AJ, Torrents A, Sorensen AE, Lian J, Greer JR, Valdevit L, Carter WB. Ultralight metallic microlattices. Science (New York, N.Y.) 2011;334:962–5. https://doi.org/10.1126/science.1211649.

[10] Zheng X, Lee H, Weisgraber TH, Shusteff M, DeOtte J, Duoss EB, Kuntz JD, Biener MM, Ge Q, Jackson JA, Kucheyev SO, Fang NX, Spadaccini CM. Ultralight, ultrastiff mechanical metamaterials. Science (New York, N.Y.) 2014;344:1373–7. https://doi.org/10.1126/science.1252291.

[11] Truszkiewicz E, Thalhamer A, Rossegger M, Vetter M, Meier G, Rossegger E, et al. Mechanical behavior of 3D -printed polymeric metamaterials for lightweight

applications. J Appl Polym Sci 2022;139:51618. https://doi.org/10.1002/app.51618.

[12] Lv W, Li D, Dong L. Study on mechanical properties of a hierarchical octet-truss structure. Compos Struct 2020;249:112640. https://doi.org/10.1016/j.compstruct.2020.112640.

[13] Fleisch M, Thalhamer A, Meier G, Raguž I, Fuchs PF, Pinter G, et al. Functional mechanical metamaterial with independently tunable stiffness in the three spatial directions. Mater Today Adv 2021;11:100155. https://doi.org/10.1016/j.mtadv.2021.100155.

[14] Taghavi M, Helps T, Huang B, Rossiter J. 3D-printed ready-to-use variable-stiffness structures. IEEE Robot Autom Lett 2018;3:2402–7. https://doi.org/10.1109/lra.2018.2812917.

[15] Cazin I, Gleirscher MO, Fleisch M, Berer M, Sangermano M, Schlögl S. Spatially controlling the mechanical properties of 3D printed objects by dual-wavelength vat photopolymerization. Addit Manuf 2022:102977. https://doi.org/10.1016/j.addma.2022.102977.

[16] Fleisch M, Thalhamer A, Meier G, Fuchs PF, Pinter G, Schlögl S, et al. Asymmetric chiral and antichiral mechanical metamaterials with tunable Poisson's ratio. APL Mater 2022;10:61105. https://doi.org/10.1063/5.0091756.

[17] Evans KE, Alderson A. Auxetic materials: functional materials and structures from lateral thinking! Adv Mater 2000;12:617–28. https://doi.org/10.1002/(SICI)1521-4095(200005)12:9<617:AID-ADMA617>3.0.CO;2-3.

[18] Ren X, Zhang Y, Han CZ, Han D, Zhang XY, Zhang XG, et al. Mechanical properties of foam-filled auxetic circular tubes: experimental and numerical study. Thin-Wall Struct 2022;170:108584. https://doi.org/10.1016/j.tws.2021.108584.

[19] Luo HC, Ren X, Zhang Y, Zhang XY, Zhang XG, Luo C, et al. Mechanical properties of foam-filled hexagonal and re-entrant honeycombs under uniaxial compression. Compos Struct 2022;280:114922. https://doi.org/10.1016/j.compstruct.2021.114922.

[20] Gao Q, Ding Z, Liao W-H. Effective elastic properties of irregular auxetic structures. Compos Struct 2022;287:115269. https://doi.org/10.1016/j.compstruct.2022.115269.

[21] Han D, Ren X, Luo C, Zhang Y, Zhang XY, Zhang XG, et al. Experimental and computational investigations of novel 3D printed square tubular lattice metamaterials with negative Poisson's ratio. Addit Manuf 2022;55:102789. https://doi.org/10.1016/j.addma.2022.102789.

[22] Wu W, Hu W, Qian G, Liao H, Xu X, Berto F. Mechanical design and multifunctional applications of chiral mechanical metamaterials: a review. Mater Des 2019;180:107950. https://doi.org/10.1016/j.matdes.2019.107950.

[23] Bacigalupo A, Gambarotta L. Homogenization of periodic hexa- and tetrachiral cellular solids. Compos Struct 2014;116:461–76. https://doi.org/10.1016/j.compstruct.2014.05.033.

[24] Auricchio F, Bacigalupo A, Gambarotta L, Lepidi M, Morganti S, Vadalà F. A novel layered topology of auxetic materials based on the tetrachiral honeycomb microstructure. Mater Des 2019;179:107883. https://doi.org/10.1016/j.matdes.2019.107883.

[25] Mousanezhad D, Haghpanah B, Ghosh R, Hamouda AM, Nayeb-Hashemi H, Vaziri A. Elastic properties of chiral, anti-chiral, and hierarchical honeycombs: a simple energy-based approach. Theor Appl Mech Lett 2016;6:81–96. https://doi.org/10.1016/j.taml.2016.02.004.

[26] Fortes MA, Teresa Nogueira M. The poison effect in cork. Mater Sci Eng: A 1989;122:227–32. https://doi.org/10.1016/0921-5093(89)90634-5.

[27] Bai Y, Zhao T, Yuan C, Liu W, Zhang H, Yang L, et al. Mechanical properties of a chiral cellular structure with semicircular beams. Materials (Basel, Switzerland) 2021;14:2887. https://doi.org/10.3390/ma14112887.

[28] Liu W, Li H, Yang Z, Zhang J, Ge X. In-plane elastic properties of a 2D chiral cellular structure with V-shaped wings. Eng Struct 2020;210:110384. https://doi.org/10.1016/j.engstruct.2020.110384.

[29] Liu W, Yang Z, Zhang J. The in-plane tensile and shear properties of novel chiral cellular structures. Mech Adv Mater Struct 2021:1–20. https://doi.org/10.1080/15376494.2021.1969607.

[30] Frenzel T, Kadic M, Wegener M. Three-dimensional mechanical metamaterials with a twist. Science (New York, NY) 2017;358:1072–4. https://doi.org/10.1126/science.aao4640.

[31] Ion A, Frohnhofen J, Wall L, Kovacs R, Alistar M, Lindsay J, Lopes P, Chen H-T, Baudisch P. Metamaterial mechanisms. In: Rekimoto J, Igarashi T, Wobbrock JO, Avrahami D, editors. Proceedings of the 29th Annual Symposium on User Interface Software and Technology - UIST '16. New York, New York, USA: ACM Press; 2016. p. 529–39.

[32] Ion A, Lindlbauer D, Herholz P, Alexa M, Baudisch P. Understanding metamaterial mechanisms. In: Brewster S, Fitzpatrick G, Cox A, Kostakos V, editors. Proceedings of the 2019 CHI conference on human factors in computing systems – CHI '19. New York, New York, USA: ACM Press; 2019. p. 1–14.

[33] Khajehtourian R, Kochmann DM. Soft adaptive mechanical metamaterials. Front Robot AI 2021;8:673478. https://doi.org/10.3389/frobt.2021.673478.

[34] Fu M-H, Zheng B-B, Li W-H. A novel chiral three-dimensional material with negative Poisson's ratio and the equivalent elastic parameters. Compos Struct 2017;176:442–8. https://doi.org/10.1016/j.compstruct.2017.05.027.

[35] Jiao C, Yan G. Design and elastic mechanical response of a novel 3D-printed hexa-chiral helical structure with negative Poisson's ratio. Mater Des 2021;212:110219. https://doi.org/10.1016/j.matdes.2021.110219.

[36] Ebrahimi H, Mousanezhad D, Nayeb-Hashemi H, Norato J, Vaziri A. 3D cellular metamaterials with planar anti-chiral topology. Mater Des 2018;145:226–31. https://doi.org/10.1016/j.matdes.2018.02.052.

[37] Wu W, Qi D, Liao H, Qian G, Geng L, Niu Y, et al. Deformation mechanism of innovative 3D chiral metamaterials. Sci Rep 2018;8:12575. https://doi.org/10.1038/s41598-018-30737-7.

[38] Lakes R. Deformation mechanisms in negative Poisson's ratio materials: structural aspects. J Mater Sci 1991;26:2287–92. https://doi.org/10.1007/BF01130170.

[39] Gibson LJ, Ashby MF. Cellular solids: structure and properties. Cambridge University Press; 1997.

[40] DIN EN ISO, 178-4: Kunststoffe - Bestimmung der Biegeeigenschaften.

[41] Geers MGD, Kouznetsova VG, Brekelmans WAM. Multi-scale computational homogenization: trends and challenges. J Comput Appl Math 2010;234:2175–82. https://doi.org/10.1016/j.cam.2009.08.077.

[42] Omairey SL, Dunning PD, Sriramula S. Development of an ABAQUS plugin tool for periodic RVE homogenisation. Eng Comput 2019;35:567–77. https://doi.org/10.1007/s00366-018-0616-4.

[43] Tchalla A, Belouettar S, Makradi A, Zahrouni H. An ABAQUS toolbox for multiscale finite element computation. Compos B Eng 2013;52:323–33. https://doi.org/10.1016/j.compositesb.2013.04.028.

[44] 3DEXPERIENCE, Micromechanics Plugin: For Abaqus/CAE, Version 1.15, 2017.

[45] DIN EN ISO, 604: Kunststoffe - Bestimmung von Druckeigenschaften.

[46] Spoerk M, Gonzalez-Gutierrez J, Lichal C, Cajner H, Berger GR, Schuschnigg S, et al. Optimisation of the adhesion of polypropylene-based materials during extrusion-based additive manufacturing. Polymers 2018;10. https://doi.org/10.3390/polym10050490.

[47] Carneiro OS, Silva AF, Gomes R. Fused deposition modeling with polypropylene. Mater Des 2015;83:768–76. https://doi.org/10.1016/j.matdes.2015.06.053.

[48] Li D, Dornadula V, Lin K, Wehner M. Position control for soft actuators, next steps toward inherently safe interaction. Electronics 2021;10:1116. https://doi.org/10.3390/electronics10091116.

[49] Gaillac R, Pullumbi P, Coudert F-X. ELATE: an open-source online application for analysis and visualization of elastic tensors. J Phys Condens Matter Inst Phys J 2016;28:275201. https://doi.org/10.1088/0953-8984/28/27/275201.

[50] van Rossum G, Drake FL. Python 3 reference manual. Scotts Valley, CA: CreateSpace; 2009.

[51] Sullivan C, Kaszynski A. PyVista: 3D plotting and mesh analysis through a streamlined interface for the Visualization Toolkit (VTK). JOSS 2019;4:1450. https://doi.org/10.21105/joss.01450.

[52] Pozniak AA, Wojciechowski KW. Poisson's ratio of rectangular anti-chiral structures with size dispersion of circular nodes. Phys Status Solidi B 2014;251:367–74. https://doi.org/10.1002/pssb.201384256.

[53] Fernandez-Corbaton I, Rockstuhl C, Ziemke P, Gumbsch P, Albiez A, Schwaiger R, et al. New twists of 3D chiral metamaterials. Adv Mater 2019;31:e1807742.

[54] Ha CS, Plesha ME, Lakes RS. Chiral three-dimensional isotropic lattices with negative Poisson's ratio. Phys Status Solidi B 2016;253:1243–51. https://doi.org/10.1002/pssb.201600055.

[55] Lipton JI, MacCurdy R, Manchester Z, Chin L, Cellucci D, Rus D. Handedness in shearing auxetics creates rigid and compliant structures. Science 2018;360:632–5. https://doi.org/10.1126/science.aar4586.

Paper C

A black-box optimization strategy for customizable global elastic deformation behavior of unit cell-based tri-anti-chiral metamaterials

Authors: Thalhamer, A.
Fleisch, M.
Schuecker, C.
Fuchs, P.F.
Schlögl, S.
Berer, M.

Advances in Engineering Software
DOI: 10.1016/j.advengsoft.2023.103553

Advances in Engineering Software 186 (2023) 103553

Contents lists available at ScienceDirect

Advances in Engineering Software

journal homepage: www.elsevier.com/locate/advengsoft

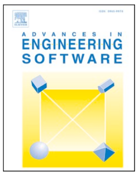

A black-box optimization strategy for customizable global elastic deformation behavior of unit cell-based tri-anti-chiral metamaterials

Andreas Thalhamer [a], Mathias Fleisch [a], Clara Schuecker [b], Peter Filipp Fuchs [a], Sandra Schlögl [a], Michael Berer [a,*]

[a] *Polymer Competence Center Leoben GmbH (PCCL), Roseggerstraße 12, Leoben 8700, Austria*
[b] *Department of Polymer Engineering and Science, Montanuniversitaet Leoben, Otto-Gloeckel Str. 2, Leoben 8700, Austria*

ARTICLE INFO

Keywords:
Finite Element Method
Homogenization
Numerical
Simulation
Interpolation

ABSTRACT

Metamaterials are a class of materials with a distinctive unit cell-based periodic architecture, often resulting in unique mechanical properties. The potential of metamaterials can be further improved by using gradients of unit cell parameters and thereby creating a specific distribution of material properties in a part. This design freedom comes with the challenge of finding new suitable design and optimization strategies. In this study, a Finite Element simulation-based optimization framework to create a predefined deformation behavior of unit cell-based metamaterials is presented. The framework consists of a numerical homogenization method to create an efficient linear elastic material representation, an interpolation scheme for a fast correlation of unit cell parameters with homogenized material properties and a black-box based optimization part. The framework is tested on a tri-anti-chiral metamaterial with additional geometric parameters and a newly developed transition unit cell. Several specified lateral deformations of simple 2D rectangular test specimens under tensile load are used as primary optimization targets and the homogenized results are validated against Finite Element simulations of fully modeled tri-anti-chiral structures. In addition, the effect of the design space and the number of design variables is studied and several combinations of optimization objectives and constraints are tested.

1. Introduction

Metamaterials are a class of synthetic materials with unusual properties based on their specific cellular design [1–3]. This unit cell (UC)-based design approach can lead to materials with uncommon mechanical properties such as auxetic behavior (negative Poisson's ratio) [4,5], variable stiffness [6,7] or a very high stiffness to weight ratio [8,9]. Due to their special deformation behavior under load, auxetic materials benefit from improved fracture toughness [10,11], energy absorption [12,13] and indention resistance [14,15]. These salient features lead to possible application scenarios in the medical [16], aerospace [17] and sport/textile industry [18,19].

However, to further improve the performance of metamaterials and tailor the material properties to specific needs and applications, new optimization strategies are required. A common approach is to optimize the material properties of metamaterials by performing topology optimization on the underlying UCs. Some of the first methods developed were used to improve the properties of already existing metamaterial designs. Schwerdtfeger et al. [20] used the well-known Solid Isotropic Material with Penalization (SIMP) method in an inverse homogenization approach with slope constraint regularization to improve the auxetic behavior of an initial structure. A more general method was developed by Behrou et al. [21]. Using a computational homogenization approach for the geometrically nonlinear regime they were able to create periodic UC-based materials with a prescribed target tangent stiffness tensor over finite strain ranges. Regarding chiral auxetic structures, Chen and Huang [22] proposed a topology optimization method based on couple stress homogenization and the floating projection topology optimization (FTPO) method for designing 3D metamaterials with chirality. Zhang et al. [23] used independent point-wise density interpolation (iPDI) and asymptotic homogenization to improve the topological design of bi-material chiral UCs.

In the past years, machine learning technology has been utilized to improve optimization methods. Kollmann et al. [24] used a convolutional neural network-based deep learning approach with energy-based topology optimization data to predict optimal 2D metamaterial UC

---

* Corresponding author.
E-mail address: michael.berer@pccl.at (M. Berer).

https://doi.org/10.1016/j.advengsoft.2023.103553
Received 13 June 2023; Received in revised form 14 September 2023; Accepted 19 October 2023

designs regarding bulk modulus, shear modulus, or Poisson's ratio. Challapalli et al. [25] implemented an inverse machine learning approach using generative adversarial networks (GANs) to optimize light weight lattice structures. A deep neural network was used by Liao et al. [26] to create a surrogate model to efficiently optimize a non-uniform rational basis spline-based parameterized tetra-chiral structure in an inverse design framework.

In addition to optimization on the UC level, the principle of metamaterials allows for spatially changing material properties via a defined distribution of UCs with varying geometric parameters. Panesar et al. [27] created functionally graded structures by defining the UC geometries based on the volume fraction distribution resulting from SIMP-based topology optimization on the macro scale. To bridge the gap between the macro scale and optimization of the underlying UCs, Zhang et al. [28] proposed a method for the concurrent topology optimization at macro and UC levels for cellular structures.

For more complex optimization goals, like prescribed deformation patterns of auxetic materials, the stiffness- or density-based topology optimization strategies are not sufficient anymore and other approaches have to be employed. To create structures with the ability to deform in a predefined way, Han and Lu [29] used an evolutionary algorithm in combination with discrete cosine transform encoding to optimize the Poisson's ratio of each reentrant honeycomb UC in a given cellular discretized structure. Recently, Liang et al. [30] developed a new method by combining a quantitative correlation between the parameters of the chiral cells and the deformation vector of specific nodes with a genetic algorithm to design structures with predefined complex deformations. Yao et al. [31] used a differential evolution algorithm to optimize the UC-based Poisson's ratio distribution of perforated metamaterials, based on five different achievable Poisson's ratios, to create a defined lateral deformation of tensile test specimens.

In this paper, a general framework for the optimization of UC-based metamaterials regarding predefined deformation behavior is proposed. The optimization is based on Finite Element (FE) simulations of a homogenized representation of the studied structure and the UC parameters are correlated to the entire elastic stiffness tensor to preserve the full global stress/strain behavior. To take the time-consuming homogenization out of the optimization loop, a linear interpolation object (LIO) is created on the homogenization data in a pre-processing step. Minimization of a given objective function is handled by the general black-box optimization software LSOPT (LS-OPT 6.0.0/Livermore Software Technology Corporation, Livermore, CA, USA). The framework is used to optimize the UC parameter distribution of a 2D tri-anti-chiral metamaterial to match a predefined deformation. In addition, the influence of the number of design variables and the usage of different objective functions are studied.

2. Optimization strategy

2.1. Framework overview

The proposed framework for optimization of UC-based materials by tuning the deformation to a specific target is shown in Fig. 1. It consists of two major parts: material pre-processing and optimization. In the material pre-processing step, the material behavior of the geometrically complex UC is broken down into a simple linear elastic material model with the use of a numerical homogenization method. Furthermore, for an efficient conversion of UC parameters to homogenized material properties, needed inside the optimization loop, a linear interpolation object is built based on the homogenization data. During the optimization, geometric UC parameters act as design variables and the evaluation function is based on FE simulations of homogenized models.

In this study, the FE models are simple 2D shapes with a displacement controlled tensile load. Output of the simulations is the deformation of specified edges. The homogenized models are partitioned into a defined number of material sections, representing sections with different unit cell parameters. This approach enables the clustering of unit cells which have the same parameters and thereby decreases the number of design variables. The deformation data of the simulations is compared to the optimization target and an error measure acts as a decision variable. The optimization algorithm then iterates and changes the design variables until the decision variable satisfies the convergence criteria, which ends the optimization. The result of the optimization is that distribution of the UC parameters in a structure which best achieves the target deformation. For the homogenization calculation and the setup of all FE models, Abaqus 2019 FEM software (Dassault Systemes, Vélizy-Villacoublay Cedex, France) is used. The simulations inside the optimization loop are solved with the Claculix FE solver, due to improved performance compared to the Abaqus solver in this special case. The setup of the FE models with the different material sections for the optimization is automated with a python script within Abaqus. The script handles the generation of the user defined boundary conditions, load case, and evaluation sets. Furthermore, it facilitates the automated partitioning of the geometry into a given number of material sections and the preparation of the input file. The following sections give a detailed description of the material pre-processing and optimization part of the framework.

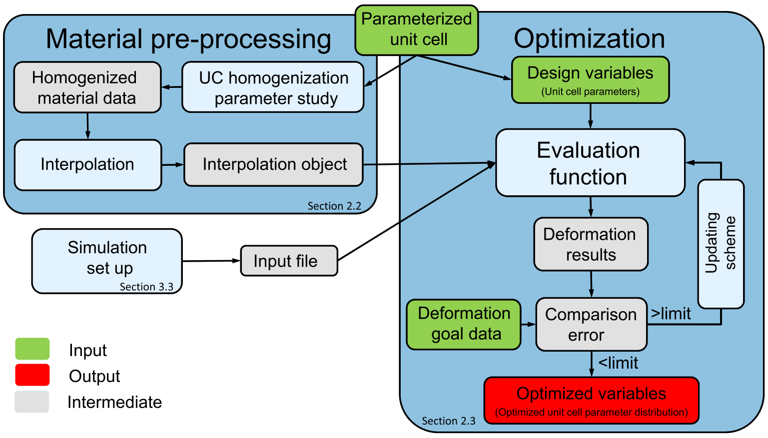

Fig. 1. General workflow of the proposed optimization framework.

2.2. *Material pre-processing*

2.2.1. *Homogenization*

To speed up the simulations inside the optimization loops and thereby increase the overall efficiency of the framework, a simplification of the complex metamaterial structures is needed. The proposed optimization strategy includes a homogenization approach to create a simple and efficient linear elastic material model based on the UCs of the material. Homogenization can be a useful tool as it allows for the mapping of UC-based properties on a macro scale [32,33]. There are several approaches for homogenizing of periodic cellular geometries, ranging from analytical to numerical methods with advantages and disadvantages depending on the complexity and specific shape of the UC under investigation. In the proposed framework, a numerical homogenization approach is implemented due to the complex geometry of the used UCs. The setup and solving of the homogenization calculations was carried out using the micromechanics plugin [34] in Abaqus 2019. For the details of the model setup refer to Section 3.3.1. The approach is based on 3D FE simulations of six individual displacement controlled unit load cases with periodic boundary conditions applied to the UC [35]. The periodic boundary conditions

$$u_i(x_2) = u_i(x_1) + \left(\frac{\partial u_i}{\partial x}\right)(x_2 - x_1) \tag{1}$$

are used to define the relative displacement of the opposing boundary surfaces. Here, $u_i(x_1)$ and $u_i(x_2)$ are the displacements in direction i of two points at surfaces on opposing sides of the UC and $(\partial u_i/\partial x)$ describes the change of the displacement u_i inside the UC between the two points. To facilitate the application of strains under consideration of the periodic boundary conditions, each of the opposing sides of the UC are coupled via a reference point. The global strain $\overline{\varepsilon} = (\varepsilon_{11}, \varepsilon_{22}, \varepsilon_{33}, \gamma_{12}, \gamma_{13}, \gamma_{23})^T$ is applied to the respective refence point and the tensor for each load case is given in Table 1 . The volume-averaged global stress of the UC, denoted as $\overline{\sigma} = (\sigma_{11}, \sigma_{22}, \sigma_{33}, \tau_{12}, \tau_{13}, \tau_{23})^T$ and calculated as

$$\overline{\sigma} = \frac{1}{V_{UC}} \int_{V_{UC}} \sigma(x) dV, \tag{2}$$

is used for each load case [36]. Here, V_{UC} is the volume of the UC and $\sigma(x)$ is the local stress distribution. Using a linear elastic anisotropic material description, the relation

$$\overline{\sigma} = \overline{C} : \overline{\varepsilon} \tag{3}$$

can be used to correlate the global stiffness tensor $\overline{C}$ to the global stress $\overline{\sigma}$ and global strain $\overline{\varepsilon}$. The full stiffness tensor $\overline{C}$ is then used to create the homogenized material model for the simulations inside the optimization loop. It should be noted that the material property directions 1, 2 and 3 correspond to the global directions X, Y and Z for the UC orientation used in this work.

2.2.2. *Interpolation of homogenized data*

The homogenization approach allows for the use of efficient simulation models during optimization. However, the homogenization itself is computationally too expensive to be included directly in the optimization iterations. Therefore, a linear interpolation object is created and used to map the material properties to the homogenized material sections depending on the geometric parameters of the UC. The LIO is built based on the data of the homogenization simulations during the preprocessing step. First, the range for the geometric parameters of the UC is defined and a number of UC geometries are homogenized to cover the entire parameter range. The number of UCs needed depends on the number of geometric variables and the targeted precision of the interpolation. The discrete field of geometric parameters and their respective homogenized stiffness tensors serves as the database for the tensor interpolation and the generation of the LIO.

Table 1
Strain-based load cases for the homogenization simulations.

Load Case (LC)	Applied Global Strain Tensor $\overline{\varepsilon}$
LC1	$\overline{\varepsilon} = (1,0,0,0,0,0)^T$
LC2	$\overline{\varepsilon} = (0,1,0,0,0,0)^T$
LC3	$\overline{\varepsilon} = (0,0,1,0,0,0)^T$
LC4	$\overline{\varepsilon} = (0,0,0,1,0,0)^T$
LC5	$\overline{\varepsilon} = (0,0,0,0,1,0)^T$
LC6	$\overline{\varepsilon} = (0,0,0,0,0,1)^T$

Tensor interpolations can be categorized into global and decomposition-based interpolation methods [37]. Whilst global methods operate on the tensor entries directly, decomposition-based methods interpolate between invariants and orientation separately. Decomposition-based methods, such as Geodesic-Loxodromes-based interpolation [38], are developed to preserve specific tensor properties better than linear tensor entry-based interpolation. But due to the numerical efficiency, linear interpolation is widely used and, with a large enough dataset, can be sufficient regarding the error in tensor properties [39]. In the proposed optimization framework, a global approach with interpolation between the tensor entries is utilized. A python module for piecewise linear interpolation in $N>1$ dimensions [40] is used to implement the interpolation and build the LIO. Using interpolation allows for the continuous calculation of the stiffness tensors based on the current design variables and the LIO has to be generated only once at the start of the optimization as long as the base material and the parameter range of a UC are not altered.

2.3. *Optimization*

2.3.1. *General optimization workflow*

The optimization is based on the black-box principal, which consists of unknown functions that, given a list of inputs, generate corresponding outputs without knowledge of the detailed internal structure [41]. For solving of simulation based black-box optimization problems, several classes of algorithms exist, including gradient-based search methods, stochastic methods, response surface methodology and heuristic methods [42,43].

In this study, the commercially available software LSOPT is utilized for optimization, details of the setup are given in Section 2.3.2. The optimization algorithm inside LSOPT requires no detailed information about the actual evaluation-function. It only asks for the possible range of design variables, the output from the evaluation function depending on the design variables, constraints if necessary, and an optimization target to compare the output with. In this study, the evaluation-function is the FE simulation of a homogenized part. The design variables are the UC parameters for different material sections of the homogenized simulation model and the output is the lateral deformation at a specific evaluation set. During the optimization, the LIO is used to convert the design variables (geometric UC parameters) to the corresponding homogenized stiffness tensor for the material model. To ensure thermodynamically meaningful values, each interpolated tensor is checked against the following stability criteria [44]

$$E_i > 0, \; G_{ij} > 0 \; \forall \; i,j = 1,2,3 \tag{4}$$

$$1 - \nu_{12}\nu_{21} - \nu_{23}\nu_{32} - \nu_{31}\nu_{13} - 2\nu_{32}\nu_{21}\nu_{13} > 0 \tag{5}$$

$$|\nu_{ij}| < \sqrt{\frac{E_i}{E_j}} \; \forall \; i,j = 1,2,3 \tag{6}$$

before it is used in the simulation.

Once the simulation has been completed, the deformation output at a defined location is compared to a predefined deformation and an error function, based on the difference between the two, is calculated. Minimization of the error function is set as the optimization objective. Details of the error function and optimization settings used are described in the next section.

2.3.2. *LSOPT settings*

The optimization itself is performed in LSOPT, using the sequential metamodel-based optimization with domain reduction [45]. Sampling for the linear polynomial metamodel is set to d-optimal point selection with the default number of simulations per iteration n_{points} calculated as

$$n_{points} = int(1.5(n_{vars}+1))+1, \tag{7}$$

with int() as the integer function and n_{vars} as the number of variables [45]. Optimization is performed using the hybrid simulated annealing algorithm on the mean square error ε of a curve matching composite, calculated as

$$\varepsilon = \frac{1}{P}\sum_{p=1}^{P} W_p\left[\frac{f_p(x)-G_p}{s_p}\right]^2, \tag{8}$$

with G_p as the points on the target curve, $f_p(x)$ the corresponding points on the computed curve and with $s_p = max|G_p|$ and W_p as weight factors [45].

Convergence is determined via the design change tolerance ε_x and the objective function tolerance ε_f. They are calculated as

$$\varepsilon_x = \frac{\| x^{(k)} - x^{(k-1)} \|}{\| d \|} \tag{9}$$

and

$$\varepsilon_f = \left|\frac{f^{(k)} - f^{(k-1)}}{f^{(k)}}\right|, \tag{10}$$

where x denotes the vector of design variables, d the size of the design space, f denotes the value of the objective function and k is the iteration number [45]. The optimization is terminated if $\varepsilon_x < tol$ and $\varepsilon_f < tol$. For this study $tol = 0.01$ is used.

2.3.3. *FE solver inside the optimization loop*

For solving the FE models during the optimization, the free Calculix FE solver is used instead of the Abaqus solver, which has been used for the homogenization and validation. The reason for the change to Calculix is the long time needed for license verification before each Abaqus simulation. Especially with small and simple models this time extends the overall function call time during the optimization significantly. Calculix has no license verification step, making it faster than Abaqus for small models. Fig. 2 shows the mean runtime for 20 simulations with Abaqus and Calculix for two simple linear elastic models with different numbers of degrees of freedom (DOF). Time is measured with a python function calling the solvers and running a simulation. The difference in function call times diminishes with increasingly complex and longer simulations as the overall solving time gradually outweighs the time for license verification.

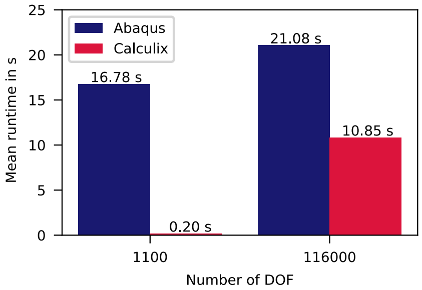

Fig. 2. Comparison of average runtime for 20 simulations between Abaqus and Calculix FE-solver.

3. Tri-anti-chiral structure

One way to create materials with auxetic behavior is to use chiral structures. The UCs of chiral structures are based on rotational centers (circles, rings, squares) with a specific number of connection struts. Distinction of the various chiral materials can be done by number of the connection struts ((3)tri-,(4)tetra-, (6)hexachiral) [46] and by the symmetry inside the UC (chiral, anti-chiral, meta-chiral) [47]. Chiral materials offer a wide range of Poisson's ratios from positive to negative [5,48,49] and therefore are very versatile regarding the achievable deformation response.

Tri-anti-chiral structures are mechanical metamaterial structures [48,50,51] well-known for their tunable Poisson's ratio. Advancing from the design of standard tri-anti-chiral structures, a design with additional geometric parameters is introduced in this study. This design permits to create structures in a broad range of Poisson's ratios (positive and negative) and a variation of the Poisson's ratio within the structure itself.

3.1. *Basic unit cell design*

The standard UC of a tri-anti-chiral structure is depicted in Fig. 3(a). It consists of four nodes with diameter D_N, arranged on a regular hexagonal grid with side length L, connected with struts of thickness T. The bounding box of the UC is given as $3L$ x $\sqrt{3}L$. The 2D-sketch is extruded by L_{zz} to create a 2.5D structure. To increase the application potential of the tri-anti-chiral structure additional geometric degrees of freedom are introduced. These additional geometric parameters allow for a broader range of obtainable Poisson's ratios from positive to negative values and they allow for a variation of the Poisson's ratio within the structure itself. A depiction of such an extended UC is shown in Fig. 3(b). Strictly speaking, the cell depicted in Fig. 3(b) is not a unit cell, since it depends on the top and bottom cells. However, for simplicity, we will refer to it as a unit cell. The nodes are no longer arranged on a regular hexagonal grid but are defined by their horizontal and vertical distance to each other. In order to keep the complexity in this study to a manageable level, the mirror symmetry along the y-axis is preserved as in the standard UC. In this way, the inner structural Poisson's ratio variation is only possible along the Y direction in Fig. 3(b). To avoid non-valid geometries, the positions and diameters of the adjacent nodes in the Y direction have to be known. Therefore, four rows of nodes are needed to fully define the UC. The adjacent bottom and top rows will be referred to as virtual nodes as they are needed for the definition but are not part of the geometry of the UC. The diameters of the nodes inside the UC are labeled as D_{N1} and D_{N2} with horizontal distance L_{x1} and L_{x2}, respectively. The vertical distance between the two rows is given as L_y. Similarly, the node diameters of the bottom and top rows are labeled as D_{Nb} and D_{Nt} with horizontal and vertical distances L_{xb}, L_{xt} and L_{yb}, L_{yt}, respectively. The horizontal extension of the UC is given as L_{xx}, resulting in a size of the UC as L_{xx} x $(L_y + L_{yb}/2 + L_{yt}/2)$. Similar to the standard UC, the nodes are connected by struts with thickness T and the sketch is extruded in Z direction by L_{zz}. A 3D-view of the UC is shown in Fig. 3(c). The geometric parameters of the UC are summarized in Table 2. A periodic unit cell is achieved if $L_{xb} = L_{x2}$, $L_{xt} = L_{x1}$, $D_{Nb} = D_{N2}$, $D_{Nt} = D_{N1}$ and $L_{yt} = L_y = L_{yb}$. With these geometric restrictions, the cell can be analyzed directly with the homogenization approach described in Section 2.2.1 to obtain the mechanical properties.

For this study, the variables T, L_y and L_{zz}, are kept constant at 0.8 mm, 15 mm and 5 mm, respectively, and D_{N1} and D_{N2} are kept constant at 5

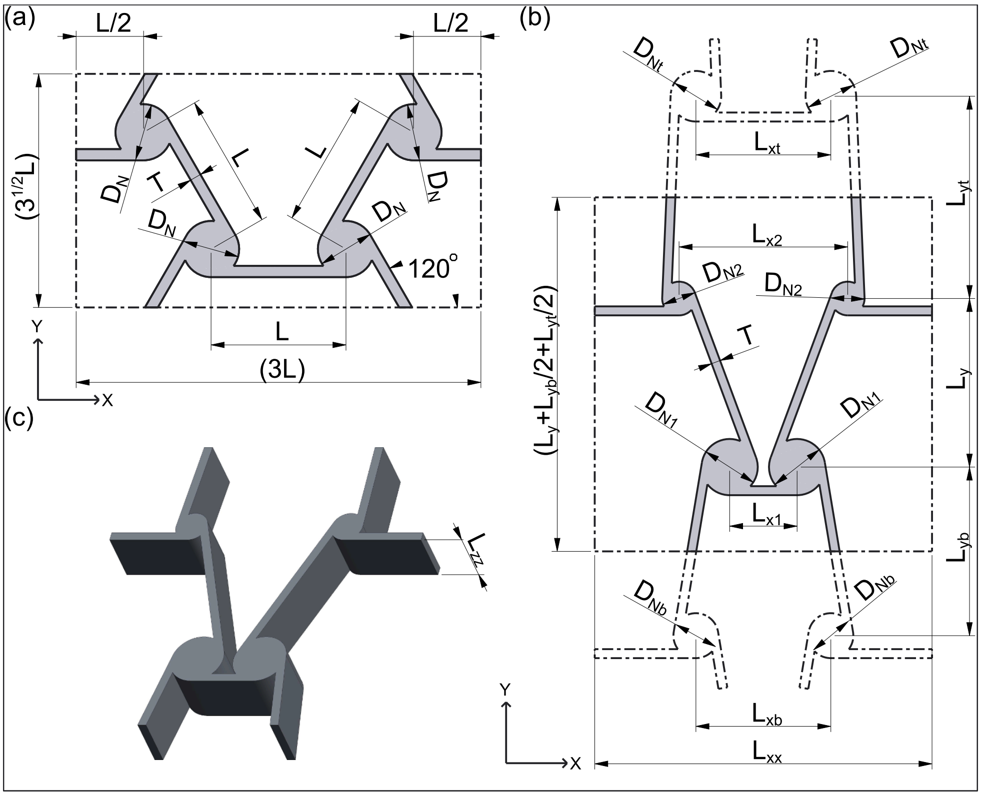

Fig. 3. Unit cell design of the tri-anti-chiral structure. (a) Standard unit cell, (b) unit cell with extended set of geometric parameters and (c) 3D-view of the extended unit cell.

Table 2
Geometric parameters of the unit cells.

Parameter	Description
Basic unit cell (Fig. 3(a))	
L	Distance between connected nodes
D_N	Diameter of the nodes
T	Thickness of connecting struts
L_{zz}	Thickness of structure in Z direction
Extended unit cell (Fig. 3(b))	
D_{N1}, D_{N2}	Diameter of first and second row of nodes
D_{Nb}, D_{Nt}	Diameter of bottom and top row of (virtual) nodes
L_{x1}, L_{x2}	Horizontal distance within first and second row of nodes
L_{xb}, L_{xt}	Horizontal distance within bottom and top row of (virtual) nodes
L_y	Vertical distance between first and second row of nodes
L_{yb}, L_{yt}	Vertical distance to bottom and top row of (virtual) nodes
L_{xx}	Side length of unit cell in X direction
T	Thickness of connecting struts
L_{zz}	Thickness of structure in Z direction

mm, only the distance L_{x1} and L_{x2} are set as design variables. This reduces the complexity of the optimization and still allows for a wide range of homogenized material properties. With L_{x1} and L_{x2} between 6 mm and 21 mm, the homogenized Poisson's ratio ν_{21} ranges from -1.47 to 0.94 and ν_{12} from -0.57 to 0.26. The homogenized Young's modulus E_2 in Y direction ranges from 1.82 MPa to 5.43 MPa and the homogenized Young's modulus E_1 in X direction ranges from 0.64 MPa to 0.82 MPa. Using a very high or low ratio of L_{x1}/L_{x2} leads to a decrease in stiffness in Y direction due to the introduction of angled struts and thus more bending deformation, whereas decreasing L_{x1} or L_{x2} leads to an increase in stiffness. Regarding the Poisson's ratio ν_{21} the most extreme values can be reached with a very high or low ratio of L_{x1}/L_{x2}. Whereby a high ratio leads to a negative and a low ratio to a positive Poisson's ratio. This change in property is caused by the varying lateral deformation behavior based on the different orientations of the vertical struts. Fig. 4 illustrates the possible homogenized material properties for the given parameter space.

3.2. *Bridge cell design for gradients*

By varying the geometric parameters of the UC, different Poisson's ratio values can be obtained. If $L_{x1} < L_{x2}$ (Fig. 5(a)), a structure with positive Poisson's ratio is obtained, whereas if $L_{x1} > L_{x2}$ (Fig. 5(b)) negative values are observed (refer to Section 3.1 for more details). To have a gradual transition between two cells with different geometric parameters, bridge cells can be defined. Fig. 5(c) shows an example of such a bridge cell, connecting a positive cell (bottom) to a negative cell (top). Alternatively, Fig. 5(d) shows a bridge cell connecting a negative cell (bottom) to a positive cell (top). A bridge cell, UC_B, connecting two unit cells, UC_1 and UC_2, is defined by the following set of equations

$$\begin{cases} L_{xt} = (L_{x1})_2 \\ L_{x2} = (L_{x2})_2 \\ L_{x1} = (L_{x1})_1 \\ L_{xb} = (L_{x2})_1 \end{cases} \tag{11}$$

where $(L_{xi})_j$ denotes the i-th length in x direction inside the j-th unit cell ($j = 1{,}2$). Using the bridge cells, five 2D structures with differing UC distributions are created for the testing of the optimization framework. Fig. 6 shows these structures including the UC designation and Table 3 documents the corresponding geometric parameter values and

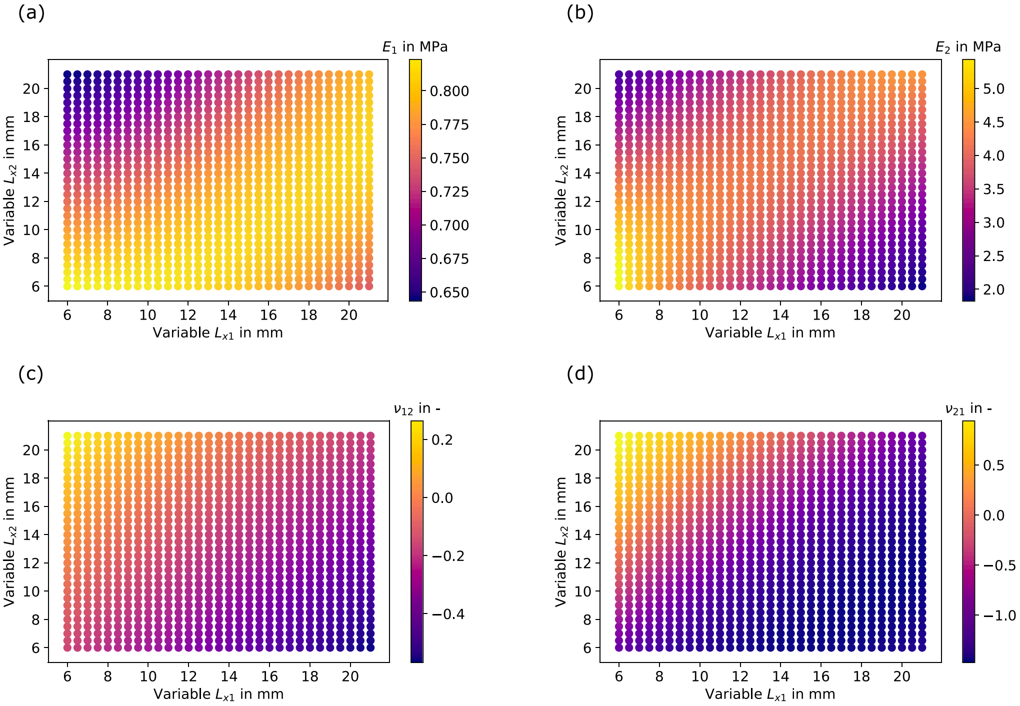

Fig. 4. Homogenized material properties for $\boldsymbol{L_{x1}}$ and $\boldsymbol{L_{x2}}$ between 6 mm and 21 mm; (a) Young's modulus E_1 in X direction, (b) Young's modulus E_2 in Y direction, (c) Poisson's ratio ν_{12} and (d) Poisson's ratio ν_{21}.

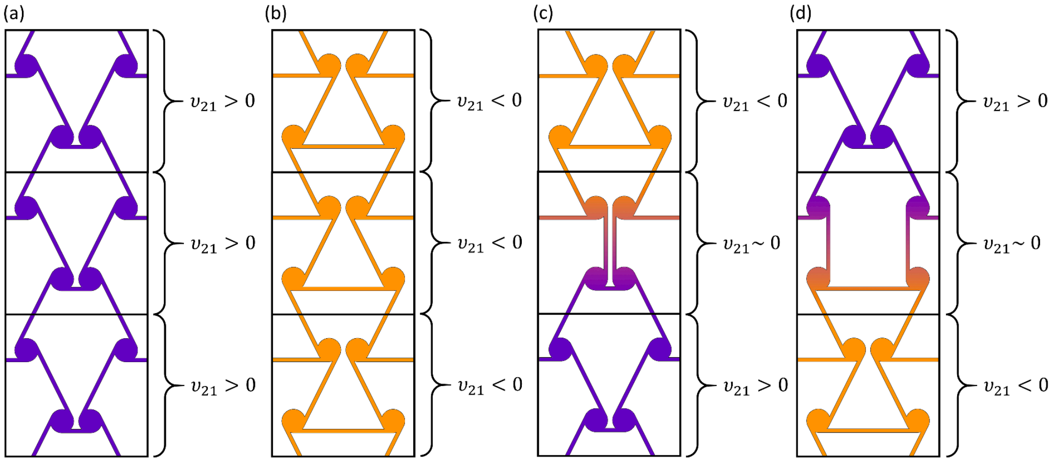

Fig. 5. Types of connections between adjacent unit cells. (a) Design with positive Poisson's ratio, (b) design with negative Poisson's ratio, (c) bridge cell from positive (bottom) to negative (top) cells and (d) bridge cell from negative (bottom) to positive (top) cell.

homogenized properties of the UCs used. The structures 1–4 have an overall dimension of 150 mm x 330 mm and structure 5 of 180 mm x 210 mm. The dimensions have been chosen to satisfy the constraints for additive manufacturing for future studies and the applicability of homogenization was verified in Section 4.1. The transition cells are not used for homogenization, only unit cells satisfying the periodic boundary conditions are homogenized. The effect of the transition cells on the overall mechanical behavior is assumed to be small if the number of individual unit cells inside a material section is high enough, which is also a general prerequisite for accurate homogenization (see Section 4.1.2)

3.3. Simulation setup

Three types of FE models on different length scales and levels of detail are used in this study. For the homogenization approach, a 3D model of only the unit cell with periodic boundary conditions is used. During the optimization, a simplified 2D homogenized model of the structures is used and for the validation of the optimization and verification of the homogenization, a 2D model with an assembly of fully

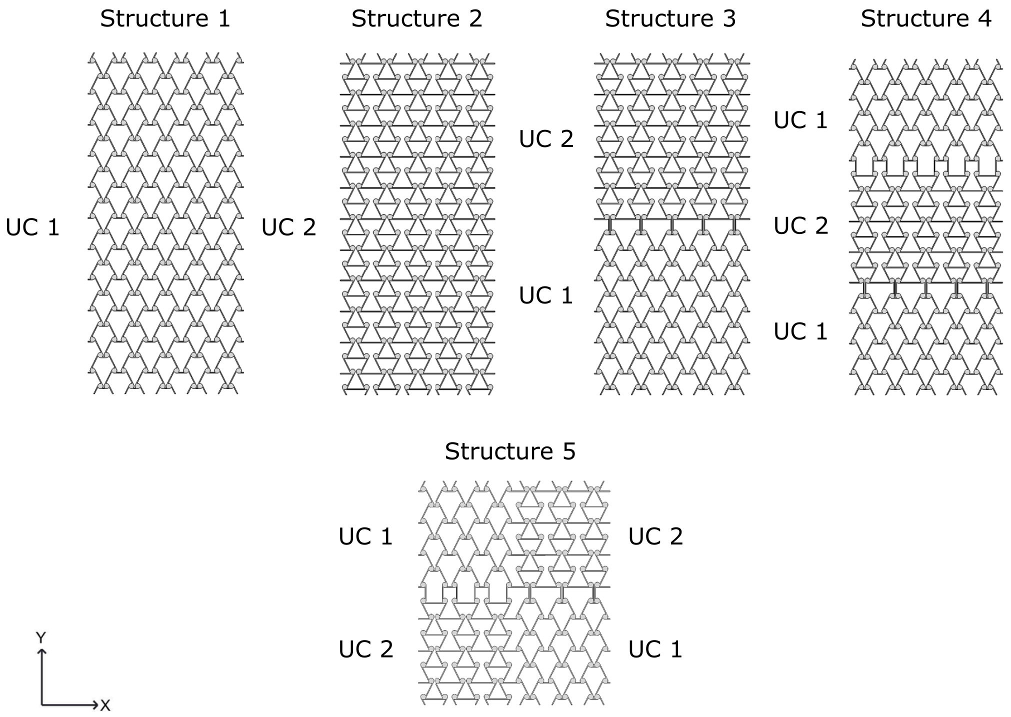

Fig. 6. The five tri-anti-chiral structures with different unit cell distributions used in this study.

Table 3
Geometric parameters and homogenized mechanical properties of the unit cells used for the tri-anti-chiral structures.

	L_{x1}	L_{x2}	E_1	E_2	ν_{12}	ν_{21}
UC 1	6 mm	21 mm	0.64 MPa	2.29 MPa	0.26	0.94
UC 2	21 mm	6 mm	0.75 MPa	1.82 MPa	−0.57	−1.38

featured UC structures is used. Examples of the three different types of FE models are shown in Fig. 7. In this section, the setup of the individual FE models regarding geometry, mesh, material model and boundary conditions is described. Furthermore, the results of a mesh study are given as basis for the element size selection.

3.3.1. Setup of models for UC homogenization (material pre-processing)

For the models of the simulation-based UC homogenization, the boundary conditions and loads for the individual UCs are set up as described in Section 2.2.1 with the help of the Abaqus micromechanics plugin. The models are meshed with reduced quadratic hexahedral continuum elements and a global seed size of 0.2 mm in the X-Y plane and two elements along the edges in Z direction. Mesh size in the X-Y plane is based on the mesh study of the fully modeled structures (see Section 3.3.3). Fig. 7(a) shows the model of an exemplary UC. A linear elastic isotropic material model with a Young's modulus of 3134 MPa and a Poisson's ratio of 0.35, derived from bending test data of PLA [7], is used for all homogenization simulations. The models are solved using the linear perturbation step without consideration of nonlinear geometry in Abaqus. Evaluation of the results and calculation of the homogenized stiffness tensor is again performed with the Abaqus micromechanics plugin.

3.3.2. Setup of optimization and verification/validation models

Both models, for the optimization and the verification, are based on a displacement-controlled extension in Y direction with the displacement on one or two lateral edges as evaluation value. The optimization model consists of a simple homogenized 2D part without any geometrical UC details. The model is divided into a number of evenly sized sections to represent the material sections with different UC parameters. The number of material sections can be set depending on the complexity of the deformation target and the size of the unit cells. Detailed information about the dimension and number of material sections is provided, for each example studied, in Section 4.3. The verification models consist of a fully modeled UC assembly. In this study, periodically arranged tri-anti-chiral UCs are used. To find the right mesh size for both models, a mesh study was conducted (see Section 3.3.3). For the optimization models, 8 node plane strain elements with a global seed size of 5 mm are used. The verification models are meshed with the same elements and a global seed size of 0.2 mm. In the optimization models, the properties for each material section are based on the homogenized stiffness tensor of the respective UC and are specified via an elastic anisotropic material model. The entries of the stiffness tensor are calculated during the optimization depending on the UC parameters (via the interpolation object). For the validation models, the same elastic isotropic material model, as used in the UC homogenization, is used. For both models, the bottom surface of the model is fixed in all directions and the top surface is displaced according to the desired load case. For a tension load case the top surface is fixed in X direction and displaced in positive or negative Y direction to create a given extension or compression respectively. For a shear load case the top surface is fixed in Y direction and displaced in positive X direction. The loading is defined in terms of the global strain ε_{Gy} and ε_{Gxy} of the entire structure, calculated as

$$\varepsilon_{Gy} = \frac{\Delta l_y}{l_y} \tag{12}$$

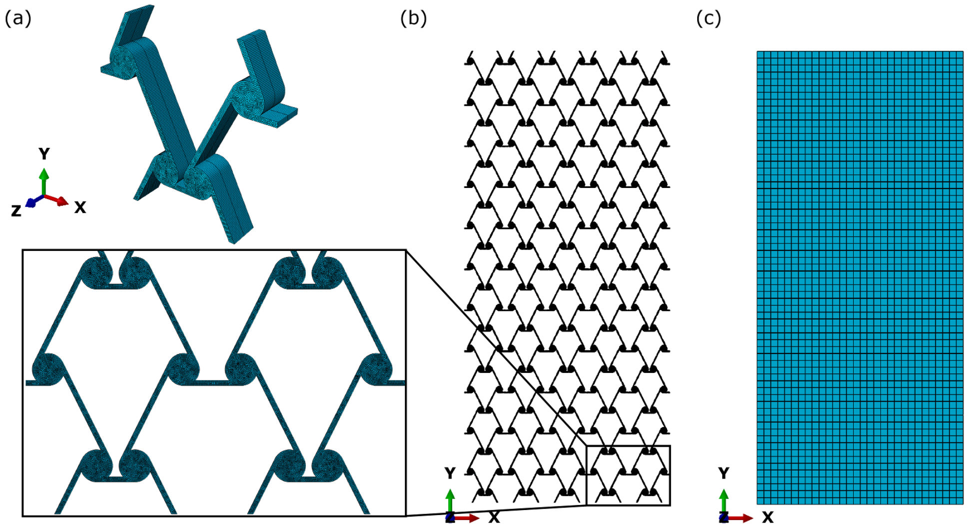

Fig. 7. Exemplary FE Model for (a) unit cell simulations (for the homogenization), (b) fully modeled simulations (for verification) and (c) a homogenized model (for optimization).

and

$$\varepsilon_{Gxy} = \frac{\Delta l_x}{l_y} \tag{13}$$

with Δl_y and Δl_x being the displacement in Y and X direction of the top surface and l_y the length of the structure in Y direction, respectively. The specific values of the applied strain are given in the respective Sections 3.3.3, 4.1 and 4.3. For the evaluation of the lateral deformation under load, node sets with all the nodes from the right and from the left vertical edge of the model, respectively, are created. Fig. 8 depicts the evaluation paths for the lateral deformation for both models. Inside the optimization framework the homogenized models are solved using the static FE solver Calculix. The verification models are solved using the Abaqus standard solver with consideration of nonlinear geometry activated.

3.3.3. *Mesh study*

To determine a suitable mesh size for both the homogenized and the fully modelled structure, a mesh study was performed for both models based on the geometry of structure 1 in Fig. 6. The global mesh seed size was varied from 1.5 mm to 0.05 mm for the fully modeled variants and from 10 mm to 0.5 mm for the homogenized variants. Both variants were solved using the Abaqus standard solver. The distribution of the lateral deformation in X direction at ε_{Gy}= 5% was used as a qualitative comparison measure. The deformation was evaluated at the lateral edge of the models on the right side of the structures as depicted in Fig. 8. For a quantitative comparison, the reaction force in Y direction at the top surface at ε_{Gy}=5% was used. In addition, the overall simulation time was evaluated to gain information about computational cost of the different mesh sizes.

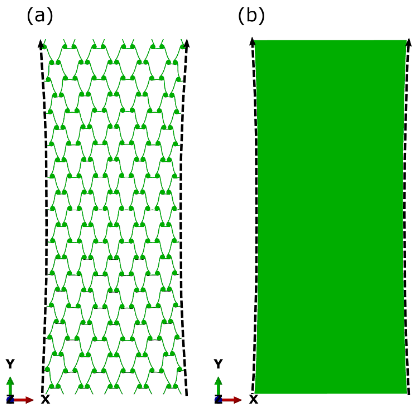

Fig. 8. Evaluation path for the lateral deformation in X direction along the right and left side for a (a) fully modeled structure and (b) a homogenized model.

Regarding the lateral deformation along the edge, no significant change of the qualitative deformation behavior is visible for both models in the considered global seed size ranges (Fig. 9). The different, slightly jagged, appearance of the deformation of the fully modeled structure is caused by the spacing and the rotation of the struts with the evaluation nodes. For the homogenized model, the evaluation of the reaction force shows no significant change with mesh size (Fig. 10(a)). This leads to the assumption that all global seed sizes between 10 mm and 0.5 mm provide suitable accuracy for this model. Hence, for the use in the optimization a global seed size of 5 mm is chosen for the homogenized model, mainly to achieve a compromise between a sufficient number of evaluation nodes at the edge of the model and simulation time.

The fully modeled structures show a trend of decreasing reaction force with smaller mesh size between 1.5 mm and 0.05 mm (Fig. 10(b)). However, below the mesh size of 0.2 mm the gain in accuracy in comparison to the increase in simulation time diminishes. Therefore, 0.2 mm is chosen as element size for the fully modeled structures. The results exhibit a noticeable difference between the homogenized model and fully modeled structure regarding the reaction force and the deformation behavior. The reasons are further investigated in more detail in Section 4.1.

4. Results

4.1. *Homogenization approach – verification and limits*

To evaluate the capability of the homogenization method for representing the overall deformation behavior of the tri-anti-chiral structures and to define the limits of this approach, full models of structure 1

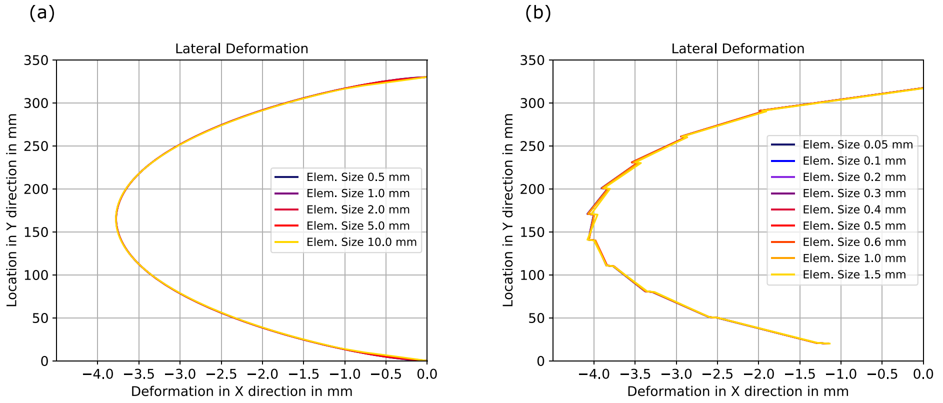

Fig. 9. Lateral deformation obtained from simulations with several element sizes for (a) the homogenized structure and (b) the fully modeled structure.

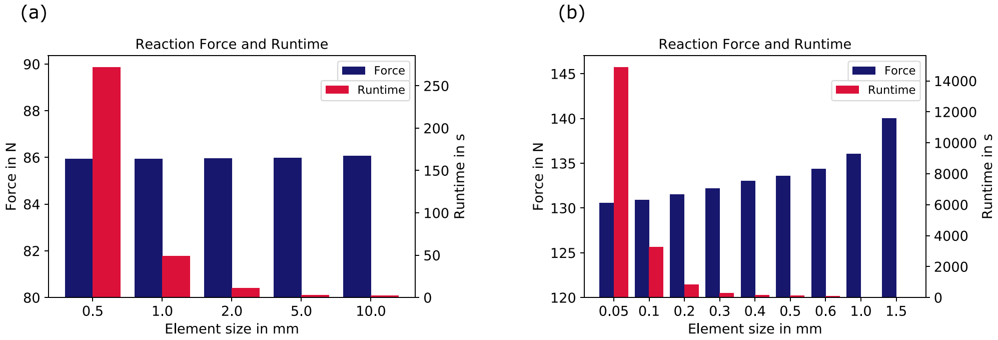

Fig. 10. Reaction force and runtime of simulations with several element sizes for (a) the homogenized structure and (b) the fully modeled structure.

and structure 2 (structure numbers according to Fig. 6) were compared to their homogenized counter parts. The models were set up, as described in Section 3.3.2 and three different load cases (tension, compression and shear) were created. The boundary conditions were chosen to correspond to a global strain of ε_{Gy}= 5%, ε_{Gy}= −5% and ε_{Gxy}= 5% for tension, compression and shear respectively. Results of the simulations were compared regarding global stress-strain behavior and lateral deformation in X direction. The lateral deformation was again evaluated on the right side of the structures on a path along the Y direction (refer to Fig. 8 for details). The global stress was calculated by dividing the reaction force in Y or X direction at the top surface by the surface of the cross section of the respective structure.

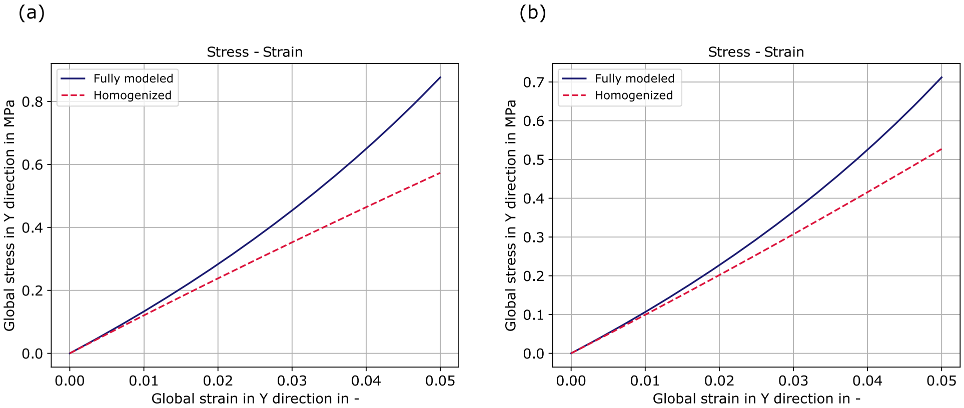

Fig. 11. Stress-strain comparison between the homogenized and the fully modeled structure for (a) structure 1 and (b) structure 2 for the tension load case (structures are numbered according to Fig. 6).

4.1.1. Load case study

Looking at the global stress-strain curves for tension in Fig. 11, a clearly non-linear behavior of the fully modeled structures with increasing stiffness at higher strains is visible. This is attributed to the complex geometry of the tri-anti-chiral UCs and their deformation behavior under tension. During global deformation of the structure, nodes of the UC start to rotate and the connection angles of the struts to the nodes change, resulting in the non-linear stress-strain behavior. As per definition, the models with the linear elastic homogenized material show only a linear stress-strain correlation. Therefore, the error in tangent modulus between the two models increases with higher global strain. In addition to the global stress-strain response, Fig. 12 shows the lateral deformation under tension for several applied global strains ε_{Gy} for homogenized and fully modeled simulation models. It is obvious that the difference in the deformation between the two models increases with higher applied global strain but the overall distribution of the deformation can be captured.

The stress-strain curve of the compression load case, shown in Fig. 13, also features a non-linear behavior for the fully modeled structures, but this time with decreasing stiffness at higher strains. Regarding the lateral deformation under compressive loads, the general trend again shows a more pronounced difference between fully modeled structures and the homogenized structures for high strains, as can be seen in Fig. 14. Prominent peaks of deformation occur near the bottom and top surface for the fully modeled structures at high strains. The homogenized models are not capable of reproducing these peaks at high strains.

Fig. 15 shows that due to their low shear modulus, only small shear stresses occur when loading with ε_{Gxy}= 5% and therefore the nonlinearity is noticeably smaller. For the shear load case the lateral movement of the nodes at the sides of the rectangle is not governed by the Poison's ratio but by the shear stiffness and the applied displacement. Due to the linear stress-strain behavior in the considered strain range, the homogenized structure can reproduce the deformation behavior of the fully modeled structure very well, as indicated by Fig. 16.

All three load cases show that the applicability of the homogenized models to represent the tri-anti-chiral structures has its limits, with tension being the most critical load case. To test the developed optimization strategy for the worst case, only tension load cases are considered for optimization tests. Consequently, to keep the relative error in the global stress of the homogenization approach under 10% and to ensure a good deformation representation, only global strains up to ε_{Gy}= 1% are used in the study for the optimization framework.

4.1.2. Size effect study

As the homogenized material describes the properties of a material consisting of an infinite amount of periodically arranged UCs, there is a minimal number of necessary UCs in a real structure for homogenization to be applicable. This limit depends on the design and size of the UCs. A size effect study was therefore conducted to evaluate the influence of the number of UCs in a structure on its global mechanical behavior. Several structures with different numbers ofUCs, ranging from 2 × 2 to 10 × 10 UCs, were created. The simulation models were set up as described in Section 3.3.2 with a tension load case and a global strain of ε_{Gy}= 5%. An exemplary selection of used structures is shown in Fig. 17(a). For the evaluation of the material properties the Young's modulus was calculated between ε_{Gy}= 0% and ε_{Gy}= 0.25% from global stress strain data and the Poisson's ratio at ε_{Gy}= 5% from global longitudinal and lateral strain.

Fig. 17(b) displays a decrease of the Young's modulus when increasing the number of UCs of a structure. The difference between each structure is diminishing with the increase in UCs. The Poisson's ratio, which is depicted in Fig. 17(c), shows a noticeable decrease between 2 × 2 and 3 × 3 UCs with only minor change beyond that. Therefore, the number of 5 × 11 UCs, of the structures for testing of the optimization (see Fig. 6), should suffice to reduce the size effect.

4.2. Interpolation quality

For the generation of the interpolation object, the stiffness tensor was calculated via homogenization of 961 UC designs with the parameters L_{x1} and L_{x2} evenly spaced between 6 mm and 21 mm. The accuracy of the interpolation scheme, regarding the mechanical properties, was tested by comparing the Young's modulus and Poisson's ratio of the interpolated and calculated stiffness tensors, respectively. To also evaluate the precision regarding the entire interpolated tensor, the normalized Frobenius norm l^2 of the difference between calculated tensor C_{calc} and interpolated tensors C_{int} was evaluated as

$$l^2_{error} = \frac{\parallel C_{calc} - C_{intF} \parallel}{\parallel C_{calcF} \parallel} \tag{14}$$

For that, l^2 for a mxn sized matrix A with its entries a_{ij} was calculated according to

$$l^2 = \parallel A \parallel_F = \sqrt{\sum_{i=1}^{m} \sum_{j=1}^{n} |a_{ij}|^2} \tag{15}$$

and the relative error of the mechanical properties between the calcu-

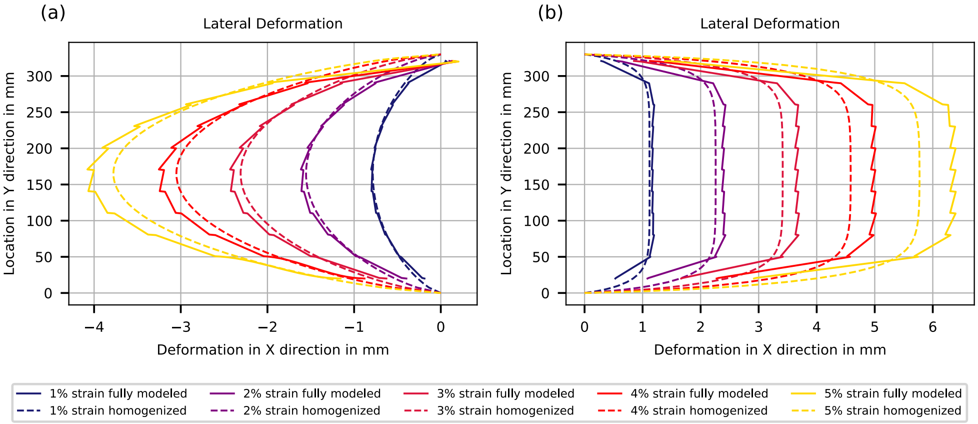

Fig. 12. Lateral deformation comparison between the homogenized and the fully modeled structure at differing global strains for (a) structure 1 and (b) structure 2 for the tension load case (structures are numbered according to Fig. 6).

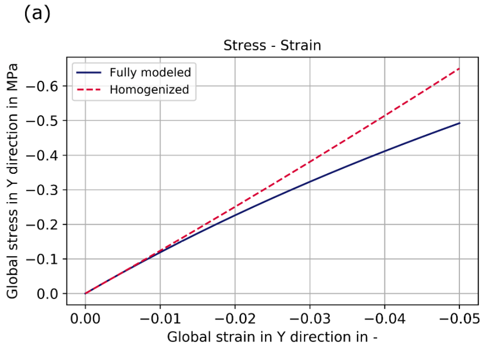

Fig. 13. Stress-strain comparison between the homogenized and the fully modeled structure for (a) structure 1 and (b) structure 2 for the compression load case (structures are numbered according to Fig. 6).

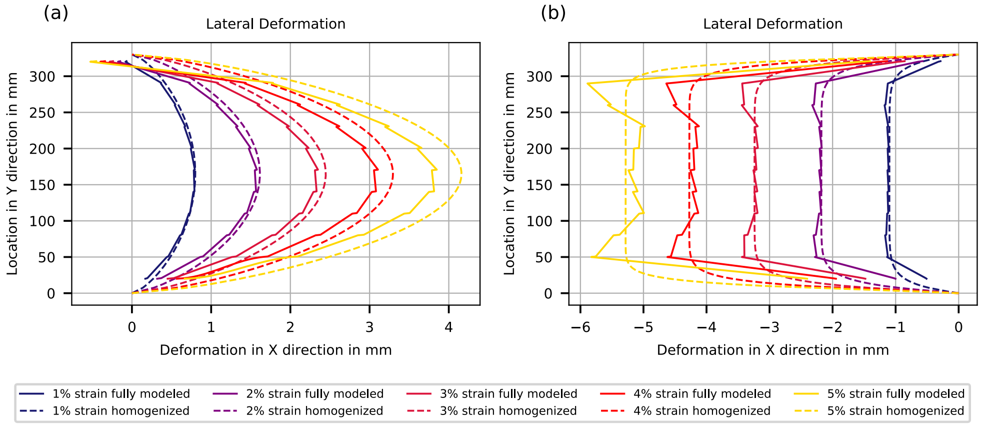

Fig. 14. Lateral deformation comparison between the homogenized and the fully modeled structure at differing global strains for (a) structure 1 and (b) structure 2 for the compression load case (structures are numbered according to Fig. 6).

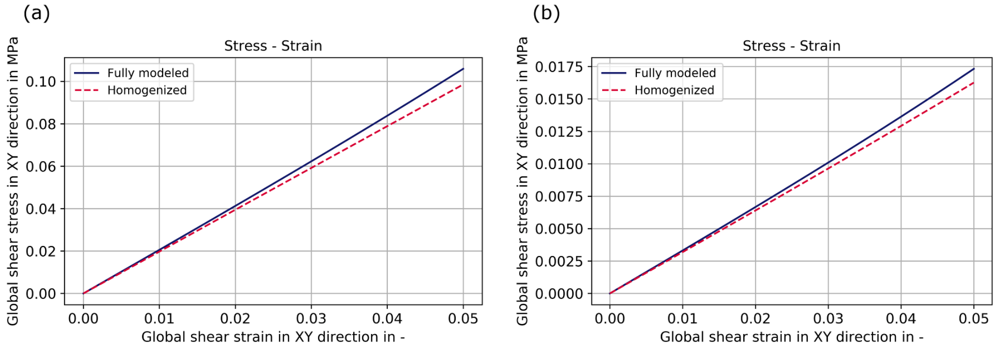

Fig. 15. Stress-strain comparison between the homogenized and the fully modeled structure for (a) structure 1 and (b) structure 2 for the shear load case (structures are numbered according to Fig. 6).

lated and interpolated tensors was computed as

$$p_{error} = abs\left|\frac{p_{calc} - p_{int}}{p_{calc}}\right| \tag{16}$$

with p_{calc} being the property (Young's modulus and Poisson's ratio) of the calculated tensor and p_{int} from the interpolated tensor. For the evaluation, 900 points in the parameter space between the data points of the LIO were evaluated.

Fig. 18 shows the relative error for the selected properties. The stiffness in both directions shows a maximum error less than 0.3% with the higher errors occurring for low L_{x1} values. On the other hand, both Poisson's ratios display a very high maximum relative error of over 40% for some individual variable combinations. The reason for this high error lies in the Poisson's ratio absolute value of near to zero for these specific

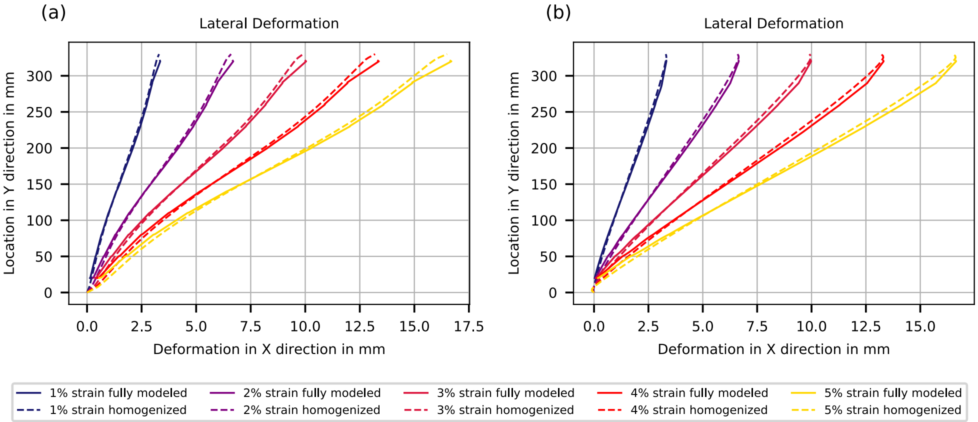

Fig. 16. Lateral deformation comparison between the homogenized and the fully modeled structure at differing global strains for (a) structure 1 and (b) structure 2 for the shear load case (structures are numbered according to Fig. 6).

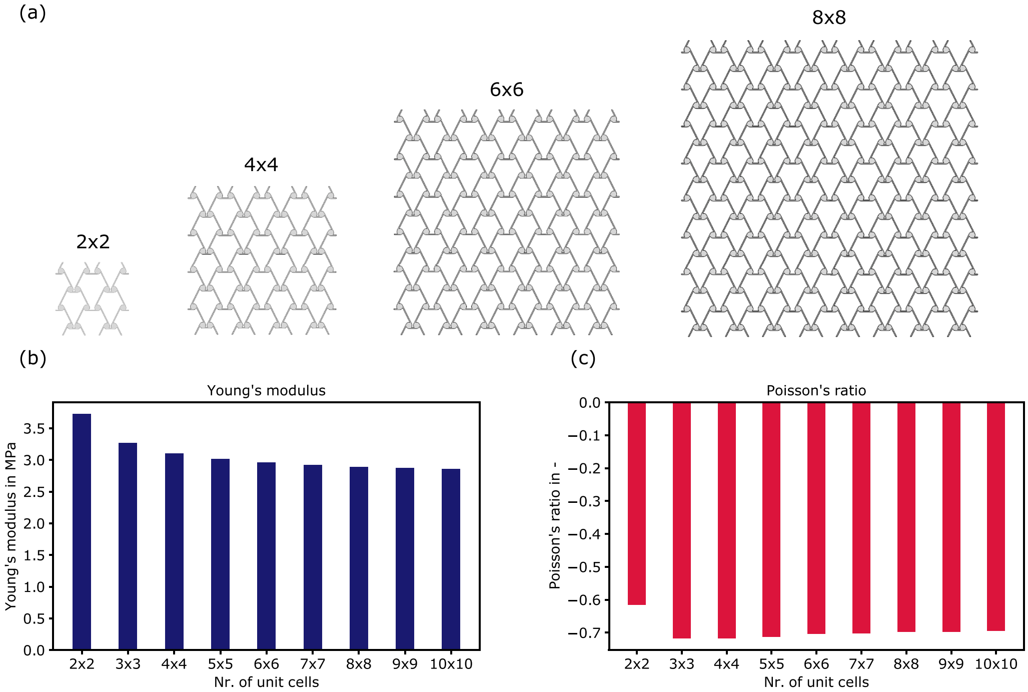

Fig. 17. Outcome of the size effect study. (a) Exemplary selection of the used structures with various numbers of unit cells and the results for the (b) Young's modulus and (c) Poisson's ratio depending on the number of unit cells.

variable combinations, as can be seen in Fig. 4. Therefore, even very small absolute deviations lead to a high relative error. Excluding the values with Poisson's ratios near to zero, reduces the maximum error to less than 0.6%. The error in the l^2 matrix norm is very low with maximum values of just above 0.007%. Altogether, the results show very good prediction capabilities of the interpolation scheme for the chosen number of data points.

4.3. Optimization

The optimization framework was tested on simple rectangular 2D models of the tri-anti-chiral structures. The objective of the optimization was to obtain a defined lateral deformation at the lateral edges of the model at a load of ε_{Gy}=1%. To specify a reasonable and achievable target deformation, a reverse-engineering approach was used. Simulations of homogenized models of structures 3–5 (according to Fig. 6), were set up (as described in Section 3.3.2) prior to the optimization. The lateral deformation of these simulations served as optimization targets and the fully modeled structures were used for validation. The UC parameters L_{x1} and L_{x2} of each homogenized material section in the FE models were employed as design variables for the optimization. For all tests the start values for L_{x1} and L_{x2} were set to 11 mm and the limits for

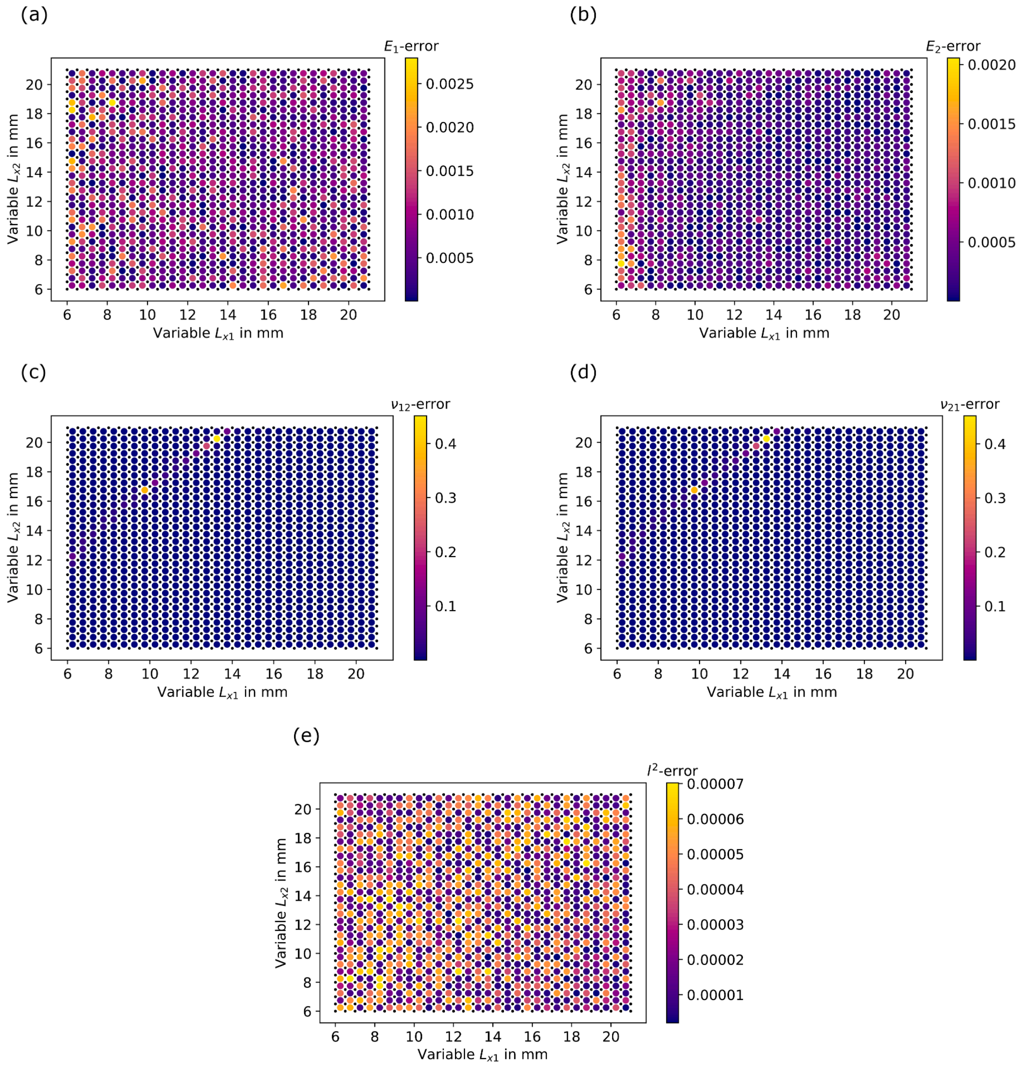

Fig. 18. Relative error of the interpolation for variable values between the interpolation grid for (a) Young's modulus in X direction $\boldsymbol{E}_1$, (b) Young's modulus in Y direction $\boldsymbol{E}_2$, (c) Poisson's ratio ν_{12}, (d) Poisson's ratio ν_{21} and (e) $\boldsymbol{l}^2$ norm.

both variables were set to 6 mm and 21 mm for the minimum and maximum values respectively. In all tests, all material sections were given the same start values, independently from the complexity of the optimization goals.

Structure 3 and structure 4 were applied for the first tests. The reproduction of the lateral deformation in X direction along the right side of the structures was set as the optimization target. Fig. 19(a) and Fig. 20(a) show the respective deformations. To ensure a high enough resolution along the direction of changing material properties, six material sections along the Y direction were used during the optimization and the distribution is shown in Fig. 19(b) and Fig. 20(b). As a result of the two UC parameters for each of the six material sections, the optimization was performed with 12 design variables. For the model with structure 3 as the input, Fig. 21 shows the optimization history with convergence after 11 iterations. For the model with structure 4 as the input, Fig. 22 depicts the progress of the optimization with convergence after 9 iterations. The distinct distributions of the two and three regions with different unit cells is reproduced accurately, as can be seen in Fig. 19(c) and Fig. 20(c), which show the Poisson's ratio $\nu_{21}$for the individual material sections of the optimized structures. With a minimum error ε in the curve matching of 1.64 10^{-5} and 2.73 10^{-5}, respectively, the homogenized lateral deformation of structure 3 and 4 is reproduced very well. Comparison to the fully modeled structure show very good agreement at the area with negative lateral deformation (positive Poisson's ratio) and small deviations at the area with positive lateral deformation (negative Poisson's ratio) for both structures. Fig. 19(d) and Fig. 20(d) display the corresponding comparison between lateral deformation of optimized model, homogenized target model and fully modeled validation structure. The deviations can be attributed to higher local strain in the area with highly negative Poisson's ratios, caused by the lower Young's modulus E_2 of the corresponding unit cells. The larger strain leads to an increased error in the linear homogenization approach.

The two models show very good convergence and accuracy regarding the optimization goal for the given optimization parameters and thereby show the suitability of the proposed framework for the given optimization task. However, the choice of the number of material

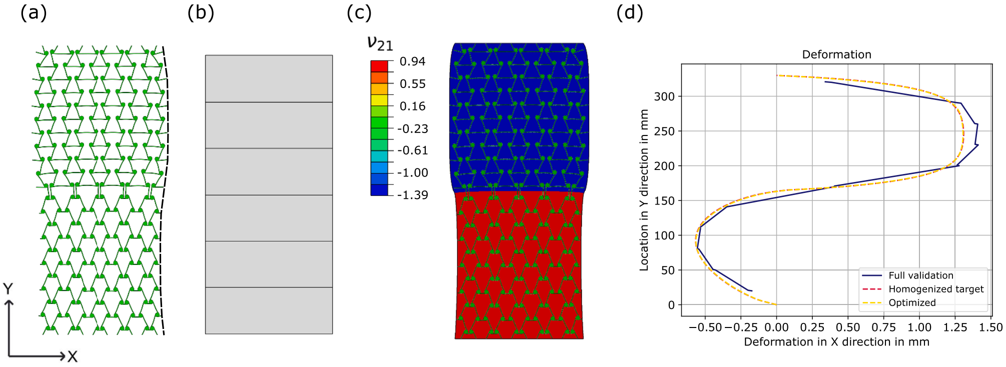

Fig. 19. Optimization results for structure 3. (a) Target deformation (deformation scale factor 5), (b) material section distribution, (c) optimized Poisson's ratio of the individual material sections (deformation scale factor 5), (d) deformation comparison of full structure, homogenized structure and optimized structure.

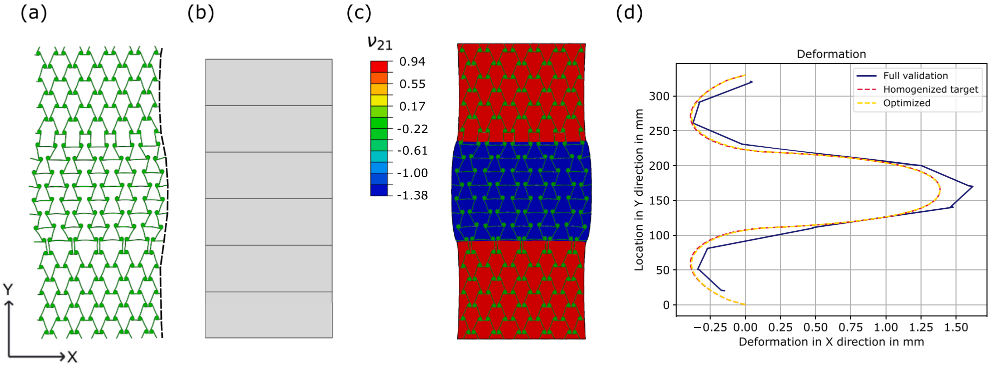

Fig. 20. Optimization results for structure 4. (a) Target deformation (deformation scale factor 5), (b) material section distribution, (c) optimized Poisson's ratio of the individual material sections (deformation scale factor 5), (d) deformation comparison of full structure, homogenized structure and optimized structure.

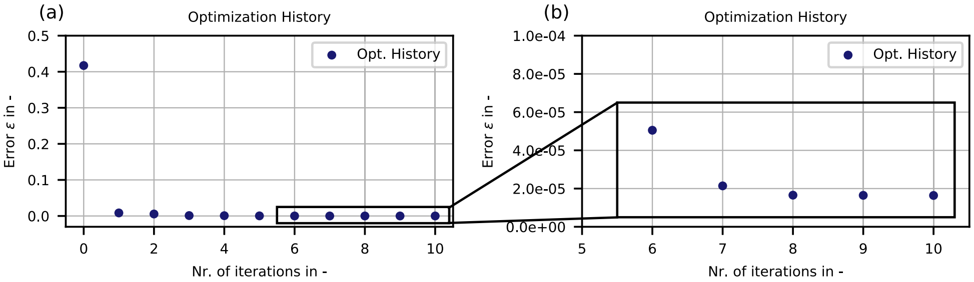

Fig. 21. Optimization history for structure 3. Evolution of the error ε for (a) the entire optimization and (b) for the last few iterations.

sections is very specific to the targeted optimization goal. To test a more general approach regarding the distribution of material sections, the simple optimization based on the deformation of structure 3 (Fig. 23(a)) was set up with two additional material sections along the X direction. Consequently, a total of 18 material sections, as shown in Fig. 23(b), and 36 design variables were created. All other optimization settings were kept the same.

As can be seen in Fig. 24, the addition of material sections in the X direction leads to a decrease in convergence rate and termination does only occur after 23 iterations. The fit of the lateral deformation on the right side is not influenced significantly. A small error ε in the curve matching of 1.55 10^{-5} shows a very good fit of the lateral deformation (Fig. 23(d)). The distribution of UC properties, on the other hand, does not match the target distribution, as shown in Fig. 23(c) for the Poisson's ratio ν_{21}. It can be seen that only the right outer most material sections follow the input distribution to achieve the targeted deformation. The addition of more material sections without addition of any constraints or objectives, enables multiple configurations to achieve the target deformation of the right side resulting in a decreased convergence rate.

To improve the convergence again and restrict the possible optimal configurations, two different strategies were pursued. One approach was to add the deformation on the left side of the input structure as objective

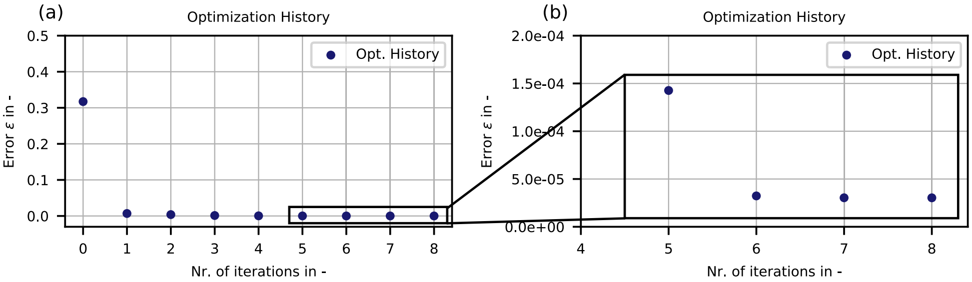

Fig. 22. Optimization history for structure 4. Evolution of the error *ε* for (a) the entire optimization and (b) for the last few iterations.

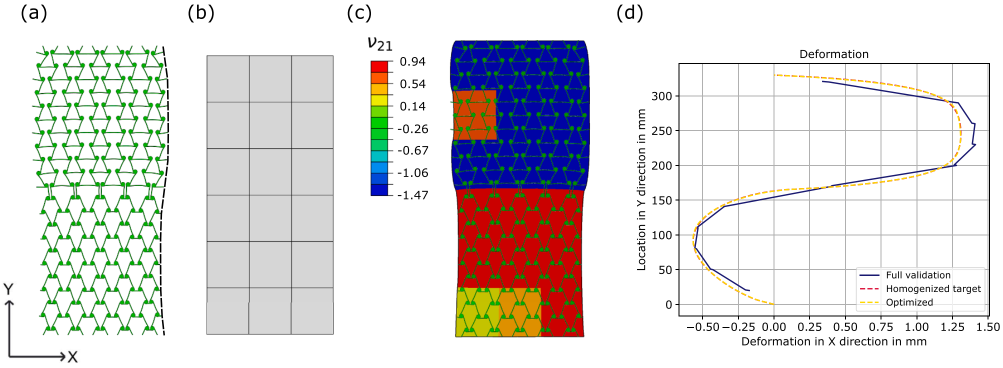

Fig. 23. Optimization results for structure 3 with additional material sections. (a) Target deformation (deformation scale factor 5), (b) material section distribution, (c) optimized Poisson's ratio of the individual material sections (deformation scale factor 5), (d) deformation comparison of full structure, homogenized structure and optimized structure.

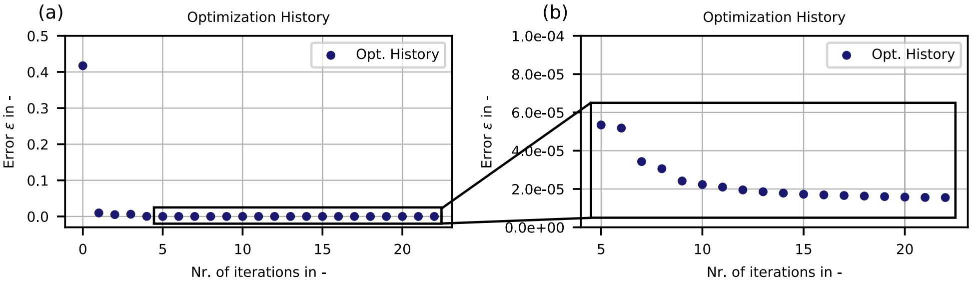

Fig. 24. Optimization history for structure 3 with additional material sections. Evolution of the error *ε* for (a) the entire optimization and (b) for the last few iterations.

by creating a second curve matching composite in LSOPT and adding it as an objective function. Subsequently, LSOPT performs the optimization on a weighted sum of both objective functions. Both weights were kept at 1. Another approach was to add a force constraint by building a mean square error ε_F for the overall reaction force in the Y direction at ε_{Gy}=1% as

$$\varepsilon_F = \left[\frac{F_{model} - F_{target}}{F_{target}}\right]^2 \tag{17}$$

Where by F_{model} describes the reaction force of the models during the simulation and F_{target} is the reaction force of the homogenized target model (in this case the target model of structure 3). The constraint is then implemented such that only models with $\varepsilon_F < 0.01$ are seen as feasible.

Adding the left side deformation improves the convergence and the optimization terminates after 11 iterations (Fig. 25). Including the force constraint improves the convergence only slightly by reducing the number of needed iterations to 21 (Fig. 26). Both approaches are able to achieve less deviations in the distribution of unit cell properties as demonstrated in Fig. 27 for the Poisson's ratio ν_{21} and the Young's modulus E_2. The more inhomogeneous distribution of the E_2 values is caused by the higher sensitivity of E_2 on small changes in the design variables $L_{x1}$and L_{x2} compared to ν_{21}. The error ε is small for both approaches and they reach good agreement regarding the deformation goal. These results highlight the importance of the proper definition of the optimization problem and the appropriate discretization (in terms of material sections) with respect to the optimization goal. Furthermore, it illustrates the flexibility of the proposed framework in terms of optimization objectives and constraints as well as design variable

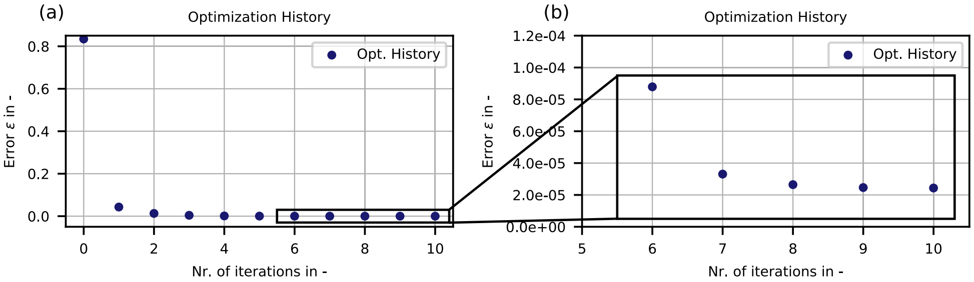

Fig. 25. Optimization history for structure 3 with additional material sections and additional left side deformation as objective. Evolution of the error ε for (a) the entire optimization and (b) for the last few iterations.

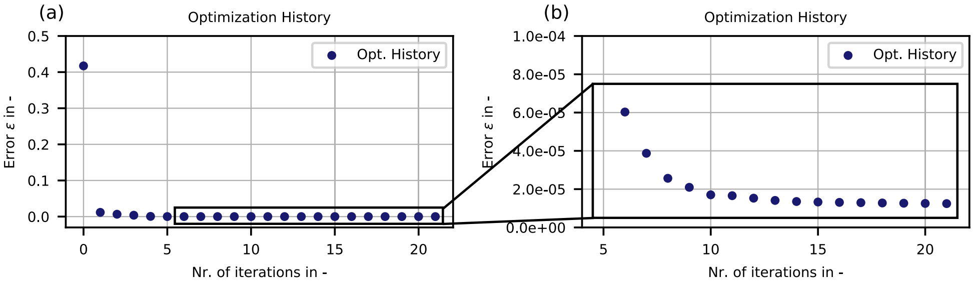

Fig. 26. Optimization history for structure 3 with additional material sections and additional force constraint. Evolution of the error ε for (a) the entire optimization and (b) for the last few iterations.

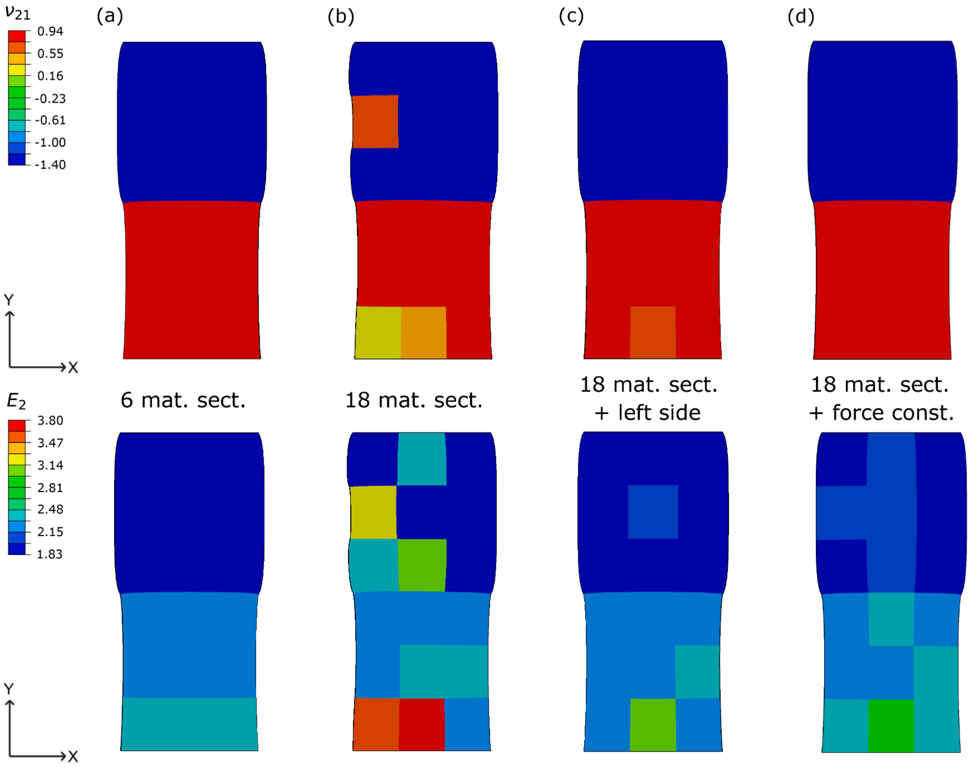

Fig. 27. Optimized Poisson's ratio and Young's modulus of the individual material sections for structure 3 with (a) 6 material sections, (b) 18 material sections, (c) 18 material sections and left side objective and (d) 18 material sections and force constraint.

discretization.

To reproduce the deformation behavior of structure 5 with different unit cells in both X and Y direction, in addition to the deformation on the right side, the deformation on the left side of the structure was added to the optimization objective. Both target deformations are shown in Fig. 28(a). To ensure a sufficiently high resolution of areas with possibly different material properties, a 4 × 4 material section matrix was chosen (Fig. 28(b)). The optimization was thus performed with 32 design variables. The increase in number of design variables and the more complex objective function result in an only slightly slower convergence of the optimization with 14 iterations (Fig. 29). A good reproduction of the four distinct areas with different UCs, shown by the Poisson's ratio ν_{21} of the individual material sections in Fig. 28(c), is achieved. Furthermore, a small error ε in the curve matching is attained for both sides of the structure, with $\varepsilon = 3.70\ 10^{-5}$ for the right and $\varepsilon = 3.61\ 10^{-5}$ for the left, respectively. Again, the validation with the fully modeled target structure shows very good agreement of the deformation curves for the areas with positive Poisson's ratio and some deviations at the areas with negative Poisson's ratio (Fig. 28(d)-(e)).

Conclusion

A Finite Element simulation-based optimization strategy for creating a predefined deformation behavior of metamaterial components by optimizing the underlying unit cell parameter distribution is proposed in this work. The main parts of the framework are a material preprocessing step with a material homogenization and the generation of a linear interpolation object as well as a black-box-based optimization part. 2D tri-anti-chiral unit cells, which allow for a wide range in material properties by changing only two unit cell parameters, are used to test the framework. The application of a linear elastic homogenization approach allows for a breakdown of the complex unit cell geometry to a simple linear elastic material model. In combination with linear interpolation between stiffness tensors of different unit cells, this results in an efficient material description for the optimization approach. Three different predefined lateral deformations of simple 2D rectangular tri-anti-chiral parts are employed as an optimization target to demonstrate the capabilities of the framework. Using the proposed framework to optimize the unit cell parameter distributions of the homogenized parts, the given target deformation can be reproduced with good convergence and accuracy. In addition, the influence of spatial distribution of material sections on the convergence and accuracy is studied. Results indicate a strong dependency of the convergence rate on the spatial distribution. However, introducing additional optimization objectives or constraints improve the convergence again. The proposed framework offers high versatility concerning the selection of optimization objectives and constraints, due to the black-box-based optimization strategy. Therefore, the developed framework is not restricted to the shown use case, but can be applied to a variety of optimization problems for unit cell-based metamaterials. Furthermore, the general homogenization approach provides flexibility regarding the types of unit cell-based materials that can be used. As a consequence, the presented framework offers a flexible tool to design and optimize metamaterial-based parts for not only lightweight purposes but also other deformation-based applications. This could lead to a higher adoption rate of metamaterial-based designs in various industries like aerospace (morphing winglets), construction (vibration and deformation dampening devices) or medical (medical devices with custom deformation behavior), to name just a few examples. However, the proposed framework is only a starting point and further development should be done to improve generality and efficiency. Furthermore, the limitations of the homogenization approach regarding minimal number of unit cells in a material section and possible maximal strain have to be considered when using the framework on a more general problem. The important part of the correct spatial discretization is, for now, guided by the problem-knowledge of the user. Therefore, future work will be focused

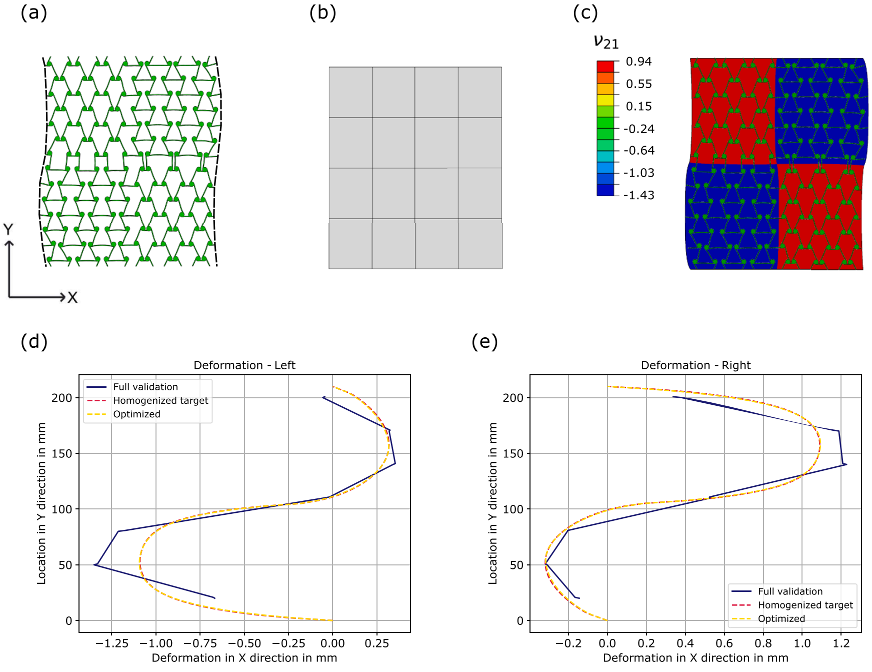

Fig. 28. Optimization results for structure 5. (a) Target deformation (deformation scale factor 5), (b) material section distribution, (c) optimized Poisson's ratio of the individual material sections (deformation scale factor 5), (d) deformation comparison of full structure, homogenized structure and optimized structure - left side, (e) deformation comparison of full structure, homogenized structure and optimized structure- right side.

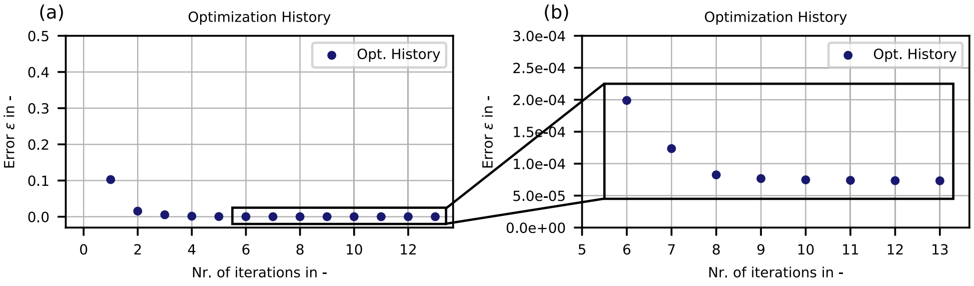

Fig. 29. Optimization history for structure 5. Evolution of the error ε for (a) the entire optimization and (b) for the last few iterations.

on an automated discretization approach to further improve the efficiency of the proposed framework.

CRediT authorship contribution statement

Andreas Thalhamer: Conceptualization, Methodology, Software, Validation, Formal analysis, Investigation, Data curation, Writing – original draft, Writing – review & editing, Visualization. **Mathias Fleisch:** Conceptualization, Methodology, Formal analysis, Investigation, Data curation, Writing – original draft, Writing – review & editing, Visualization. **Clara Schuecker:** Conceptualization, Validation, Supervision, Writing – review & editing. **Peter Filipp Fuchs:** Resources, Supervision, Writing – review & editing, Funding acquisition. **Sandra Schlögl:** Supervision, Writing – review & editing, Project administration, Funding acquisition. **Michael Berer:** Conceptualization, Validation, Data curation, Resources, Supervision, Writing – review & editing, Project administration, Funding acquisition.

Declaration of Competing Interest

The authors declare that they have no known competing financial interests or personal relationships that could have appeared to influence the work reported in this paper.

Data availability

Data will be made available on request.

Acknowledgment

The research work of this study was performed in the COMET-Module project “CHEMITECTURE“ (project-no.: 21647048) at the Polymer Competence Center Leoben GmbH (PCCL, Austria) within the framework of the COMET-program of the Federal Ministry for Climate Action, Environment, Energy, Mobility, Innovation and Technology and the Federal Ministry for Digital and Economic Affairs with contributions by the Department of Polymer Engineering and Science / Montanuniversitaet Leoben. The PCCL is funded by the Austrian Government and the State Governments of Styria, Lower Austria and Upper Austria.

References

[1] Barchiesi E, Spagnuolo M, Placidi L. Mechanical metamaterials: a state of the art. Math Mech Solids 2019;24:212–34. https://doi.org/10.1177/1081286517735695.
[2] Christensen J, Kadic M, Kraft O, Wegener M. Vibrant times for mechanical metamaterials. MRC 2015;5:453–62. https://doi.org/10.1557/mrc.2015.51.
[3] Surjadi JU, Gao L, Du H, Li X, Xiong X, Fang NX, Lu Y. Mechanical metamaterials and their engineering applications. Adv Eng Mater 2019;21:1800864. https://doi.org/10.1002/adem.201800864.
[4] Kolken HMA, Zadpoor AA. Auxetic mechanical metamaterials. RSC Adv 2017;7:5111–29. https://doi.org/10.1039/C6RA27333E.
[5] Fleisch M, Thalhamer A, Meier G, Fuchs PF, Pinter G, Schlögl S, Berer M. Asymmetric chiral and antichiral mechanical metamaterials with tunable Poisson’s ratio. APL Mater 2022;10:61105. https://doi.org/10.1063/5.0091756.
[6] Taghavi M, Helps T, Huang B, Rossiter J. 3D-printed ready-to-use variable-stiffness structures. IEEE Robot Autom Lett 2018;3:2402–7. https://doi.org/10.1109/LRA.2018.2812917.
[7] Fleisch M, Thalhamer A, Meier G, Raguž I, Fuchs PF, Pinter G, Schlögl S, Berer M. Functional mechanical metamaterial with independently tunable stiffness in the three spatial directions. Mater Today Adv 2021;11:100155. https://doi.org/10.1016/j.mtadv.2021.100155.
[8] Zheng X, Lee H, Weisgraber TH, Shusteff M, DeOtte J, Duoss EB, Kuntz JD, Biener MM, Ge Q, Jackson JA, Kucheyev SO, Fang NX, Spadaccini CM. Ultralight, ultrastiff mechanical metamaterials. Science 2014;344:1373–7. https://doi.org/10.1126/science.1252291.
[9] Bauer J, Meza LR, Schaedler TA, Schwaiger R, Zheng X, Valdevit L. Nanolattices: an emerging class of mechanical metamaterials. Adv Mater Weinheim 2017:29. https://doi.org/10.1002/adma.201701850.
[10] Choi JB, Lakes RS. Fracture toughness of re-entrant foam materials with a negative Poisson’s ratio: experiment and analysis. Int J Fract 1996;80:73–83. https://doi.org/10.1007/BF00036481.
[11] Donoghue JP, Alderson KL, Evans KE. The fracture toughness of composite laminates with a negative Poisson’s ratio. Phys Status Solidi B 2009;246:2011–7. https://doi.org/10.1002/pssb.200982031.
[12] Zhang J, Lu G, You Z. Large deformation and energy absorption of additively manufactured auxetic materials and structures: a review. Compos Part B: Eng 2020;201:108340. https://doi.org/10.1016/j.compositesb.2020.108340.
[13] Lu Q, Qi D, Li Y, Xiao D, Wu W. Impact energy absorption performances of ordinary and hierarchical chiral structures. Thin Walled Struct 2019;140:495–505. https://doi.org/10.1016/j.tws.2019.04.008.
[14] Chan N, Evans KE. Indentation resilience of conventional and auxetic foams. J Cell Plast 1998;34:231–60. https://doi.org/10.1177/0021955x9803400304.
[15] Alderson KL, Pickles AP, Neale PJ, Evans KE. Auxetic polyethylene: the effect of a negative poisson’s ratio on hardness. Acta Metall Mater 1994;42:2261–6. https://doi.org/10.1016/0956-7151(94)90304-2.
[16] Lvov VA, Senatov FS, Veveris AA, Skrybykina VA, Díaz Lantada A. Auxetic metamaterials for biomedical devices: current situation, main challenges, and research trends. Materials (Basel) 2022;15. https://doi.org/10.3390/ma15041439.
[17] Bornengo D, Scarpa F, Remillat C. Evaluation of hexagonal chiral structure for morphing airfoil concept. Proc Inst Mech Eng Part G J Aerosp Eng 2005;219:185–92. https://doi.org/10.1243/095441005x30216.
[18] Duncan O, Shepherd T, Moroney C, Foster L, Venkatraman P, Winwood K, Allen T, Alderson A. Review of auxetic materials for sports applications: expanding options in comfort and protection. Appl Sci 2018;8:941. https://doi.org/10.3390/app8060941.
[19] Wang Z, Hu H. Auxetic materials and their potential applications in textiles. Text Res J 2014;84:1600–11. https://doi.org/10.1177/0040517512449051.
[20] Schwerdtfeger J, Wein F, Leugering G, Singer RF, Körner C, Stingl M, Schury F. Design of auxetic structures via mathematical optimization. Adv Mater Weinheim 2011;23:2650–4. https://doi.org/10.1002/adma.201004090.
[21] Behrou R, Ghanem MA, Macnider BC, Verma V, Alvey R, Hong J, Emery AF, Kim HA, Boechler N. Topology optimization of nonlinear periodically microstructured materials for tailored homogenized constitutive properties. Compos Struct 2021;266:113729. https://doi.org/10.1016/j.compstruct.2021.113729.
[22] Chen W, Huang X. Topological design of 3D chiral metamaterials based on couple-stress homogenization. J Mech Phys Solids 2019;131:372–86. https://doi.org/10.1016/j.jmps.2019.07.014.
[23] Zhang H, Luo Y, Kang Z. Bi-material microstructural design of chiral auxetic metamaterials using topology optimization. Compos Struct 2018;195:232–48. https://doi.org/10.1016/j.compstruct.2018.04.058.
[24] Kollmann HT, Abueidda DW, Koric S, Guleryuz E, Sobh NA. Deep learning for topology optimization of 2D metamaterials. Mater Des 2020;196:109098. https://doi.org/10.1016/j.matdes.2020.109098.
[25] Challapalli A, Patel D, Li G. Inverse machine learning framework for optimizing lightweight metamaterials. Mater Des 2021;208:109937. https://doi.org/10.1016/j.matdes.2021.109937.

[26] Liao Z, Wang Y, Gao L, Wang Z-P. Deep-learning-based isogeometric inverse design for tetra-chiral auxetics. Compos Struct 2022;280:114808. https://doi.org/10.1016/j.compstruct.2021.114808.

[27] Panesar A, Abdi M, Hickman D, Ashcroft I. Strategies for functionally graded lattice structures derived using topology optimisation for Additive Manufacturing. Addit Manuf 2018;19:81–94. https://doi.org/10.1016/j.addma.2017.11.008.

[28] Zhang Y, Xiao M, Li H, Gao L, Chu S. Multiscale concurrent topology optimization for cellular structures with multiple microstructures based on ordered SIMP interpolation. Comput Mater Sci 2018;155:74–91. https://doi.org/10.1016/j.commatsci.2018.08.030.

[29] Han Y, Lu W. Evolutionary design of nonuniform cellular structures with optimized Poisson's ratio distribution. Mater Des 2018;141:384–94. https://doi.org/10.1016/j.matdes.2017.12.047.

[30] Liang X, Shan J, Zhou X, Li S, Yu W, Liu Z, Wen Y, Liang B, Li H. Active design of chiral cell structures that undergo complex deformation under uniaxial loads. Mater Des 2022;217:110649. https://doi.org/10.1016/j.matdes.2022.110649.

[31] Yao J, Su Y, Scarpa F, Li Y. An optimization approach to design deformation patterns in perforated mechanical metamaterials using distributions of Poisson's ratio-based unit cells. Compos Struct 2022;281:115015. https://doi.org/10.1016/j.compstruct.2021.115015.

[32] Geers MGD, Kouznetsova VG, Brekelmans WAM. Multi-scale computational homogenization: trends and challenges. J Comput Appl Math 2010;234:2175–82. https://doi.org/10.1016/j.cam.2009.08.077.

[33] Fleisch M, Thalhamer A, Meier G, Huber PAF, Fuchs PF, Pinter G, Schlögl S, Berer M. Chiral-based mechanical metamaterial with tunable normal-strain shear coupling effect. Eng Struct 2023;284:115952. https://doi.org/10.1016/j.engstruct.2023.115952.

[34] 3D experience, micromechanics plugin: for Abaqus/CAE, Version 1.15, 2017.

[35] Omairey SL, Dunning PD, Sriramula S. Development of an ABAQUS plugin tool for periodic RVE homogenisation. Eng Comput 2019;35:567–77. https://doi.org/10.1007/s00366-018-0616-4.

[36] Tchalla A, Belouettar S, Makradi A, Zahrouni H. An ABAQUS toolbox for multiscale finite element computation. Compos Part B: Eng 2013;52:323–33. https://doi.org/10.1016/j.compositesb.2013.04.028.

[37] Krauß C, Kärger L. Tensor interpolation in virtual manufacturing chains for fiber reinforced composites. Int J Mech Sci 2022;226:107378. https://doi.org/10.1016/j.ijmecsci.2022.107378.

[38] Kindlmann G, Estépar RSJ, Niethammer M, Haker S, Westin C-F. Geodesic-loxodromes for diffusion tensor interpolation and difference measurement. Med Image Comput Comput Assist Interv 2007;10:1–9. https://doi.org/10.1007/978-3-540-75757-3_1.

[39] Kratz A, Auer C, Stommel M, Hotz I. Visualization and analysis of second-order tensors: moving beyond the symmetric positive-definite case. Comput Graphics Forum 2013;32:49–74. https://doi.org/10.1111/j.1467-8659.2012.03231.x.

[40] Virtanen P, Gommers R, Oliphant TE, Haberland M, Reddy T, Cournapeau D, Burovski E, Peterson P, Weckesser W, Bright J, van der Walt SJ, Brett M, Wilson J, Millman KJ, Mayorov N, Nelson ARJ, Jones E, Kern R, Larson E, Carey CJ, Polat İ, Feng Y, Moore EW, VanderPlas J, Laxalde D, Perktold J, Cimrman R, Henriksen I, Quintero EA, Harris CR, Archibald AM, Ribeiro AH, Pedregosa F, van Mulbregt P. SciPy 1.0: fundamental algorithms for scientific computing in Python. Nat Methods 2020;17:261–72. https://doi.org/10.1038/s41592-019-0686-2.

[41] Shan S, Wang GG. Survey of modeling and optimization strategies to solve high-dimensional design problems with computationally-expensive black-box functions. Struct Multidisc Optim 2010;41:219–41. https://doi.org/10.1007/s00158-009-0420-2.

[42] Amaran S, Sahinidis NV, Sharda B, Bury SJ. Simulation optimization: a review of algorithms and applications. Ann Oper Res 2016;240:351–80. https://doi.org/10.1007/s10479-015-2019-x.

[43] Carson Y, Maria A. Simulation optimization: methods and applications. In: Proceedings of the 1997 Winter Simulation Conference; 1997. p. 118–26.

[44] Vannucci P. Anisotropic elasticity. Singapore: Springer Singapore; 2018.

[45] N. Stander, A. Basudhar, W. Roux, K. Witowski, T. Eggelston, T. Goel, K. Craig, LS-OPT user's manual: a design optimization and probabilistic analysis tool for the engineering analyst, 2019.

[46] Lorato A, Innocenti P, Scarpa F, Alderson A, Alderson KL, Zied KM, Ravirala N, Miller W, Smith CW, Evans KE. The transverse elastic properties of chiral honeycombs. Compos Sci Technol 2010;70:1057–63. https://doi.org/10.1016/j.compscitech.2009.07.008.

[47] Wu W, Hu W, Qian G, Liao H, Xu X, Berto F. Mechanical design and multifunctional applications of chiral mechanical metamaterials: a review. Mater Des 2019;180:107950. https://doi.org/10.1016/j.matdes.2019.107950.

[48] Mousanezhad D, Haghpanah B, Ghosh R, Hamouda AM, Nayeb-Hashemi H, Vaziri A. Elastic properties of chiral, anti-chiral, and hierarchical honeycombs: a simple energy-based approach. Theoret Appl Mech Lett 2016;6:81–96. https://doi.org/10.1016/j.taml.2016.02.004.

[49] Pozniak AA, Wojciechowski KW. Poisson's ratio of rectangular anti-chiral structures with size dispersion of circular nodes. Phys Status Solidi B 2014;251:367–74. https://doi.org/10.1002/pssb.201384256.

[50] Alderson A, Alderson KL, Attard D, Evans KE, Gatt R, Grima JN, Miller W, Ravirala N, Smith CW, Zied K. Elastic constants of 3-, 4- and 6-connected chiral and anti-chiral honeycombs subject to uniaxial in-plane loading. Compos Sci Technol 2010;70:1042–8. https://doi.org/10.1016/j.compscitech.2009.07.009.

[51] Hu LL, Luo ZR, Zhang ZY, Lian MK, Huang LS. Mechanical property of re-entrant anti-trichiral honeycombs under large deformation. Compos Part B: Eng 2019;163:107–20. https://doi.org/10.1016/j.compositesb.2018.11.010.

Paper D

An optimization strategy for customizable global elastic deformation of unit cell-based metamaterials with variable material section discretization

Authors: Thalhamer, A.
Fleisch, M.
Schuecker, C.
Fuchs, P.F.
Schlögl, S.
Berer, M.

Submitted
DOI: -

An optimization strategy for customizable global elastic deformation of unit cell-based metamaterials with variable material section discretization

Andreas Thalhamer[a),b)], Mathias Fleisch[a),b)*], Clara Schuecker[b)], Peter Filipp Fuchs[a)], Sandra Schlögl[a)], Michael Berer[a)]

[a)] Polymer Competence Center Leoben GmbH (PCCL), Sauraugasse 1, 8700 Leoben, Austria

[b)] Department of Polymer Engineering and Science, Montanuniversitaet Leoben, Otto Gloeckel-Str. 2, 8700 Leoben, Austria

*Corresponding author: mathias.fleisch@stud.unileoben.ac.at, mathias.fleisch@pccl.at

Abstract

Metamaterials with their distinctive unit cell-based periodic architecture feature a wide range of possible properties with unusual characteristics and a high potential for optimization. Due to their complex interaction between unit cell geometry and material properties, as well as their inherent multi-scale nature, suitable optimization strategies need to be developed for metamaterials. One potential approach is to optimize the distribution of unit cells within a part to achieve a predefined deformation response. However, a significant challenge lies in determining the appropriate number and distribution of areas with varying properties (material sections) to facilitate an efficient optimization. In this study, a variable material section discretization scheme is presented, which is aimed at automatically updating the discretization to enhance the efficiency of metamaterial optimizations. This scheme is implemented as an extension to a previously proposed Finite Element simulation-based optimization framework for unit cell-based metamaterials. The framework includes a numerical homogenization method and interpolation scheme for efficiently correlating unit cell parameters with homogenized material properties, coupled with a black-box optimization method. In the present study, the previously proposed framework was extended to incorporate a scheme for monitoring and adjusting the material section discretization during the optimization process. To assess the effectiveness of the implemented routine, it was tested in conjunction with a genetic algorithm for optimizing the parameter distribution of a 2D tri-anti-chiral metamaterial to match a predefined lateral deformation under load.

Keywords: Finite Element Method, Homogenization, Optimization, Simulation, Genetic Algorithm

1 Introduction

Artificial structured materials based on periodically arrayed unit cells (UCs), also known as metamaterials, are a class of materials with a wide range of possible properties with unusual characteristics. The definition of metamaterials include materials with uncommon electromagnetic, acoustic, seismic, thermal, mass transport and mechanical properties [1]. In mechanical metamaterials the UC-based design can lead to material properties such as a high stiffness to weight ratio [2,3], a variable stiffness in multiple spatial directions [4,5] and auxetic behavior [6,7]. In addition to the vast amount of possible designs with unique material properties [8], the UC-based architecture of metamaterials results in a high degree of customizability. On the one hand, this provides the possibility to change the underlying UC geometry of the material to adapt the overall properties of a part. On the other hand, it allows for the addition of custom property gradients on a part by changing the distribution of UCs with different geometric parameters. However, to fully take advantage of the customizability and the multi-scale nature of metamaterials, new optimization strategies are required.

A common approach for optimization on the UC level, specifically for the optimization of the UC geometry to reach defined material properties, is the use of topology optimization in combination with a numerical homogenization approach [9–13]. Various topology optimization approaches have been proposed in UC optimization. Commonly used ones include the well-known solid isotropic material with penalization method [9,10] and the bi-directional evolutionary structural optimization method [14]. In recent years, machine learning approaches such as generative adversarial networks [15] and convolutional neural networks [16,17] have been proposed to improve the efficiency of the existing methods. To take full advantage of the multi-scale design of metamaterial parts, multiple approaches for simultaneous optimization at UC level and at macro scale level have been developed [14,18,19].

The commonly used topology optimization approaches, however, are limited regarding more complex optimization targets such as a predefined deformation behavior under load. Black-box-based parameter optimization strategies offer a more general alternative. Heuristic methods, including Genetic Algorithms (GA) and Evolutionary Strategies (ES), are a common class of algorithms for solving of simulation-based black-box optimization problems [20]. GA and ES are algorithms based on the concepts of natural evolution and usually include selection, crossover, and mutation steps. Regarding the predefined deformation behavior of auxetic structures, multiple methods using evolutionary algorithms have been proposed. Yao et al. [21] used a differential evolution algorithm to optimize the distribution of five different UCs with varying Poisson’s ratio inside a test specimen. In another study, Han and Lu [22] used an evolutionary algorithm to optimize the Poisson’s ratio distribution of reentrant honeycomb structures to create a given deformation under tension. Recently, Liang et al. [23] combined a genetic algorithm with a quantitative correlation between the parameters of chiral cells and their deformation vector to design structures with predefined deformations.

Most methods previously developed for the optimization of deformation behavior of metamaterials use homogenized representations of the metamaterial UCs with a fixed number of uniformly sized material sections with changeable parameters. This spatial material section discretization (MSD) plays an important role in achieving a defined deformation target for a given part. When using a fixed MSD, the knowledge of the necessary resolution of the MSD has to be acquired in advance. This can lead to time-consuming trial and error approaches as well as increased computational effort or decreased accuracy if the wrong MSD is chosen. Another point that has received little consideration is the inclusion of additional constraints into metamaterial optimization methods for creating predefined deformations of a given part. Therefore, the presented work focuses on an MSD updating scheme for the automated local refinement of the MSD based on a given variable field. The developed method relies on the implementation of soft constraints, which are used to control the refinement. In this study, the gradients of the geometric UC variables of a metamaterial part are used as an example for a possible variable field for controlling the MSD refinement. The scheme is implemented into an adapted version of a general metamaterial optimization framework developed in a previous study [24]. The framework uses a homogenization-based pre-processing step to create the correlation between geometric UC parameters and the entire elastic stiffness tensor of a given metamaterial in combination with a black-box optimization strategy. In this study, the framework is extended to include a scheme for monitoring and changing the resolution of the MSD during the optimization based on the gradients of the UC variables. The implemented scheme is tested on the optimization of the UC parameter distribution of a 2D tri-anti-chiral metamaterial [24] with the goal to match a predefined lateral deformation under load. In addition, comparisons between optimizations with and without the MSD updating scheme are used to evaluate the improvement in efficiency and accuracy of the proposed method.

2 Optimization strategy

2.1 Overview of the general strategy

The general structure of the presented method is based on the optimization framework previously proposed in [24]. Therefore, only a summary is presented here, and readers are directed to the original work for a comprehensive description. The framework was developed to optimize the UC distribution of metamaterials to create a specific deformation behavior under load. It is separated into two main parts, a material pre-processing part and an optimization part.

In the material pre-processing step, the correlation between the design of the UC with its various geometric parameters and the homogenized material properties is established. Linear interpolation between the entries of the stiffness tensors of UCs with different geometric parameters is used to create the correlation. Numerical homogenization based on six displacement-controlled simulations with unit load cases and periodic boundary conditions is employed to calculate the full linear elastic stiffness tensor of the UCs. For the creation of the interpolation object, a large enough dataset of homogenized UCs needs to be provided. Depending on the number of geometric parameters of the given UC and the targeted accuracy, this process can entail significant computational costs. However, the interpolation object has to be created only once for a given metamaterial and in turn allows for a very efficient correlation between UC parameter and material property during the optimization.

The optimization part itself is based on the black-box principle. For this study, Finite Element (FE) simulations of simple 2D shapes with a displacement controlled tensile load act as the black-box. The inputs to the black-box and thereby the optimization variables are the geometric UC parameters of the given metamaterial. The output of the black-box in this case is the difference between the simulated deformation and the target deformation of the given structure. The FE models inside the optimization are homogenized representations of the actual metamaterial. They are partitioned into a number of material sections representing the sections with different UC parameters. This approach permits to cluster UCs with the same geometric parameters and thereby decreases the number of optimization variables for the optimization. During optimization, the deformation data of the homogenized simulation is compared to the deformation target and the error is used as the decision variable. The selected optimization algorithm iterates and changes the optimization variables until a stopping criterion is met. The result of the optimization is the UC distribution of a structure, which achieves the deformation with the smallest deviation to the target deformation.

In the original framework, the commercial optimization tool LSOPT (LS-OPT 6.0.0/Livermore Software Technology Corporation, Livermore, CA, USA) had been used and the number of material sections was kept constant during the optimization. In this study, a scheme was incorporated into the framework to facilitate the adaptation of the material section discretization during optimization, allowing for adjustments in the number of material sections. Furthermore, the commercial optimization tool was replaced by a genetic algorithm implemented in Python to facilitate the interface between the optimization and the MSD update scheme. In this updated framework, the optimization starts with an initial MSD and after a specified number of iterations, the MSD is locally refined based on the gradient of the current variables in each material section. The optimization is then continued with the updated MSD. The optimization is stopped when either the stopping criteria from the genetic algorithm or the stopping criteria from the MSD updating scheme are satisfied. The essential setup of the extended optimization framework is shown in Figure 1.

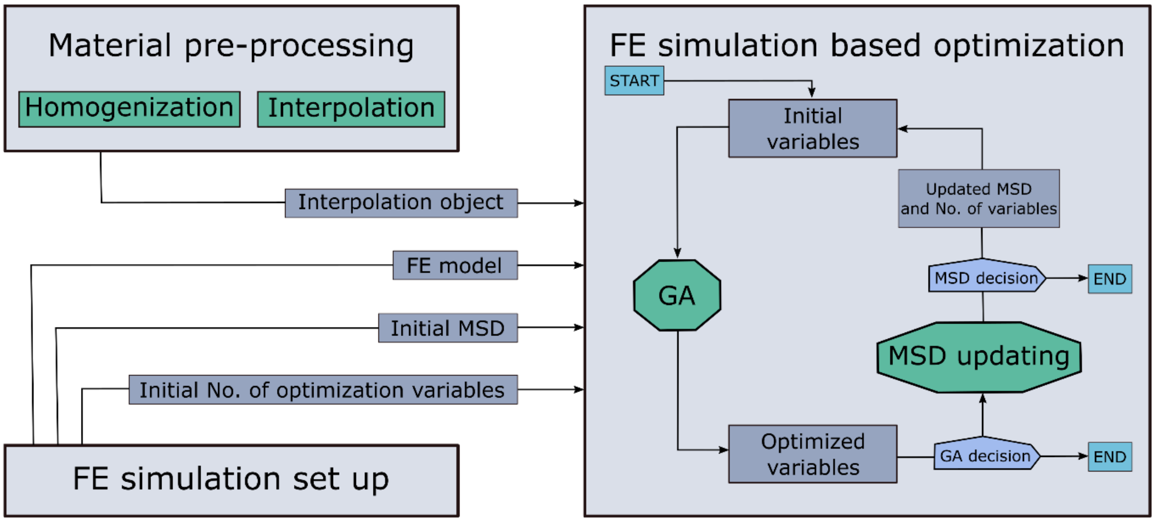

Figure 1: Overview of the general setup and the individual parts of the developed framework (GA: genetic algorithm, MSD: material section discretization).

2.2 Description of the material section discretization (MSD) updating concept

The concept is based on the integration of an MSD evaluation and update algorithm into a genetic optimization algorithm. During the optimization, the MSD algorithm links the resolution of the MSD to a variable field of the metamaterial part. Because the MSD algorithm is not connected directly to the objective of the optimization, the influence of the MSD on the accuracy and efficiency of the optimization depends strongly on the selected variable field. In the case of this study, the gradient of the geometric UC parameters was chosen as the underlying field for the MSD algorithm. This geometric parameter gradient is used since a reduction is expected to decrease the gradients in material properties between the UCs. Additionally, high parameter gradients may pose a problem for processability. However, in this study, the parameter gradient only serves to demonstrate the implementation of the developed framework and no detailed survey on its influence on the material property gradient, stress concentration, or processability has been performed. Due to the use of the geometric UC parameters as optimization variables in this study, the parameter gradient corresponds to the optimization variable gradient.

Herein, the aim of the MSD updating concept is to reduce the variable gradient as well as to enhance the optimization efficiency of the GA by refining the MSD only in areas where variable gradients exceed a specified limit. This limit is a soft constraint on the variable gradient as it only reduces the gradient by refining the MSD but does not directly interfere with the optimization algorithm. The general sequence of the GA-based optimization with the integrated MSD updating scheme is as follows:

(1) The data matrices of the MSD algorithm are initialized based on the user input for the minimum and maximum MSD size and the spatial discretization of the given part.
(2) The variables of the initial MSD are exported to the GA algorithm where they serve as an initial population. For the first run of the GA algorithm, the variables of the initial population are randomly generated inside the parameter space of the given UC.
(3) The GA is started and for each generation the parent selection, crossover, mutation, and fitness evaluation steps are performed.

(4) The optimized variables are exported back to the MSD algorithm after a defined number of generations.
(5) The MSD algorithm updates the variables with the optimized ones and calculates the gradients of the variables in each material section.
(6) Based on the calculated gradients and given decision criteria, the MSD is updated.
(7) The variables of the new MSD are exported again to the GA where they are used as initial population.
(8) The entire process is stopped when either the stopping criterion of the MSD algorithm or one of the stopping criteria of the GA is satisfied.

Figure 2 shows the general sequence of the MSD updating concept. A more detailed description of the GA and MSD part are provided in section 2.2.1 and section 2.2.2, respectively.

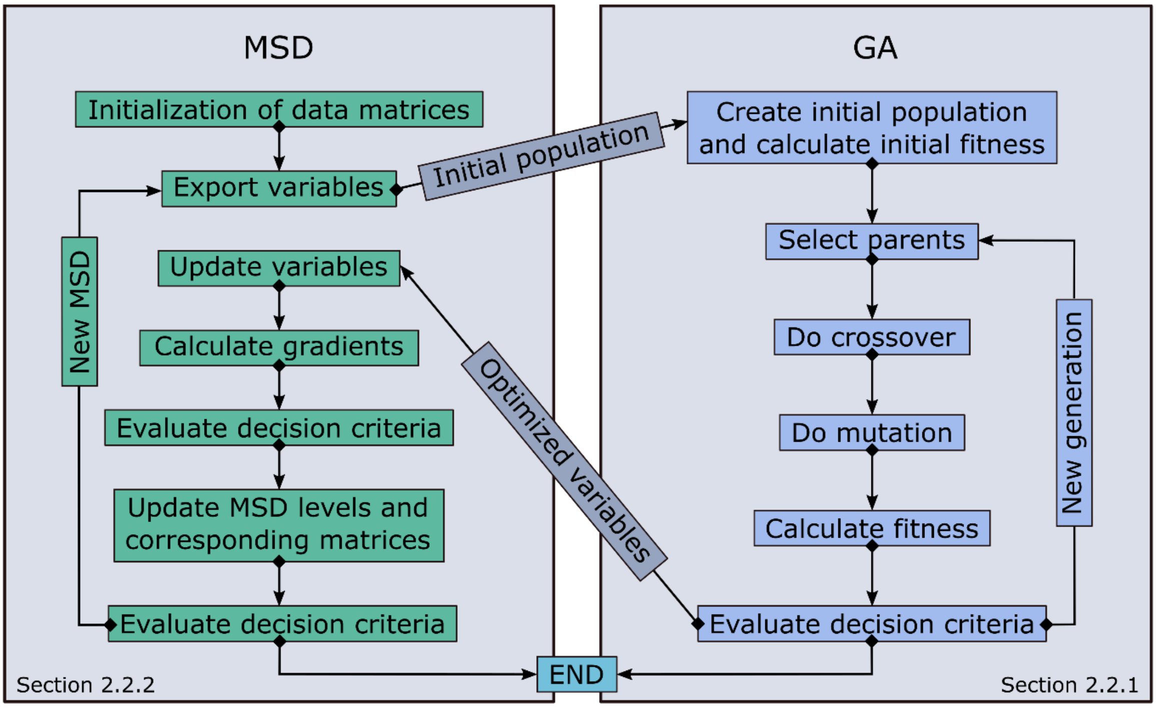

Figure 2: Illustration of the workflow involving the material section discretization (MSD) algorithm and the genetic algorithm (GA), as well as the coupling between them.

2.2.1 GA setup

To optimize the distribution of the geometric UC variables on a part, aiming to replicate a predetermined lateral deformation, the GA performs crossover and mutation operations on a population of variables and a fitness-based selection. Each individual in the population is a complete set of all UC variables of a part. Evaluation of the fitness of a given variable set is achieved by a FE simulation of the given part based on these variables. The interpolation object is then used to efficiently create the necessary homogenized material properties for the material model. The simulation is solved using the Calculix FEM solver. Afterwards, the deformation results of the simulation are compared to the deformation target and the reciprocal of the comparison error is used as the fitness measure. All operations are repeated to create a new generation until a stopping criterion is met. The integration of the GA into the framework is carried out in Python using the Pygad [25] package. The methods used for parent selection, crossover, and mutation as well as the used population size, mutation rate and number of mating parents are stated in Table 1. An overview and description of the possible GA settings is shown in Table 2. The methods and values were chosen based on experience and a small optimization pre-study. For the calculation of the comparison error between the FE simulation-based deformation and the target deformation the mean square error ε_{MS} is calculated as

$$\varepsilon_{MS} = \frac{1}{P}\sum_{p=1}^{P} W_p \left[\frac{S_p - T_p}{max|T_p|}\right]^2 , \tag{1}$$

with P being the number of points along the curves, W_p the weight factors, T_p the points on the target curve and S_p being the corresponding points on the computed curve. The fitness of a given variable set during the optimization is then evaluated as

$$fit = \frac{1}{\varepsilon_{MS}}. \tag{2}$$

To stop the GA, several stopping criteria are implemented. There are two main reasons for stopping the GA: one is to facilitate the export of the optimized variables to the MSD algorithm and the other is the completion of the optimization. Stopping for the variable export is performed if the number of the current generation k reaches a specified limit k_{MSDlim} that is if $k \geq k_{MSDlim}$. When a stop is triggered with this criterion, the variable set with the highest fitness is saved and exported to the MSD algorithm. If no change is made during the MSD updating process, the GA is simply restarted with the population of the last generation of the previous run. If the MSD is changed, then the GA is restarted with a new population based on the last generation of the previous run and the additional variables created in the MSD update scheme (see section 2.2.2 for more details). The overall completion of the optimization process occurs if one of the following three stopping criteria is met.

(1) *Fitness saturation*: if the maximum fitness of a generations does not improve over a given period of generations, that is if $max(fit_k) \leq max(fit_{k-1})$ for k_{satlim} times.

(2) *Maximum generation limit*: if the number of the current generation k reaches a specified limit k_{GAlim}, that is if $k \geq k_{GAlim}$.

(3) *Maximum fitness limit*: if the maximum fitness $max(fit_k)$ of the current generation reaches a specified limit fit_{lim}, that is if $max(fit_k) \geq fit_{lim}$.

Table 1: Settings of the genetic algorithm used for testing the MSD framework.

GA setting	**Type/Value**
Parent selection type	Stochastic universal selection
Crossover type	Uniform
Mutation type	Random
Mutation rate	5%
Population size	40
Number of mating parents	20

2.2.2 MSD updating algorithm

To adapt the MSD during the optimization, an algorithm for storing, evaluating, and updating the MSD for 2D problems is added to the GA process. The algorithm is implemented in Python and its data structure is shown in Figure 3. The labels of the data matrices are highlighted with quotation marks in the following section, for better identification. Information about the spatial discretization of the given part is imported from the initial FE simulation input file. For the considered 2D problem, the discretization is based on a rectangular bounding box with dimensions $b\ x\ h$ surrounding a given part and the user input of the size of a single UC with dimension $b_{UC}\ x\ h_{UC}$. The correlating data is arranged in a boolean $m\ x\ n$ sized 'Material distribution' matrix with

$$m = \left\lceil \frac{h}{h_{UC}} \right\rceil \tag{3}$$

and

$$n = \left\lceil \frac{b}{b_{UC}} \right\rceil. \tag{4}$$

The matrix represents the areas with and without material inside the bounding box and is used as a mask for all the other data matrices inside the framework. The capability to locally change the MSD resolution is provided by arranging the data in separate MSD levels. The first level has a theoretical resolution of $m\ x\ n$ different material sections before applying the discretization mask, whereas the actual number depends on the shape of the part inside the bounding box. With each increase in level, the material sections are clustered into $2\ x\ 2$ sections to generate a new grid. Therefore, the second level only has $m/2\ x\ n/2$ theoretical material section and the third $m/4\ x\ n/4$. This leads to a theoretical number of material sections N_L at level L calculated as

$$N_L = \left\lceil \frac{m}{2^{L-1}} \right\rceil\ x\ \left\lceil \frac{n}{2^{L-1}} \right\rceil. \tag{5}$$

The number of levels is defined by the user prior to the optimization. As illustrated in Figure 3, the names of the material sections from each level are stored in a $m\ x\ n\ x\ N_L$ sized 'MSD level-based material names' matrix. The information about the current level of each individual material section during optimization is stored in its own $m\ x\ n$ sized 'Current MSD level' matrix. This matrix is used to keep track of and update the local refinement during optimization. By using the information about the current MSD level and looking up the correlating material name in the 'MSD level-based material names' matrix, a separate $m\ x\ n$ sized 'Current material names' matrix is created. For the number of variables for each UC, N_V, a $m\ x\ n\ x\ N_V$ sized 'Current variables' matrix is used to store the current variable values V_i for each material section. A 'Material dictionary' is then used to allocate the current variables to the correlating material section name and to act as data interface for the GA.

The optimization always starts at the highest defined MSD level, that is with the coarsest discretization. During the optimization, at the start of an MSD updating step, the optimized variables are written first to the 'Material dictionary'. Then the new variable values are used to update the 'Current variables' matrix. Based on the updated variables, the gradients $\frac{\partial V_i}{\partial x}$ and $\frac{\partial V_i}{\partial y}$ of each variable V_i are calculated for each material section and stored in a $m\ x\ n\ x\ N_V$ sized 'Gradients' matrix. The gradients are then used to evaluate if the level, and thereby the discretization, of the individual material sections needs to be changed. In this study, this evaluation consists of the comparison of the highest of the two gradients in x and y direction against a defined limit. For each variable V_i an individual limit can be specified. The information whether any of the variables have exceeded the gradient limit is stored in a $m\ x\ n$ sized boolean 'Decision' matrix. The level of a material section in the ‘Current level’ matrix is then decreased based on the ‘Decision’ matrix, if the level is not already at 1. Afterwards the ‘Current material names’ matrix is updated based on the new levels. The ‘Material dictionary’ is then filled with the new material sections and corresponding variables. For material sections that have not been updated the old variables are kept. For the new material sections, created due to a level change, the old variable values of the material section from one level above are used as initial values. The updated ‘Material dictionary’ is then used to again generate an initial population for the GA to continue with the optimization. After each MSD updating cycle, an *MSD saturation* stopping criterion is evaluated. The optimization is stopped if there is no MSD refinement for MSD_{lim} times. An overview and description of the settings for the MSD algorithm can be found in Table 2.

Table 2: Overview and description of the settings for the genetic algorithm (GA) [25] and material section discretization (MSD) parts of the framework

GA Settings	**Description**
Parent selection type	Algorithm for the parent selection process
Crossover type	Algorithm for the crossover process
Mutation type	Algorithm for the mutation process
Mutation rate	Percentage of the generation to perform mutation on
Population size	Number of individuals in each generation
Number of mating parents	Number of parents selected for crossover
Maximum fitness limit (fit_{lim})	Value for the maximum fitness limit stopping criterion
Maximum generation limit (k_{GAlim})	Value for the maximum generation limit stopping criterion
Fitness saturation (k_{satlim})	Value for the fitness saturation stopping criterion
MSD Settings	**Description**
MSD generation limit (k_{MSDlim})	Number of generations after which the MSD update is performed
MSD saturation limit (MSD_{lim})	Value for the MSD saturation stopping criterion
MSD levels	Number of refinement levels of the MSD algorithm
MSD refinement limit	Limit of the chosen field variable for the refinement decision

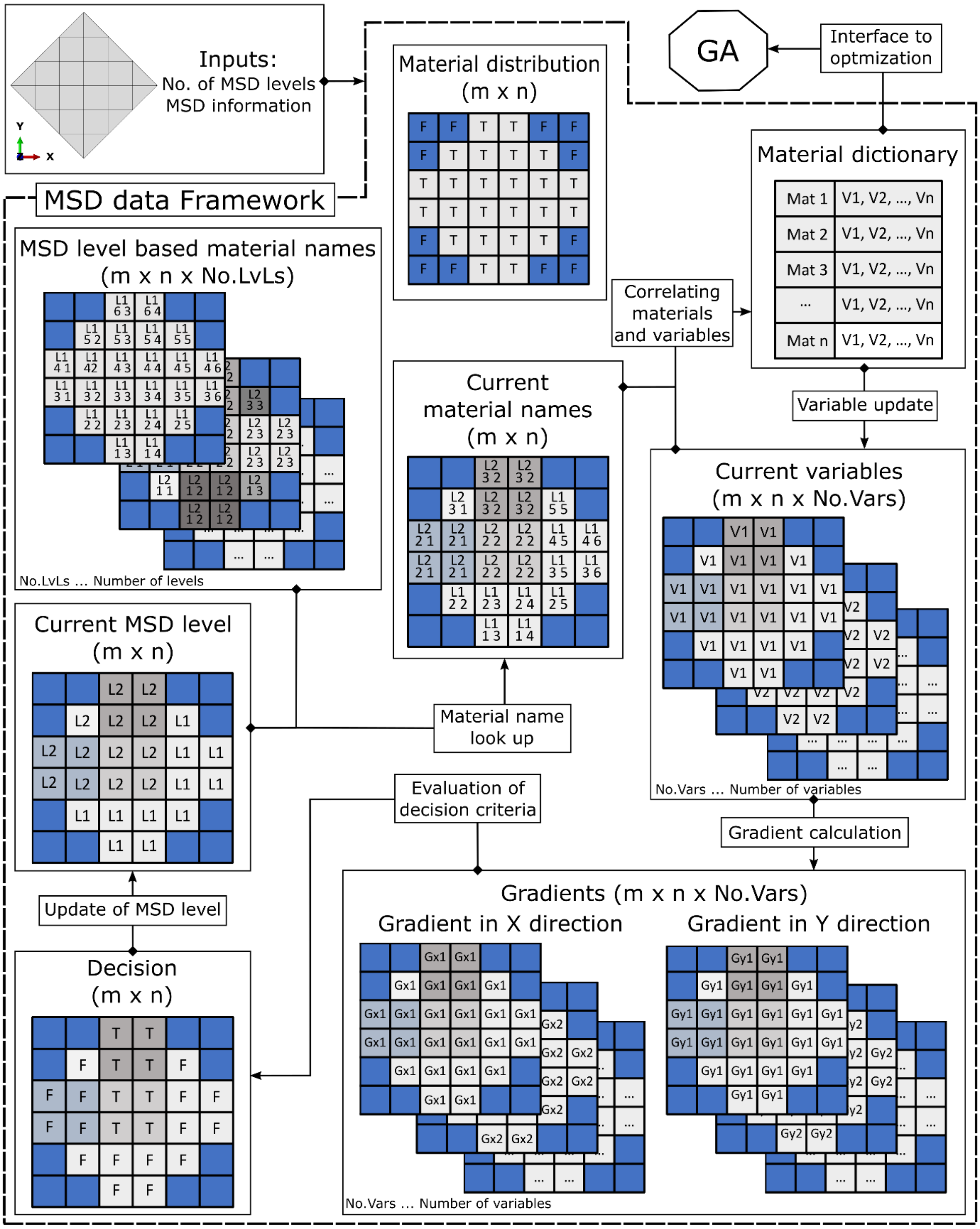

Figure 3: Data structure and processes of the material section discretization (MSD) updating scheme.

3 Simulation setup

3.1 Tri-anti-chiral structure

One way to achieve auxetic behavior and a wide range of potential Poisson's ratios is to use the principle of chiral metamaterials. Chiral metamaterials are based on UCs consisting of rotational centers (circles, rings, squares) connected by a specific number of struts. These connections lead to a rotation of the nodes at the rotational center under mechanical load due to the deformation of the struts resulting in the customizable [26] and often auxetic [27–31] behavior of chiral metamaterials.

The many different kinds of chiral structures can be classified by the number of the connection struts ((3) tri-,(4) tetra-, (6) hexachiral) [29] or by the symmetry inside the UC (chiral, anti-chiral, meta-chiral) [32].

The extended framework presented in this study was tested with the adapted tri-anti-chiral metamaterial described in [24]. It was used with only two changeable geometric UC parameters L_{x1} and L_{x2}, as shown in Figure 4(a). The other geometric parameters of the UC were kept constant. The overall size was specified at 15x15 mm and the diameter of the nodes at the rotational centers was set to 5 mm with a thickness of 0.8 mm for the connecting struts. Despite the reduced number of parameters, this design of the UC allows for a wide range of possible Poisson's ratios and is therefore suitable for the optimization of lateral deformation patterns. With L_{x1} and L_{x2} between 6 mm and 21 mm, the Poisson's ratio ν_{21} ranges from -1.47 to 0.94 and ν_{12} from -0.57 to 0.26 [24] (with ν_{jk} denoting the deformation in k direction under a load in j direction). A detailed description of the UC and the process of creating the interpolation object can be found in the original work [24].

3.2 Setup of models for testing

The models were based on a simple 2D rectangular part with a displacement-controlled extension in the Y direction. The dimensions of the part are 150 mm and 330 mm (width x height). The part was partitioned into multiple material sections for use with the MSD updating algorithm (see section 2.2). Details about the initial number of partitions for each tested sample are provided in section 4. The mesh was created with quadrilateral 4-node plane strain elements with a global seed size of 5 mm. Figure 4(b) shows the meshed part with the path for the evaluation of the lateral deformation. The properties of the individual material sections were based on the homogenized stiffness tensor created by the interpolation object and depend on the geometric parameters of the respective UC. The material was specified as an elastic anisotropic material model. Two different boundary condition setups were considered. For the comparison with LSOPT in section 4.1, the bottom surface was fixed in all directions to recreate the boundary condition of the previous study [24]. Due to the symmetric setup of the examples using the MSD update scheme in section 4.2, the bottom surface was fixed only in Y direction with an additional X symmetry boundary condition in the Y-Z plane. For both setups, the top was displaced uniformly in Y direction to achieve the desired global engineering strain ε_{Gy}, calculated as

$$\varepsilon_{Gy} = \frac{\Delta l_y}{l_{y,0}}, \tag{6}$$

with Δl_y being the displacement of the top surface in Y direction, and $l_{y,0}$ the initial length of the structure in Y direction.

Throughout the optimization process, the models were solved using the static Calculix FE solver, chosen for its improved performance in this particular scenario. [24]. The lateral deformation was evaluated as the displacement in X direction along the right edge of the rectangle. The general setup of the simulation models was performed in the Abaqus 2019 CAE software (Dassault Systemes, Vélizy-Villacoublay Cedex, France). The process of partitioning the part into the different material sections and converting the input file for the Calculix solver was automated with a Python script.

The capabilities of our extended optimization framework were tested with various target deformations of the FE models. Firstly, the performance of the newly implemented routine was assessed against the initial framework to verify that the desired improvement had been achieved. Additionally, the new framework underwent testing with various deformation targets, and the impact of the MSD updating scheme on the optimization results was examined. The tri-anti-chiral structure, described in section 3.1, was used for all the tests. In addition, the previously described interpolation object [24], was used for the correlation between the UC parameters and the material properties. The UC parameters L_{x1} and L_{x2} act as optimization variables and the range for both was set to 6 mm-21 mm for all optimizations. The aim of the optimizations was to achieve a variable distribution that minimizes the comparison error for a specified deformation target. In this study, the target was a predetermined lateral deformation at the right edge of the model subjected to a specified global tensile displacement load in the y-direction. All optimizations were performed on a workstation PC equipped with 2x Intel Xeon Gold 6238R CPUs and 512 GB RAM.

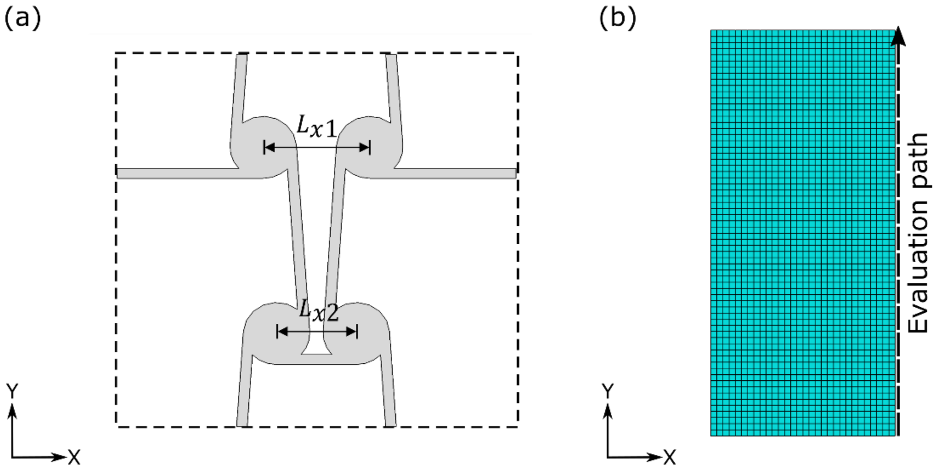

Figure 4: (a) Example of the tri-anti-chiral UC with the two considered geometrical parameters and (b) the meshed 2D part used for the virtual testing with the evaluation path at its right edge.

4 Results and discussion

4.1 Comparison with LSOPT

To evaluate the performance of the newly implemented Python-based genetic algorithm (GA), tests were performed using the new framework, while maintaining a fixed material section discretization (MSD). To this end, two fixed MSDs with 1x6 (Figure 5(a)) and 3x6 (Figure 5(b)) individual sections were generated, respectively. The effect of the MSD updating scheme was then tested by generating 4x16 individual sections with 3 MSD Levels (Figure 5(c)) on the part. The FE models were set up as described in Section 3.2 with a tensile strain of ε_{Gy}=0.2 %. The small strain load was chosen to stay inside the valid range of the homogenization method determined in [24]. Figure 5 shows the deformation target for all examples. The performance was evaluated by comparing it to the initially used framework based on LSOPT [24].

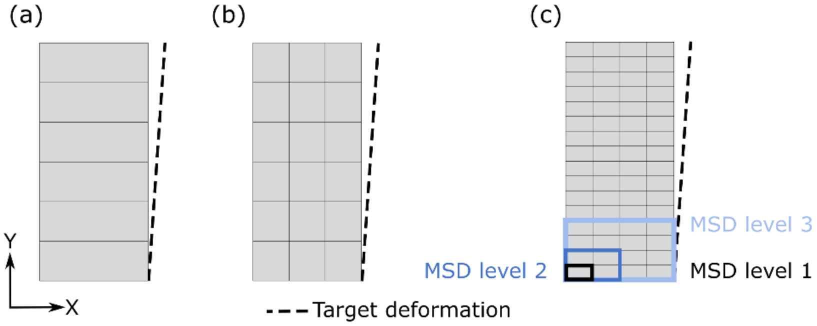

Figure 5: Tri-anti-chiral-based 2D parts with their respective deformation targets under global tension for the comparison to the original framework with (a) 1x6 fixed sections, (b) 3x6 fixed sections and (c) 4x16 sections with 3 MSD levels. The target deformations are exaggerated for better visualization.

Evaluation of the Python-based GA was carried out by setting up optimizations with a *Maximum generation limit* of 1000 generations and with a *Maximum fitness limit* of 0.049 and 15.15 for the models with 1x6 and 3x6 material sections, respectively. These fitness limits are based on the maximum achieved fitness obtained from optimizations of the corresponding structures using the original framework. No *Fitness saturation* criteria were used in this case. During the optimization of the model with 6 sections, the GA reached the fitness limit of the original framework with LSOPT after 127 generations. However, the runtime is significantly higher with the GA needing 2266 s and LSOPT needing 917 s to reach the same fitness. Figure 6(a) shows the comparison of fitness and runtime for the model with 6 sections. As shown in Figure 6(b) there is only a small difference between the deformation of the two frameworks, but both are unable to reproduce the target deformation with the given settings and boundary conditions. For the model with 3x6 sections, the GA was not able to reach the fitness limit and stopped after 1000 generations with a fitness of 9.42. This resulted in a significant increase in runtime compared to LSOPT, as illustrated in Figure 7(a). The deformation depicted in Figure 7(b), on the other hand, shows no significant difference between the two optimizers, both being able to reproduce the given target deformation quite well. Both comparisons of the 6 and 3x6 section models show that the Python-based GA on its own is less efficient, with longer runtimes compared to LSOPT, but the qualitative results of the optimized deformations are very similar.

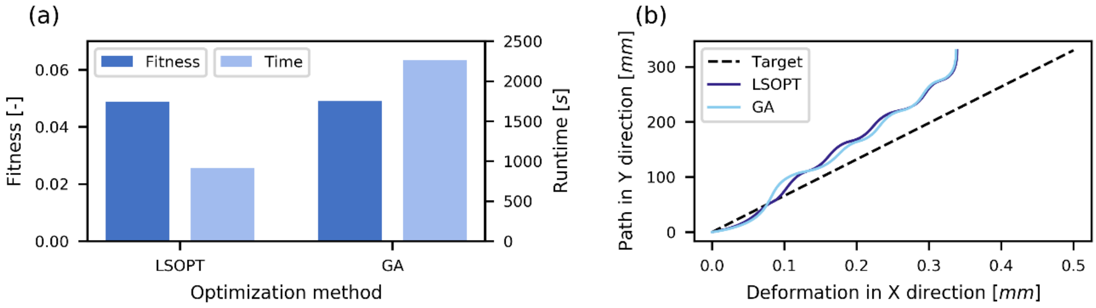

Figure 6: Comparison between the original framework with LSOPT and the new framework with the Python-based GA for the model with 1x6 fixed material sections: (a) fitness and runtime and (b) the lateral deformation.

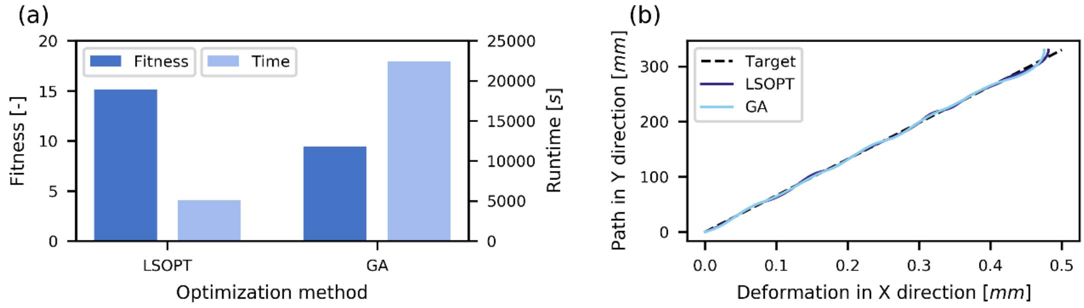

Figure 7: Comparison between the original framework with LSOPT and the new framework with the Python-based GA for the model with 3x6 fixed material sections: (a) fitness and runtime and (b) the lateral deformation.

In order to confirm that the MSD updating scheme yields the intended enhancements in efficiency and convergence behavior, the model comprising 4x16 sections and 3 MSD levels was set up and optimized using the new framework. The *MSD refinement limit* of the variable gradient was set to $1.0\,\frac{mm}{Mat.\ sect.}$ for both variables L_{x1} and L_{x2}. The MSD updating scheme was called after every 75 generations and no *MSD saturation* stopping criterion was considered. Two different versions were considered regarding the GA stopping criteria. One version (MSD-FIT) used a *Maximum generation limit* of 1000 generations and a *Maximum fitness limit* of 15.15, the other version (MSD-GEN) used only a *Maximum generation limit* of 1000 generations. The first version was used to assess the potential for improving runtime, while the second version was utilized to evaluate the possibility of enhancing the fitness value.

The results of both versions were compared to the results of the models with 3x6 fixed sections optimized with the Python-based GA and with LSOPT. Figure 8(a) shows the comparison of the runtime and fitness for all 4 optimizations. With the MSD updating scheme, the time to achieve the same fitness as the original framework was reduced from 5111 s to 1392 s. After completing 1000 generations, the MSD updating scheme had also improved the achievable fitness from 15.15 of the original framework to 19.2. However, the qualitative difference in the optimized deformation, as shown in Figure 8(b), is only minor. It also has to be noted that although the model with the 3x6 fixed sections optimized with the GA and the MSD-GEN variant both performed 1000 generations during optimization, the MSD-GEN runtime was significantly shorter. This effect is attributed to the periodic clearing of the optimization memory after each MSD update during the optimization.

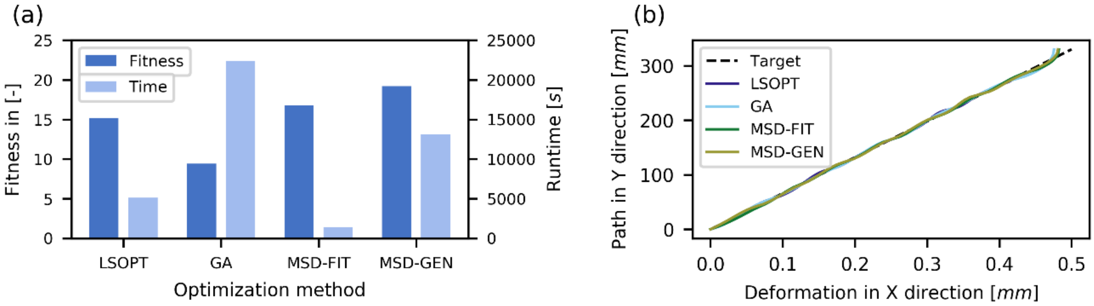

Figure 8: Comparison between the two models with 4x16 material sections, 3 MSD levels and two different stopping criteria as well as the models with 3x6 fixed sections optimized using both, the new framework with the Python-based GA and the original framework with LSOPT: (a) fitness and runtime and (b) the lateral deformation.

Both optimizations using the MSD updating scheme reached their maximum fitness after only one refinement step, which resulted in 16 material sections. The MSD-GEN variant performed further refinement steps based on the variable gradient, but none of them led to an improvement of the fitness, as can be seen in the convergence plot depicted in Figure 9. The plot also shows that the fitness for both variants using the active MSD updating scheme is very low until the first refinement is performed after 75 generations. In contrast, the fitness of the variant with the fixed MSD increases immediately. Because of the difference in the procedure of the optimization algorithm, the convergence of the LSOPT variant is not included in the plot.

The resulting variable and gradient distribution for the variables L_{x1} and L_{x2} for all variants are depicted in Figure 10 and Figure 11, respectively. From all tested variants only MSD-FIT and MSD-GEN show a similar distribution of the variables on the part. The variant using LSOPT has very dissimilar variable distributions, despite reaching nearly the same fitness. This shows the existence of multiple configurations which are able to achieve the deformation target and again highlights the importance of an efficient MSD to decrease the number of possible configurations. Furthermore, in addition to the enhanced performance of the optimization, the MSD updating scheme reduced the maximum spatial gradient of the variables compared to the original framework. In summary, for the selected example, employing the MSD updating scheme results in a reduced time to achieve the same fitness as the original framework. Additionally, it leads to higher fitness if run for the full 1000 generations.

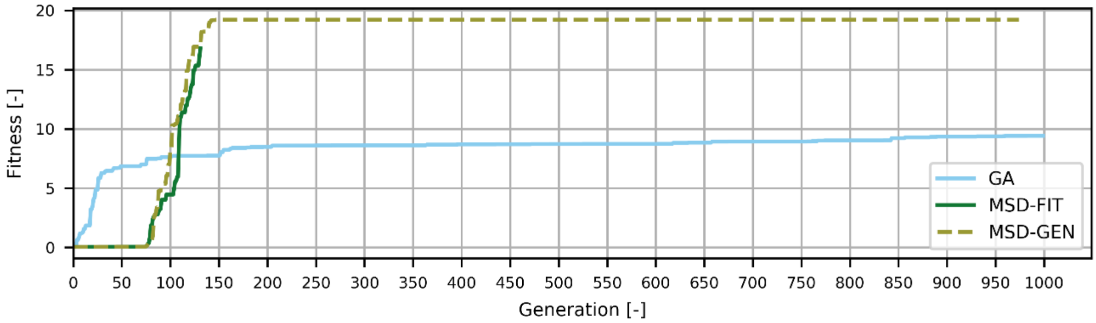

Figure 9: Convergence plot for the new framework - comparison between the fixed MSD (GA), the MSD-FIT and the MSD-GEN setups, which were used in the comparison to the original framework.

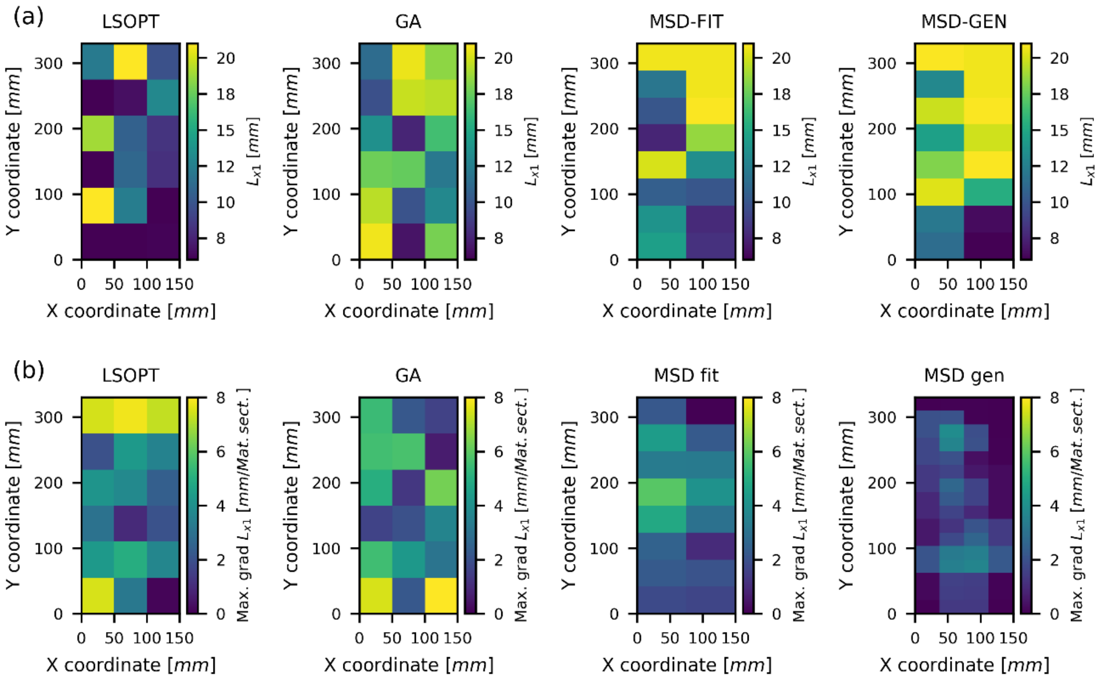

Figure 10: Comparison between the two models with 4x16 material sections, 3 MSD levels and two different stopping criteria as well as the models with 3x6 fixed sections optimized using both, the new framework with the Python-based GA and the original framework with LSOPT: (a) the variable L_{x1} and (b) maximum gradient of L_{x1}.

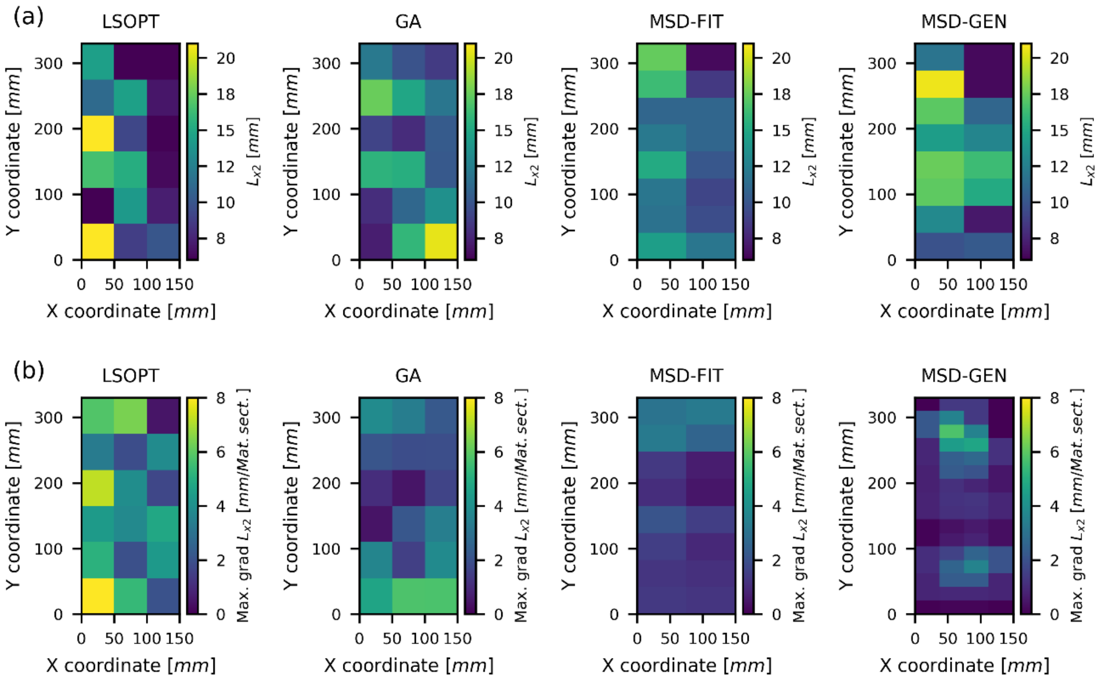

Figure 11: Comparison between the two models with 4x16 material sections, 3 MSD levels and two different stopping criteria as well as the models with 3x6 fixed sections optimized using both, the new framework with the Python-based GA and the original framework with LSOPT: (a) the variable L_{x2} and (b) maximum gradient of L_{x2}.

4.2 MSD optimization tests

To further study the capabilities of the MSD updating scheme, three different models were set up as described in Section 3.2, using a tensile strain of ε_{Gy}=1.0 % and various deformation targets. The tensile strain was increased to facilitate the representation of more complex deformation targets. For each model, 1x32 individual sections with 3 MSD levels were created. This time the parts were only discretized in Y direction to decrease the complexity and to improve the visual comprehensibility of the results. The deformation targets and the different discretization levels for the three different models are illustrated in Figure 12. For each deformation target, three variants with different optimization settings were performed. To create a baseline for the performance of the Python-based genetic algorithm (GA) without the MSD updating scheme, one variant (GA) was set up with a fixed MSD of 1x8 sections. To evaluate the performance of the MSD updating scheme in comparison to the baseline, two variants with active MSD updating and various stopping criteria were set up. One version (MSD-FIT) used a *Maximum generation limit* of 1000 generations and a *Maximum fitness limit* corresponding to the result of the baseline variant, the other version (MSD-GEN) used only a *Maximum generation limit* of 1000 generations. Similar to Section 4.1, the first version was employed to assess the potential for runtime improvement, while the second version was used to evaluate the possibility of enhancing the fitness value. For the MSD refinement, the limit in the variable gradient was set to 1.0 $\frac{mm}{UC}$ for both variables, L_{x1} and L_{x2}. The MSD updating scheme was called after every 75 generations and no *MSD saturation* stopping criterion was considered.

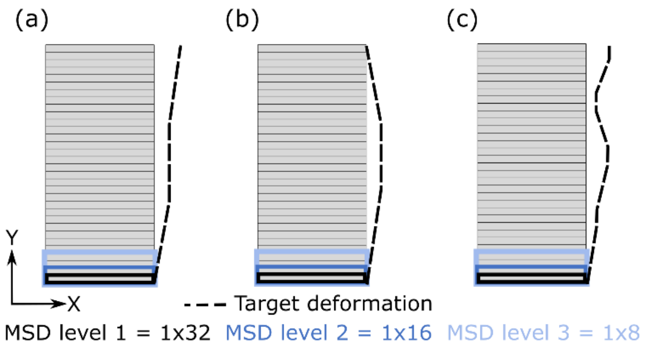

Figure 12: Tri-anti-chiral-based 2D parts with their respective deformation targets under global tension and with the 3 MSD levels used to achieve (a) a single-step, (b) a trapezoidal and (c) a complex target deformation. The deformation targets are exaggerated for better visualization.

4.2.1 Single-step target deformation

The single-step target deformation shown in Figure 12(a) consists of two positive slopes and a constant plateau of lateral deformation. Figure 13 shows the fitness, the time to reach maximum fitness, and the deformation behavior for all three variants. The MSD-FIT variant, with the activated MSD updating scheme, took 8429 s to reach the fitness of the GA baseline variant, which required 22356 s. After the full 1000 generations the MSD-GEN variant showed only a small increase in fitness (4.04) compared to the baseline GA variant (3.54). Qualitatively, the deformation aligns well with the target deformation for all variants, only the MSD-GEN variant shows some visible deviation at the plateau region. The convergence behavior (Figure 14) shows a fast increase of the fitness for the approximately 100 first generations of the GA variant with a rather slow increase afterwards. By contrast, the variants with active MSD updating show a steady increase over the generations. Figure 15 and Figure 16 show the comparison of the variable gradient and the variable distribution on the given part after optimization for L_{x1} and L_{x2}, respectively. The refinement of the MSD created 22 material sections along the Y direction for both variants with activated MSD updating scheme. This again led to an overall decrease in the gradient, although some individual UCs displayed an increased gradient.

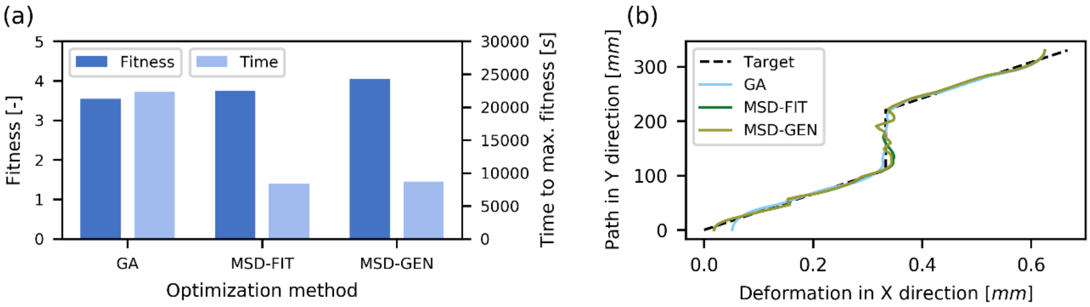

Figure 13: Comparison between the different optimization variants for (a) fitness and runtime until maximum fitness is reached and (b) the lateral deformation for the single-step target deformation specified in Figure 12(a).

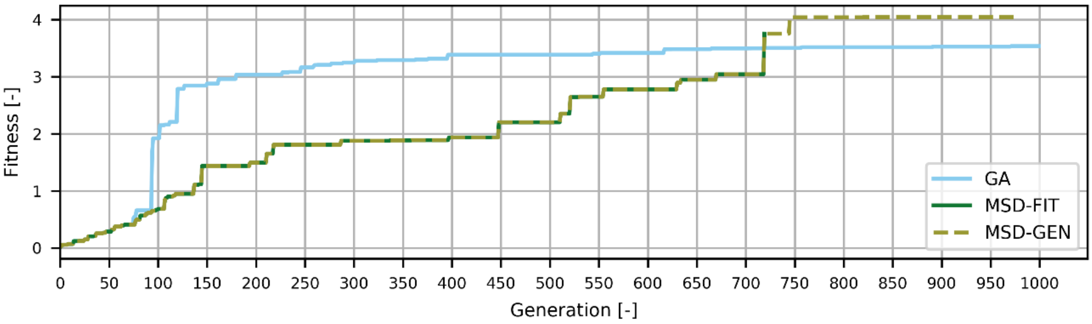

Figure 14:Convergence plot for the new framework – comparison between the fixed MSD (GA), the MSD-FIT and the MSD-GEN setups, which were used to achieve the single-step target deformation specified in Figure 12(a).

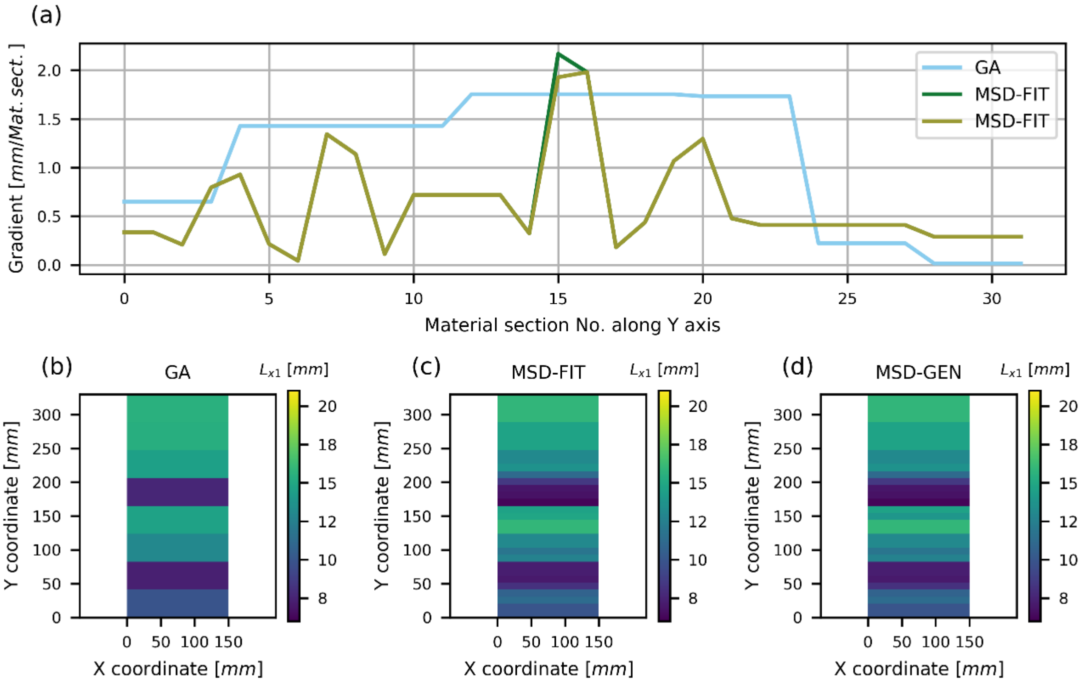

Figure 15: Comparison of the variable gradient and the variable distribution for variable L_{x1} in case of the single-step target deformation. (a) Variable gradient along the Y direction for the three optimization variants. Variable distribution for (b) the GA setup,(c) the MSD-FIT setup and (d) for the MSD-GEN setup.

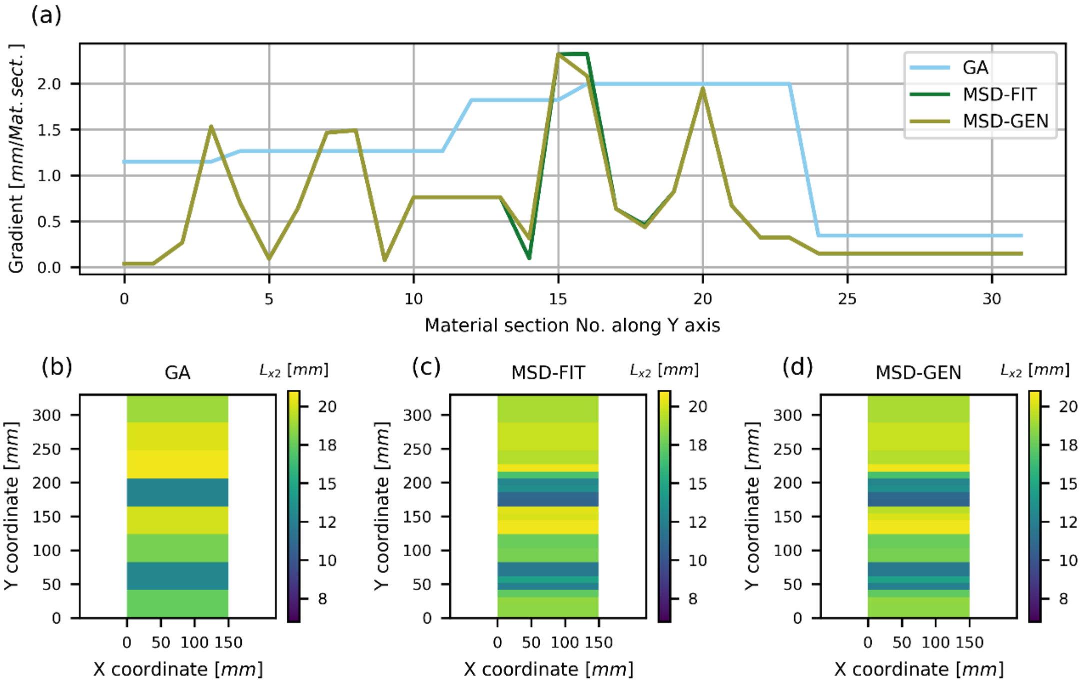

Figure 16: Comparison of the variable gradient and the variable distribution for variable L_{x2} in case of the single-step target deformation. (a) Variable gradient along the Y direction for the three optimization variants. Variable distribution for (b) the GA setup, (c) the MSD-FIT setup and (d) for the MSD-GEN setup.

4.2.2 Trapezoidal target deformation

The trapezoidal target deformation, shown in Figure 12(b), consists of a positive slope, a constant plateau, and a negative slope of lateral deformation. Figure 17 shows the fitness, the time to reach maximum fitness, and the deformation behavior for all three variants. Using the activated MSD updating scheme, the MSD-FIT variant achieved the fitness level of the GA baseline variant in 1560 s instead of the 19446 s required otherwise. After the full 1000 generations the MSD-GEN variant increased the fitness compared the baseline GA variant (1.6 vs. 0.99). Qualitatively, the deformation aligns well with the target deformation for all variants. Nevertheless, the variants with activated MSD updating scheme show a better fit for the transition between positive slope and the constant deformation plateau. The convergence behavior (Figure 18) shows a similarly fast increase of the fitness for approximately the first 80 generations for all variants. Afterwards, the fitness of the baseline GA variant increases only in a few small steps, whereas the fitness in the MSD-GEN variant exhibits faster growth and shows one significant increase occurring around the 830th generation. Figure 19 and Figure 20 show the comparison of the variable gradient and the variable distribution on the given part after optimization for the variables L_{x1} and L_{x2}, respectively. The refinement of the MSD created 13 and 19 material sections along the Y direction for the MSD-FIT and MSD-GEN variants, respectively. Once more, this resulted in a general decrease in the gradient, although certain individual UCs displayed an increased gradient.

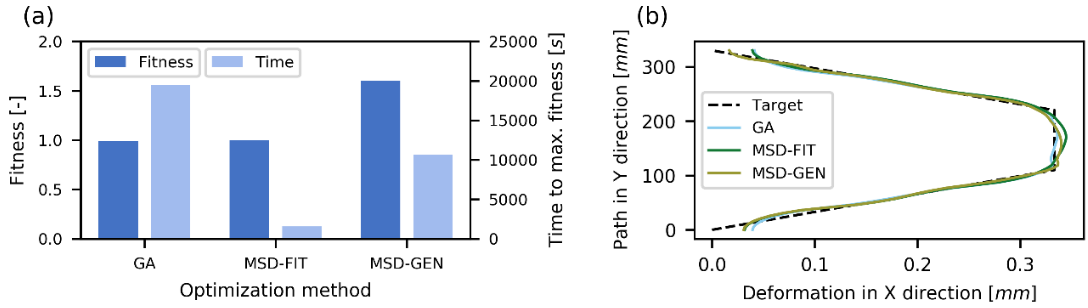

Figure 17: Comparison between the different optimization variants for (a) fitness and runtime until maximum fitness is reached and (b) the lateral deformation for the trapezoidal target deformation specified in Figure 12(b).

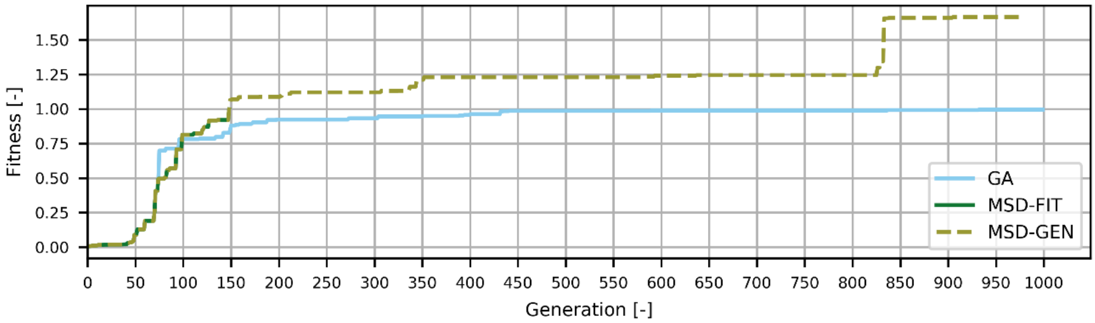

Figure 18:Convergence plot for the new framework – comparison between the fixed MSD (GA), the MSD-FIT and the MSD-GEN setups, which were used to achieve the trapezoidal target deformation specified in Figure 12(b).

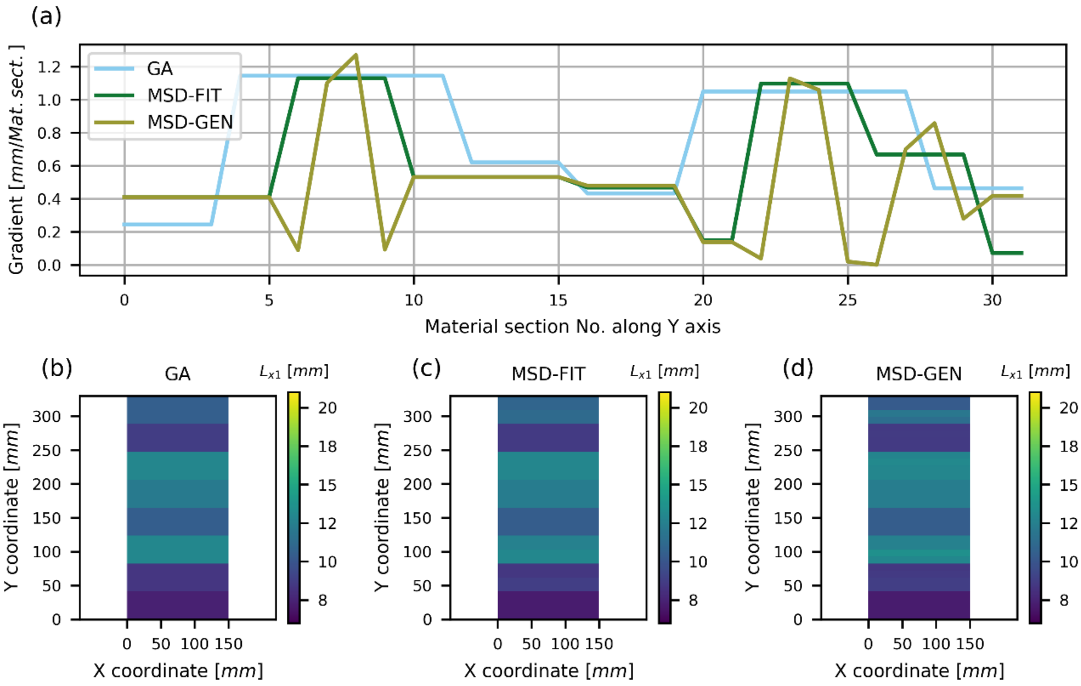

Figure 19: Comparison of the variable gradient and the variable distribution for variable L_{x1} in case of the trapezoidal target deformation. (a) Variable gradient along the Y direction for the three optimization variants. Variable distribution for (b) the GA setup,(c) the MSD-FIT setup and (d) for the MSD-GEN setup.

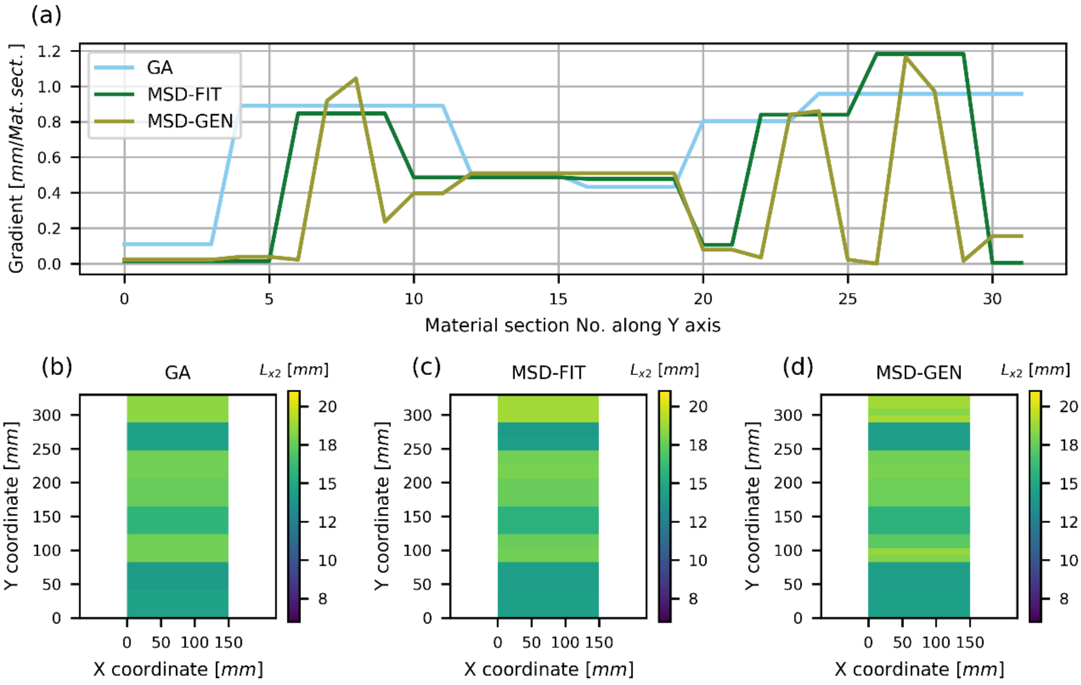

Figure 20: Comparison of the variable gradient and the variable distribution for variable L_{x2} in case of the trapezoidal target deformation. (a) Variable gradient along the Y direction for the three optimization variants. Variable distribution for (b) the GA setup, (c) the MSD-FIT setup and (d) for the MSD-GEN setup.

4.2.3 Complex target deformation

The complex target deformation, shown in Figure 12(c), consists of a combination of positive slopes, constant plateaus, and negative slopes of lateral deformation. Figure 21 shows the fitness, the time to reach the maximum fitness, and the deformation behavior for all three variants. With the MSD updating scheme activated, it took the MSD-FIT variant 4872 s to reach the fitness level of the GA baseline variant, which required 22432 s. After the full 1000 generations the MSD-GEN variant increased the fitness only to 0.92 compared to 0.87 for the baseline GA variant. Consequently, there was no further increase in fitness from the MSD-FIT to the MSD-GEN variant. Qualitatively, the deformation aligns well with the target deformation for all variants. However, the small plateaus of constant deformation pose a challenge to the optimization framework. The optimized deformation over- or undershoots the target primarily due to the minimal size of the given material sections. The convergence behavior (Figure 22) exhibits a comparable fast rise in fitness during the initial approximately 100 generations across all variants. Afterwards the fitness of the baseline GA variant increases steadily, whereas the variants with active MSD updating scheme show a significant increase until the 330th generation, where the maximum fitness is reached. Figure 23 and Figure 24 show the comparison of the variable gradient and the variable distribution on the given part after optimization for the variables L_{x1} and L_{x2}, respectively. The refinement of the MSD created 20 material sections along the Y direction for the variants with active MSD updating scheme. Generally, as before, this resulted in an overall decline in the gradient, with some individual UCs showing an increase.

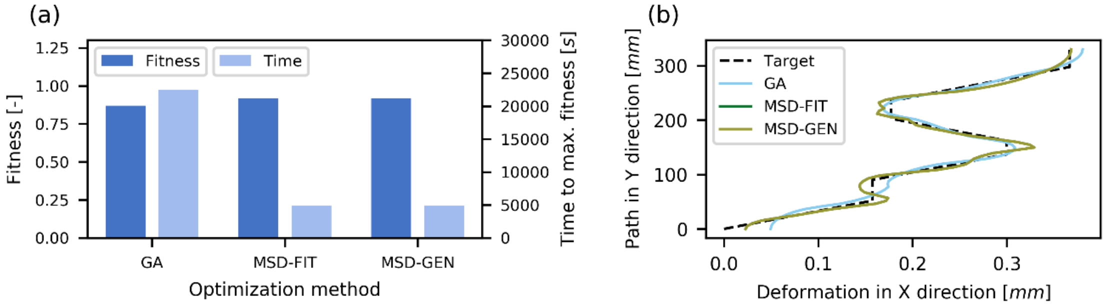

Figure 21: Comparison between the different optimization variants for (a) fitness and runtime until maximum fitness is reached and (b) the lateral deformation for the complex target deformation specified in Figure 12(c).

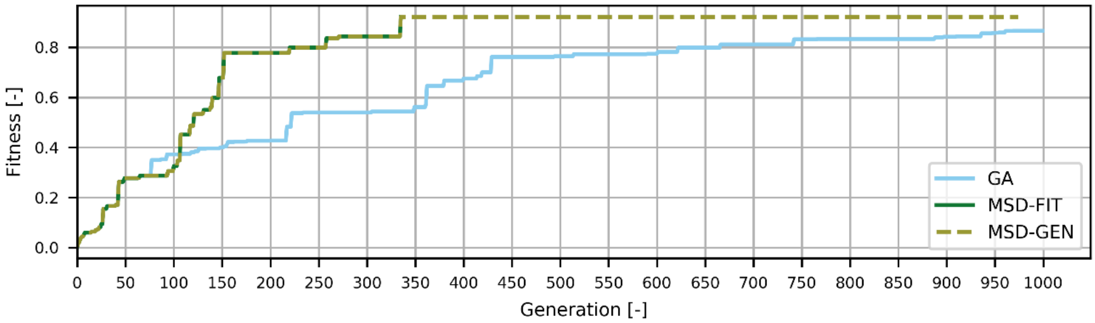

Figure 22: Convergence plot for the new framework – comparison between the fixed MSD (GA), the MSD-FIT and the MSD-GEN setups, which were used to achieve the complex target deformation specified in Figure 12(c).

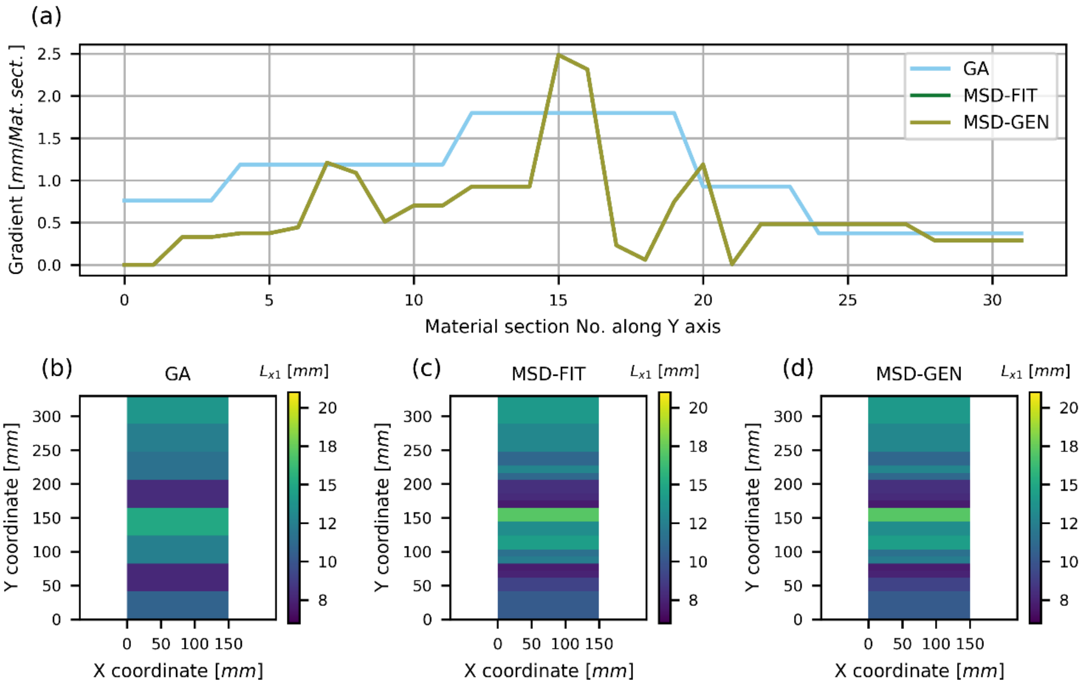

Figure 23: Comparison of the variable gradient and the variable distribution for variable L_{x1} in case of the complex target deformation. (a) Variable gradient along the Y direction for the three optimization variants. Variable distribution for (b) the GA setup,(c) the MSD-FIT setup and (d) for the MSD-GEN setup.

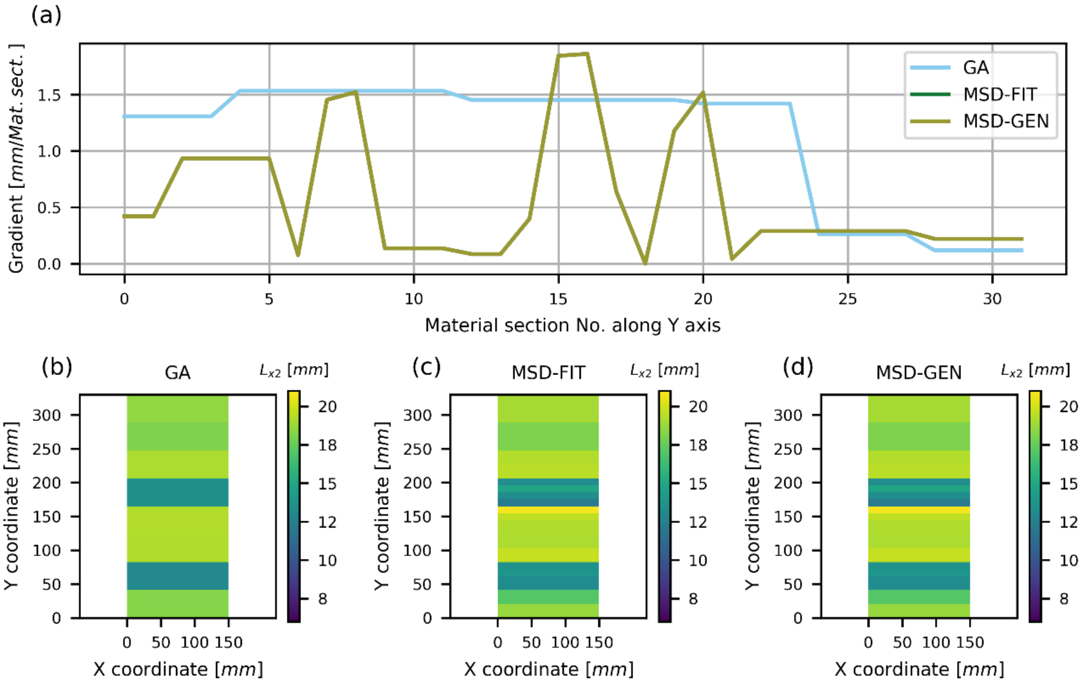

Figure 24: Comparison of the variable gradient and the variable distribution for variable L_{x2} in case of the complex target deformation. (a) Variable gradient along the Y direction for the three optimization variants. Variable distribution for (b) the GA setup, (c) the MSD-FIT setup and (d) for the MSD gen setup.

4.3 Discussion

When looking only at the optimization algorithm, the change from LSOPT to the Python-based genetic algorithm (GA) led to a decrease in performance. The combination of a GA with a surrogate modeling approach, which is implemented in LSOPT, significantly reduces the simulation calls, and thereby increases the efficiency in relation to the Python-based GA. The open-source Python implementation of the GA, however, facilitates easy adaptation and integration of additional software routines, exemplified by the inclusion of the MSD updating scheme outlined in this study. To improve the efficiency of the GA, further work is required to identify the best GA settings for each optimization. Moreover, implementing a surrogate modelling approach to the GA represents a potential measure to decrease the overall runtimes especially when employing the framework with 3D simulations. Adding the MSD updating scheme to the GA resulted in a decrease in the time required to reach the maximum fitness compared to the original framework with LSOPT. In addition, the local refinement of the MSD, based on the variable gradient, reduced the number of material sections and thereby increased the efficiency of the optimization. This shows that using a high number of material sections to find the best distribution is an insufficient strategy and leads to inefficient optimizations. No general trend can be observed regarding the effect of the MSD updating scheme on the convergence behavior. It depends on the individual optimization case and the respective target deformation. In some cases, this led to a fast increase in fitness at the beginning, while in other instances it resulted in a continuous increase. However, in all tested cases the maximum fitness reached as well as the time to reach this fitness were improved with respect to the variants with the GA only. Furthermore, the local refinement of the MSD scheme led to a global decrease in the variable gradient. Nevertheless, the absence of a strict constraint on the gradient during the MSD updating caused the refinement to lead, in some cases, to a local increase of the variable gradient in individual material sections. The implementation of such an additional hard constraint has the potential to solve this issue, but the effect on the optimization efficiency will have to be evaluated.

5 Conclusion

This study describes an automated material section discretization refinement in a Finite Element simulation-based optimization strategy to create a predefined deformation behavior of metamaterial components. Previous research showed a significant influence of the number and distribution of the material sections on the convergence behavior [24]. Therefore, an automated updating of the discretization is necessary to decrease the trial and error runs needed to find the appropriate material section discretization for a given optimization problem. The developed scheme for updating the material section discretization was implemented as an extension to an already existing optimization framework presented in a previous study [24]. To facilitate the extension, the optimization algorithm was changed to a genetic algorithm implemented in Python. The scheme for the automated discretization is based on an algorithm for storing, evaluating, and updating the material section discretization with a data interface to the GA process. The refinement is controlled by a user defined variable field.

The extended framework was tested with a 2D tri-anti-chiral metamaterial with the optimization target to match a predefined deformation under a given load by optimizing the UC parameter distribution. For this study, the refinement was controlled by the spatial gradient of the geometric parameters which correspond to the gradient of the optimization variables. The developed automated refinement scheme was able to improve the efficiency for all tests by reducing the optimization time to reach a given fitness value. Due to the chosen variable field for controlling the refinement, the framework reduced the overall variable gradient.

The addition of the automated material section discretization is a significant generalization for the proposed optimization framework, which lessens the user involvement and effort for defining the optimal number of material sections. However, to improve the efficiency of the framework, future research should focus on the optimization of the genetic algorithm's settings. Furthermore, to reduce the number of Finite Element simulations conducted during the optimization, and hence the overall runtime, the viability of using surrogate models should be evaluated.

An additional topic for future studies is the translation of the homogenized material sections back to the corresponding UC geometries to create the actual metamaterial part. Depending on the size, complexity, and distribution of the UCs, as well as the overall shape of the part, this step presents some challenges concerning the connections and transitions between the individual UCs. Solving these challenges in an efficient way, and thus ensuring the manufacturability of the optimized part is the next step towards a complete optimization framework for metamaterial components.

Acknowledgement

The research work of this study was performed within the COMET-Module projects "CHEMITECTURE" (project-no.: 21647048) and "Repairtecture" (project-no.: 904927) at the Polymer Competence Center Leoben GmbH (PCCL, Austria) within the framework of the COMET-program of the Federal Ministry for Climate Action, Environment, Energy, Mobility, Innovation and Technology and the Federal Ministry for Labour and Economy with contributions by the Department of Polymer Engineering and Science / Montanuniversitaet Leoben. The PCCL is funded by the Austrian Government and the State Governments of Styria, Lower Austria and Upper Austria.

References

[1] J.E. Holliman, H.T. Schaef, B.P. McGrail, Q.R.S. Miller, Review of foundational concepts and emerging directions in metamaterial research: design, phenomena, and applications, Mater. Adv. 3 (2022) 8390–8406. https://doi.org/10.1039/D2MA00497F.

[2] X. Zheng, H. Lee, T.H. Weisgraber, M. Shusteff, J. DeOtte, E.B. Duoss, J.D. Kuntz, M.M. Biener, Q. Ge, J.A. Jackson, S.O. Kucheyev, N.X. Fang, C.M. Spadaccini, Ultralight, ultrastiff mechanical metamaterials, Science 344 (2014) 1373–1377. https://doi.org/10.1126/science.1252291.

[3] J. Bauer, L.R. Meza, T.A. Schaedler, R. Schwaiger, X. Zheng, L. Valdevit, Nanolattices: An Emerging Class of Mechanical Metamaterials, Adv. Mater. Weinheim. 29 (2017). https://doi.org/10.1002/adma.201701850.

[4] M. Taghavi, T. Helps, B. Huang, J. Rossiter, 3D-Printed Ready-To-Use Variable-Stiffness Structures, IEEE Robot. Autom. Lett. 3 (2018) 2402–2407. https://doi.org/10.1109/LRA.2018.2812917.

[5] M. Fleisch, A. Thalhamer, G. Meier, I. Raguž, P.F. Fuchs, G. Pinter, S. Schlögl, M. Berer, Functional mechanical metamaterial with independently tunable stiffness in the three spatial directions, Materials Today Advances 11 (2021) 100155. https://doi.org/10.1016/j.mtadv.2021.100155.

[6] H.M.A. Kolken, A.A. Zadpoor, Auxetic mechanical metamaterials, RSC Adv. 7 (2017) 5111–5129. https://doi.org/10.1039/C6RA27333E.

[7] M. Fleisch, A. Thalhamer, G. Meier, P.F. Fuchs, G. Pinter, S. Schlögl, M. Berer, Asymmetric chiral and antichiral mechanical metamaterials with tunable Poisson's ratio, APL Materials 10 (2022) 61105. https://doi.org/10.1063/5.0091756.

[8] M. Fleisch, A. Thalhamer, S. Schlögl, P.F. Fuchs, G. Pinter, M. Berer, MetamaterialFinder: A software framework for discovering and analyzing mechanical metamaterials based on simple closed curves, Advances in Engineering Software 192 (2024) 103626. https://doi.org/10.1016/j.advengsoft.2024.103626.

[9] J. Schwerdtfeger, F. Wein, G. Leugering, R.F. Singer, C. Körner, M. Stingl, F. Schury, Design of auxetic structures via mathematical optimization, Adv. Mater. Weinheim. 23 (2011) 2650–2654. https://doi.org/10.1002/adma.201004090.

[10] R. Behrou, M.A. Ghanem, B.C. Macnider, V. Verma, R. Alvey, J. Hong, A.F. Emery, H.A. Kim, N. Boechler, Topology optimization of nonlinear periodically microstructured materials for tailored homogenized constitutive properties, Composite Structures 266 (2021) 113729. https://doi.org/10.1016/j.compstruct.2021.113729.

[11] W. Chen, X. Huang, Topological design of 3D chiral metamaterials based on couple-stress homogenization, Journal of the Mechanics and Physics of Solids 131 (2019) 372–386. https://doi.org/10.1016/j.jmps.2019.07.014.

[12] Y. Wang, Z. Luo, N. Zhang, Z. Kang, Topological shape optimization of microstructural metamaterials using a level set method, Computational Materials Science 87 (2014) 178–186. https://doi.org/10.1016/j.commatsci.2014.02.006.

[13] H. Zhang, Y. Luo, Z. Kang, Bi-material microstructural design of chiral auxetic metamaterials using topology optimization, Composite Structures 195 (2018) 232–248. https://doi.org/10.1016/j.compstruct.2018.04.058.

[14] L. Xia, P. Breitkopf, Concurrent topology optimization design of material and structure within FE2 nonlinear multiscale analysis framework, Computer Methods in Applied Mechanics and Engineering 278 (2014) 524–542. https://doi.org/10.1016/j.cma.2014.05.022.

[15] A. Challapalli, D. Patel, G. Li, Inverse machine learning framework for optimizing lightweight metamaterials, Materials & Design 208 (2021) 109937. https://doi.org/10.1016/j.matdes.2021.109937.

[16] H.T. Kollmann, D.W. Abueidda, S. Koric, E. Guleryuz, N.A. Sobh, Deep learning for topology optimization of 2D metamaterials, Materials & Design 196 (2020) 109098. https://doi.org/10.1016/j.matdes.2020.109098.

[17] A.P. Garland, B.C. White, S.C. Jensen, B.L. Boyce, Pragmatic generative optimization of novel structural lattice metamaterials with machine learning, Materials & Design 203 (2021) 109632. https://doi.org/10.1016/j.matdes.2021.109632.

[18] A. Panesar, M. Abdi, D. Hickman, I. Ashcroft, Strategies for functionally graded lattice structures derived using topology optimisation for Additive Manufacturing, Additive Manufacturing 19 (2018) 81–94. https://doi.org/10.1016/j.addma.2017.11.008.

[19] Y. Zhang, M. Xiao, H. Li, L. Gao, S. Chu, Multiscale concurrent topology optimization for cellular structures with multiple microstructures based on ordered SIMP interpolation, Computational Materials Science 155 (2018) 74–91. https://doi.org/10.1016/j.commatsci.2018.08.030.

[20] Y. Carson, A. Maria, Simulation Optimization: Methods and Applications, in: Proceedings of the 1997 Winter Simulation Conference, pp. 118–126.

[21] J. Yao, Y. Su, F. Scarpa, Y. Li, An optimization approach to design deformation patterns in perforated mechanical metamaterials using distributions of Poisson’s ratio-based unit cells, Composite Structures 281 (2022) 115015. https://doi.org/10.1016/j.compstruct.2021.115015.

[22] Y. Han, W. Lu, Evolutionary design of nonuniform cellular structures with optimized Poisson's ratio distribution, Materials & Design 141 (2018) 384–394. https://doi.org/10.1016/j.matdes.2017.12.047.

[23] X. Liang, J. Shan, X. Zhou, S. Li, W. Yu, Z. Liu, Y. Wen, B. Liang, H. Li, Active design of chiral cell structures that undergo complex deformation under uniaxial loads, Materials & Design 217 (2022) 110649. https://doi.org/10.1016/j.matdes.2022.110649.

[24] A. Thalhamer, M. Fleisch, C. Schuecker, P.F. Fuchs, S. Schlögl, M. Berer, A black-box optimization strategy for customizable global elastic deformation behavior of unit cell-based tri-anti-chiral metamaterials, Advances in Engineering Software 186 (2023) 103553. https://doi.org/10.1016/j.advengsoft.2023.103553.

[25] A.F. Gad, PyGAD: An Intuitive Genetic Algorithm Python Library, 2021. http://arxiv.org/pdf/2106.06158v1.

[26] M. Fleisch, A. Thalhamer, G. Meier, P.A.F. Huber, P.F. Fuchs, G. Pinter, S. Schlögl, M. Berer, Chiral-based mechanical metamaterial with tunable normal-strain shear coupling effect, Engineering Structures 284 (2023) 115952. https://doi.org/10.1016/j.engstruct.2023.115952.

[27] A. Alderson, K.L. Alderson, D. Attard, K.E. Evans, R. Gatt, J.N. Grima, W. Miller, N. Ravirala, C.W. Smith, K. Zied, Elastic constants of 3-, 4- and 6-connected chiral and anti-chiral honeycombs subject to uniaxial in-plane loading, Composites Science and Technology 70 (2010) 1042–1048. https://doi.org/10.1016/j.compscitech.2009.07.009.

[28] S. Tabacu, R.F. Negrea, D. Negrea, Experimental, numerical and analytical investigation of 2D tetra-anti-chiral structure under compressive loads, Thin-Walled Structures 155 (2020) 106929. https://doi.org/10.1016/j.tws.2020.106929.

[29] A. Lorato, P. Innocenti, F. Scarpa, A. Alderson, K.L. Alderson, K.M. Zied, N. Ravirala, W. Miller, C.W. Smith, K.E. Evans, The transverse elastic properties of chiral honeycombs, Composites Science and Technology 70 (2010) 1057–1063. https://doi.org/10.1016/j.compscitech.2009.07.008.

[30] Y.J. Chen, F. Scarpa, Y.J. Liu, J.S. Leng, Elasticity of anti-tetrachiral anisotropic lattices, International Journal of Solids and Structures 50 (2013) 996–1004. https://doi.org/10.1016/j.ijsolstr.2012.12.004.

[31] D. Mousanezhad, B. Haghpanah, R. Ghosh, A.M. Hamouda, H. Nayeb-Hashemi, A. Vaziri, Elastic properties of chiral, anti-chiral, and hierarchical honeycombs: A simple energy-based approach, Theoretical and Applied Mechanics Letters 6 (2016) 81–96. https://doi.org/10.1016/j.taml.2016.02.004.

[32] W. Wu, W. Hu, G. Qian, H. Liao, X. Xu, F. Berto, Mechanical design and multifunctional applications of chiral mechanical metamaterials: A review, Materials & Design 180 (2019) 107950. https://doi.org/10.1016/j.matdes.2019.107950.

Paper E

A Simulation-Based Assessment of Print Accuracy for Microelectronic Parts Manufactured with DLP 3D Printing Process

Authors: Thalhamer, A.
Fuchs, P.F.
Strohmeier, L.
Hasil, S.
Wolfberger, A.

2022 23rd International Conference on Thermal, Mechanical and Multi-Physics Simulation and Experiments in Microelectronics and Microsystems (EuroSimE)
DOI: 10.1109/EuroSimE54907.2022.9758869

A Simulation-Based Assessment of Print Accuracy for Microelectronic Parts Manufactured with DLP 3D Printing Process

A. Thalhamer, P. Fuchs, L. Strohmeier, S. Hasil, A. Wolfberger
Polymer Competence Center Leoben GmbH (PCCL)
Roseggerstraße 12, 8700 Leoben, Austria
andreas.thalhamer@pccl.at

Abstract

Due to its printing speed and high resolution, digital light processing (DLP) additive manufacturing technology has a steadily growing field of applications. Considering the possibility of DLP multi material printing, the creation of fully 3D printed complex conductive structures for microelectronic applications is a potential use case. However, to guarantee the geometric precision, a method to assess the printing process induced geometric deviations is required. In this study, the first parts of a modular simulation framework for describing the DLP 3D printing process were developed. The framework was designed to model the process-specific layer-by-layer curing and the resulting effects such as shrinkage due to crosslinking, residual stresses and curing-dependent mechanical properties. Cure depending elastic material properties were considered together with the chemical shrinkage to account for possible warpage. Additional modules were developed to account for effects like reaction-based heat generation, curing in cavities due to light penetration of printed layers as well as the release force during removal from the build platform. The framework was implemented in the Abaqus FEA software (Dassault Systèmes Simulia Corp, Providence, RI.). The capabilities of the framework were tested on four simple geometries including a PCB-like structure to show the potential for printed microelectronic parts. Results of the simulation showed the successful prediction of effects like warpage and print through error and were in good agreement with findings from the literature. The presented results showed the potential of the framework to predict the DLP process inherent manufacturing imprecision and is thus a good basis for the further development of multi material printing of electronic structures.

1. Introduction

In additive manufacturing (AM) or 3D printing processes, 3D structures are built based on layer-by-layer addition of material, therefore enabling a high design freedom regarding the complexity of the produced part [1]. The field of application for AM technologies is steadily growing and due to its continuous development over the last years it has found its way into the production of microelectronic parts [2–5]. Due to the recent development in conductive filled 3D printable resins [6–8] and the possibility for multi-material printing [9] , photopolymerization based 3D printing methods have become another candidate for printing of microelectronic systems. The digital light processing, which is based on the projection of a light pattern on photo-curable resins offers the advantage of high-resolution prints in combination with fast printing times due to the illumination of a complete slice each layer [10]. Due to its complex nature, a robust prediction of the process induced influences on the printed part is challenging. However, to reduce the number of trial and error iterations in process optimization, a reliable modelling approach is necessary. A DLP process simulation framework should be able to calculate the evolution of degree of cure (cure kinetics) in the material depending on the process parameters, calculate the material properties depending on the degree of cure and the process environment as well as consider the layer build up during printing. Experimental characterization and modelling of the curing kinetics has been done for a variety of photo curable resins [11–16] and also the material property evolution during curing has been studied for several materials [17–21]. However, only few studies on the combination of the, above mentioned, components into a comprehensive process simulation framework for the DLP method has been done so far. Gao et al. [22] developed a Multiphysics approach to modelling the DLP process that solved the governing equations for the chemical kinetics model and the thermo-mechanical model using COMSOL Multiphysics®. Westbeek et al. [23] predicted the deformed geometry of vat photo-polymerized parts including the 3D light distribution of each pixel in a multi-physical modelling framework. Recently Zhang et al. [24] implemented constitutive models for material property evolution coupled with shrinkage during photocuring in Abaqus Finite Element Analysis (FEA) software to predict the shape distortion in printed microfluidic channels and overhanging structures.

In this work a modular framework for the assessment of process induced deformation and imprecisions in the DLP 3D printing process is implemented in the Abaqus 2019 FEA software (Dassault Systèmes Simulia Corp, Providence, RI.). The modular set up allows for choosing the level of complexity used in the process description and thereby distinguishes the presented work from other frameworks in the literature. It enables to adapt the framework to the accuracy requirements, the available computational resources and the available material data. This work is the first step in the development of a simulation framework for conductive multi-material DLP 3D printing and presents the foundation for further work. Therefore, a simple autocatalytic cure model together with a Cure Hardening Instantaneous Linear Elastic (CHILE) model combined with chemical shrinkage strain calculation was implemented into a layer by layer activated Finite Element (FE) model. The cure kinetics were

978-1-6654-5836-8/22/$31.00 ©2022 IEEE

experimentally characterised for a custom developed 3D printing resin which was designed with later addition of conductive fillers in mind. Mechanical properties were taken from the literature for now. The overall function and prediction capability of the framework was tested on different geometries.

In the following, the DLP method is described in section 2 and the used material is detailed in section 3. The main parts of the simulation framework are presented in section 4 and the additional modules of the framework in section 5. Section 6 gives an overview of the used methods for material characterisation. In section 7 the results of material model fitting and the results of the simulation with simple geometries are discussed and conclusions are made in the last section.

2. DLP method

The DLP 3D printing process is based on the layer-by-layer build up utilizing light induced polymerization of photo sensitive resins to create individual layers. The DLP method can be subdivided into ‘top down’ and ‘bottom up’ techniques, depending on the location of the light source in reference to the resin vat. The following description refers to the ‘bottom up’ technique and a principle sketch of the process is shown in Figure 1. At the start of the process the build platform is submerged into the resin in the vat. The build platform is lowered until the gap between the bottom of the vat and the platform reaches the specified layer height. The cross-section of the first layer is then projected on the resin through the bottom of the vat. After the specified layer curing time, the build platform is moved up to the position of the next layer, thereby removing the printed layer from the bottom of the vat and allowing resin to flow again into the gap between platform and vat bottom. These steps are then repeated until all layers are cured and the part is fully printed. To enable fully 3D printed electronic parts manufactured with the DLP process, a multi material technique is required. A common approach to achieve prints with multiple materials is to use a system with exchangeable vats or automated vat movement systems [8, 25, 26]. Only the single material DLP process is considered in this work. However, in the future it is planned to expand the simulation work to a multi material process, as the development of an efficient and automated multi material DLP printer for electrically conductive parts is the overall goal of the project in which the work of this study is imbedded.

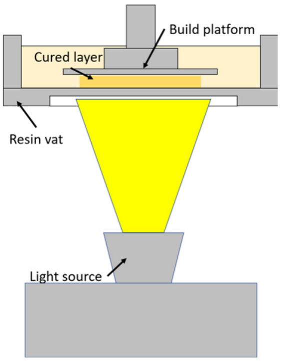

Figure 1: Principle sketch of a 'bottom up' DLP printing set up

3. Material

The material used in this work was optimized for general good performance in the DLP process as well as good performance in combination with conductive fillers. The formulation is composed of an epoxide main constituent, a photoacid generator and sensitizer for polymerization initiation and a reactive diluent. A cycloaliphatic epoxide 3,4-epoxycyclohexylmethyl-3’-4’-epoxycyclohexane carboxylate (ECC) was selected as the main component for the DLP resin. The photopolymerization is induced with an iodium-based photoacid generator Bis(4-dodecylphenyl)iodonium hexafluoroantimonate (PAG) paired with a thioxanthone-based sensitizer 2-chloro-4-propxythioxanthone (CPTX). As reactive diluent 3-Ethyl-3-oxetanemethanol (OX) was applied. ECC, PAG, and CPTX were purchased from Arkema, Colombes, France, whereas OX was obtained from TCI Chemicals, Tokyo, Japan. All chemicals were used without further purification.

4. Simulation framework.

The framework for the simulation of the DLP 3D printing technique is based on the FE method with an incorporated cure kinetics model and cure depending material properties, implemented in the Abaqus FEA software. The main parts of the framework are the handling of the layer-by-layer build up with moving boundary conditions, the determination of the time, intensity and temperature dependent curing in each layer and the calculation of the cure depending material properties. The main components of the framework are depicted in Figure 2 and a detailed look at the main subroutine of the simulation is shown in Figure 3. Each part is described in more detail in the following paragraphs.

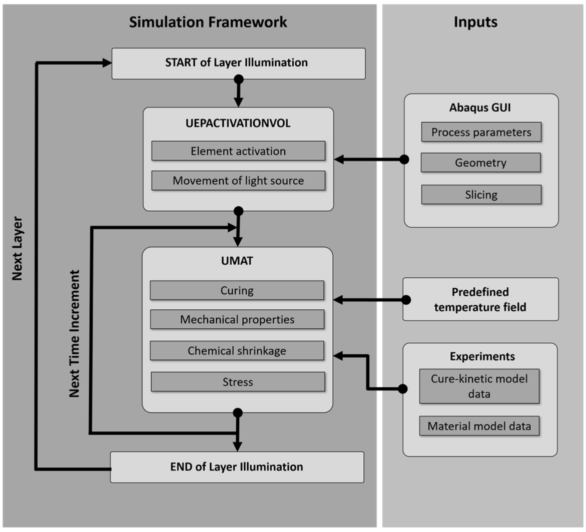

Figure 2: Components of the DLP process simulation framework

Pre-processing of the model: The simulation set up, including generation of the necessary data for the layer activation and curing, is handled by an automated python script in Abaqus. The process parameters like layer thickness, illumination time per layer, illumination intensity and process temperature are processed to create the input file and the necessary data for the subroutines of the framework. For the model set up the geometry is imported, then sliced to create the individual layers and subsequently meshed. The material parameters for the UMAT are automatically generated and the initial temperature is set based on the input data. To account for the sticking of the bottom layer to the build platform, all nodes at the bottom surface are fixed against movement in all directions. In the last step, the fixation of the bottom nodes is deactivated to simulate the removing of the part from the build platform. To facilitate an easy model set up, a simple GUI for the input of all necessary parameters was created.

Layer activation: The "build-up" of each layer starts with the activation of the elements of the current layer and the positioning of the BC of the light source to its appropriate position. This part is handled by the UEPACTIVATIONVOL subroutine in combination with an Eventseries definition. The Eventseries specifies the z coordinate of the light source BC depending on time and therefore which elements should be activated beneath it. Thus, it is used to define the two important process parameters layer height and illumination time of each layer. The information of the position of the light source is then passed to the UMAT subroutine, which handles the calculation of degree of cure and material properties. After element activation, each integration point (IP) is checked if it is inside the illuminated area. Therefore, the z coordinate of the IP's is compared to the position of the light source. If the IP is in the illuminated area, the curing at this point is calculated next by evoking the routine for the cure kinetics model.

Cure kinetics modelling: The model used in this work is a temperature and intensity dependent autocatalytic curing model. The autocatalytic model used in this work is based on the work from Sesták and Berggren [27]. As shown in [12], with the addition of an intensity term the model can be used for the description of the photopolymerization of cycloaliphatic epoxy resins. The principle formulation of the used model is shown in Equation 1

$$\dot{\alpha} = k(I(z),T)\left(1-\frac{\alpha}{\alpha_{max}}\right)^{n}\left(\frac{\alpha}{\alpha_{max}}\right)^{m} \qquad (1)$$

with α as the degree of cure, $\dot{\alpha}$ as the curing rate and α_{max} as the maximal achievable degree of cure. Furthermore, n and m are the reaction order and the autocatalytic exponent respectively. $k(I(z),T)$ is the reaction rate constant, it describes the influence of temperature and light intensity on the cure kinetics. The intensity dependency of the rate constant is described with a simple power function and the fitting parameter β (Equation 2). The temperature dependency is modelled with an Arrhenius term with the activation energy E_a, the gas constant R and the pre-exponential factor A (Equation 3).

$$k(I(z),T) = k_0(T)I(z)^{\beta} \qquad (2)$$

$$k_0(T) = A\,exp\left(\frac{-E_a}{RT}\right) \qquad (3)$$

The decrease of the light intensity inside the resin due to absorption can be modelled with the Beer-Lambert law [12, 22, 24] (Equation 4). It is used to describe the intensity of the light I depending on the distance z travelled in a medium and the corresponding absorption coefficient c_a.

$$I(z) = I_0 e^{-c_a z} \qquad (4)$$

Numerically integrating the curing rate, calculated with Equation 1, over time allows the computation of the degree of cure in each IP depending on temperature and local light intensity. The values for the degree of cure and curing rate are stored in state variables to make them accessible for the calculation of the cure depending material properties. The model parameters were fitted based on photo DSC measurements and bottom exposure 3D printing experiments. The details of the fitting procedure are explained in section 7.

Material property calculation: To predict the actual material properties of a 3D printed part after and during the process, it is necessary to calculate the properties depending on the degree of cure and the process temperature. A well-known material model to describe the evolution of the elastic properties during the curing of resins is the Cure Hardening Instantaneous Linear Elastic (CHILE) model [28]. It models a linear correlation between Young's modulus and degree of cure. It can be fitted with DMA measurements at different curing states. For the DLP simulation framework, in this work, a five step multi-linear CHILE model (Equation 5) was adapted from [29] and implemented into the UMAT subroutine. Thereby T denotes the current temperature and $T_g(\alpha)$ the glass transition temperature depending on the degree of cure. E^n are the moduli of individual sections of the model and T_{Cn} are the critical Temperature, which define the boundaries of the sections. The pure elastic CHILE model was chosen as a first material model due to its simple implementation and calibration and the possibility to extend it to a quasi-viscoelastic formulation if needed [30]. It should be mentioned here that due to the modularity of the proposed framework the change of material model is possible without the need of big modifications to any of the other parts of the framework.

$$\mathrm{E}\begin{cases} E^1 & T^* \leq T_{C1} \\ E^2 + \frac{T^*-T_{C2}}{T_{C1}-T_{C2}}(E^1 - E^2) & T_{C1} < T^* \leq T_{C2} \\ E^3 + \frac{T^*-T_{C3}}{T_{C2}-T_{C3}}(E^2 - E^3) & T_{C2} < T^* \leq T_{C3} \\ E^4 + \frac{T^*-4}{T_{C3}-T_{C4}}(E^3 - E^4) & T_{C3} < T^* \leq T_{C4} \\ A_e exp(-KT^*) & T_{C4} < T^* \leq T_{C5} \\ E^5 & T_{C5} < T^* \end{cases}$$

$$T^* = T - T_g(\alpha) \tag{5}$$

The Young's modulus from the CHILE model is then used in the standard non-isothermal linear elastic material model in Abaqus. The Poisson's ratio of the material was taken as constant with no cure dependency [23]. To describe the chemical shrinkage caused by the curing reaction, an additional shrinkage strain was added to the model with a linear correlation between degree of cure and shrinkage [21]. The coefficient for the chemical shrinkage is based on the maximum shrinkage at full cure, which was determined during the photo rheology measurement (see section 6). In addition to the shrinkage, the thermal expansion is considered and is implemented using the coefficient of thermal expansion (CTE) as a linear correlation between temperature and expansion. For this first implementation of the framework, the CTE was kept independent from the degree of cure due to high effort of input data generation as well as the small influence of thermal expansion compared to the chemical shrinkage. Both, thermal expansion and chemical shrinkage, are only activated after the material reaches the degree of cure at which gelation takes place. The point of gelation can be determined via photo-rheology measurements (see section 6). Thermal expansion is only considered when using the sequential thermal approach, described in the following section.

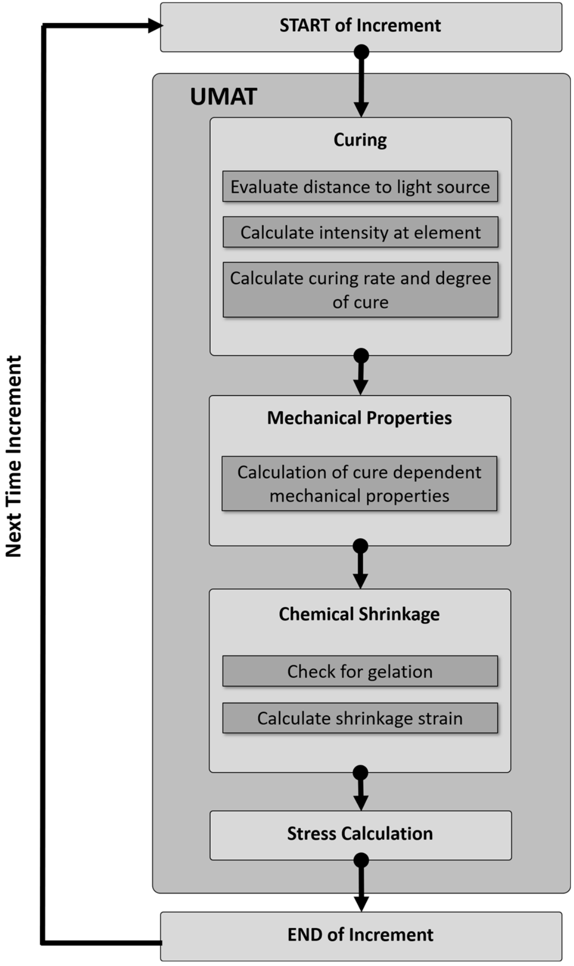

Figure 3: Sequence of the performed steps in the UMAT subroutine

5. Detail framework modules

The following section describes additional modules that can be used to consider some effects, occurring during printing, in more detail. The modules include a sequential thermal simulation, the consideration of uncured surrounding resin and the inclusion of a release force after each layer is printed. These modules are not necessary for the essential function of the framework but can be added if necessary.

<u>Sequential thermal approach</u>: To add heating effects like the heat flux due to the light illumination and the heat generation due to the exothermic curing reaction, the framework also includes the possibility to perform a preceding decoupled heat transfer simulation. The heat input caused by the light illumination is modelled via a heat flux boundary condition at the position of the illuminated faces. The heat of the exothermic reaction is implemented

via a HETVAL subroutine and is based on the calculated curing rate. The heat transfer simulation has the same structure of subroutines as the general framework regarding the element activation and cure calculation. However, in contrast to the general framework, in the heat transfer simulation the HETVAL subroutine is used as the main building block instead of a UMAT subroutine. Passing over of the temperature distribution to the mechanical simulation for the duration of the entire printing process is done by means of a predefined field at each simulation step. Material input parameter for the heat transfer simulation are the curing kinetics model parameter, the heat capacity and the thermal conductivity.

Surrounding resin and actual slicing: When printing small channels, cavities or overhanging structures, the penetration of the light through the current layer will cure resin filling the cavity and as a consequence lead to deviation of the actual geometry. This is also known as print through error. Due to computational limits, so far only the, to be printed, part is considered without the surrounding resin. Therefore, an optional addition was made to the framework to include also the uncured resin around the part. This optional method is limited to details of a part, as it is computational very demanding. In contrast to the main method, during the slicing in the pre-processing step the geometry data of each slice is saved into a separate subroutine for the verification of the illumination pattern. After the slicing, the geometry of the model is replaced by a block of resin material which is slightly larger in all dimensions. The new subroutine is then called in the main framework to check if the IP's are beneath the actual light source. Therefore, for the IP's beneath the light source a point in polygon algorithm is used to review if the current IP is inside the boundaries of the illuminated slice on the x-y plane. In the last step of the simulation all elements with a degree of cure beneath the gel point are deleted to create the finished part geometry. This additional module of the framework allows for the consideration of effects like the print through error as well as more realistic definition of the thermal boundary conditions. For a better distinction between the two approaches, the one with encompassing resin is labelled as "detailed method" and the one without as "global method".

Release force: In the actual DLP printing process, between the printing of each layer, removal from the illuminated surface is necessary to prepare for the curing of the next layer. This removal leads to a force on the unfinished part. To enable the possibility to account for this force, an additional step between each layer-build-step is generated. In this step a uniform load is then applied on the top surface of the last cured layer. At the moment this method can only give an estimate of the momentary stress in the unfinished part during this removal steps, due to the linear elastic material model without any plasticity or viscoelasticity effects.

6. Material characterization

Curing kinetics: The curing kinetic model of the framework was fitted with data based on photo-DSC experiments at different temperatures and irradiation intensities. The measurements were performed on a Photo-DSC 204 F1 Phoenix from Netzsch (Erich NETZSCH GmbH & Co. Holding KG, Selb, Germany) coupled with the 200W high pressure mercury lamp Omnicure S2000 (Lumen Dynamics Group Inc, Mississauga, Canada) equipped with a 400-500 nm Filter. For each measurement about 8mg of resin were used in open aluminium crucibles. The DSC measurements were performed under nitrogen atmosphere and the sequence was as followed:

1. Heating to specified constant temperature
2. 5 min holding at the temperature to reach equilibrium
3. Start of measurement and 10 min illumination with given light intensity
4. 5 min pause
5. Again 10 min illumination with given light intensity to create reference curve for subtraction

For the evaluation of the curing kinetics, the DSC heat flow output from step 5 was subtracted from step 2 to eliminate the influence of the cured material. Calculation of the curing rate $\dot{\alpha}$ was done by relating the measured heat flow dH/dt to the theoretical enthalpy H_{theo} of the curing reaction as expressed in Equation 6.

$$\dot{\alpha} = \frac{d\alpha}{dt} = \frac{dH/dt}{H_{theo}} \qquad (6)$$

The degree of cure was calculated by integrating the area beneath the curing rate curve. For characterizing the influence of the temperature during illumination on the curing kinetics, isothermal experiments at 25, 30, 40, 50, 60, and 70°C at a constant light intensity of 50mW/cm^2 were performed. The effect of the light intensity on the curing rate was determined by measuring with 15, 20, 40, 50, 60, 80mW/cm^2 light intensity at 25 and 50°C.

Intensity distribution: The decrease of light intensity in the material was determined by bottom exposure tests. Therefore, circles with 10mm diameter were printed without build platform and different illumination times. After printing, the thickness of each circle was measured. Three samples were printed for each illumination time. To create a correlation between the light intensity in the part and the thickness of the printed part, the Beer-Lambert law from Equation 4 is formulated in terms of energy dose and rewritten to express the thickness z (Equation 7-9)

$$D(z) = D_0 e^{-c_a z} \qquad (7)$$

$$D = I * t \qquad (8)$$

$$z = \left(\frac{1}{c_\alpha}\right)(ln\, D_0 - ln\, D_c) \qquad (9)$$

with D_0 as the initial energy dose and D_c as the critical energy dose for gelation [22]. Parameters D_c and c_α were then fitted with the experimental data from the bottom exposure tests.

Rheology measurement: Rheology data was determined using a photo-rheometer from Anton Paar (Anton Paar GmbH, Graz, Austria), which was coupled with a light source to enable illumination during measurements. With this setup, the measurement of the evolution of the viscosity and complex shear modulus during curing is possible. The experiment was performed with a maximal shear deformation of 1% and an oscillation frequency of 1Hz at 25°C. The light intensity of the illumination was set to 15,5mW/cm^2 and was kept constant throughout the measurement. The initial gap between the plates was 0.1mm and the Force between the plates was kept constant at 0.01N

7. Results and discussion

Fitting of the curing model: Based on the heat flow of the curing reaction, determined by photo-DSC, the curing rate and degree of cure were calculated as described in section 6. Therefor a theoretical enthalpy H_{theo} of 621 J/g was used for the reaction of the resin. As depicted in Figure 4 and Figure 5, the maximum heat flow is strongly affected by the temperature and light intensity. By elevating the temperature, the mobility of the species is enhanced, resulting in a positive impact on the curing rate. In addition, a stronger light intensity increases the monomer conversion due to the generation of more reactive radicals.

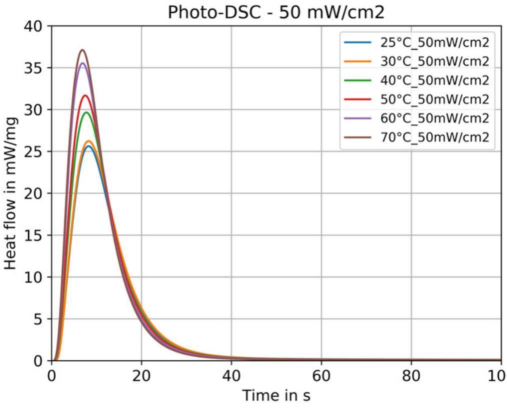

Figure 4: Photo-DSC results at constant 50mW/cm^2 and different temperatures

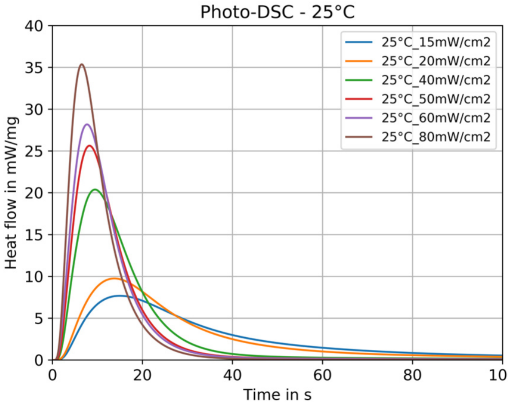

Figure 5: Photo-DSC results at constant 25°C and different light intensities

A least square method in combination with the LSOPT (Livermore Software Technology Corporation, Livermore, CA, USA) optimization tool was used to fit the parameters of the autocatalytic model described in section 4. Therefore, all six measurement at different Temperatures and constant light intensity together with the six measurements at different intensities and 25°C were used to fit the model parameters. The remaining six measurements at different intensities and 50°C were used to validate the model. The parameters used for the fitting as well as their values are listed in Table 1. The determined parameters allowed for a very good description of the temperature dependent behaviour of the curing rate and overall degree of cure in the measured temperature range, as shown in Figure 6.

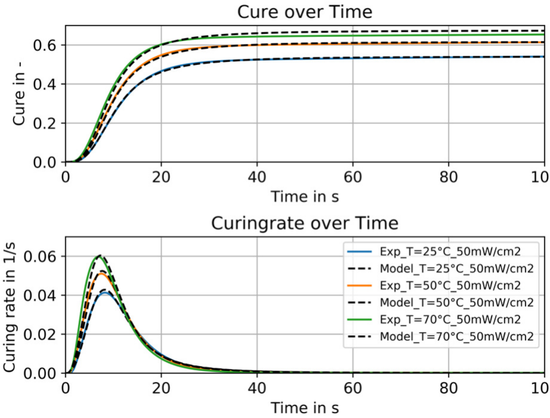

Figure 6: Comparison between Photo-DSC measurements and curing model for constant 50mW/cm^2 and different temperatures

The fitted model also achieved a good agreement for the intensity dependent behaviour down to 40mW/cm^2. Beneath this intensity the model starts to underestimate the final degree of cure, but at the beginning until the maximum of the curing rate it still fits very well. This is due to the fact, that for light intensities under 40mW/cm^2

the fitting parameter n is not independent of the light intensity any more. Comparisons between the model and the experiment for the intensity dependent behaviour are shown in Figure 7. Overall the fitted autocatalytic model was able to calculate the curing kinetic of the used material under illumination with reasonable accuracy.

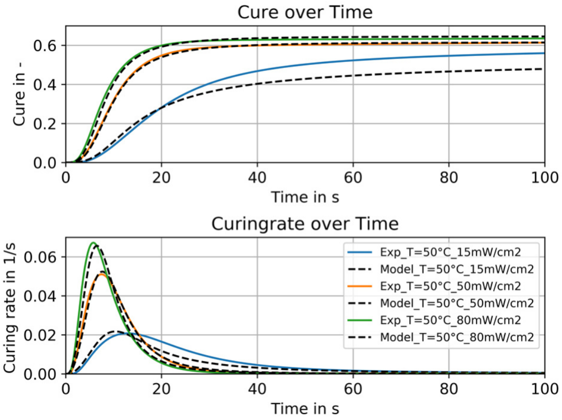

Figure 7: Comparison between Photo-DSC measurements and curing model for constant 50°C and different intensities

Table 1: Parameter of the curing model determined by the fitting process

Parameter	**Value**
n	1.44
m	0.65
A	0.33 s^{-1}
E_a	6524.84 $Jmol^{-1}$
β	0.48

An absorption coefficient c_α for the Beer-Lambert law of 13.12 mm^{-1} was determined by fitting of Equation 9 to the results of the bottom exposure test. The results of the calculated print thickness in comparison to the measured one is presented in Figure 8.

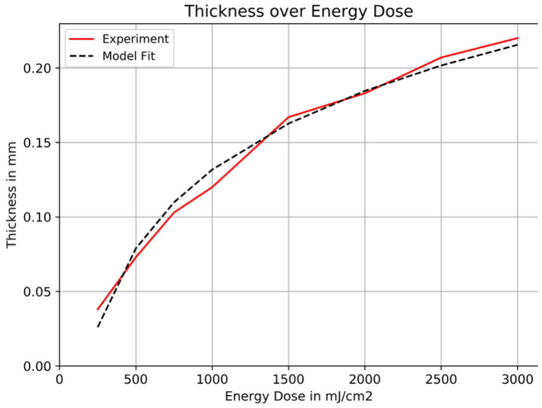

Figure 8: Comparison of experiment and model for the bottom exposure tests

Gel point and shrinkage: Gelation of a resin is defined as the point, when the molecular weight approaches the maximum during curing [31]. The gel point was evaluated as the point of the crossover between dynamic storage shear modulus and dynamic loss shear modulus in the rheology measurement [31]. For the tested resin the gel point occurred after about 16 seconds after the start of illumination at 60s, as is depicted in Figure 9. When correlated with the photo-DSC measurement with the corresponding light intensity, this led to an occurrence of gelation at the maximum of the curing rate and at a calculated degree of cure of 0.12. The shrinkage of the material was determined by observing the distance between the two plates at constant force during the measurement. During curing of the material, the gap decreased from 0.1mm to 0.093mm which corresponds to a maximal chemical shrinkage strain of 7% in the thickness direction.

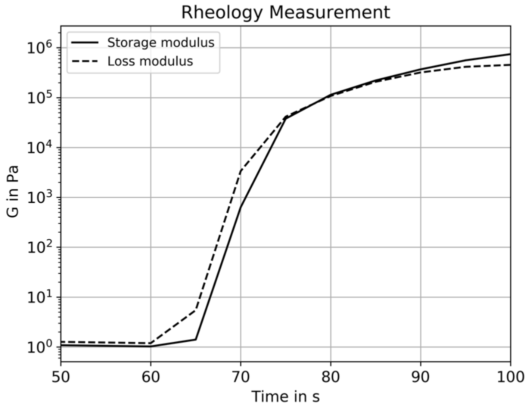

Figure 9: Shear loss and storage modulus over time with measurement starting at 60s

Test simulations: For testing of the simulation framework capabilities to predict the stress evolution during printing and the possible warpage after printing, three different geometries (a beam, a bridge-like structure and a PCB-like structure) were simulated with the global method. In addition, one simulation with the local method was performed on a structure containing small channel geometries to test the prediction of effects like the print through error. All simulations were set up with a layer thickness of 0.05mm with layer illumination times between 10 and 20 s. The process temperature was set to 35°C and the initial intensity of the light source was set to 50mW/cm^2. The parameters of the cure kinetics model, the value for the chemical shrinkage and the absorption coefficient were taken from the characterization in the sections above. The parameters for the material model were adopted from [29]. No release force and thermal simulations were considered due to the lack of experimental data. Each layer illumination was performed in a single step and the FE analysis is solved using C3D8 brick elements and the Abaqus standard implicit solver.

For the first simulation a simple beam with dimension 20x2x1mm (x-y-z), with printing in positive z direction, was set up with an overall mesh size of 0.25mm and one element per layer thickness. The layer illumination time was set to 10s and 20s respectively and to induce warpage at the end of printing, the last layer was illuminated additional 20s. For both simulations the additional illumination of the last layer led to an increase in degree of cure at the top of the beam resulting in warpage of the outer edges in positive z direction after printing, as depicted in Figure 10.

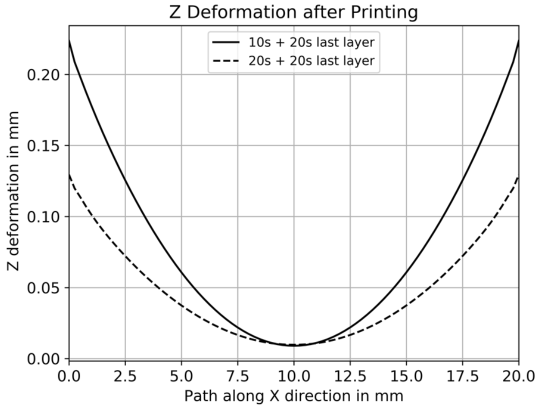

Figure 10: Warpage in z direction along the x direction of the beam for 10s and 20s layer illumination time

Comparing the two illumination times, the simulation with 20s showed an overall increase in degree of cure and an increase of tension stress in x direction before removing the build platform boundary condition, as shown in Figure 11 and Figure 12 respectively. On the other hand, simulations with 10s showed a larger difference in the degree of cure between the top layer and the layers beneath. In combination with the overall less degree of cure and thereof smaller Young's modulus resulting in a more pronounced warpage for 10s illumination time. The overall simulated warpage behaviour of the beam is in good agreement with observations from previous studies [22].

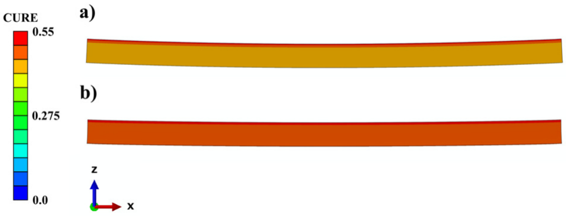

Figure 11: Degree of cure after printing for a) 10s and b) 20s of illumination time per layer

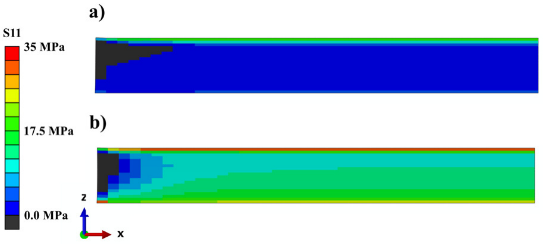

Figure 12: Stress in x direction of left half of the beam before removing from the platform for a) 10s and b) 20s illumination time per layer

The second geometry to test the capabilities of the framework regarding stress and warpage prediction was a simple bridge-like structure as depicted in Figure 13. The layers were again stacked in positive z direction and the overall mesh size was set to 0.1mm and one element per layer thickness. For this structure the illumination time was kept constant at 20s for all layers.

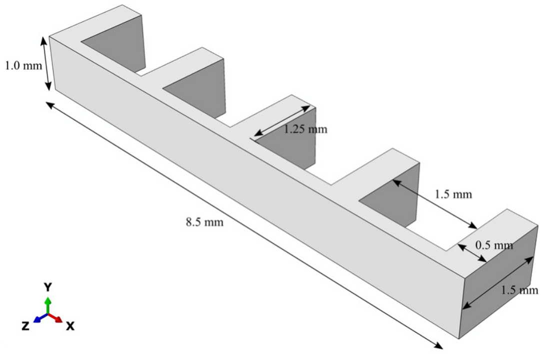

Figure 13: Dimensions of the bridge-like structure

Due to the geometry of the printed structure as well as the orientation during printing, a distinctive stress distribution, as shown in Figure 14a) developed before the build platform boundary condition was deactivated. At the top of the structure tensile stresses along the x direction were prominent, whereas on the surface between the pillars as well as on the side of the pillars compression stresses developed. Figure 14b) shows the resulting warpage of the structure based on the described stress distribution after the build platform boundary condition was deactivated. The overall deformation behaviour of this specific structure and print direction agrees well with results found in the literature [24].

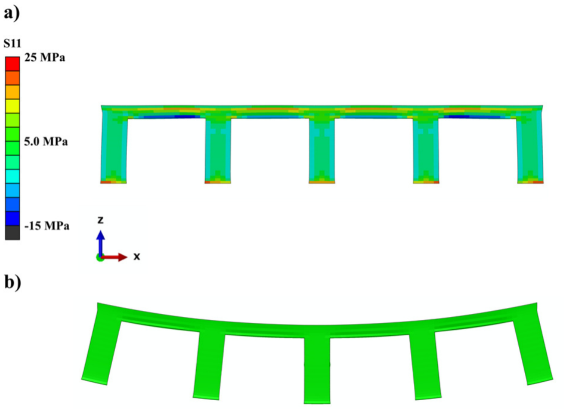

Figure 14: a) Residual stress in x direction bevor removing from the build platform b) warpage after removing from the build platform

To show a possible application of the framework regarding DLP printing of microelectronic parts, a PCB-like structure was set up to evaluate residual stresses and deformation after printing. The model is shown in Figure 15 and consists of a 10x5x0.5mm (x-y-z) plate with 0.1mm deep lanes cut into the top. The layers were again stacked in positive z direction and the overall mesh size was set to 0.25mm and one element per layer thickness. Layer illumination time was set to 10s.

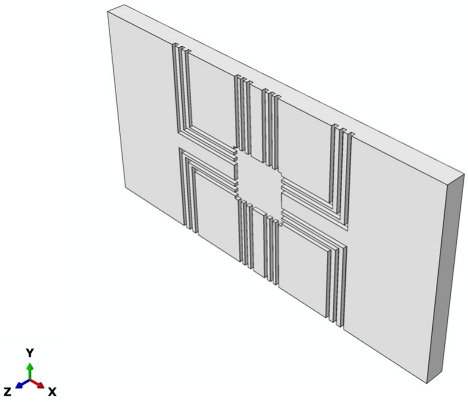

Figure 15: Geometry of the PCB-like structure

During actual DLP printing, the attachment of the part to the build platform is often improved by extending the illumination time of the first layer. In the simulation of the PCB-like structure this was considered by adding 20s to the illumination time of the first layer. The additional illumination time led to a gradient in degree of cure and thereby causing warpage of the structure. Figure 16 shows the deformed structure with a distinct increase of residual stress in x direction at the end of the simulation. The increased stresses mainly occurred at the surface of the lanes and at the bottom of the structure. In regard to multi material printing, the information about warpage and residual stresses could be used to evaluate the interface stress between conductive and non-conductive material and thereby assess the risk of delamination or detaching of conductive parts.

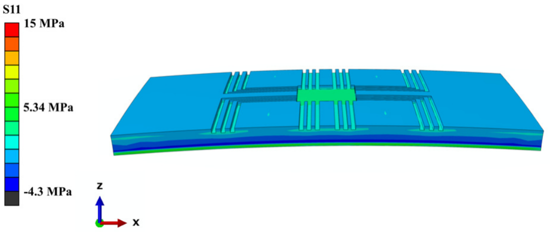

Figure 16: Residual stresses in x direction in the deformed PCB-like structure after printing

To test the capability of the presented framework to account for the print through effect, a simulation with a structure with a small circular and quadratic hole perpendicular to the print direction was set up. Figure 17 shows the dimension of the structure. The layers were again stacked in positive z direction and the overall mesh size was set to 0.1mm and one element per layer thickness. Layer illumination time was set to 10s.

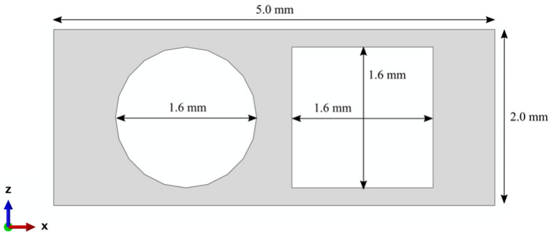

Figure 17: Dimensions of the geometry with small rectangular and circular channel

To account for the uncured resin surrounding the part, the local method described in section 5 was used. Looking at the resulting degree of cure and part geometry at the end of the simulation in Figure 18, a notable print through error can be seen. The rectangular channel as well as the circular channel decreased in height form 1.6mm to 1.37mm due to light penetration during printing of the layers on the topside of the channels. These results illustrate the capability of the framework to consider the effect of the print through error and are in good agreement with previous studies [24].

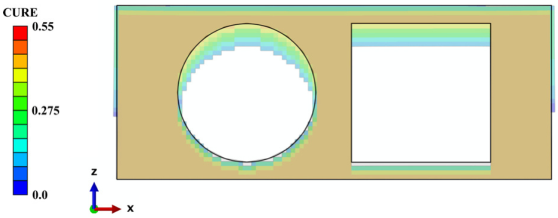

Figure 18: Degree of cure for the printed structure as well as a comparison between input geometry (black frame) and actual printed geometry

8. Conclusion

3D printing of microelectronic parts enables combining and integrating of different functions in a single package with a complex geometrical structure. To ensure the accuracy and thereby the function of the parts in the early design process a method to assess the process dependent deformation and imprecisions is necessary. In this study a modular simulation framework for the DLP 3D printing process was presented. The cure kinetics of a customized resin were characterized for the implementation in the framework. The capabilities to predict warpage after printing and imprecisions due to print through effects were evaluated on simple test geometries. Within the simulation approach the distribution of the degree of cure based on the illumination time of each layer as well as the related residual stresses driven by the chemical shrinkage could be predicted and used to assess the induced warpage after printing. Using an additional detailed local method, the framework was also used to account for curing inside of designed cavities due to light penetration through printed layers. The presented simulations show that the presented modular approach has a high potential to support the development of 3D printed electronics. Further research will focus on additional toolbox features and a validation against printing experiments on a multi-material DLP printer.

Acknowledgements

The research work was performed within the COMET-Module project "Chemitecture" (project-no.: 21647048) at the Polymer Competence Center Leoben GmbH (PCCL, Austria) within the framework of the COMET-program of the Federal Ministry for Transport, Innovation and Technology and the Federal Ministry for Digital and Economic Affairs with contributions by Montanuniversität Leoben, Technische Universität Dortmund, BTO-Epoxy GmbH, In-Vision Technologies AG and TDK Electronics AG. The PCCL is funded by the Austrian Government and the State Governments of Styria, Lower Austria and Upper Austria.

References

[1] I. Gibson, D. W. Rosen, and B. Stucker, *Additive Manufacturing Technologies*. Boston, MA: Springer US, 2010.

[2] B.-H. Lu, H.-B. Lan, and H.-Z. Liu, "Additive manufacturing frontier: 3D printing electronics," *Opto-Electronic Advances*, vol. 1, no. 1, pp. 1–10.

[3] A. H. Espera, J. R. C. Dizon, Q. Chen, and R. C. Advincula, "3D-printing and advanced manufacturing for electronics," *Prog Addit Manuf*, vol. 4, no. 3, pp. 245–267.

[4] P. F. Flowers, C. Reyes, S. Ye, M. J. Kim, and B. J. Wiley, "3D printing electronic components and circuits with conductive thermoplastic filament," *Additive Manufacturing*, vol. 18, pp. 156–163.

[5] S.-Y. Wu, C. Yang, W. Hsu, and L. Lin, "3D-printed microelectronics for integrated circuitry and passive wireless sensors," *Microsyst Nanoeng*, vol. 1, no. 1.

[6] E. Fantino *et al.,* "3D Printing of Conductive Complex Structures with In Situ Generation of Silver Nanoparticles," *Advanced materials (Deerfield Beach, Fla.)*, vol. 28, no. 19, pp. 3712–3717.

[7] G. Gonzalez *et al.,* "Development of 3D printable formulations containing CNT with enhanced electrical properties," *Polymer*, vol. 109, pp. 246–253.

[8] Q. Mu *et al.,* "Digital light processing 3D printing of conductive complex structures," *Additive Manufacturing*, vol. 18, pp. 74–83.

[9] D. Han and H. Lee, "Recent advances in multi-material additive manufacturing: methods and applications," *Current Opinion in Chemical Engineering*, vol. 28, pp. 158–166.

[10] H. Quan, T. Zhang, H. Xu, S. Luo, J. Nie, and X. Zhu, "Photo-curing 3D printing technique and its challenges," *Bioactive materials*, vol. 5, no. 1, pp. 110–115.

[11] C. Esposito Corcione, A. Greco, and A. Maffezzoli, "Photopolymerization kinetics of an epoxy-based resin for stereolithography," *J. Appl. Polym. Sci.*, vol. 92, no. 6, pp. 3484–3491.

[12] B. Golaz, V. Michaud, Y. Leterrier, and J.-A.E. Månson, "UV intensity, temperature and dark-curing effects in cationic photo-polymerization of a cycloaliphatic epoxy resin," *Polymer*, vol. 53, no. 10, pp. 2038–2048.

[13] M. M. Emami and D. W. Rosen, "An Improved Vat Photopolymerization Cure Model Demonstrates Photobleaching Effects," in *Proceedings of the 29th Annual International*.

[14] T. Rehbein, A. Lion, M. Johlitz, and A. Constantinescu, "Experimental investigation and modelling of the curing behaviour of photopolymers," *Polymer Testing*, vol. 83.

[15] V. Sipani, A. Kirsch, and A. B. Scranton, "Dark cure studies of cationic photopolymerizations of epoxides: Characterization of kinetic rate constants at high conversions," *J. Polym. Sci. A Polym. Chem.*, vol. 42, no. 17, pp. 4409–4416.

[16] V. Y. Voytekunas, F. L. Ng, and M. J.M. Abadie, "Kinetics study of the UV-initiated cationic polymerization of cycloaliphatic diepoxide resins," *European Polymer Journal*, vol. 44, no. 11, pp. 3640–3649.

[17] M. Atai and D. C. Watts, "A new kinetic model for the photopolymerization shrinkage-strain of dental composites and resin-monomers," *Dental materials : official publication of the Academy of Dental Materials*, vol. 22, no. 8, pp. 785–791.

[18] R. Brighenti, M. P. Cosma, L. Marsavina, A. Spagnoli, and M. Terzano, "Multiphysics modelling of the mechanical properties in polymers obtained via photo-induced polymerization," *Int J Adv Manuf Technol*, vol. 117, 1-2, pp. 481–499.

[19] K. N. Long, T. F. Scott, H. Jerry Qi, C. N. Bowman, and M. L. Dunn, "Photomechanics of light-activated

polymers," *Journal of the Mechanics and Physics of Solids*, vol. 57, no. 7, pp. 1103–1121.

[20] Lovell. Lale G., H. Lu, J. E. Elliotdt, J. W. Stansbury, and C. N. Bowman, "The effect of cure rate on the mechanical properties of dental resins," *Dental materials : official publication of the Academy of Dental Materials*, vol. 17, pp. 504–511.

[21] J. Wu *et al.,* "Evolution of material properties during free radical photopolymerization," *Journal of the Mechanics and Physics of Solids*, vol. 112, pp. 25–49.

[22] K. Gao, B.L.J. Ingenhut, A.P.A. van de Ven, F. O. Valega Mackenzie, and A. T. ten Cate, "Multiphysics modelling of photo-polymerization in stereolithography printing process and validation," in *Proceedings of the 2018 Comsol Conference in Lausanne*.

[23] S. Westbeek, J.J.C. Remmers, J.A.W. van Dommelen, H. H. Maalderink, and M.G.D. Geers, "Prediction of the deformed geometry of vat photo-polymerized components using a multi-physical modeling framework," *Additive Manufacturing*, vol. 40, no. 24.

[24] Q. Zhang *et al.,* "Design for the reduction of volume shrinkage-induced distortion in digital light processing 3D printing," *Extreme Mechanics Letters*, vol. 48, no. 3.

[25] Q. Ge, A. H. Sakhaei, H. Lee, C. K. Dunn, N. X. Fang, and M. L. Dunn, "Multimaterial 4D Printing with Tailorable Shape Memory Polymers," *Scientific reports*, vol. 6.

[26] B. Khatri, M. Frey, A. Raouf-Fahmy, M.-V. Scharla, and T. Hanemann, "Development of a multi-material stereolithography 3D printing device," *Micromachines*, vol. 11, no. 5.

[27] J. Šesták and G. Berggren, "Study of the kinetics of the mechanism of solid-state reactions at increasing temperatures," *Thermochimica Acta*, vol. 3, no. 1, pp. 1–12.

[28] S. R. White and H. T. Hahn, "Process Modeling of Composite Materials: Residual Stress Development during Cure. Part I. Model Formulation," *Journal of Composite Materials*, vol. 26, no. 16, pp. 2402–2422.

[29] O. Yuksel, M. Sandberg, I. Baran, N. Ersoy, J. H. Hattel, and R. Akkerman, "Material characterization of a pultrusion specific and highly reactive polyurethane resin system: Elastic modulus, rheology, and reaction kinetics," *Composites Part B: Engineering*, vol. 207, no. 26.

[30] N. Zobeiry, R. Vaziri, and A. Poursartip, "Computationally efficient pseudo-viscoelastic models for evaluation of residual stresses in thermoset polymer composites during cure," *Composites Part A: Applied Science and Manufacturing*, vol. 41, no. 2, pp. 247–256.

[31] W. Brostow, S. H. Goodman, and J. Wahrmund, "Epoxies," in *Handbook of Thermoset Plastics*: Elsevier, 2014, pp. 191–252.

Paper F

Thermomechanical and Electrical Material Characterization for a DLP Printing Process Simulation of Electrically Conductive Parts

Authors: Thalhamer, A.
Rossegger, E.
Hasil, S.
Hrbinic, K.
Feigl, V.
Pfost, M.
Fuchs, P.F.

2023 24th International Conference on Thermal, Mechanical and
Multi-Physics Simulation and Experiments in Microelectronics
and Microsystems (EuroSimE)
DOI: 10.1109/EuroSimE56861.2023.10100754

Thermomechanical and Electrical Material Characterization for a DLP Printing Process Simulation of Electrically Conductive Parts

A. Thalhamer[1], E. Rossegger[1], S. Hasil[1], K. Hrbinič[1], V. Feigl[1], M. Pfost[2], P. Fuchs[1]
[1]Polymer Competence Center Leoben GmbH (PCCL), Leoben, Austria
[2]TU Dortmund University, Chair of Energy Conversion, Dortmund, Germany
andreas.thalhamer@pccl.at

Abstract

Due to the steady development of conductive filled resins and multi-material techniques for the digital light processing (DLP) additive manufacturing technology, fabrication of complex conductive structures for microelectronic applications is becoming a potential use case for this technology. When processing electrically conductive systems, temperature effects are of special importance, as the highly filled systems often need elevated temperatures for an increase in reaction rate and to decrease viscosity to achieve printability. Thus, an accurate calculation of the temperature distribution during the process is needed for accurate process modeling. This study describes the thermomechanical material characterization and kinetic modelling including exothermic heat generation during curing for a thermal simulation as part of a DLP process simulation framework. The key properties for the simulation, such as specific heat capacity, thermal diffusivity and reaction enthalpy were characterized and compared between specifically developed conductive and non-conductive acrylic resins. In addition, the temperature dependent mechanical properties were studied and the electrical conductivity of the filled material was measured. A simulation was set up to calculate the heat generation due to the exothermic reaction during printing and the results were validated against measured data from printing trials with the non-conductive material. The results of this work show the temperature dependence of important properties of unfilled and electrically conductive materials for the thermal DLP process simulation and the capabilities of the proposed simulation strategy to calculate the temperature distribution during the process.

1. Introduction

Digital light processing (DLP) is an additive manufacturing technic based on the light induced polymerization of photo sensitive resins [1]. The illumination of a complete layer at once in combination with high resolution projectors result in the possibility to print models with small details and fast print speeds [2]. Other additive manufacturing methods have already stepped into the field of microelectronic parts production [3–6] and due to the development of conductive fillers [7–9] and multi material printing [10, 11], also the DLP method has become a candidate for printing of microelectronic structures. As a result of the complex nature of the DLP method, finding optimal process parameters for a good print quality is often a challenging task. Process simulations help to decrease the number of trial and error iterations and improve the printed part quality. Few different frameworks have been developed so far [12–16]. As highly filled systems often need elevated temperatures for an increase in reaction rate and to decrease viscosity, knowledge of the thermal material properties and temperature distribution during the process are key factors for a reliable DLP simulation. Characterization of mechanical properties [17–21] and curing kinetics [22–27] of photosensitive resins have been discussed in the literature. Other works also cover thermal characterization and temperature development during curing [28, 29]. The proposed study tries to extend the current state of the art by performing thermomechanical characterization of electrically conductive and non-conductive resins for modelling of a DLP process. Therefore, the specific heat capacity (c_p), the thermal diffusivity (α_t) and exothermic heat generation were characterized for specifically developed electrically conductive and non-conductive acrylic resins. Furthermore, a curing kinetic model was fitted with photo DSC data and bottom exposure test data from the non-conductive resin to complete the necessary input for the thermal DLP simulation. In addition, the electrical conductivity of the material was determined and the temperature dependent mechanical properties were studied. The acquired data was used to set up a thermal simulation framework for the curing process during a DLP process in the Finite Element Analysis (FEA) software Abaqus (Abaqus cae 2019 - Dassault Systèmes Simulia Corp). The framework includes the layer-by-layer buildup of the printed parts and an autocatalytic curing model to calculate the curing rate, the evolving degree of cure and the resulting exothermal heat generation. Validation of the thermal simulation was performed by comparing the results to temperature measurements taken from 3D printing experiments.

2. Material and methods

2.1. Material

The basic unfilled resin used in this work was optimized for overall fast curing behavior and good printability in combination with conductive fillers. Therefore, the formulation composes of the photoinitiator bisacylphosphine oxide (BAPO; purchased from Sigma Aldrich), 1,6-hexanediole diacrylate (HDDA; obtained from Allnex GmbH) and a commercially available resin (LIQCREATE clear impact - Liqucreate). To achieve electrical conductivity, 10, 14 and 18 V% Ag-coated dendritic copper particles (purchased from GGP Metalpowder AG) and 0.025 wt% carbon nanotubes (provided by bto-epoxy GmbH) were added to the base

979-8-3503-4597-1/23/$31.00 ©2023 IEEE

resin. The conductive material is referred to as filled and the non-conductive as unfilled.

2.2. Specific heat capacity

The c_p of the fully cured systems was determined using a differential scanning calorimeter (DSC4000 -Perkin Elmer Instruments LLC) with a reference sapphire sample. The unfilled resin samples were cured in an UV oven with 405nm (Form Cure - Formlabs GmbH) at 80°C for 1h. Curing of the filled material was done by activating the additional thermal initiator in the oven (T5042-Heraeus Noblelight GmbH) at 130°C for 3h. 30mg of the filled and unfilled resin were used respectively. The measurements were performed with a heating rate of 10K/min in a temperature range from 25°C and 95°C.

2.3. Thermal diffusivity

The diffusivity α_t of the cured systems was measured using a laser flash analysis system (LFA 467 HyperFlash - NETZSCH-Gerätebau GmbH). Four measurement points between 25°C and 100 °C were evaluated under nitrogen atmosphere with a spot size of 3.7 mm and a laser pulse width of 0.05 ms. Samples of the unfilled material were prepared by 3D printing (Photon Mono - Shenzhen Anycubic Technology Co., Ltd.) 1 mm thick circles with a diameter of 25 mm and post curing them for 1h at 80°C in a UV oven with 405 nm (Form Cure - Formlabs GmbH). For the filled material, 25 mm x 25 mm x 1 mm squares were molded and curing was achieved by activating the additional thermal initiator in the oven (T5042-Heraeus Noblelight GmbH) at 130°C for 3 h. Exemplary samples for both materials are shown in Figure 1.

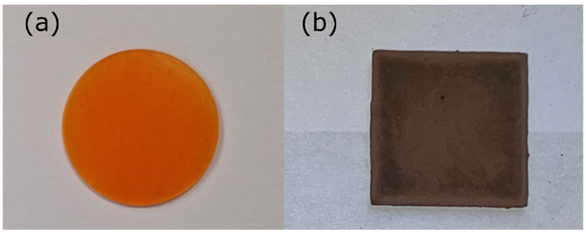

Figure 1: Exemplary samples of the (a) unfilled and (b) filled material for the LFA measurements.

2.4. Mechanical properties

The temperature dependent Young's modulus was measured with a dynamical mechanical analyzer (DMA/SDTA861e – Mettler – Toledo GmbH). The tests were performed in tensile mode with a frequency of 1 Hz and a maximal amplitude of 10 µm in a temperature range from 20°C to 200°C with the heating rate set to 2 K/min. The higher end temperature compared to the other test methods was chosen to capture the glass transition. For both materials the sample geometry was a 25 mm x 4 mm x 1 mm rectangle. Figure 2 shows an exemplary unfilled and filled sample. The unfilled samples were prepared by 3D printing (Photon Mono - Shenzhen Anycubic Technology Co., Ltd.) and post curing for 1h at 80°C in a UV oven with 405nm (Form Cure - Formlabs GmbH). The samples of the filled material were prepared by molding and cured by activating the additional thermal initiator in the oven (T5042-Heraeus Noblelight GmbH) at 130°C for 3h.

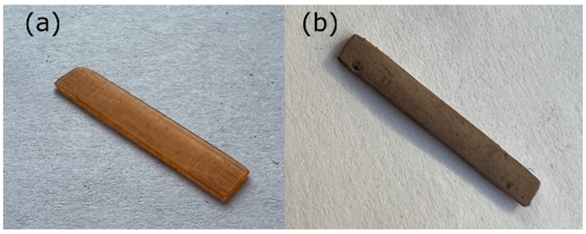

Figure 2: Exemplary sample of the (a) unfilled and (b) filled material for DMA testing.

2.5. Curing kinetics

The reaction enthalpy of the unfilled and filled material was measured using a photo DSC (DSC 204 F1 Phoenix - Erich NETZSCH GmbH & Co. Holding KG) coupled with a 200 W high pressure mercury lamp (Omnicure S2000 - Lumen Dynamics Group Inc) equipped with a 400-500 nm filter. A sample mass of 8 mg was used in open aluminum crucibles. Experiments were performed at 25°C and 35 mW/cm^2. The measurements were performed under nitrogen atmosphere. The following sequence of heating and illumination steps was followed for each measurement:

1. Heating to specified constant temperature
2. 5 min holding at the temperature to reach equilibrium
3. Start of measurement and 10 min illumination with given light intensity
4. 5 min pause
5. Again 10 min illumination with given light intensity to create reference curve for subtraction

To eliminate the influence of the cured material during evaluation, the heat flow output from step 5 was subtracted from step 2. The curing rate $\dot{\alpha}$ was calculated from the measured heat flow dH/dt and the maximal overall measured heat of reaction H_{max} with equation (1).

$$\dot{\alpha} = \frac{d\alpha}{dt} = \frac{dH/dt}{H_{max}} \tag{1}$$

For the evaluation of the decrease of light intensity through the thickness of the material and to get data of the printing times per layer height, bottom exposure test results were used. Therefore, circles with a diameter of 10 mm were printed with 7.9 mW/cm^2 at room temperature on a 3D printer without installed build platform (Dual Light Prototype 3D printer - W2P Engineering GmbH). Samples with various illumination times were produced and the thickness of each sample was measured.

2.6. Electrical conductivity

The specific conductivity of the filled material was determined with four-point (force and sense) measurements, the spacing of the four needles was 1 mm. Since the contact resistance was comparatively high with respect to the sample resistance, the voltage difference between the sense needles was rather small. Nevertheless, to achieve a high accuracy, a semiconductor parameter analyzer with four independent source-measurement channels was used, allowing full control over the two force needles to ensure that the voltages appearing at the two sense needles were always in the measurement range with the highest resolution. The samples were prepared by molding and cured by activating the additional thermal initiator in the oven (T5042-Heraeus Noblelight GmbH) at 130°C for 3h. The sample geometry was a 25 mm x 4 mm x 1 mm rectangle.

2.7. 3D printing for temperature validation

The experiments to validate the simulated temperature rise during printing were performed on a custom 3D printer with multi material capabilities (Doppio 3D printer - W2P Engineering GmbH) equipped with a high-performance light engine (Firebird Light Engine - In-Vision Technologies AG). Ambient temperature in the build chamber was measured with three integrated temperature sensors. The temperature during the curing of the resin was measured via a K-type thermocouple connected to a MCP9600 converter on a computer (Raspberry Pi 3B - Raspberry Pi Ltd). The thermocouple was calibrated as stated in [30]. The thermocouple was placed at the bottom of the vat (refer to Figure 3) and the temperature of the resin during curing was measured at 0.1 s intervals without a build platform present.

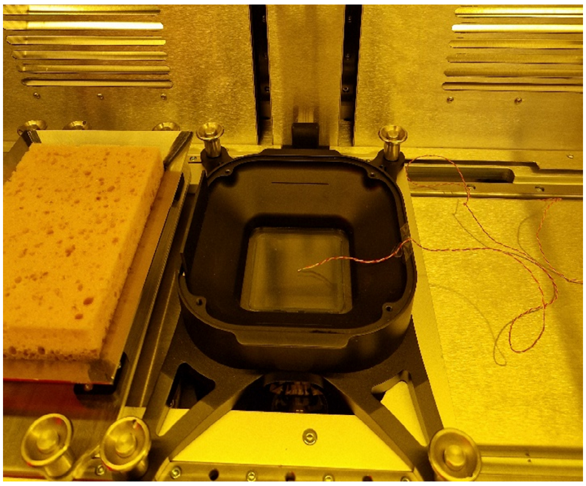

Figure 3: Setup for the validation measurements during printing with placement of the thermocouple inside the vat.

3. Simulation methodology

The thermal simulation approach, illustrated in this work, is part of a DLP process simulation framework developed in previous works [16]. The approach is based on the FE method with an included cure kinetics model to calculate the exothermic reaction enthalpy. In addition, a sequential element activation allows for the simulation of the layer-by-layer build up including evolving boundary conditions. The thermal simulation approach was implemented in the Abaqus FEA software and Figure 4 depicts the general functioning of the approach.

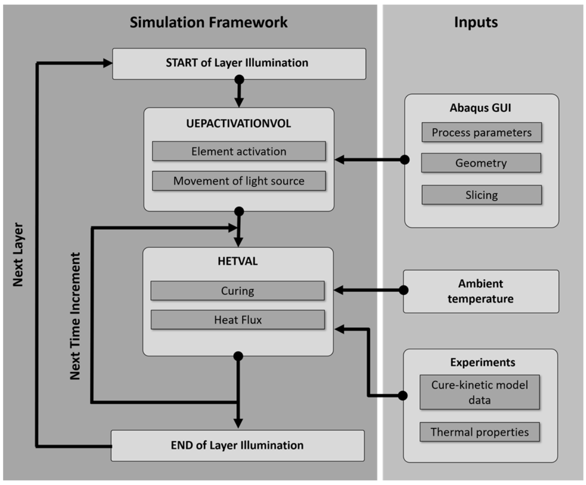

Figure 4: General workflow of the thermal part for the DLP process simulation framework.

For each layer of a sliced model, the UEPACTIVATIONVOL subroutine of the framework uses the given process parameter, geometric data and slicing information to activate the necessary elements and move the simulated light source to the right position. During the light illumination phase, the curing rate and the arising heat flux are calculated inside the HETVAL subroutine based on the temperature information and the thermal and curing properties of the current material. Each layer is solved in a separate time step and the temperature distribution is calculated using a transient heat transfer step in Abaqus.

3.1. Curing calculation

To calculate the curing and the associated heat generation in each integration point, a temperature and intensity dependent autocatalytic model, based on the work of Sesták and Berggren [31], was used. With addition of an intensity term and normalization with the maximum attainable degree of cure, the model can be applied to photopolymerization reactions [23]. Equation (2) shows the used formulation of the autocatalytic model with $\dot{\alpha}$ as the curing rate, α as the degree of cure, $\alpha_{\max}(I)$ as the intensity dependent maximal attainable degree of cure, $k(I(z),T)$ as the reaction rate constant and with n and m being reaction order and the autocatalytic exponent respectively.

$$\dot{\alpha} = k(I(z),T)\left(1-\frac{\alpha}{\alpha_{max}(I)}\right)^{n}\left(\frac{\alpha}{\alpha_{max}(I)}\right)^{m} \qquad (2)$$

The reaction rate constant describes the intensity and temperature dependent behavior of the reaction according to equation (3) and (4) respectively. Whereas equation (5) is used to describe the intensity dependence of the maximal attainable degree of cure $\alpha_{max}(I)$ with the fitting parameter a, b and c.

$$k(I(z),T) = k_0(T)I(z)^{\beta} \qquad (3)$$

$$k_0(T) = A\,exp\left(\frac{-E_a}{RT}\right) \qquad (4)$$

$$\alpha_{max}(I) = a + b * (1 - exp(\frac{-c * I}{1000})) \qquad (5)$$

The absorption of the light and the accompanied reduction of light intensity inside the layers can be described with the Beer-Lambert law [12, 14, 23] as stated in equation (6). This allows to calculate the intensity $I(z)$ depending on the distance z travelled in a medium and the corresponding absorption coefficient c_a.

$$I(z) = I_0 e^{-c_a z} \qquad (6)$$

3.2. Boundary conditions

Using equation (7) inside the HETVAL subroutine, the information of the current curing rate $\dot{\alpha}$,the overall maximal reaction enthalpy H_{max} and the density ρ in each integration point is used to calculate the internal volumetric heat flux $\dot{H}_V$ which is caused by the curing reaction.

$$\frac{dH_V}{dt} = \dot{H}_V = \dot{\alpha} * H_{max} * \rho \qquad (7)$$

To account for the surrounding resin around the printed part, a defined amount of additional "resin elements" around the printed part can be added. For the validation tests, no build platform is used, therefore on the sides and the top of model a fixed temperature boundary condition is applied to account for the temperature in the resin vat. At the bottom of the vat an anti-adhesion foil and a glass plate are located. They have been included with their respective specific heat, thermal conductivity and density values. Between the glass and the air in the chamber beneath the vat a surface film condition was used. The heat input caused by the light illumination was neglected due to its small influence compared to the heat input caused by the exothermic reaction. The used boundary conditions are presented in Figure 5.

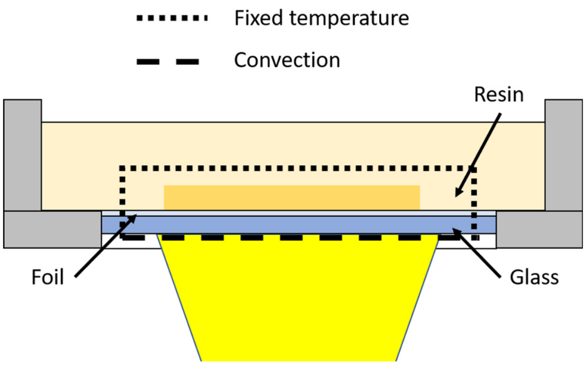

Figure 5: Boundary conditions for the validation simulations.

4. Results

4.1. Selection of filled system

To choose the right amount of conductive fillers for the electrically conductive resin, the printability was evaluated with bottom exposure tests and the electrical performance was tested by performing conductivity measurements. Figure 6 shows the results of the bottom exposure test for the filled system with 10 V%, 14 V% and 18 V% of the conductive fillers respectively. Between 10 V% and 14 V% only at 100 s illumination time a measurable difference in the resulting layer thickness was detected. Above 100 s there was no discernable difference between the materials with 10 V% and 14 V% regarding the measured thickness. The material with 18 V%, showed an overall lower thickness for all illumination times.

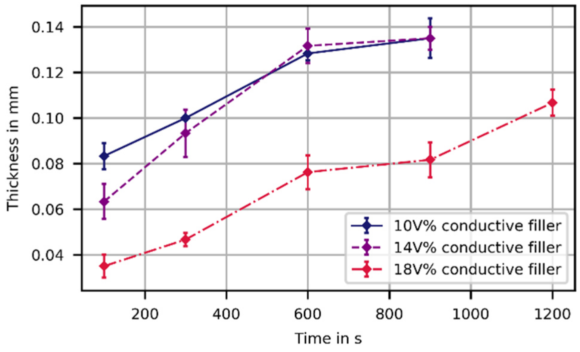

Figure 6 :Resulting thickness at various illumination times for the filled system with 10 V%, 14 V% and 18 V% conductive filler.

Figure 7 depicts the results of the electrical conductivity measurements. A clear trend for a decreasing conductivity with decreasing filler content is visible. Compared to other conductive resins in the literature, the proposed resin system has a higher conductivity than the reported resins with only carbon nanotubes used as fillers [8, 9] but lower conductivity values than a reported system with silver coated copper flakes [32]. To create the optimal compromise between printability and electrical conductivity, the system with 14 V% filler content was chosen and used for the remaining part of this study.

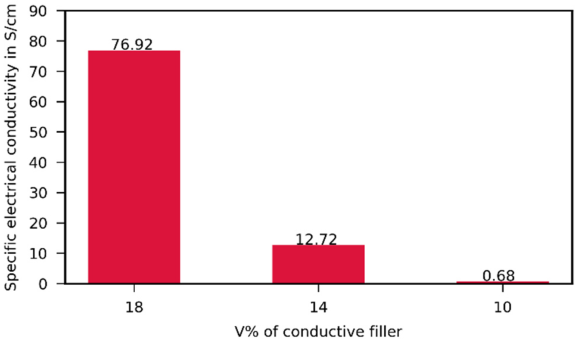

Figure 7: Results of the electrical conductivity measurements for the filled system with 10 V%, 14 V% and 18 V% of conductive filler.

4.2. Cure kinetics

The heat flow, measured in photo DSC experiments, was used to gain information about the internal heat generation during the reaction as well as the overall curing speed. For the comparison between the filled and unfilled material, photo DSC measurements were performed with isothermal conditions at 25°C with 35 mW/cm^2 light intensity for three filled and unfilled samples respectively. Figure 8 depicts a significant higher heat flow for the unfilled material than for the filled one. Regarding the printing process this means faster curing for the same layer height or a larger layer height in the same time for the unfilled material. It also signifies more heat generation during the printing. In the filled material, the fillers absorb or reflect light and thereby decrease the penetration depth of the light which leads to overall less material reacting or a slower reaction due to lower intensities. Furthermore, there is less reactive material in the same sample mass due to the additional fillers.

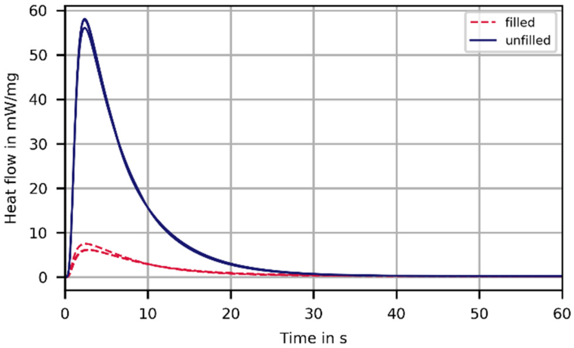

Figure 8:Heat flow of photo DSC measurements at 25°C and 35mw/cm^2 for filled and unfilled resin samples.

4.3. Thermal properties

The two major parameters for the proposed thermal simulation are the c_p and the thermal conductivity λ. The c_p was measured directly and the results are displayed in Figure 9. The c_p values are higher for the filled material with a decrease in difference between filled and unfilled material with rising temperatures. This behaviour is contrary to the expected decrease of c_p values for the filled system compared to the unfilled one [33]. In combination with the results of the DMA tests (refer to section 4.4) it is assumed that the samples were not fully cured and therefore exhibited the unexpected behaviour. λ was calculated via equation (8) and is depending on the thermal diffusivity α_t, the c_p and the density ρ of the material. Results of the measured values for α_t and calculated λ are shown in Figure 10 and Figure 11 respectively. The addition of metallic fillers led to a significant increase in thermal diffusivity over the entire measured temperature range. Under consideration of the densities and equation (8), this leads to an overall higher thermal conductivity of the filled material. This is explained by the high thermal conductivity of the metal filler in comparison to the unfilled material, leading to increased heat transfer whilst exhibiting poor heat retention [33].

$$\alpha_t(T) = \lambda * c_p(T) * \rho \qquad (8)$$

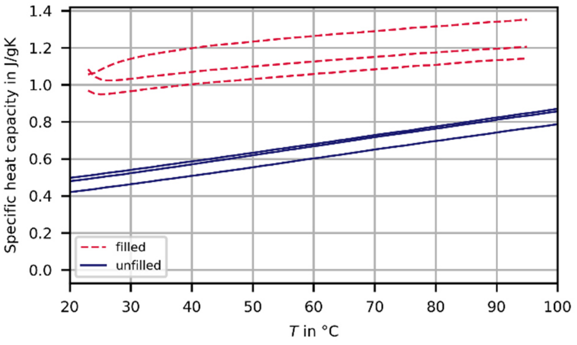

Figure 9: Results of the specific heat capacity measurements for filled and unfilled samples from 25°C to 95°C.

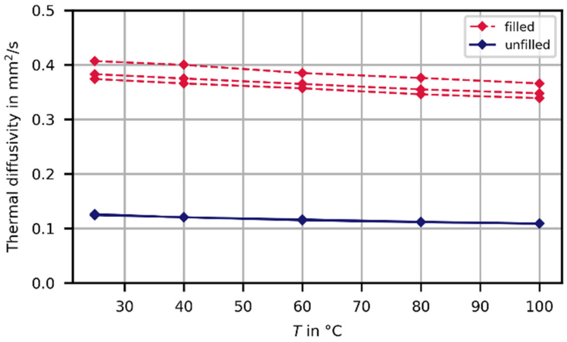

Figure 10: Results of the thermal diffusivity measurements for filled and unfilled samples from 25°C to 100°C.

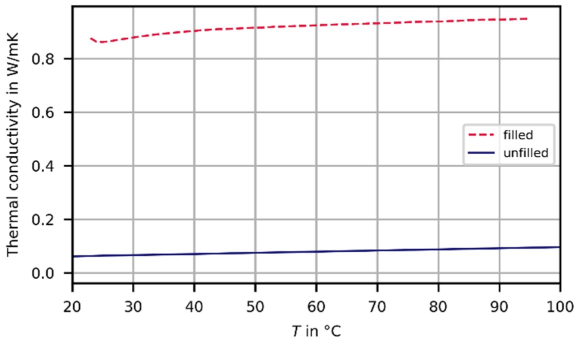

Figure 11: Results of the calculated thermal conductivity for filled and unfilled samples from 25°C to 95°C.

4.4. Mechanical properties

The mechanical properties themselves are not needed for the actual thermal simulation, but they are an important factor when choosing the material for an application. Furthermore, the thermomechanical properties act as input for the subsequent mechanical simulation which is described in [16]. Therefore, the results of DMA measurements were included in this study to show the effect of the conductive fillers on the thermomechanical properties and the corresponding data of the storage modulus E' is displayed in Figure 12. Three filled and unfilled samples were measured. From the unfilled ones only one gave valid results, the other failed prematurely. Regarding the modulus, the filled material shows a high variance, due to inhomogeneous particle distributions and surface defects caused by the molding process. All filled samples exhibited a lower modulus than the unfilled material up until about 170°C. This behavior is contrary to other findings in the literature [34–36], which report an increase in modulus for polymers filled with hard and rigid particles. In combination with the measured increase in modulus after 150°C and the results of the c_p measurements this leads to the assumption that the chosen curing procedure does not suffice to reach full cure.

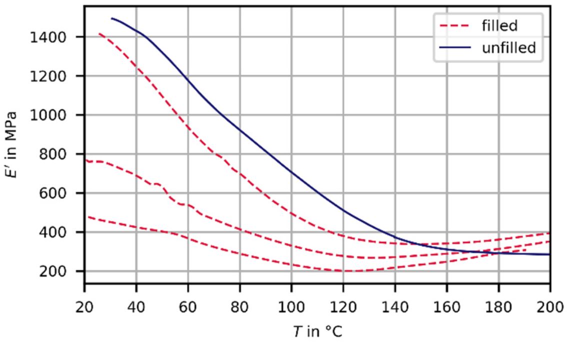

Figure 12: Storage modulus E′ over temperature from DMA measurements of the filled and unfilled material from 25°C to 200°C.

4.5. Thermal simulation of the printing process

In addition to the characterization of the thermal properties, a cure kinetics model is needed for the thermal simulations of the printing process. Therefore, the autocatalytic model, described in section 3.1, was fitted with photo DSC measurements of the unfilled material at different temperatures and light intensities. For the temperature dependency, testing was done with 35 mW/cm^2 at 25, 30, 40, 50, 60 and 70°C. To evaluate the intensity dependency testing was done at 25°C with 5, 15, 25, 35, and 45 mW/cm^2. To reduce the influence of decreasing light intensity inside the material sample, the sample mass was reduced to 2mg for the photo DSC measurements. The detailed method of fitting is described in [16] and the fitted parameter of the curing model are listed in Table 1. The fitted data for the temperature dependency is shown in Figure 13 (for better visibility only three temperatures are plotted).

Table 1: Fitted parameter for the autocatalytic curing model.

Parameter	**Value**
n	2.62
m	0.65
A	0.40 s^{-1}
E_a	45.94.84 $Jmol^{-1}$
β	0.16
a	0.48
b	0.49
c	243.27 cm^2mW^{-1}
c_a	7.45mm^{-1}

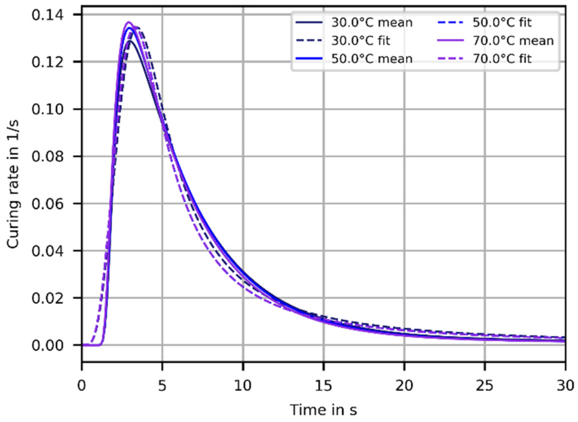

Figure 13: Photo DSC data and fitted cure kinetics model for various temperatures at 35mW/cm^2 for the unfilled material.

At the measured intensity the material showed only a small temperature dependency with similar curing rate curves for all temperatures and a better fit of the curing model at higher temperatures. The results at different intensities showed only a noticeable change in the curing rate beneath 15 mW/cm^2. The model has a good overall agreement with a better fit for lower intensities, as is shown in Figure 14 (for better visibility only three intensities are plotted). Due to the high reactivity of the developed material, the measured dependency of the curing rate on temperature and intensity is small compared to other work in the literature [37, 38]. To take the decrease of light intensity inside the material into account, the Beer-Lambert law (equation (6)) was fitted to bottom exposure tests. Figure 15 depicts the comparison between the bottom exposure tests and the fitted Beer-Lambert law for the thickness of the samples plotted over the illumination time. There is good agreement between model and measurements. The fitted absorption coefficient c_a is listed in Table 1.

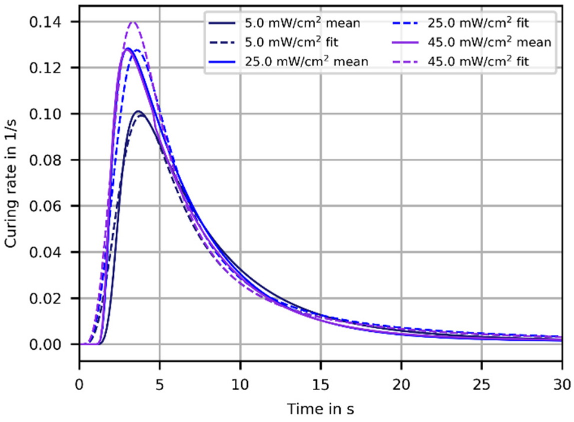

Figure 14: Photo DSC data and fitted cure kinetics model for various light intensities at 25°C for the unfilled material.

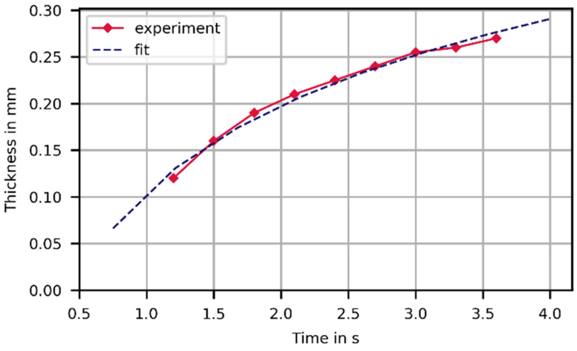

Figure 15: Comparison between bottom exposure test results and fitted Beer-Lambert model for the unfilled material.

To validate the proposed thermal modelling approach, a simulation for printing a simple 10 mm x 10 mm square without a build platform was set up. The model consists of a resin section, a foil section and a glass section and the boundary conditions are set as described in section 3.2. The model was meshed with an element side length of 0.5 mm in the X-Y plane and with 0.1 mm, 0.1 mm and 0.5 mm in Z direction in the resin, foil and glass sections respectively.

The model and the used mesh are shown in Figure 16(a) and Figure 16(b) respectively. The thermal material properties for the glass and foil are known and were used as constants without temperature dependency. For the resin section the characterized temperature dependent properties were used. For the curing model the parameters from Table 1 were used. The illumination was set to 35 mW/cm^2 for 10s. The averaged temperature along a path, representing the uninsulated part of the thermocouple inside the resin, was used to create the results for the comparison with the validation measurement from actual printing experiments. The position of the “virtual” thermocouple in the simulation model is shown in Figure 17.

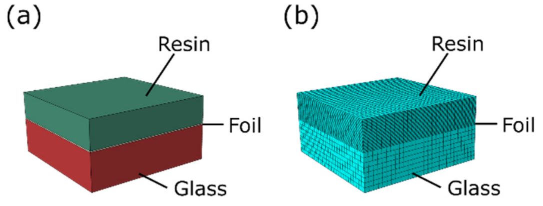

Figure 16: (a) Material sections and (b) mesh of the model for the validation simulation.

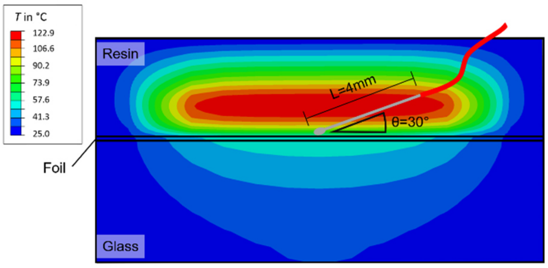

Figure 17: Position of the "virtual" thermocouple for the evaluation of the temperature during the simulation superimposed on the temperature distribution after 10 s illumination.

The height of the resin section was set to 3 mm based on a study with 5 different heights. The results are presented in Figure 18 and show the effect of the resin section height on the temperature evaluated along the specified path of the thermocouple during illumination. Above 3 mm thickness of the resin section, no influence of the boundary condition on the evaluated temperature could be seen. Using the stated parameter and model settings, the simulation was performed and the results were compared to the measurement of the actual printing process. The comparison between the simulation and the measurements is shown in Figure 19. One out of the three measurement curves deviate significantly from the other two at the end of the illumination. This was caused by extensive warping of the curing resin, which caused the thermocouple to be lifted slightly and therefore measuring lower temperatures. At the beginning of the illumination phase, the rise of temperature in the simulation lagged behind the measurement. However, the maximal temperature at the end of the illumination was in good agreement with the measurement. The overall rise in temperature during the illumination of the printing tests could be modeled with sufficient accuracy considering the simplifications used during modelling. Therefore, the results of the comparison illustrate the capability of the proposed thermal simulation strategy to model the temperature distribution during printing inside a DLP process simulation framework.

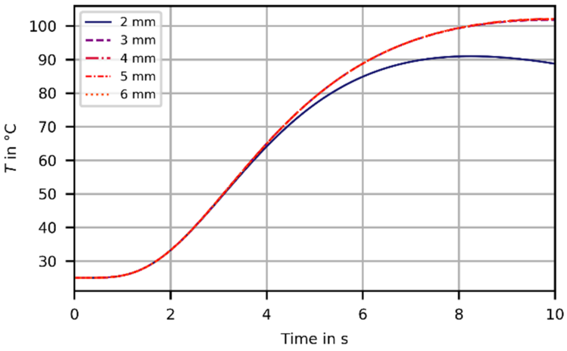

Figure 18: Averaged temperature along the virtual thermocouple during 10s illumination at 35mW/cm^2 for different resin section heights.

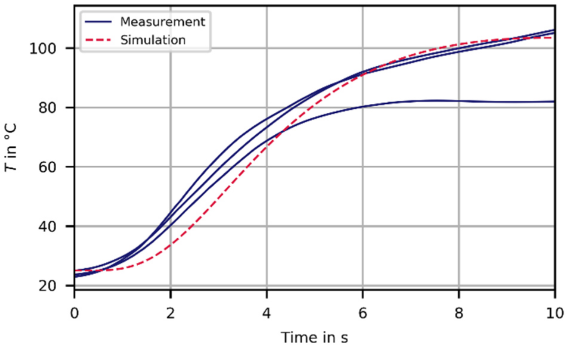

Figure 19: Comparison of the temperature development inside the unfilled resin for a 10s illumination period at 35mW/cm^2 between measurement and simulation.

Conclusions

Using the DLP method to manufacture microelectronic parts offers the possibility to integrate multiple functions into a single package using a single manufacturing step. To help with the complex design procedure, a reliable process simulation is necessary. One key parameter of printing and modelling highly filled electrically conductive resins is process temperature. In this study the thermomechanical and electrical material characterizations for selection and modelling of a specifically developed filled and unfilled 3D printing resin were performed and a thermal modelling strategy proposed. Adding 14V% of the electrically conductive filler to the base resin lead to a conductivity of 12.72 S/cm and a significant rise in thermal conductivity. Unexpected results for the mechanical properties as well as the c_p measurements were caused by not fully cured samples. For the unfilled material a simulation model was set up using the proposed methodology and the resulting temperature development inside the resin was validated against temperature measurements taken during a 3D printing experiment. Comparison between simulation and experiment showed an overall good agreement with small deviations at the start of the illumination. The addition of cure depending thermal properties could improve the results of the simulation and will be the focus of further studies.

Acknowledgments

The research work was performed within the COMET-Module project "Chemitecture" (project-no.: 21647048) at the Polymer Competence Center Leoben GmbH (PCCL, Austria) within the framework of the COMET-program of the Federal Ministry for Transport, Innovation and Technology and the Federal Ministry for Digital and Economic Affairs with contributions by Montanuniversität Leoben, Technische Universität Dortmund, BTO-Epoxy GmbH, In-Vision Technologies AG and TDK Electronics AG. The PCCL is funded by the Austrian Government and the State Governments of Styria, Lower Austria and Upper Austria.

References

[1] I. Gibson, D. W. Rosen, and B. Stucker, *Additive Manufacturing Technologies*. Boston, MA: Springer US, 2010.

[2] H. Quan, T. Zhang, H. Xu, S. Luo, J. Nie, and X. Zhu, "Photo-curing 3D printing technique and its challenges," *Bioactive materials*, vol. 5, no. 1, pp. 110–115.

[3] B.-H. Lu, H.-B. Lan, and H.-Z. Liu, "Additive manufacturing frontier: 3D printing electronics," *Opto-Electronic Advances*, vol. 1, no. 1, pp. 1–10.

[4] A. H. Espera, J. R. C. Dizon, Q. Chen, and R. C. Advincula, "3D-printing and advanced manufacturing for electronics," *Prog Addit Manuf*, vol. 4, no. 3, pp. 245–267.

[5] P. F. Flowers, C. Reyes, S. Ye, M. J. Kim, and B. J. Wiley, "3D printing electronic components and circuits with conductive thermoplastic filament," *Additive Manufacturing*, vol. 18, pp. 156–163.

[6] S.-Y. Wu, C. Yang, W. Hsu, and L. Lin, "3D-printed microelectronics for integrated circuitry and passive wireless sensors," *Microsyst Nanoeng*, vol. 1, no. 1.

[7] E. Fantino *et al.*, "3D Printing of Conductive Complex Structures with In Situ Generation of Silver Nanoparticles," *Advanced materials (Deerfield Beach, Fla.)*, vol. 28, no. 19, pp. 3712–3717.

[8] G. Gonzalez *et al.*, "Development of 3D printable formulations containing CNT with enhanced electrical properties," *Polymer*, vol. 109, pp. 246–253.

[9] Q. Mu *et al.,* “Digital light processing 3D printing of conductive complex structures,” *Additive Manufacturing*, vol. 18, pp. 74–83.

[10] D. Han and H. Lee, “Recent advances in multi-material additive manufacturing: methods and applications,” *Current Opinion in Chemical Engineering*, vol. 28, pp. 158–166.

[11] B. Khatri, M. Frey, A. Raouf-Fahmy, M.-V. Scharla, and T. Hanemann, “Development of a multi-material stereolithography 3D printing device,” *Micromachines*, vol. 11, no. 5.

[12] K. Gao, B.L.J. Ingenhut, A.P.A. van de Ven, F. O. Valega Mackenzie, and A. T. ten Cate, “Multiphysics modelling of photo-polymerization in stereolithography printing process and validation,” in *Proceedings of the 2018 Comsol Conference in Lausanne*.

[13] S. Westbeek, J.J.C. Remmers, J.A.W. van Dommelen, H. H. Maalderink, and M.G.D. Geers, “Prediction of the deformed geometry of vat photo-polymerized components using a multi-physical modeling framework,” *Additive Manufacturing*, vol. 40, no. 24.

[14] Q. Zhang *et al.,* “Design for the reduction of volume shrinkage-induced distortion in digital light processing 3D printing,” *Extreme Mechanics Letters*, vol. 48, no. 3.

[15] Y. Gao, L. Xu, Y. Zhao, Z. You, and Q. Guan, “3D printing preview for stereo-lithography based on photopolymerization kinetic models,” *Bioactive materials*, vol. 5, no. 4, pp. 798–807.

[16] A. Thalhamer, P. Fuchs, L. Strohmeier, S. Hasil, and A. Wolfberger, “A Simulation-Based Assessment of Print Accuracy for Microelectronic Parts Manufactured with DLP 3D Printing Process,” in *2022 23rd International Conference on Thermal, Mechanical and Multi-Physics Simulation and Experiments in Microelectronics and Microsystems (EuroSimE)*, St Julian, Malta, Apr. 2022 - Apr. 2022, pp. 1–11.

[17] R. Brighenti, M. P. Cosma, L. Marsavina, A. Spagnoli, and M. Terzano, “Multiphysics modelling of the mechanical properties in polymers obtained via photo-induced polymerization,” *Int J Adv Manuf Technol*, vol. 117, 1-2, pp. 481–499.

[18] K. N. Long, T. F. Scott, H. Jerry Qi, C. N. Bowman, and M. L. Dunn, “Photomechanics of light-activated polymers,” *Journal of the Mechanics and Physics of Solids*, vol. 57, no. 7, pp. 1103–1121.

[19] Lovell. Lale G., H. Lu, J. E. Elliotdt, J. W. Stansbury, and C. N. Bowman, “The effect of cure rate on the mechanical properties of dental resins,” *Dental materials : official publication of the Academy of Dental Materials*, vol. 17, pp. 504–511.

[20] J. Wu *et al.,* “Evolution of material properties during free radical photopolymerization,” *Journal of the Mechanics and Physics of Solids*, vol. 112, pp. 25–49.

[21] S. Y. Hong *et al.,* “Experimental investigation of mechanical properties of UV-Curable 3D printing materials,” *Polymer*, vol. 145, pp. 88–94.

[22] C. Esposito Corcione, A. Greco, and A. Maffezzoli, “Photopolymerization kinetics of an epoxy-based resin for stereolithography,” *J. Appl. Polym. Sci.*, vol. 92, no. 6, pp. 3484–3491.

[23] B. Golaz, V. Michaud, Y. Leterrier, and J.-A.E. Månson, “UV intensity, temperature and dark-curing effects in cationic photo-polymerization of a cycloaliphatic epoxy resin,” *Polymer*, vol. 53, no. 10, pp. 2038–2048.

[24] M. M. Emami and D. W. Rosen, “An Improved Vat Photopolymerization Cure Model Demonstrates Photobleaching Effects,” in *Proceedings of the 29th Annual International Solid Freeform Fabrication Symposium*.

[25] T. Rehbein, A. Lion, M. Johlitz, and A. Constantinescu, “Experimental investigation and modelling of the curing behaviour of photopolymers,” *Polymer Testing*, vol. 83.

[26] E. Andrzejewska, “Photopolymerization kinetics of multifunctional monomers,” *Progress in Polymer Science*, vol. 26, no. 4, pp. 605–665.

[27] Y. Li, Q. Mao, J. Yin, Y. Wang, J. Fu, and Y. Huang, “Theoretical prediction and experimental validation of the digital light processing (DLP) working curve for photocurable materials,” *Additive Manufacturing*, vol. 37, no. 2.

[28] M. Atai and F. Motevasselian, “Temperature rise and degree of photopolymerization conversion of nanocomposites and conventional dental composites,” *Clinical oral investigations*, vol. 13, no. 3, pp. 309–316.

[29] K. Sekmen, T. Rehbein, M. Johlitz, A. Lion, and A. Constantinescu, “Thermal analysis and shrinkage characterization of the photopolymers for DLP additive manufacturing processes,” *Continuum Mech. Thermodyn.*, vol. 1, no. 4, p. 593.

[30] D. Rapp, “On the viability of the Laser Flash method for fast and total thermal characterisation of polymers,” Master-Thesis, Chair of Material Science and Testing of Polymers, Montanuniversität Leoben, Leoben,Austria, 2021.

[31] J. Šesták and G. Berggren, “Study of the kinetics of the mechanism of solid-state reactions at increasing temperatures,” *Thermochimica Acta*, vol. 3, no. 1, pp. 1–12.

[32] S.-C. Tsai, L.-H. Chen, C.-P. Chu, W.-C. Chao, and Y.-C. Liao, “Photo curable resin for 3D printed conductive structures,” *Additive Manufacturing*, vol. 51, no. 4.

[33] B. Özbay, A. Bekem, İ. E. Serhatlı, S. Öztürk, and M. E. Bulduk, “Effects of copper fillers on mechanical and electrical properties of selective laser sintered PA 12-Cu composites,” *Materials Technology*, vol. 37, no. 10, pp. 1541–1553.

[34] D. Pinto, L. Bernardo, A. Amaro, and S. Lopes, “Mechanical properties of epoxy nanocomposites

using titanium dioxide as reinforcement – A review," *Construction and Building Materials*, vol. 95, no. 2, pp. 506–524.

[35] G. J. Papakonstantopoulos, M. Doxastakis, P. F. Nealey, J.-L. Barrat, and J. J. de Pablo, "Calculation of local mechanical properties of filled polymers," *Physical review. E, Statistical, nonlinear, and soft matter physics*, vol. 75, 3 Pt 1.

[36] S.-Y. Fu, X.-Q. Feng, B. Lauke, and Y.-W. Mai, "Effects of particle size, particle/matrix interface adhesion and particle loading on mechanical properties of particulate–polymer composites," *Composites Part B: Engineering*, vol. 39, no. 6, pp. 933–961.

[37] A. Maffezzoli and R. Terzi, "Effect of irradiation intensity on the isothermal photopolymerization kinetics of acrylic resins for stereolithography," *Thermochimica Acta*, vol. 321, 1-2, pp. 111–121.

[38] M. C. Rusu, C. Block, G. van Assche, and B. van Mele, "Influence of temperature and UV intensity on photo-polymerization reaction studied by photo-DSC," *J Therm Anal Calorim*, vol. 110, no. 1, pp. 287–294.